Tunable supercontinuum source for fluorescence spectroscopy

Roger William Peter Fenske

Submitted for the degree of Doctor of Engineering

Heriot-Watt University

School of Engineering and Physical Sciences

October 2014

ABSTRACT

This thesis describes the experimental investigations concerning the integration and optimisation of a supercontinuum source into a fluorescence lifetime spectrometer. [Fluorescence lifetime spectrometers based on Time Correlated Single Photon Counting (TCSPC) have long suffered from the lack of a compact, broadband excitation source. The source should ideally emit picosecond pulses with a repetition rate adjustable up to megahertz. Supercontinuum sources are an ideal candidate.]

Various commercial supercontinuum sources were evaluated. Initial work was carried out on a source with a standard endlessly single-mode photonic crystal fibre (PCF) with a short wavelength limit of 450 nm, followed by later work with a source using high-Δ PCF (a PCF with a large air filling fraction), that had an emission down to 400 nm, and a prototype source with a tapered fibre that had emission to ~320 nm. Key parameters including pulse width, pulse position and pulse height distribution were found to be very wavelength dependent, and their behaviour is explained by theory. The measured pulse widths of the supercontinuum sources were found to be typically ~100 ps, with longer durations found at the blue extreme of the spectra. Analysis of the data showed that this was due to the broadened pulses being a superposition of two pulse sequences with different dispersion characteristics. It was shown that, by taking account of the particular optical and temporal properties of a supercontinuum source, it was possible to make high quality fluorescence lifetime measurements of standard fluorophores such as fluorescein, anthrascene and erythrosine B.

A novel device was constructed and evaluated for the wavelength separation of a supercontinuum source based on wedge interference filters. Initial prototypes of the device were able to measure the fluorescence emission spectra of common fluorophores and adequately separate a supercontinuum. Further iterations of the design, employing multiple filters, allowed for the construction of a device that included bandwidth control. The device allowed the transmission bandwidth to be tuned from ~6 nm to >50 nm with a transmission of >70 % for bandwidths >8 nm. The transmission figures achieved are better than any alternative form of wavelength separation, for example devices based on acousto-optic tunable filters (AOTFs) and diffraction gratings.

A novel monochromator for fluorescence studies was also constructed using a wedge interference filter simultaneously with a diffraction grating. The design had improved

performance compared to a single grating based monochromator in terms of stray light, with only a small drop in throughput and no change in instrument footprint. The stray light performance was found to be comparable to that of a double monochromator over the spectral range of the filter.

ACKNOWLEDGEMENTS

First of all I would like to thank my academic supervisor Professor Derryck Reid for his helpful advice, proofing skill and for nudging me towards finishing the thesis. I am indebted to Dr Richard Dennis for his support over many, many years and for sticking with this project beyond a well-deserved retirement. I would also like to thank Professor S. Desmond Smith for his help and advice. His considerable knowledge of and experience with interference filters was invaluable.

I would like to thank Professor Richard Warburton for his support in the initial stages of this project.

I would like to thank Dr Dirk Näther whose creativeness, ingenuity and enthusiasm was very much appreciated. I am also grateful to Dr Andrew Dick for his programming expertise and everyone else at Edinburgh Instruments who supported me during this project.

I also thank Fianium, particularly Dr Adam Devine for measuring the band edge steepness of the filters and Dr John Clowes.

Parts of this work were supported by the Technology Strategy Board under the "Advanced White Light Fibre Laser and Applications in Medical Imaging (WhiteLase)" Programme.

ACADEMIC REGISTRY
Research Thesis Submission

Name*:*	Roger Fenske		
School/PGI:	Engineering and Physical Sciences		
Version: *(i.e. First, Resubmission, Final)*	Final	Degree Sought (Award **and** Subject area)	Doctor of Engineering in Photonics

Declaration

In accordance with the appropriate regulations I hereby submit my thesis and I declare that:

1) the thesis embodies the results of my own work and has been composed by myself
2) where appropriate, I have made acknowledgement of the work of others and have made reference to work carried out in collaboration with other persons
3) the thesis is the correct version of the thesis for submission and is the same version as any electronic versions submitted*.
4) my thesis for the award referred to, deposited in the Heriot-Watt University Library, should be made available for loan or photocopying and be available via the Institutional Repository, subject to such conditions as the Librarian may require
5) I understand that as a student of the University I am required to abide by the Regulations of the University and to conform to its discipline.

* *Please note that it is the responsibility of the candidate to ensure that the correct version of the thesis is submitted.*

Signature of Candidate*:*		Date:	

Submission

Submitted By *(name in capitals):*	ROGER FENSKE
Signature of Individual Submitting:	
Date Submitted:	

For Completion in the Student Service Centre (SSC)

Received in the SSC by *(name in capitals):*			
Method of Submission *(Handed in to SSC; posted through internal/external mail):*			
E-thesis Submitted (mandatory for final theses)			
Signature:		Date:	

TABLE OF CONTENTS

LIST OF FIGURES

LIST OF PUBLICATIONS

Year	Type	Full reference
2006	C	R. Fenske, D. Näther, M. Goossens, and S. Smith, "New light sources for time-correlated single-photon counting in commercially available spectrometers," Opt. East 2006, 2006.
2006	C	D. Nather, R. Fenske, R. Hurteaux, S. Majno, and S. Smith, "Time-correlated single photon counting: an advancing technique in a plate reader for assay development and high throughput screening," PROCEEDINGS-SPIE, 2006.
2009	P	Roger Fenske, Dirk U. Näther, Richard B. Dennis and John Clowes "The Supercontinuum Laser as a Flexible Source for Quasi-Steady State and Time Resolved Fluorescence Studies" Methods and Applications of Fluorescence, 2009
2009	O	"The supercontinuum laser as a flexible source for quasi-steady state and time resolved fluorescence studies," FLIM09, 2009
2010	C	R. Fenske, D. Näther, R. Dennis, and S. Smith, "The supercontinuum laser as a flexible source for quasi-steady state and time resolved fluorescence studies," *SPIE LASE,* 2010.
2010	X	R. Fenske, D. Nather, and S. Smith, "Monochromator comprising variable wavelength selector in combination with tunable interference filter," *US Pat. App. 13/123,931*, 2009.

Types of output:

C = conference proceeding

O = oral conference paper

P = poster conference paper

X = patent application

CHAPTER 1 - INTRODUCTION

Fluorescence spectroscopy involves measuring the wavelength dependence of the interaction between a sample and light. The sample is excited with light of a particular wavelength, some of the light is absorbed by the sample and re-emitted at a longer wavelength as a result of molecular processes. Studying the spectral properties of the absorption and emission can reveal information about these processes and the structure of the molecule. Fluorescence lifetime spectroscopy adds an extra dimension by measuring the average time a molecule stays in the excited state before emitting a photon and returning to the ground state.

Edinburgh Instruments manufacture high-end steady-state and lifetime fluorescence spectrometers. It is important to the company that they continue to innovate, in order to develop improved products. The aim at the beginning of this project was to investigate new technologies that could be used to improve the flexibility and sensitivity of their products.

This chapter will introduce the processes and techniques of fluorescence lifetime spectroscopy. It will review the current excitation sources used and introduce a new possible source, based on the supercontinuum effect that offers superior flexibility. It will also introduce a method of wavelength separation involving interference filters that could offer benefits in terms of sensitivity.

The experiments and research described in this thesis led to the first published work on the application of commercial supercontinuum sources in fluorescence spectroscopy, the first paper explaining the technical considerations of using a supercontinuum source with fluorescence lifetime spectrometers and a second paper, expanding the work, and with a description of wavelength and bandpass control of a supercontinuum with wedge interference filters. The output from this thesis also led to the first commercial monochromator product for wavelength and bandpass control of supercontinuum sources based on variable interference filters. The product has since been optimised further leading to dozens of units sold both as a component integrated into Edinburgh Instruments fluorescence spectrometers and as an OEM product. Fluorescence spectrometers with a combination of grating and variable interference filters for improved stray light rejection have also been sold into the market as beta test units.

1.1 Fluorescence lifetime spectroscopy

1.1.1 Theory

The emission of "cold" light from any substance is known as luminescence and occurs from electronically excited states. Photoluminescence is the emission caused by the absorption of light and can be separated into two categories: phosphorescence and fluorescence. Phosphorescence is the emission of light from a triplet excited state i.e. the excited electron has the same spin orientation as its corresponding ground state electron (see Figure 1.1). Direct transitions to the ground state are forbidden [1] and the emission rates are slow (10^3-10^0 s^{-1}), this means that phosphorescence lifetimes are generally of the order of milliseconds to seconds.

Fluorescence occurs in systems with singlet excited states, that is to say, the electron in the excited orbital has opposite spin (is paired) to the second electron in the ground state. In this case, the return of the electron to the ground state is spin-allowed and may occur rapidly by the emission of a photon (see Figure 1.1). The emission rates of fluorescence are fast (typically of the order of 10^8 s^{-1}), therefore a typical fluorescence lifetime is ~10 ns; however this value can vary from hundreds of nanoseconds to tens of picoseconds depending on the fluorophore (fluorescent substance). Most fluorophores are aromatic molecules although there are exceptions such as lanthanide elements.

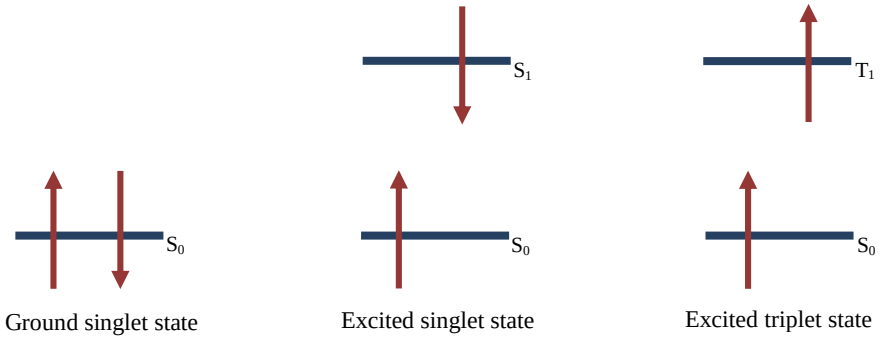

Figure 1.1 Spin of the outer electrons of molecules in the ground state and excited singlet and triplet states. Transition from the triplet excited state to the ground state involves a change in electronic state which is more improbable (and therefore slower).

One of the first observations of fluorescence was made on a solution of quinine in sunlight by Sir John Frederick William Herschel in 1845 [2]. Almost one hundred years later it was the desire to monitor quinine and other substances as antimalarial drugs that led to the development, by the United States Department of Defence, of the first practical fluorescence spectrometer [3].

The meaning of the lifetime of a fluorophore is best represented by a Jabłoński diagram [4], see Figure 1.2. This diagram shows the energy required to excite a fluorophore from the ground state (S_0) to the first excited state (S_1), the relaxation of the molecule to the lowest vibrational level of S_1 and the possible routes that the molecule may take to get back to the ground state. The lifetime of the excited state is defined by the average time the molecule spends in the excited state prior to return to the ground state. For the fluorophore in Figure 1.2, the lifetime is given by Equation (1.1) [5]:

$$\tau = \frac{1}{\Gamma + k_{nr}} \tag{1.1}$$

Where Γ is the radiative decay rate constant and k_{nr} is the non-radiative decay rate constant.

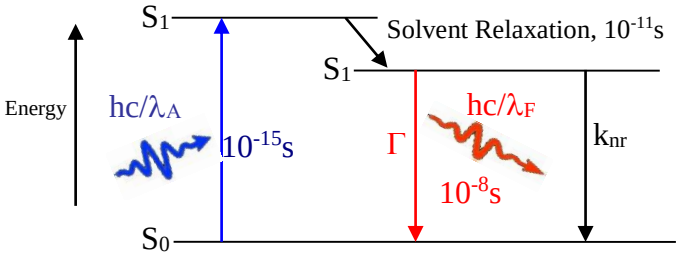

Figure 1.2 Jabłoński diagram of fluorescence

The lifetime, where there are no nonradiative processes present, is known as the intrinsic or natural lifetime and is simply the inverse of the fluorescence decay rate constant given by Equation (1.2).

$$\tau_n = \frac{1}{\Gamma} \tag{1.2}$$

The lifetime of a fluorophore is directly related to the rate at which the observed fluorescence intensity decreases following an excitation pulse. A sample of fluorophore excited with a delta function shaped pulse of light results in an initial population (n_0) of fluorophores in the excited state. The excited–state population decays with a rate dependent on the decay rate constants of the fluorophore and is given by Equation (1.3)

$$\frac{dn(t)}{dt} = -(\Gamma + k_{nr})n(t) \tag{1.3}$$

Where $n(t)$ is the number of excited molecules at time t following excitation.

The emission is a random event and each excited fluorophore has the same probability of emitting in a given period of time. Equation (1.3) may be combined with Equation (1.1), integrated and then written in terms of time dependent intensity to yield the expression for a single exponential decay (Equation (1.4)).

$$I(t) = I_0 e^{-\frac{t}{\tau}} \tag{1.4}$$

where I_0 is the intensity at time t=0 after excitation.

The fluorescence quantum yield is the ratio of the number of photons emitted to the number of photons absorbed (Equation (1.5)).

$$QY = \frac{\sum \varepsilon}{\sum \alpha} \tag{1.5}$$

where α is the photons absorbed and ε is the photons emitted.

The quantum yield can also be described as the probability that an excited state fluorophore will emit a photon. The excited state is depopulated by radiative and non-radiative processes, therefore the quantum yield is also the fraction of fluorophores that will decay through emission (Figure 1.2) i.e. the quantum yield can also be given by Equation (1.6).

$$QY = \frac{\Gamma}{\Gamma + k_{nr}} \tag{1.6}$$

The intensity and lifetime of fluorescence can be quenched by many different processes; this has the effect of decreasing the fluorescence intensity emitted (reducing the quantum yield) and shortening the lifetime. Quenching can occur by different mechanisms. Collisional quenching is illustrated in Figure 1.3, it occurs when the excited state fluorophore is deactivated upon contact with some other molecule in solution. Looking at Figure 1.3 and Equation (1.1), it is clear that extra non-radiative molecular processes in general will have the effect of altering the quantum yield and the lifetime. In Figure 1.3 the fluorophore is returned to the ground state during a diffusive encounter with a quencher [5]. The rate constant of fluorescence quenching depends linearly on the concentration of the quencher. Typical fluorescence quenchers are oxygen, heavy metal ions, halogens and a variety of organic molecules. The mechanism of quenching can vary, for instance quenching by heavy metal ions and halogens occurs due to spin-orbit coupling and intersystem crossing to triplet states.

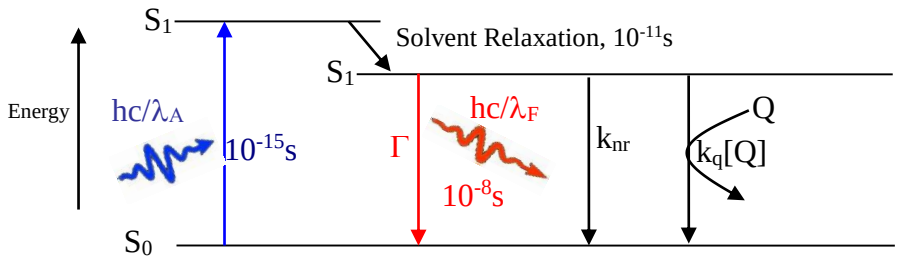

Figure 1.3 Jabłoński diagram with quenching

Other processes can also alter the decay rate of an excited state molecule, such as Förster Resonance Energy Transfer (FRET), discovered by Theodor Förster in 1946 [6]. FRET is an interaction of two molecules in which the emission band of one molecule (known as the donor) overlaps the absorption band of the other (known as the acceptor). When FRET occurs the energy of the excited donor molecule transfers immediately into the acceptor molecule. The energy transfer process does not involve any light absorption or emission; instead the donor and acceptor are coupled by a dipole-dipole interaction i.e. there is no intermediate photon. A Jabłoński diagram showing the FRET process is shown in Figure 1.4. The extent of the energy transfer is determined by the distance between the donor and acceptor and the extent of the spectral overlap between the emission spectrum of the donor and the absorption spectrum of the acceptor. The rate of the energy transfer $k_T(r)$ is given by Equation (1.7).

$$k_T(r) = \frac{1}{\tau_D}\left(\frac{R_0}{r}\right)^6 \qquad (1.7)$$

where R_0 is the Förster distance, r is the distance between the donor and the acceptor and τ_D is the lifetime of the donor (when there is no energy transfer taking place).

The Förster distance is the distance at which the resonance energy transfer efficiency is 50 % efficient (typically 2 – 6 nm) [6]. At the Förster distance ($r=R_0$) the donor emission will have halved and at increasing distance the energy transfer rate from the donor to the acceptor decreases with the sixth power of the distance (r^{-6}) and is therefore only noticeable at distances shorter than 10 nm. This happens to be comparable in size to biological macromolecules, meaning that FRET can be used as a ruler for measuring distances in biological samples (Section 1.1.2).

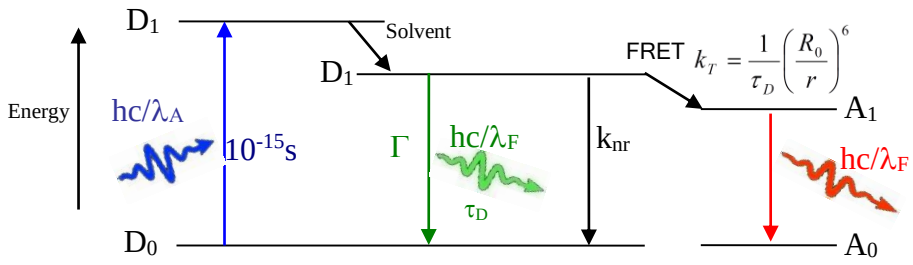

Figure 1.4 Jabłoński diagram with FRET showing the energy levels of the donor (D) and acceptor (A) molecules

1.1.2 Why measure the fluorescence lifetime

Steady-state measurements are generally simpler and require less complex electronics than time resolved measurements. However, time resolved measurements can lead to a deeper understanding of the processes being investigated. Steady-state measurements give an average of the time-resolved phenomena over the intensity decay of the sample and much of the molecular information available from fluorescence is lost during the time averaging process. Macromolecules can frequently exist in more than a single conformation and the decay time of the bound probe may depend on this conformation. Time-resolved measurements may reveal a double exponential decay (i.e. two decay times) and thus the presence of more than one conformational state; whereas the steady-state intensity would only reveal an average intensity, dependent on a weighted average of the two decay times.

For almost all fluorophores the fluorescent lifetime depends on the concentration of ions, on the oxygen concentration and on the pH. There are many other reasons for measuring the time-resolved fluorescence of fluorophores. In the presence of energy transfer, decay information can reveal how the acceptors are distributed around the donor molecules. Many fluorescent molecules have a protonated and a deprotonated form, the spectra of these different forms can be virtually identical, however, the fluorescent lifetimes may be different. Time-resolved information can also reveal whether quenching is due to complex formation with the ground state fluorophores, or due to diffusion. Therefore, in fluorescence, a great deal of the molecular information content is available only by making time-resolved measurements. In time resolved measurements, unlike steady state measurements, the results are largely insensitive to photobleaching. Photobleaching occurs when a fluorophore permanently loses the ability to fluoresce due to photon-

induced chemical damage and covalent modification. The average power of light incident during short pulsed excitation is far lower than in continuous illumination, therefore there is less likelihood of photoinduced damage to the molecule.

Quenching of the fluorescence intensity can occur by a variety of non-molecular mechanisms that may be of no interest to a researcher: such as attenuation of the incident light by the fluorophore itself or by some other absorbing species or by some change in the sensitivity of the instrument. Such issues do not affect the fluorescence lifetime.

The most important point for biological applications is that the fluorescent lifetime of dyes depends more or less on the binding to proteins, DNA or lipids [5], [7], [8]. The lifetime can therefore be used to probe the local environment of the dye molecules on a molecular scale, independently of the concentration of the fluorescing molecules. This is of great benefit for biological samples, where the dye concentration is often unknown or inhomogeneous.

The technique of time resolved fluorescence spectroscopy can be used along with the phenomenon of FRET (see previous section) as the sizes of biological macromolecules are comparable to the distance over which FRET can occur [9]. Measuring the amount of FRET taking place can be used to study the binding states of proteins in immunoassays by labelling different proteins with the donor and acceptor. When FRET occurs the lifetime of the fluorescence decay of the acceptor changes toward that of the donor, therefore monitoring the ratio of the acceptor fluorescence lifetimes where FRET occurs, to the lifetimes where there is no FRET, can indicate the amount of protein binding occurring in a sample. In addition, FRET can be used as a spectroscopic ruler for measuring the distances between sites on proteins [10]. Work is continuing into biological applications using fluorescence lifetime measurement techniques such as with employing fluorescence lifetime plate-readers [11].

1.1.3 Lifetime measurement techniques

Two methods of measuring time-resolved fluorescence are in widespread use and operate in either the time domain or the frequency domain. In the time domain technique the time-dependent intensity is measured following the excitation pulse and the decay time may be calculated from the time it takes for the intensity to decease to e^{-1} (~ 37 %) of its initial value, i.e. the measured intensity is directly related to the intensity decay from the fluorophores (Equation (1.4)). The most common technique employed in the time domain

is known as time correlated single photon counting (TCSPC). In the frequency-domain, or phase-modulation method, the sample is excited with intensity-modulated light (typically a sine wave modulation). The intensity of the light is varied at a high frequency in comparison to the reciprocal of the decay time. When a fluorescent sample is excited in this manner, the emission is at the same frequency; however, the emission frequency is phase shifted due to the lifetime of the sample. The lifetimes can then be determined by measuring the phase-shift between excitation and emission and the degree of modulation [12].

The techniques of phase modulation and the time-resolved pulsed excitation fluorescence are basically interchangeable via a Fourier Transform (FT), the Fourier transform of a sine wave gives a pulse and vice-versa [13]. The most relevant difference between TCSPC and the phase technique is that TCSPC works at extremely low emission intensity but cannot exploit high intensities, the reverse is true for the phase technique.

The principle of TCSPC is the detection of single photons and the measurement of their arrival times in respect to a reference signal (usually from the light source) [14], [15], [16], [17]. It makes use of the fact that the probability of detecting one photon in one signal period is far less than one, therefore it is not necessary to provide for the possibility of detecting several photons in one signal period. It is important to ensure no more than one photon event per light flash is detected as multiphoton events effect the statistics and lead to erroneous results (pulse pile-up) [17]. In TCSPC the times that photons are recorded, in relation to the reference pulse, are used to build up a histogram of photon times. Single photon counting is a statistical method and a high repetition rate light source is required to accumulate a sufficient number of photon events for a required data precision. The TCSPC electronics can be compared to a fast stopwatch with two inputs; a start and a stop input, see Figure 1.5. The time measurement for one start-stop sequence will be represented by adding a "1" in the memory location with an address proportional to the detection time. With a high repetition light source millions of start-stop sequences can be measured in a short time. The resulting histogram displays time (channels) versus intensity (counts per channel). Generally at least one of the input pulses to the TCSPC electronics will be a pulse generated by a single photon. Single photons can be detected by photodetectors having an intrinsically high gain [18]. The majority of photodetectors are photomultiplier tubes (PMTs) or micro-channel plate photomultiplier tubes (MCP-PMTs) although other single photon sources such as avalanche photodiodes may also be used [19], [20].

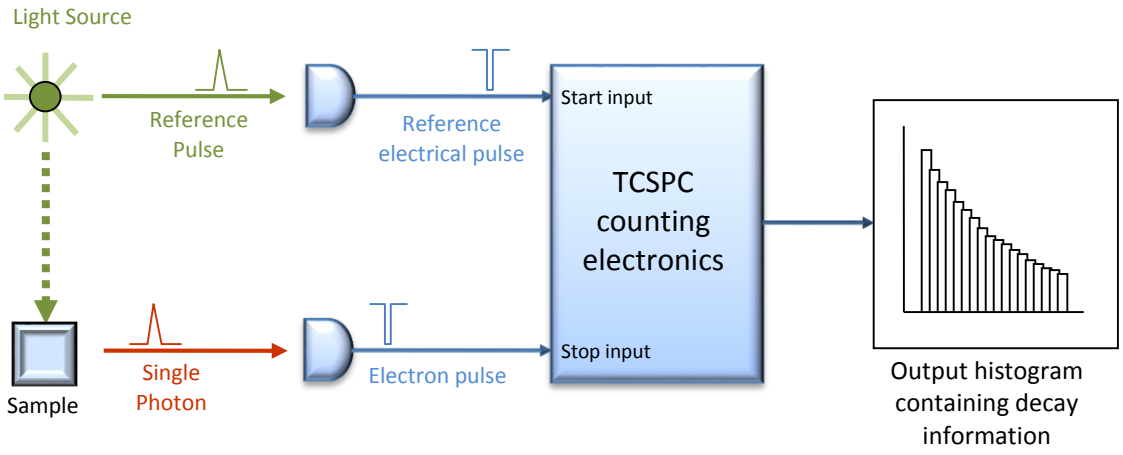

Figure 1.5 Principle of TCSPC

The main electrical components for signal processing in TCSPC are Constant Fraction Discriminators (CFD), electrical delays, the Time-to Amplitude Converter (TAC), amplifiers, an Analogue to Digital Converter (ADC) and digital memory. A diagram of the electrical setup is shown in Figure 1.6. At the input of the electronics, incoming pulses are evaluated with respect to pulse height using a simple threshold level (only pulses higher than a set threshold will be accepted for further signal processing. This allows small amplitude noise pulses to be readily eliminated. The CFDs on both the start and stop inputs then analyse the pulse shapes of the individual pulses. The portion of the steepest slope of the initial edge on the incoming pulses (negative in the case of PMTs) is taken as a criterion for the temporal position. The portion of the slope taken will depend on the fraction, constant fraction (or shaping) delay and zero-crossing level. The settings for the threshold, fraction, constant fraction delay and zero crossing level depend on the detector used. The CFDs are used to minimise pulse jitter caused by the variation in pulse heights outputted by a single photon counting detector. At the output of the CFD pulses are re-shaped to a standard height and shape. They are then delayed by an electronic shifting delay, this is used to allow the decay measurement to be positioned on the time axis. The time-to–amplitude converter is a fast electronic clock triggered by the start and stop pulses. The start pulse initiates the growth of a voltage ramp and the arrival time of the stop pulse determines the height of the voltage ramp. Once the ramp voltage is fixed it will remain constant for a defined period. The TAC output pulses can then be amplified, effectively stretching the time axis and maximising the temporal resolution. The time range is determined by the minimum and maximum amplified voltages

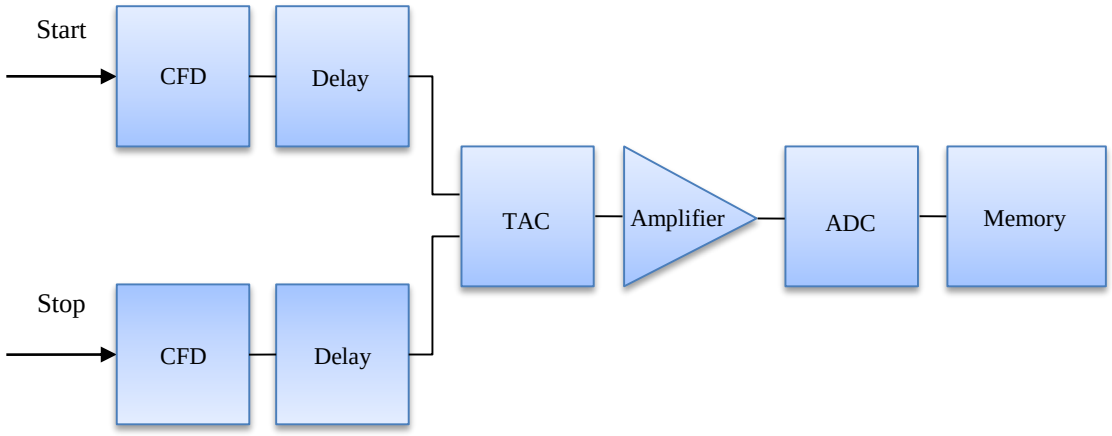

Figure 1.6 Simple Schematic of TCSPC electronics

The amplified TAC output voltage is effectively an analogue pulse with a height corresponding to a measured time of a single start-stop sequence. The ADC is then used to digitise the information by measuring the pulse height with discrete steps. The ADC resolution determines how many discrete time values are possible. All possible measured TAC pulses will therefore be directed to different time bins. The width of the time bin is the ratio of the full time range and the resolution of the ADC in channels; this also gives the time resolution (in time per channel).

This thesis will centre on measurements of fluorescence employing the technique of TCSPC. The remainder of the thesis will investigate potential light source and monochromator/spectrometer design to maximise the effectiveness of fluorescence lifetime measurements using TCSPC in terms of sensitivity, temporal resolution and cost effectiveness.

1.2 Light sources for a commercial fluorescence spectrometer

1.2.1 Desirable features for light sources for use in commercial spectrometers

When evaluating the practicality of a light source for use in a commercial fluorescence lifetime spectrometer intended for use as a general laboratory instrument, many factors have to be considered including the following:

Ease of use – The light source should be “turnkey” and simple enough to operate that users are not required to have previous optoelectronic experience or a deep understanding

of how the device operates, although a basic understanding of all the components of an instrument being used is always recommended.

Robustness – The instrument is often operated in a general purpose biology or chemistry lab and therefore should not have excessively strict environmental operational parameters (temperature, air purity, humidity, vibrational isolation). The light source should be able to operate on a standard lab bench and be able to suffer occasional knocks without difficulty.

Size – Although the device does not need to be small, it should not be large enough to be the dominating component in the size of a commercial spectrometer. As this is a general instrument, it does not always have a dedicated laboratory, therefore size restraints can become an issue, so the light source must be able to connect to the spectrometer without appearing obtrusive.

Maintenance requirements – A major factor to be considered in terms of maintenance is that the users may not have any prior optics training, therefore any maintenance should be minimal and as straight forward as possible. If the light source has to be realigned regularly it will reduce the number of users able to operate the system and inhibit its effectiveness as a general lab instrument.

Service – Any components likely to require replacement periodically such as air filters or flashlamps should be easily accessible and replaceable by the customer.

Compatibility with the rest of the optical system – The light source should be able to connect to current commercially available spectrometers without any redesign to the spectrometer. Therefore, factors such as the output beam height from the light source should be matched to the optical height of the instrument. If the light source was to be connected to the excitation monochromator for spectral selection, the output optics of the light source would have to be matched with the numerical aperture and focal length of the monochromator.

Price – The cost of the light source should not be disproportionate to the cost of the rest of the fluorescence spectrometer. By increasing the functionality of the instrument and possibly negating the need for some other standard components, the cost of a light source as a percentage of the overall instrument cost can rise, however, it should still be low enough to be affordable to researchers looking to purchase a high end general purpose fluorescence spectrometer.

Tunability – Monochromatic light sources such as laser diodes are very useful as light sources for instruments with specific applications such as assay development, preclinical diagnostics and drug discovery where the same probe or emitting species is always being studied. However, in a fluorescence lifetime spectrometer designed to be used as a general lab instrument, some degree of tunability is particularly advantageous. General lab instruments may be used to measure a wide variety of samples with vastly different absorption spectra. The ability to tune the excitation light source to the peak of the absorption spectrum of the sample would be a very useful attribute, as it allows much shorter measurement times, reduces the chances of exciting impurities within the sample volume and allows a much wider variety of samples to be measured.

Dual functionality – If a pulsed light source could be sufficiently tunable and have enough spectral brightness in the UV-visible range, it could be used to perform quasi steady-state measurements as well as lifetime. This could lead to a single photon counting spectrometer with a single light source able to measure steady state spectra and lifetimes from picoseconds to microseconds.

Pulse width – As discussed in Section 1.1.1, molecules typically florescence with lifetimes in the order of nanoseconds. Therefore to accurately measure the decays of these samples by TCSPC the pulse width of eth source should be nanoseconds or less.

Repetition rate – As discussed in Section 1.1.3, TCSPC is a statistical method that can only count as a maximum of one photon for every twenty excitation flashes, therefore a high (>10 kHz) frequency is required to have reasonable measurement times. If the frequency is too high, however, the sample will not relax to the ground state before the next excitation pulse. Therefore the source should have a variable repetition rate to allow flexibility in sample measurement: for longer lifetimes the repetition rate can be reduced to allow the full decay to be captured and for shorter lifetimes the rate can be increased to reduce measurement time.

1.2.2 Nanosecond flashlamps

Before the advent of semiconductor picosecond diode lasers in the UV and visible regions of the spectrum, the majority of TCSPC fluorescence measurements were made using a spark discharge lamp (nanosecond flashlamp) [21], [22]. The nanosecond flashlamp works by discharging a high voltage between two electrodes; the discharge is gated using a thyratron. Both electrodes are charged to a high voltage and, when the thyratron is gated

on, it rapidly discharges the top electrode to ground potential. When this occurs there is a spark discharge across the electrodes. The spectral profile of this discharge is dependent on the filler gas in the electrode chamber and the temporal profile is dependent on the size of the gap, pressure and purity of the gas and cleanliness of the electrodes.

The nanosecond flashlamp provides excitation pulses with lower energy than most lasers, however, it can produce a spectral continuum from the vacuum-UV to infra-red (<1000 nm) depending on the filler gas used. The most popular filler gas is hydrogen as it has a continuous spectrum with maximum emission in the UV and the narrowest temporal profile. The repetition rate of a nanosecond flashlamp is typically 40 kHz.

The nanosecond flashlamp is a versatile, established, light source which has led to its use over many years in fluorescence lifetime spectrometers. There are, however, some drawbacks to its use. The TCSPC technique constrains the maximum measurable emission rate to a small percentage of the source repetition rate to ensure no more than one emission photon reaches the detector after each excitation (if more than one arrives, only the initial photon would be measured leading to a skewing of the statistics and inaccuracy – pulse pile up (see Section 1.1.3). In practice, measuring an emission photon at an average of one time in every 20 excitation events (or 5 %) makes the pulse pile up problem statistically insignificant [16], [17]. Given that the maximum repetition rate of the lamp is 40 kHz, this means that the maximum detectable emission rate is 2000 photon counts per second, irrespective of fluorescence yield of the sample. In addition the lamp requires regular maintenance in order to maintain its performance (to remove deposits from gas impurities the electrodes need to be removed, cleaned and realigned on average after every 50 hours of operation). Additional disadvantages in some cases are the relatively broad temporal pulse width (~1 ns), which can limit the study of particularly rapid events and the wavelength dependence of the temporal profile.

1.2.3 Synchrotron radiation

TCSPC measurements have been made using the Bremsstrahlung of synchrotron radiation as a source [23]. The benefit is the broad spectrum and the potential tunability. However, the broad temporal pulse width (>1 ns) and the limited availability (because of the high cost) today make this light source practically obsolete for fluorescence techniques.

1.2.4 Titanium-sapphire lasers

Titanium-Sapphire (Ti:Sapphire) lasers have the benefits of short pulse width, tunability and a high repetition rate (typically of the order of 80 MHz). Pulse width can vary, depending on the model, from a small number of femtoseconds to tens of picoseconds (shorter than the fastest available TCSPC detector), tunable from around 680-1080 nm depending on the model [24]. Ti:Sapphire lasers used to require frequent realignment and fine-tuning to maintain performance; however, computer-controlled, self-adjusting Ti:Sapphire lasers are now available which are close to being turn-key devices [25], [26]. The high power and short pulse width mean that two photon excitation of samples can be possible using these lasers [27] (e.g. samples with absorption at 530 nm may be excited using the fundamental output). The spectral range of the Ti:Sapphire laser can be extended to lower wavelengths with the use of Second Harmonic Generation (SHG), Third Harmonic Generation (THG), Optical Parametric Oscillators (OPOs) and Optical Parametric Amplifiers (OPAs).

Although the high repetition rate of many Ti:Sapphire lasers (the frequency is determined by the resonator length) makes the problem of pulse pile up inconsequential, it sets an upper limit on the fluorescence lifetimes that can be measured – a fluorophore takes around 10 times its lifetime to stop emitting light [5]. In practice, a sample can be re-excited before it has finished emitting completely; however, errors in the measured lifetime become significant at much more than 4-5 times the lifetime effectively limiting the maximum lifetime that can be measured in a straightforward manner with an 80 MHz Ti:Sapphire to around 3 ns [17]. The majority of organic fluorophores have lifetimes longer than this. A pulse picker (employing either a Pockels cell or acousto-optic modulator) may be used to reduce the repetition rate of the source. Pulse pickers can have disadvantages though as they can generate RF noise synchronous with the pulses which can make TCSPC measurements difficult.

TCSPC is a digital technique, therefore the noise statistics are Poissonian (square root of the signal). This allows measurement of fluorescence decays down to the baseline i.e. over 4 orders of magnitude in a semi-log scale of photon counts against time. Pulse pickers generally have a contrast ratio up to 75:1 for the adjacent pulse [28], therefore the pulse picker generally does not fully suppress the unwanted pulses meaning that secondary pulses at the fundamental frequency leak through and re-excite the sample and affect the measured decay (making it harder to extract an accurate lifetime). This problem can be alleviated by performing SHG or another non-linear process after the pulse picker

as the nonlinear effect itself will further enhance the contrast ratio; however, the high amplitude RF frequencies often have to be employed in the pulse picker increasing the chance of RF interference in the detection electronics.

The main drawback to Titanium Sapphire lasers is cost. Ti:Sapphire lasers are an order of magnitude too expensive to be used in an economically priced fluorescence spectrometer. The addition of other peripheral devices such as harmonic generators and pulse pickers that are required for most measurements of fluorescence decays add considerably to the expense.

1.2.5 Picosecond pulsed semiconductor diode lasers

Gain-switched pulsed semiconductor diode lasers are extremely reliable and do not require any maintenance and alignment during normal operation. They are monochromatic sources (typically 1 - 2 nm linewidth), with a variable repetition rate up to megahertz frequencies and pulse widths varying from less than 50 ps (FWHM) to a few hundred picoseconds, depending on the wavelength and manufacturer. Diode lasers are commercially available at wavelengths of: 375 nm 405 nm, 445 nm, 470 nm, 485 nm 515 nm and 635 nm and at many discrete wavelengths above 635 nm [29].

Diode lasers have a small cavity (a few micrometers) and operate in the single-transversal mode. This implies that the radiation can, in theory, be focused into a diffraction-limited spot, however, the small cavity size means light is emitted over a wide angle. Additionally, the cavity geometry means that the laser has an elliptical beam profile. Collimating this source is not straightforward. An elliptical collimated beam can be produced using an aspherical lens, though the beam quality is not generally important for measurements of fluorescence samples in a spectrometer. The bulk semiconductor material often generates spontaneous emission at wavelengths above the lasing wavelength, therefore band or edge pass filters have to be used to clean up the laser emission (transmitting the laser wavelength and blocking higher wavelengths). Picosecond pulsed diode lasers are reliable, cheap sources that are an ideal source for specific TCSPC applications (such as when only a single excitation wavelength is required). They are also useful in TCSPC based fluorescence lifetime spectrometers; however, because they are inherently monochromatic, it can become expensive depending on how many excitation wavelengths are of interest to the researcher. Additionally there are regions of the spectrum where pulsed diode lasers are not readily available (for instance between 515-635 nm).

1.2.6 Sub-nanosecond light emitting diodes

Light emitting diodes (LEDs), like laser diodes, are extremely reliable, robust, compact and require no maintenance. They have typical pulse widths of just less than 1 ns, bandwidths of 10 - 20 nm and can have a variable repetition rate up to megahertz frequencies [29]. As with the picosecond diode lasers, the diode itself tends to emit therefore interference filters should be used on the output of the diodes. The LED is an extended source, meaning it is difficult to collimate and focus. They are available in a broader range of wavelengths than diode lasers in many discrete wavelengths from 250 nm to the infrared. The UV versions of the diodes are popular for applications such as protein studies by direct excitation [30], studies into copper based dye-sensitised solar cells [31] and the measurement of ligand lifetimes from within rare earth complexes [32].

1.3 Supercontinuum generation

Supercontinuum generation is the spectral broadening of the narrow bandwidth of a laser pulse into a broad continuum spanning more than an optical octave (from a wavelength to twice that wavelength) through a nonlinear process. Supercontinuum generation has been performed for many years: early experiments involved focussing high peak power picosecond or femtosecond pulses (typically from a mode-locked laser) into sapphire, glass or water [33], [34]. The drawback to this technique was that expensive pump sources able to deliver pulses with megawatt peak powers were required in order to generate the supercontinua (because of the complex processes involved involving the coupling of spatial and temporal effects).

Confining the high peak power pulses in an optical fibre removes the spatial dimension, reducing the complexity and vastly increasing the interaction length of the focused pulse and the material (silica fibre in this case). Different wavelengths travel down an optical fibre at different speeds (because of the wavelength dependence of the refractive index of the fibre material). The wavelength dispersion properties of an optical fibre together with its nonlinear properties play a critical role in how a short optical pulse propagates and, in certain circumstances, the generation of a supercontinuum.

The dispersion properties of the fibre can be described by the mode-propagation constant β (Equation (1.8)) and the Taylor series expansion around the centre frequency (ω_0) of the pulse spectrum, shown in Equation (1.9).

$$\beta_m = \left(\frac{\delta^m \beta}{\delta \omega^m}\right)_{\omega=\omega_0} \quad (m = 0,1,2 \ldots) \tag{1.8}$$

$$\beta(\omega) = n(\omega)\frac{\omega}{c} = \beta_0 + \beta_1(\omega - \omega_0) + \frac{1}{2}\beta_2(\omega - \omega_0)^2 + \cdots, \tag{1.9}$$

The β_1 and β_2 parameters can be related to the refractive index (n) and refractive index derivatives by Equations (1.10) and (1.11).

$$\beta_1 = \frac{1}{\vartheta_g} = \frac{n_g}{c} = \frac{1}{c}\left(n + \omega\frac{\delta n}{\delta \omega}\right) \tag{1.10}$$

$$\beta_2 = \frac{1}{c}\left(2\frac{\delta n}{\delta \omega} + \omega\frac{\delta^2 n}{\delta \omega^2}\right) \tag{1.11}$$

Where the group velocity (υ_g) describes the velocity of the envelope of an optical pulse passing down an optical fibre and n_g is the group index. The broadening of this optical pulse is known as the group velocity dispersion (GVD), β_2 is the GVD parameter.

The dispersion parameter (D) of a fibre [35] can be related to β_1 and β_2 by Equation (1.12).

$$D = \frac{\delta \beta_1}{\delta \lambda} = -\frac{2\pi c}{\lambda^2}\beta_2 \tag{1.12}$$

In order to see how dispersion relates to the group velocity, the group velocity dispersion and the group index, an example of a dispersion curve for a typical silica fibre is shown in Figure 1.7. It shows that at ~1300 nm there is no dispersion, this is the zero dispersion wavelength (ZDW) of the fibre.

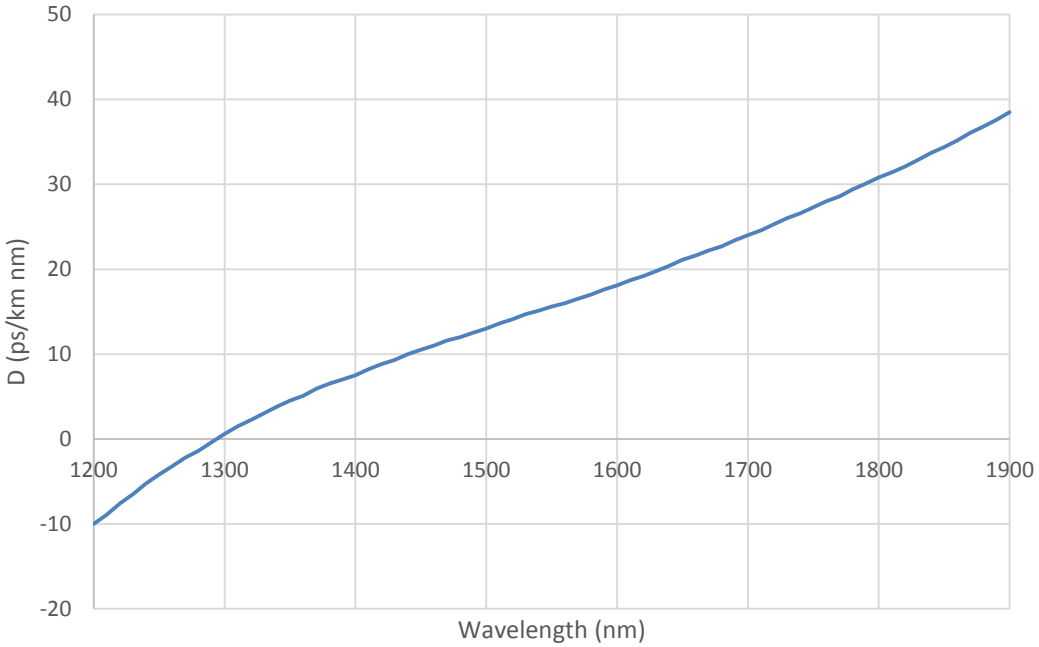

Figure 1.7 Wavelength dependence of the Dispersion parameter D for a typical silica fibre

Equation (1.12) shows that integrating the dispersion with respect to the wavelength thus gives the curve of β_1, which is shown in Figure 1.8.

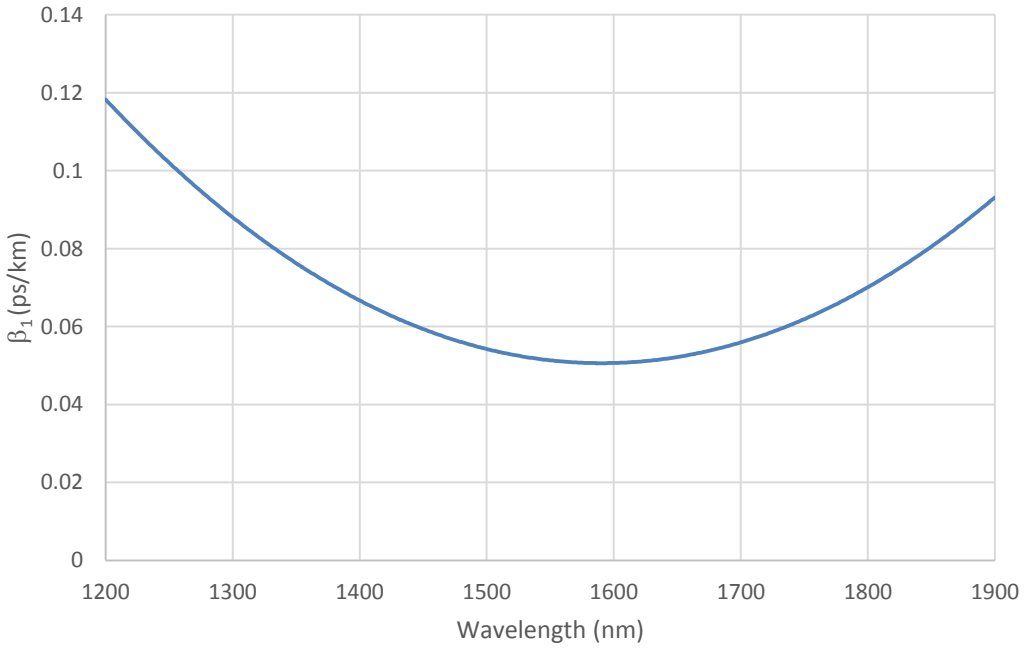

Figure 1.8 Wavelength dependence of the β_1 parameter for a typical silica fibre

The group velocity dispersion (β_2) can also be calculated using the second half of Equation (1.12), this is shown in Figure 1.9.

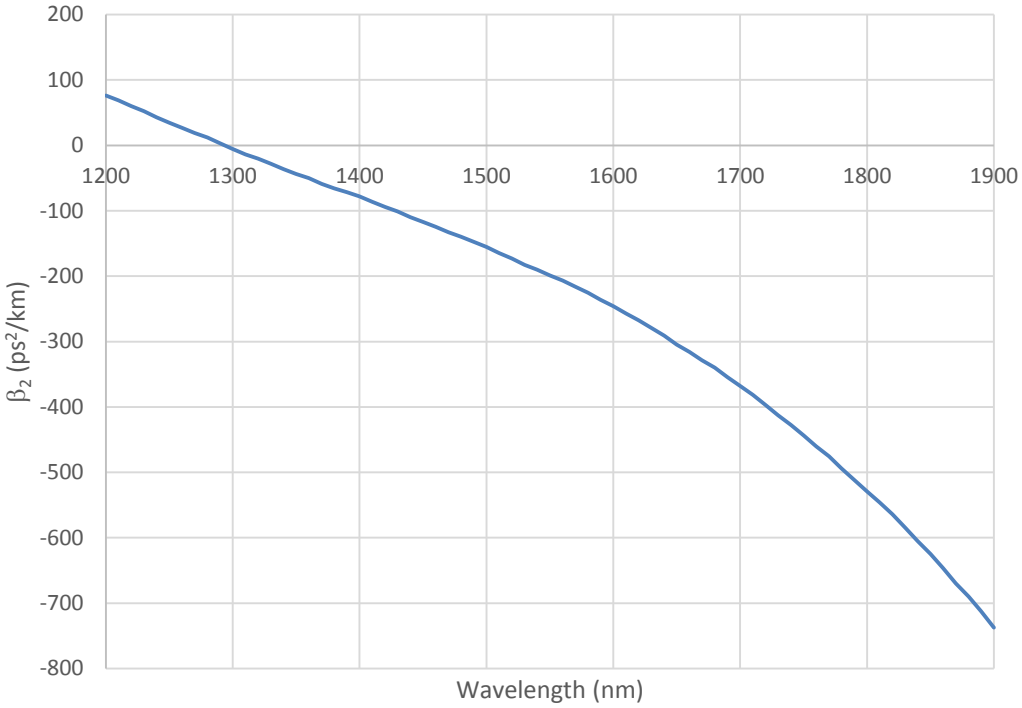

Figure 1.9 Group velocity dispersion (GVD) for a typical silica fibre

As shown in Equation (1.10), the wavelength dependence of the group velocity is simply the inverse of β_1, as shown in Figure 1.10.

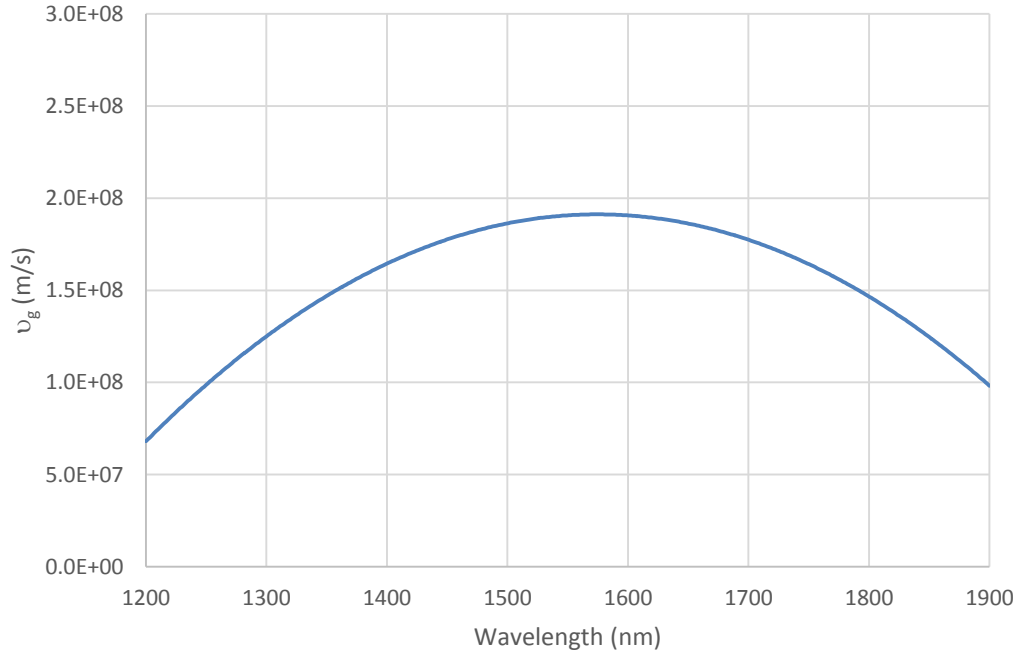

Figure 1.10 Wavelength dependence of the group velocity (υ_g) for a typical silica fibre

As shown in Equation (1.10), the group index (n_g) is simply the β_1 parameter multiplied by the speed of light, it thus has the same wavelength dependence as β_1 as shown in Figure 1.11.

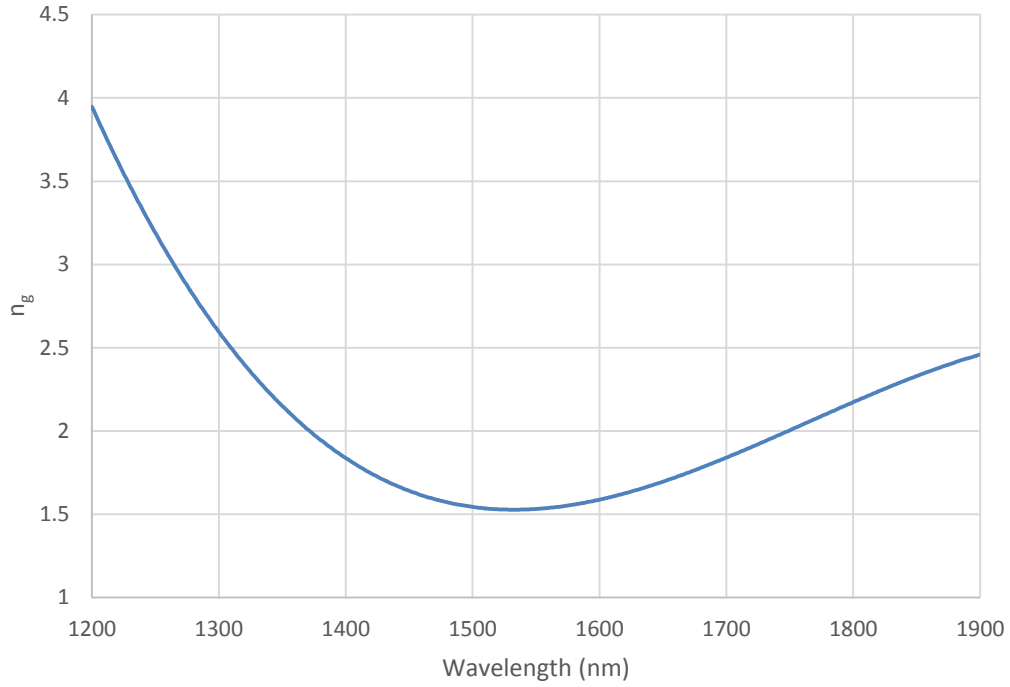

Figure 1.11 Wavelength dependence of the group index (n_g) for a typical silica fibre

The fibre design parameters such as core radius and difference in refractive index between core and cladding can alter the parameters of D and thus β_1 and β_2 allowing the zero dispersion wavelength (ZDW) to be shifted.

Supercontinuum generation in optical fibres involves only the coupling of dynamic processes in the temporal domain (as the spatial domain is determined by the waveguide properties of the optical fibre). Standard silica fibres have been used for supercontinuum generation with visible picosecond pump pulses [36]. Because the group velocity dispersion (GVD) of silica fibres is ~1.3 μm, using visible pump sources means that the fibre is pumped in the normal GVD regime (dispersion decreases with decreasing wavelength). In this region supercontinuum generation is generated by Raman scattering, self-phase modulation (SPM), cross-phase modulation (XPM) and four wave mixing [37], [38]. Pumping in the anomalous GVD region allows the production of solitons that do not broaden temporally, thus retaining the high peak powers required for supercontinuum generation [39], [40].

There are two different regimes for supercontinuum generation in optical fibres, one process is dominant when ultrashort (femtosecond) pulses are used as a pump source and a different process when picosecond pulsed, nanosecond pulsed or continuous wave pump sources are used. In both regimes a single wavelength is converted into a broad spectrum

through a complex combination of nonlinear effects stemming from a small third order nonlinearity in the silica.

Photonic crystal fibres (PCFs) are a type of glass optical fibre in which the cladding contains a regular array of microscopic air holes along the entire length of the fibre. The size and position of the holes determine the optical behaviour of the fibre. It is possible to change the zero dispersion wavelength (ZDW) of the fibre below the intrinsic ZDW of silica [41], therefore with careful design the ZDW of the PCF can be designed to match the pump laser. In addition the effective area of the fibre that the light propagates down is reduced in a PCF, therefore the intensity is increased and the thus the nonlinear effect is greater [42]. PCFs were first used together with Ti:Sapphire lasers in the year 2000 to generate broad supercontinuua from the 400 nm to above 1500 nm [43], [44].

A light source based on a photonic crystal fibre pumped by a compact chip or fibre laser has the possibility of becoming a versatile and popular light source for fluorescence lifetime spectrometers based on time correlated single photon counting. Compact light sources employing supercontinuum fibres can have a broad visible continuum, picosecond pulse widths and megahertz repetition rates making it appear an ideal light source for a general purpose TCSPC based lifetime fluorescence instrument.

1.3.1 Ultrashort pump pulse regime

The ultrashort or soliton fission regime dominates when a suitable photonic crystal fibre is pumped in the anomalous GVD domain with a femtosecond pulse with sufficient peak power to constitute a higher-order soliton. This is perturbed and breaks into a series of lower amplitude sub-pulses (1^{st}-order solitons) [45]. Solitons are isolated optical pulses that propagate down the fibre without experiencing any dispersion. By contrast, when a fibre is pumped with an ultrafast pulse in the normal GVD regime, SPM dominates. The SPM leads to some spectral broadening [46], however, it is accompanied by temporal broadening which causes a rapid decrease in peak power limiting the extent of the spectral broadening.

Ideal solitons are rarely directly excited, in the ultrashort regime they fission from higher orders, whereas with longer pulses they evolve from modulation instability (see Section 1.3.2). The envelope field of a soliton can be described by Equation (1.13).

$$E_{sol}(z,t) = \sqrt{P_0} sech\left(\frac{t}{\tau_0}\right) exp\left(iz\frac{\beta_2}{2\tau_0^2}\right) \quad (1.13)$$

Where P_0 is the soliton power and τ_0 is the soliton duration. The soliton propagates down the fibre with a phase shift of $\beta_2/(2\tau_0^2)$, where β_2 is the group velocity dispersion (GVD) parameter. The soliton power is given by Equation (1.14).

$$N^2 = \frac{\gamma P_0 \tau_0^2}{|\beta_2|} \quad (1.14)$$

Where N is the soliton order, $N=1$ representing a fundamental soliton and γ is the nonlinear coefficient which is given by Equation (1.15).

$$\gamma = \frac{2\pi n_2}{\lambda A_{eff}} \quad (1.15)$$

Where λ is the pump wavelength, n_2 is the nonlinear refractive index of silica ($2\text{x}10^{-20}$ m^2/W) and A_{eff} is the effective mode area of the fibre.

Therefore, for the fundamental soliton the phase shift could also be described by $\gamma P_0/2$ and is therefore a function of the nonlinear refractive index which modifies the propagation constant (β) of the soliton. Because solitons propagate unchirped, the frequency components of the soliton move with the group velocity of the soliton central frequency. This in turn means that the effective propagation constant of a soliton with a central frequency of ω_{sol} can be given by Equation (1.16) at ω.

$$\beta_{sol}(\omega) = \beta(\omega_{sol}) + \delta_\omega \beta(\omega_{sol})[\omega - \omega_{sol}] + \frac{\gamma P_0}{2} \quad (1.16)$$

This means that the effective propagation constant of a soliton is not equal to the propagation constant of the fibre. This leads to dispersive wave interactions (see Section 1.3.2).

A higher order soliton is a collection of co-propagating fundamental solitons with the same group velocities ($N > 1$). They can, however, have different peak powers and durations and, as there is no binding energy between them, small perturbations can lead to fissioning of the constituent soliton orders [47]. The perturbations that lead to the break-up of the higher order solitons can be dispersive or Raman effects; the longer the pulse width the more effect there is from Raman (at over 200 fs Raman is the dominant cause of the break-up). The individual solitons are ejected one at a time in order of

decreasing peak power, with the highest peak power (shortest duration) solitons having the largest difference in group velocity from the pump wavelength (fastest propagating).

Following the initial soliton fission each individual soliton experiences a continuous shift to longer wavelengths by soliton self-frequency shift because the Raman gain overlaps with the individual soliton bandwidths [48]. This soliton fission and Raman self-frequency shift can describe the spectral broadening in the anomalous GVD region, however, not the normal GVD region.

The process of soliton fission also leads to short wavelength features generated in the normal GVD region of the supercontinuum spectra. These features are caused by dispersive wave generation which is seeded from the initial process of soliton fission [49], [50]. The ejected solitons from the initial pulse are also affected by higher-order dispersion. This higher order dispersion can lead to the transfer of energy from the soliton to a narrow-band resonance in the normal GVD regime. This can lead to a low amplitude temporal pedestal [51], [52].

The nature of the supercontinuum radiation produced is clearly dependent on the pulse dispersion properties of the fibre [53], however, it is also influenced by the mode field diameter [54], the input pulse polarisation [55], [56] and the input pulse chirp [57]. Further spectral components of the supercontinuum are produced due to the interaction between (the linear) dispersive waves and (the nonlinear) solitons in the photonic crystal fibre [58]. The propagation distance, i.e. the length of the fibre, is a crucial parameter in determining the shape and extent of the spectra produced; however, it is not the case that the longer the fibre the larger the spectral range. It has been shown [59] that even when the fibre is too short (5.7 mm) for the occurrence of multiple soliton fission, the self-phase modulation alone (along with the dispersive wave generation) may produce a broad continuum extending from 350 nm to 3 μm.

1.3.2 Long pump pulse regime

Modulation instability (MI) in nonlinear optics is a phenomenon where small variations in intensity of the waveform lead to a modulation of the pump pulse entering the fibre. This modulation can cause the pump envelope to break and evolve into a train of femtosecond, soliton like pulses. The process leads to a similar result as the soliton fission described in Section 1.3.1, because it is seeded from noise the process is actually modulation instability-induced breakup [45].

For soliton fission process to dominate, modulation instability must not occur [47]. For modulation instability to occur, the pump pulse duration must be significantly larger than the modulation instability period. Because the modulation instability period scales with peak power, it is not possible to define a pulse duration below which soliton fission occurs. It can, however, be defined in terms of soliton order. For an ideal shaped high-order soliton at input and at peak power, the ratio of pump pulse duration (τ_0) to MI period (T_{MI}) is given by Equation (1.17).

$$\frac{\tau_0}{T_{MI}} = \frac{N}{\sqrt{2}\pi} \qquad (1.17)$$

From Equation (1.17) it can be seen that when $\tau_0 >> T_{MI}$, $N >> 4.44$. This is, however, an extreme limit, as the peak power is only maintained locally for a fraction of the pulse duration in a $sech^2$ pulse (Equation (1.13) shows the envelope of a soliton to be a $sech^2$ function). Assuming a constraint of $\tau_0/T_{MI} \sim 5$, leads to $N \sim 22$. A typical PCF with a zero dispersion wavelength of 835 nm, a hole pitch of 1.4 μm and hole diameter of 1.6 μm will have a GVD β_2=-11.83 ps^2m^{-1} and a figure for the non-linear parameter γ=0.11 $W^{-1}m^{-1}$ when pumped with a wavelength of 835 nm [45]. Assuming a pump power of P_0=10 kW, using Equation (1.14), the pulse duration required to pump with a fundamental soliton (N=1) is 3.3 fs, however, to pump with a higher order soliton of N=22, the pulse duration would have to be 72 fs. These parameters are readily achievable with femtosecond mode-locked Ti:Sapphire sources.

However, all-fibre, picosecond sources used in commercial supercontinuum sources use a picosecond pump source. If we assume typical pump parameters to be 2 W average power, 20 MHz repetition rate and a 5 ps pulse duration (i.e. a peak power of 20 kW). Assuming the same fibre parameters as described in the previous paragraph (and altering the non-linear parameter to 0.086 $W^{-1}m^{-1}$ to account for the pump wavelength of 1064 nm) gives an N=1910 (using Equation (1.14)). Therefore, all the supercontinuum sources discussed and used in the succeeding chapters of this thesis will be operating in the modulation instability regime.

When the pump pulse is coupled into the fibre the modulation instability breaks the picosecond pulse into a series of femtosecond, soliton like pulses. These pulses excite dispersive waves in the normal GVD region through processes including dispersive wave generation. Following this, the solitons start to self-frequency shift due to intra-pulse

Raman scattering. As this occurs dispersive waves may be trapped and pushed to shorter wavelengths.

Modulation instability describes the process in the time domain. This is the same physics as four-wave mixing (FWM), which is described in the frequency domain [60]. That is to say another way to describe the supercontinuum generation from long pump pulses is phasematched four wave mixing, generating sidebands at equal frequencies from the pump [56]. The gain for the four wave mixing is provided by the intensity dependence of the refractive index of silicon. The required conservation of energy and phase matching lead to Equations (1.18) and (1.19) [35].

$$2\omega_{pump} = \omega_{signal} + \omega_{idler} \qquad (1.18)$$

$$2k_{pump} = k_{signal} + k_{idler} + 2\gamma P \qquad (1.19)$$

Where ω_j are the frequencies of the pump, signal and idler waves; k_j are the wavevectors (propagation constants) of the modes and P is the peak pump power and γ is the nonlinear coefficient which is given by Equation (1.15).

$$\gamma = \frac{2\pi n_2}{\lambda A_{eff}} \qquad (1.20)$$

Energy conservation and phase matching determine the wavelength at which there is maximum gain in a given fibre which depends on the chromatic dispersion of the fibre. As discussed in Section 1.3, the zero dispersion wavelength of a photonic crystal fibre can be designed to be shorter than the pump wavelength (which is usually between 1000-1100 nm). Using a specifically designed photonic crystal fibre, dispersion of the pump radiation propagating down the fibre creates phase matched side bands (the solutions of Equation (1.19)) which are broad and close to the pump wavelength. As the radiation propagates down the fibre, the sidebands increase in intensity and act as pumps for further four-wave mixing processes. This can become a cascade process generating a broad, reasonably flat continuum spanning the visible and near infrared part of the spectrum. Theoretical models of the four wave mixing process in a particular PCF have been shown to match well with experimental data [61].

1.4 Interference filters

1.4.1 Theory

Interference effects of light incident on a thin film were first studied by Robert Hooke [62], Robert Boyle and Sir Isaac Newton; however, it was 1801, almost 150 years later, until these effects were satisfactorily explained by Thomas Young [63]. The first thin film coatings were made and observed by Joseph Fraunhofer [64]. Fraunhofer noted the anti-reflection nature of his coatings, but failed to notice the corresponding increase in transmission. This, coupled with the fact that optical systems at the time were not overly complicated, meant that Fraunhofer did not follow his research into the development of antireflection coatings for glass. It was not until the beginning of the twentieth century that a method for producing artificial antireflection coatings was developed by Taylor [65] and expanded for different glasses by Kollmorgen [66] using the technique of chemical etching.

At around the same time, at the end of the nineteenth century, the Fabry-Pérot interferometer was invented [67]. This device has become one of the main thin-film structures and forms the basis of the simplest band pass filters. A Fabry-Pérot etalon, known as a multiple-beam interferometer due to the large number of beams involved in the interference, is shown in Figure 1.12 and consists of two flat plates separated by a distance, d_s. It is important that these two plates are parallel to a high degree of accuracy. The complex amplitudes of the transmission and reflection coefficients can be worked out from basic theory [68], [69]. The amplitude ($A^{(r)}(p)$) of the electric field vector of the reflected light is given by Equation (1.21). Where p is the reflected wave number (p=1 being the first reflected wave)

$$\begin{aligned} A^{(r)}(p) &= \left[r_a + t_a t_b r_b e^{i\delta}\left(1 + r_b^2 e^{i\delta} + \cdots + r_b^{2(p-2)} e^{i(p-2)\delta}\right)\right] A^{(i)} \\ &= \left[r_a + \left(\frac{1 - r_b^{2(p-1)} e^{i(p-1)\delta}}{1 - r_b^2 e^{i\delta}}\right) t_a t_b r_b e^{i\delta}\right] A^{(i)} \end{aligned} \qquad (1.21)$$

where r_a and r_b are the reflection coefficients and t_a and t_b the transmission coefficients for the two plates a and b. The phase difference δ varies by an amount corresponding to a double pass of the spacer and is given by Equation (1.22).

$$\delta = \frac{4\pi n_s d_s \cos\theta_s}{\lambda} \qquad (1.22)$$

where θ_s is the angle of incidence of the incident radiation with respect to the normal, λ is the wavelength of the incoming radiation and n_s is the refractive index of the spacer.

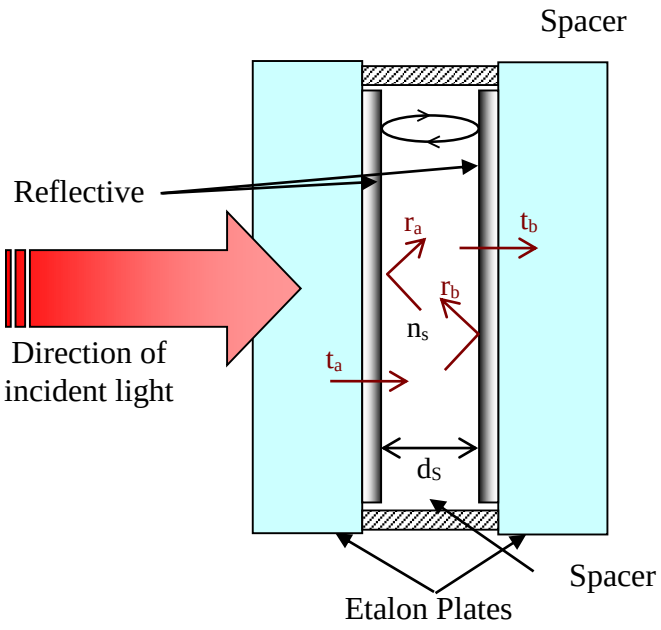

Figure 1.12 Diagram of a Fabry-Pérot etalon

The transmissivity, *T*, and reflectivity, *R*, of the plates are given by Equations (1.23) and (1.24) respectively.

$$t_a t_b = T \qquad (1.23)$$

$$r_a^2 = r_b^2 = R \qquad (assuming\ r_a = -r_b) \qquad (1.24)$$

Assuming no absorption, the reflectivity and transmissivity of the plate surfaces are related by Equation (1.25).

$$R + T = 1 \qquad (1.25)$$

For a sufficiently long spacer plate (or small incident angle) there will be a high number of reflected waves. As $p \to \infty$ and assuming that the two plates have the same reflectivity the amplitude of the electric field vector reduces from Equation (1.21) to (1.26) and using Equations (1.23), (1.24) and (1.25) it reduces further to Equation (1.27).

$$A^{(r)} = -\frac{r_b\left[1-(r_b^2+t_at_b)e^{i\delta}\right]}{1-r_b^2e^{i\delta}}A^{(i)} \tag{1.26}$$

$$A^{(r)} = -\frac{\left(1-e^{i\delta}\right)\sqrt{R}}{1-Re^{i\delta}}A^{(i)} \tag{1.27}$$

where $A^{(r)} \equiv A^{(r)}(\infty)$

Using a derivation of Euler's formula: $\cos\delta = \frac{e^{i\delta}+e^{-i\delta}}{2}$, the intensity of the reflected light ($I^{(r)} = A^{(r)}A^{(r)*}$) can be given by Equation (1.28).

$$I^{(r)} = -\frac{(2-2\cos\delta)R}{1+R^2-2R\ \cos\delta}I^{(i)} = \frac{4R\sin^2\frac{\delta}{2}}{(1-R)^2+4R\sin^2\frac{\delta}{2}}\ I^{(i)} \tag{1.28}$$

Similar to the case for the reflection, the amplitude ($A^{(t)}(p)$) of the electric field vector of the transmitted light is given by Equation (1.29).

$$\begin{aligned} A^{(t)}(p) &= t_at_b\left[1+r_b^2e^{i\delta}+\cdots+r_b^{2(p-1)}e^{i(p-1)\delta}\right]A^{(i)} \\ &= \left(\frac{1-r_b^{2p}e^{ip\delta}}{1-r_b^2e^{i\delta}}\right)t_at_bA^{(i)} \end{aligned} \tag{1.29}$$

As $p \to \infty$ and assuming that the two plates have the same reflectivity the amplitude of the electric field vector reduces from Equation (1.29) to Equation (1.30)

$$A^{(t)} = \frac{t_at_b}{1-r_b^2e^{i\delta}}A^{(i)} \tag{1.30}$$

where $A^{(t)} \equiv A^{(t)}(\infty)$

Which becomes Equation (1.31) (using Equations (1.23) and (1.24)).

$$A^{(t)} = \frac{T}{1-Re^{i\delta}}A^{(i)} \tag{1.31}$$

The intensity of the transmitted light ($I^{(r)} = A^{(r)}A^{(r)*}$) can thus be described by Equation (1.32). This together with Equation (1.28) are known as *Airy's formulae* [69].

$$I^{(t)} = -\frac{T^2}{1 + R^2 - 2R\ \cos\delta} I^{(i)} = \frac{T^2}{(1-R)^2 + 4R\sin^2\frac{\delta}{2}}\ I^{(i)} \qquad (1.32)$$

Using Equation (1.25), the fraction of the light intensity can be rewritten as Equation (1.33)

$$\frac{I^{(t)}}{I^{(i)}} = \frac{1}{1 + \frac{4R}{(1-R)^2}\sin^2\frac{\delta}{2}} \qquad (1.33)$$

Or Equation (1.34)

$$\frac{I^{(t)}}{I^{(i)}} = \frac{1}{1 + F\sin^2\frac{\delta}{2}} \qquad (1.34)$$

where:

$$F = \frac{4R}{(1-R)^2} \qquad (1.35)$$

Therefore the Fabry-Pérot interferometer has a transmission maximum when there is no phase change caused by reflections between the plates (δ=0). For a plane incident wave (θ=0) this occurs when the wavelength is equal to twice the optical distance (nd) between the two reflective surfaces by rearranging Equation (1.22) into m=0,1,2….

$$m = \frac{\delta}{2\pi} = \frac{2n_s d_s}{\lambda} \qquad m=0,1,2\ldots \qquad (1.36)$$

Equation (1.36) also shows the presence of higher orders. The free spectral range of the filter is the range of wavelengths around the transmitted peak that is blocked by the filter. By rearranging Equation (1.33) and (1.36) and plotting with respect to wavelength, Figure 1.13 shows the transmission profile for a Fabry-Pérot filter with an optical distance between reflective surfaces of 375 nm (a spacer material 500 nm thick with a refractive index of 1.5). As well as a peak transmission at 750 nm (twice the optical distance), there are also transmission peaks at integer fractions – 375 (750/2), 250 (750/3).

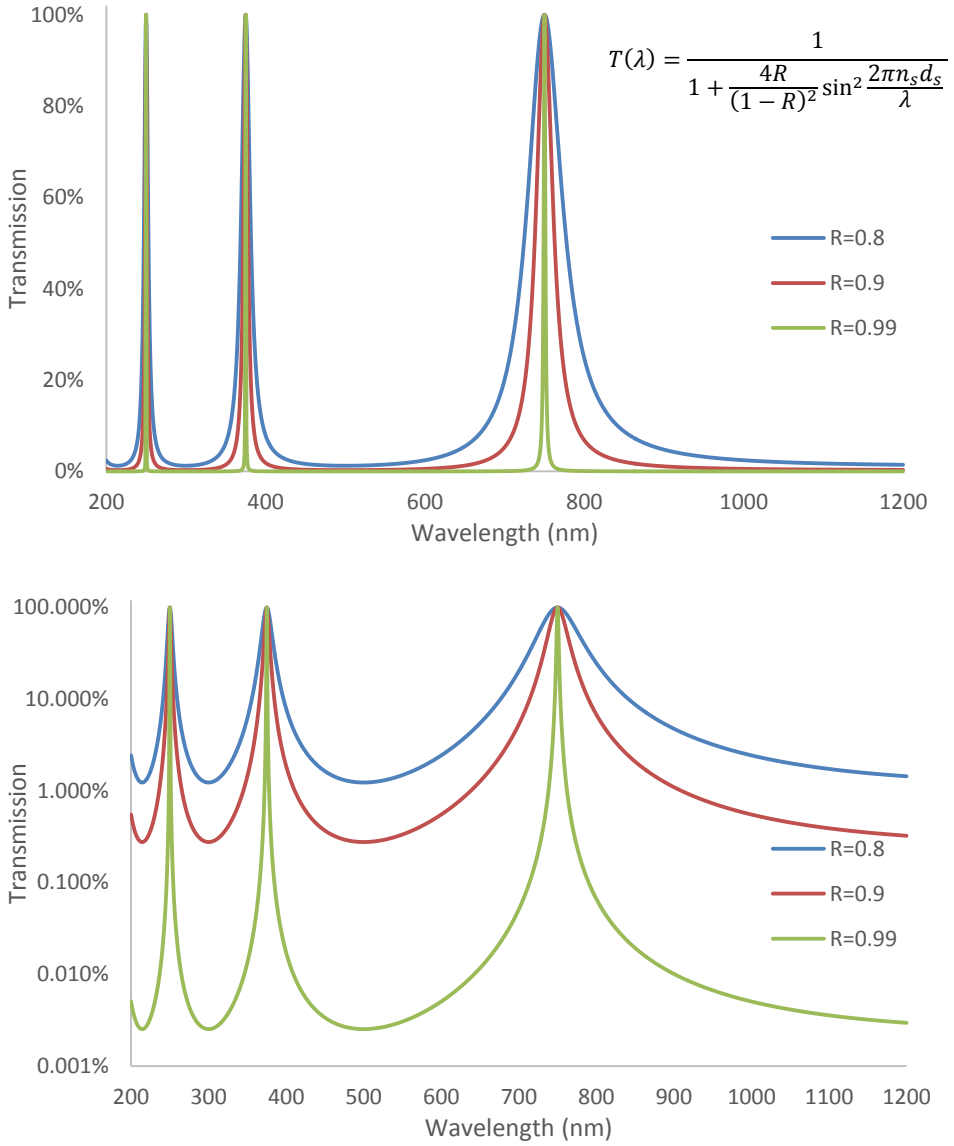

Figure 1.13 Transmission of a Fabry-Pérot filter with an optical distance of 375 nm with various reflective surfaces (top – linear, bottom -semi-log)

At other wavelengths, destructive interference of the transmitted wave fronts reduces transmitted intensity toward zero, i.e. the rest of the light is reflected back toward the source. It can be seen from Equations (1.25) and (1.34) and Figure 1.13 that as the reflectivity of the plates increases, the widths of the transmitted band of radiation becomes narrower and the out of band blocking increases. The response of a Fabry-Pérot interferometer as a band-pass filter is therefore significantly improved by using high reflection multi-layered quarter wave coatings as the plates of the interferometer. An example of a Fabry-Pérot interference filter, made using thin film coatings, is shown in Figure 1.14.

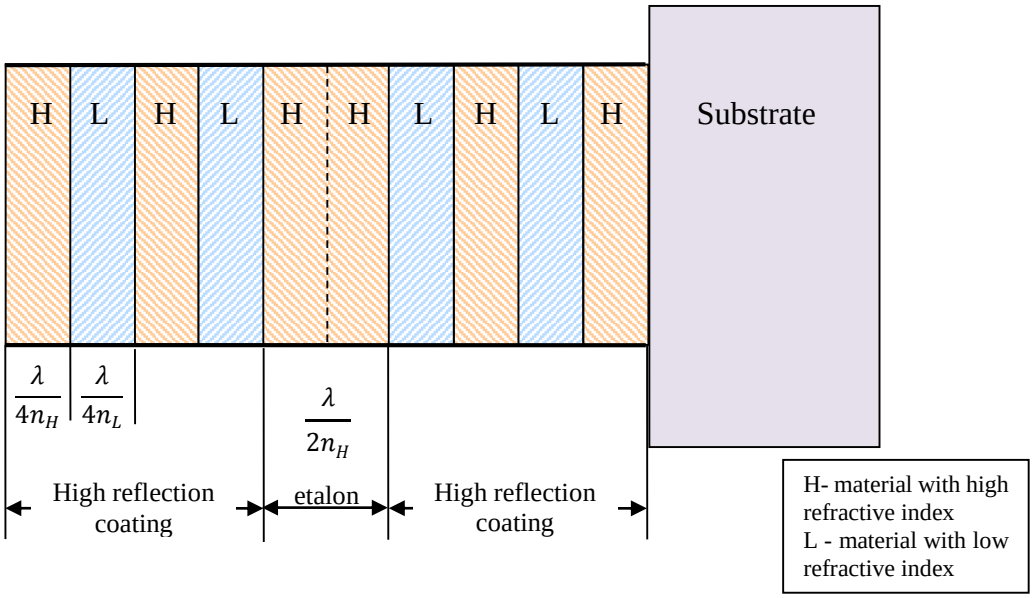

Figure 1.14 Example of a Fabry-Pérot filter based on thin film coatings

The quarter-wave stacks block light most efficiently at $\lambda=\lambda_0/n_{layer}$ i.e. when the wavelength is equal to 4 times the width of each layer. When the wavelength begins to approach $2\lambda_0$, the quarter waves will become transmissive. Increasing the width of the etalon to λ or even 2λ will narrow the width of the transmitted peak but will also reduce the free spectral range as the spectral distance between the transmitted orders will reduce.

At present the vast majority of monochromators contain some form of diffraction grating. This type of system is preferred as they give the best combination of wavelength coverage and resolution. However, fine spectral resolution is not always an important consideration, especially when measuring broad spectral features associated with biological samples. In such instances the intensity of radiation transmitted by the monochromator, along with the stray light rejection ratio becomes of primary concern. This is where an interference filter based device could be of benefit.

The idea of an interference filter based monochromator is not new, it was first discussed by Smith and Heavens in 1957 [70]. Previous designs employed a variable air gap (for the infra-red [70]) or graded interference filters [71]. The main advancement that has brought the implementation of such a device closer to reality is the improvement in thin film coatings technology. Interference filters can now be designed to give defined transmission shapes, pass bands and rejection ratios with much better tolerances than ever before and thoroughly tested using computer programs such as *Essential McLeod* (Thin Film Center Inc.) before manufacture.

1.4.2 An interference filter based monochromator

A diffraction grating only disperses light in one dimension, therefore the apertures of a diffraction grating based monochromator employ slits; the entrance slit controls the incident angle of the radiation on the grating and an exit slit selects a cone of light dispersed by the grating. In this manner the width of the slits, together with the focal length of the monochromator and the density of the grooves on the grating control the bandwidth of the monochromator. The efficiency of the monochromator is reduced as, although the gratings are generally blazed to maximise the efficiency at a particular wavelength, at wavelengths away from that wavelength the efficiency decreases. Generally the strength of the signal is reduced by 50 % at two thirds and 1.8 times the blaze wavelength as more light is transmitted in the zero order and higher orders. For comparison dielectric interference filters can be made with low losses and transmissions greater than 90 %.

An interference filter based monochromator would have efficiency advantages over a monochromator containing a diffraction grating. Light transmitted through an interference filter is not lost to higher orders and because the wavelength separation occurs in two dimensions, entrance and exit slits would not have to be used; therefore circular or elliptical symmetry may be employed with consequent energy gains. Figure 1.15 shows a comparison between the geometries of an interference filter based monochromator and a typical monochromator employing a diffraction grating.

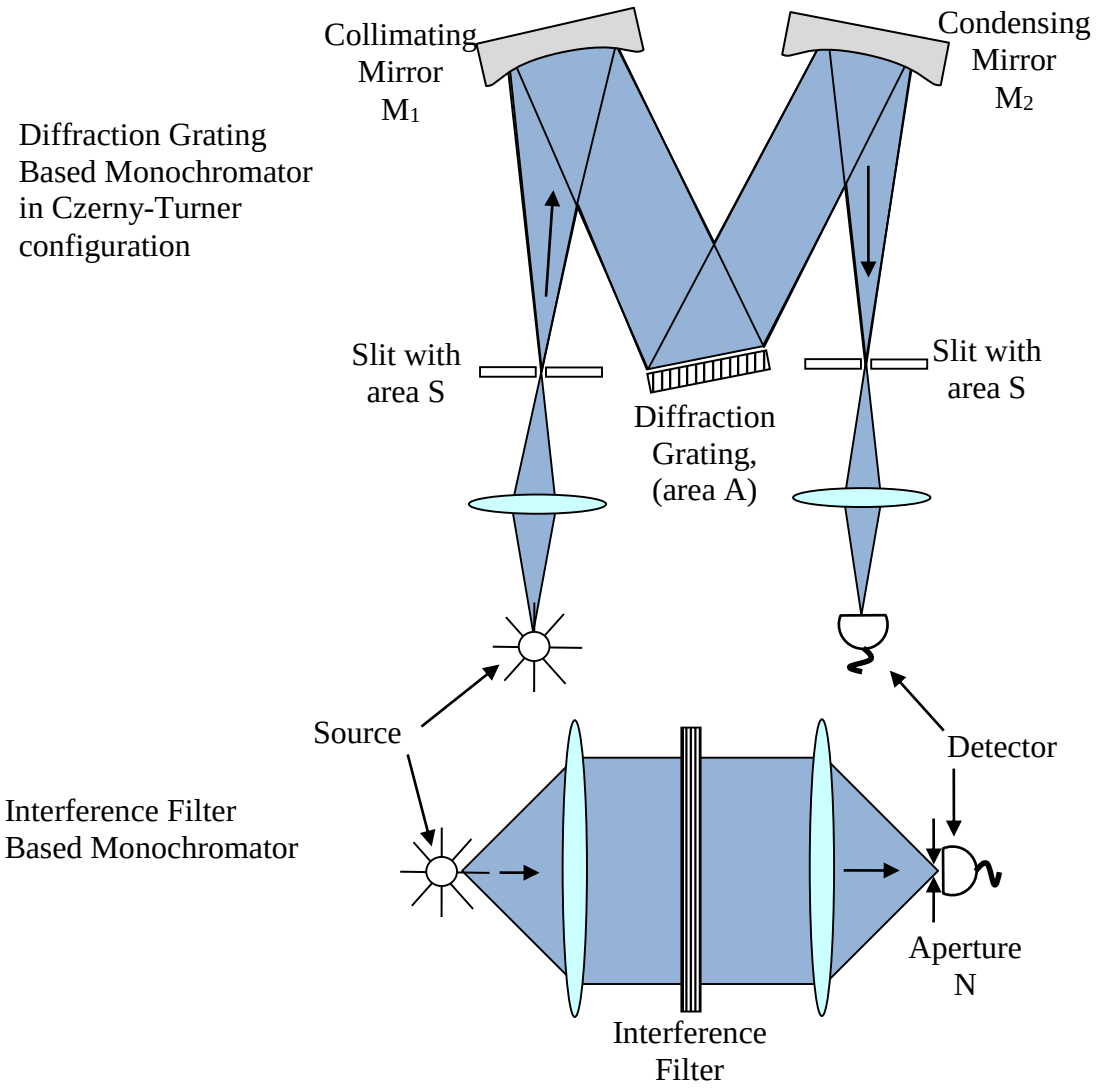

Figure 1.15 Comparison of the optical geometries for a diffraction grating based monochromator (above) and a monochromator based on an interference filter (below)

A monochromator can be characterised by its luminosity (L) and its resolving power ($P = \lambda/\Delta\lambda$). Luminosity is the energy or flux reaching the detector from a source of unit luminance (B) and is a function of the resolving power. In order to compare the relative merits of a grating monochromator and an interference filter monochromator, the relative luminosity has been worked out in comparison to the resolving power. These calculations of relative flux throughputs were first discussed by Jacquinot in 1954 [72].

1.4.3 Flux through a diffraction grating based monochromator

The flux (F_G), that is the optical power, reaching a detector on the end of a grating based monochromator excited by a source of luminance B at wavelength λ is given by Equation (1.37)

$$F_G = \frac{BSA\delta\lambda T_G}{f^2} \qquad (1.37)$$

where: T_G is the transmission coefficient of the instrument, A is the area of the grating, S is the areas of the entrance and exit slits (assuming they are equal), f is the focal length of the mirrors, M_1 and M_2, assuming $f_{M1}=f_{M2}$ and $\delta\lambda$ is the bandwidth of radiation transmitted by the instrument.

The luminance of a source is the total amount of light emitted by it and is defined in terms of the flux (F) per unit projected area (A) and per unit solid angle (Ω), Equation (1.38)

$$B = \frac{\delta F}{\delta A \cos\theta \, \delta\Omega} \qquad (1.38)$$

where θ is the angle to the normal.

The area of the entrance and exit slits of a monochromator can be defined by their height (l) and width (w), i.e. $S=lw$. This allows S to be written in terms of the angular dispersion of the light from the grating at the exit slit, $\delta\alpha$. This depends on the focal length of the mirrors and the width of the slit, i.e. $\delta\alpha=w/f$.

This can also be written in terms of bandwidth:

$$\delta\lambda = \frac{d\lambda}{d\alpha}\delta\alpha = \frac{d\lambda}{d\alpha}\frac{w}{f} \qquad (1.39)$$

therefore:

$$w = \delta\lambda \frac{d\alpha}{d\lambda} f \, , \qquad (1.40)$$

so that:

$$S = l\frac{d\alpha}{d\lambda}\delta\lambda f \, , \qquad (1.41)$$

The flux may therefore be written in terms of angular dispersion, Equation (1.42).

$$F = B\frac{l}{f}\frac{d\alpha}{d\lambda}(\delta\lambda)^2 AT \, , \qquad (1.42)$$

Thus the flux obtainable at a given resolution depends on the ratio of slit height to focal length as well as the angular dispersion of the grating and the area.

Assuming a blazed grating is used, the blaze efficiency is dependent on the angle and hence the wavelength as well as the polarisation of the incident radiation. The normal area of a blazed grating incident with radiation may be represented by Equation (1.43).

$$A_n \frac{d\alpha}{d\lambda} = A\frac{2\sin(\phi)}{\lambda}, \qquad (1.43)$$

where ϕ is the blaze angle.

1.4.4 Flux through an interference filter based monochromator

An interference based monochromator system can be thought of as having a collimating lens (to collimate the light from the point radiation source) an interference filter (this can be considered as a low order Fabry-Pérot etalon) and a condensing lens to focus the light through an aperture (*N*) onto a detector (Figure 1.15). The aperture limits the angle of incidence of the collected radiation to a cone with a semi-angle of Φ.

Summing all beams from normal incidence to Φ will then give the form of the transmitted band (as a function of wave number ω). Jacquinot showed [72] that the transmitted flux (F_I) of such a monochromator will be given by Equation (1.44).

$$F_I = \frac{1}{4}\pi B T_I A_I \Omega \delta\lambda, \qquad (1.44)$$

where T_I is the maximum of transmitted band of the interferometer, A_I is the area of the plates of the etalon and Ω is the solid angle of acceptance of detector (determined by aperture, *N*).

The solid angle of acceptance may also be described by the Equation (1.45)

$$\Omega = 2\pi\frac{\delta\lambda}{\lambda}, \qquad (1.45)$$

Therefore the flux passed by an interference filter based monochromator may be given by Equation (1.46).

$$\begin{aligned} F_I &= \frac{\pi^2}{2}\frac{B T_I A_I \Omega(\delta\lambda)^2}{\lambda} \\ &\approx 4.9\frac{B T_I A_I \Omega(\delta\lambda)^2}{\lambda} \end{aligned} \qquad (1.46)$$

1.4.5 Comparing a grating and an interference filter based device

To compare the luminosity transmitted by the interference filter based monochromator with a diffraction based monochromator, the fluxes and therefore the luminosity of the two devices may be compared to give Equation (1.47)

$$\frac{F_I}{F_G} = \frac{4.9 T_I B A_n}{2\sin(\phi) T_G B A \left(l/f \right)} \qquad (1.47)$$

For the same bandwidth of transmitted radiation and device area and assuming a typical blaze angle of 30º, the Equation (1.47) becomes:

$$\frac{F_I}{F_G} = 2.5 \frac{f}{l} \qquad (1.48)$$

The angular slit height for a grating monochromator (*l/f*) is normally around $^1/_{30}$ i.e. for a 300 mm focal length monochromator, the ratio would become:

$$\frac{F_I}{F_G} \sim 75 \qquad (1.49)$$

Therefore, there should be a potential gain in luminosity of up to a factor of 75 [70], [72], [73].

1.4.6 The effect of a focused beam through an interference filter

The main drawback of the interference based monochromator described above is that the area of the filter incident by the radiation has to be large; therefore tuning the wavelength pass band by means of a linear wedge filter design would require an unfeasibly large filter. However, the filter may also be placed in a convergent beam, providing that the maximum angle of incidence is sufficiently restricted. In such a system, radiation from a source would be focused on to an interference filter and the transmitted light would then be collected and focused on to a detector by a second lens.

Polster showed [74] that the intensity transmitted by an interference filter based monochromator can be represented by Equation (1.50).

$$I(\psi_o) = \frac{1}{\frac{1}{2}\varepsilon_L \sqrt{(1+F)}} \tan^{-1} \frac{\sqrt{(1+F)} \tan\left(\frac{1}{2}\varepsilon_L \right)}{1 + F / \left(1 + \cot\frac{1}{2}(\psi_o + \varepsilon_L) \cot\frac{1}{2}(\psi_o) \right)} \qquad (1.50)$$

where ψ is the phase difference between successive beams ($\psi = 4\pi t\omega\cos\phi$), $\psi_o = 4\pi t\omega$ and ε_L is an expression for the maximum phase difference between beams introduced by the angle of incidence Φ.

In the situation where a focused beam is incident on the interference filter, the same equation describes the transmitted intensity but ε_L is determined by the cone of acceptance of the second lens. Performance of the grating is obviously reduced by using non-parallel light, but this reduction in performance is mitigated by the use of a high refractive index spacer (see Figure 1.14).

It was shown by Smith in 1958 that the angle scanning behaviour of a Fabry-Pérot multilayer filter may be characterised by a monolayer with an effective refractive index n^* [75]. Simple analytical expressions can be used to determine the degradation of spectral profile resulting from a cone of incident light being used for a chosen design of filter.

1.4.7 The use of different types of filter design

The Fabry-Pérot filter has a pass-band shape that has long tails to either side of the transmission maxima, however this shape can be improved by effectively coupling Fabry-Pérot etalons in series. Smith showed the performance of combining two of these filters together. These coupled arrangements are known as double half-wave (DHW), triple half wave (THW) filters and so on depending on the number of filters that are combined in there construction. These multiple half-wave filters have a transmission band with sharper edges. These also tend to have a superior stray-light rejection ratio.

The effect of nonparallel light on the performance of double half wave filters has been studied empirically and experimentally by Pidgeon and Smith [75], [76]. The findings indicated that DHW filters that are superior to a given Fabry-Pérot filter also have a marginal advantage in non-parallel light.

1.4.8 Wedge interference filters

As discussed in Section 1.4.1, the idea of an interference filter based monochromator is not new, however, the interference filter used in this research is of a continuous wedge design. Previous interference filter based spectrometers worked by varying directly the width of an air spacer in the Fabry-Pérot etalon. However, this technique is very sensitive to vibration and would require precision alignment, especially in the visible region. Filter

manufacturing techniques have now advanced to a stage where variable thickness thin film layers can be deposited. This means that the width of the etalon and even the quarter wave stacks can be varied on a substrate. The coating technique involves placing a mask between the deposition source and the filter substrate. The mask is designed with an aperture that varies linearly, so that more coating material is deposited on one side of the substrate than the other. The resultant filter then has a series of layers and therefore optical properties that vary with position. An illustration is shown in Figure 1.16.

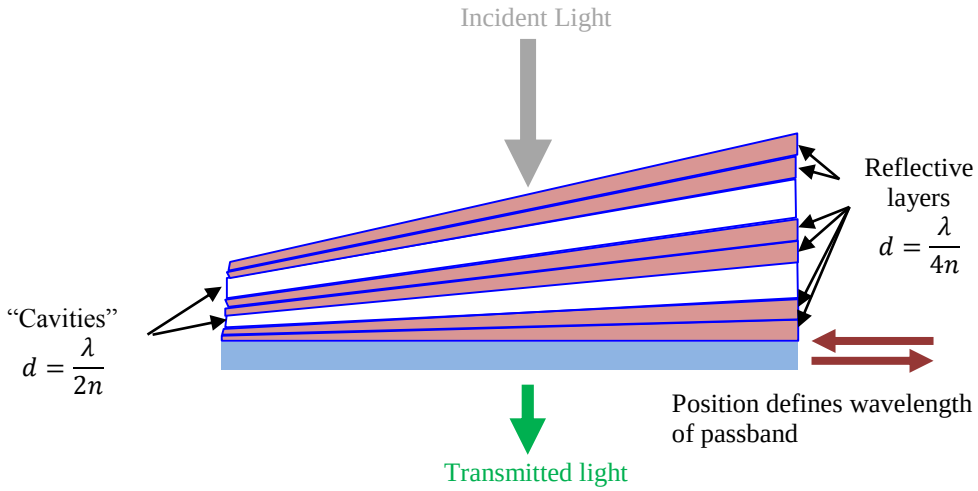

Figure 1.16 Illustration of a linear wedge interference filter

By this method, the band edge or even the peak transmission of the filter may be altered continuously simply by moving the filter laterally. This movement can be done using a motor.

1.5 Conclusions and thesis structure

This chapter has introduced fluorescence lifetime spectroscopy and the various excitation sources currently used. It was found that there is a requirement for a broadband, high repetition rate, short pulse, and turnkey excitation source for fluorescence lifetime spectroscopy. The supercontinuum effect was discussed, it was found that with careful design of a photonic crystal fibre and careful selection of the source it is possible to generate a broad spectrum extending from the UV to >2000 nm. A supercontinuum source with the appropriate design has the prospect of being an ideal source for fluorescence lifetime spectroscopy. Chapter 2 of this thesis will introduce various supercontinuum sources and evaluate their suitability as an excitation source for use in a commercial fluorescence spectrometer employing TCSPC.

The theory and design of multilayer optical filters was discussed from a simple Fabry-Pérot etalon to a tunable wedge interference filter. The wedge interference filter offers the possibility of a high throughput, tunable monochromator without a diffractive element. This could be an ideal method of wavelength separation for a supercontinuum as it maintains the spatial properties of the source. Chapter 3 of this thesis will evaluate various designs for wavelength separation of a supercontinuum source based on wedge interference filters.

Wavelength separation in fluorescence spectrometers is predominantly carried out using diffraction grating based monochromators. As has been shown in this chapter, a wedge interference filter offers the possibility of far greater throughput, however, the grating monochromator has advantages in terms of flexibility and fine bandwidth control. Chapter 4 of this thesis will evaluate the benefits of combining both elements to create a monochromator based on both a diffraction grating and a wedge interference filter.

CHAPTER 2 - THE INTEGRATION OF A SUPERCONTINUUM SOURCE INTO A FLUORESCENCE SPECTROMETER AND THE EVALUATION OF NOVEL UV ENHANCED DEVICES

This chapter describes the integration of various photonic crystal fibre (PCF) based supercontinuum sources into a commercial fluorescence spectrometer. Exploratory measurements were made with the first generation of commercial supercontinuum sources. These have a rather restricted wavelength range for fluorescence applications due to the lack of UV output, the extent of the supercontinuum generated from these devices does not extend below 450 nm. This limits their appeal as a flexible light source for fluorescence spectrometers, although they remain useful for the excitation of many visible absorbing fluorophores and samples such as quantum dots. More in-depth studies were then carried with the next generation of supercontinuum sources utilising a differently structured photonic crystal fibre (PCF). These sources emit light into the UV (<400 nm) and therefore are more applicable as a flexible excitation source. Following this, novel supercontinuum sources with output even further into the UV were characterised. Finally, commercial supercontinuum sources from other manufacturers are discussed and critically compared as potential excitation sources for fluorescence spectroscopy.

2.1 Characterisation of the performance of the first generation of commercial supercontinuum sources for TCSPC applications

As previously discussed in Section 1.3, the extent of a supercontinuum produced by the nonlinear effects in a PCF is determined by the wavelength dependence of the group index of the fibre. The fibre used in such a source is an endlessly single mode (ESM) PCF (i.e. a fibre with no higher order mode cut-off). A scanning electron micrograph of a similar fibre is shown in Figure 2.1. When the PCF is pumped by a source with a wavelength close to the minimum of the group velocity a soliton is produced that undergoes a self-frequency shift in the red direction (Figure 2.2). The red extent is determined by the optical loss (caused by OH^- absorption in the fibre) and dispersion. The blue wavelengths are generated by four-wave mixing between the red wavelength side and the pump [45]. Therefore, the shortest blue wavelength will be the wavelength with the group index equal to that of the extreme red component (group velocity matching), Figure 2.3. [45], [77]–[79]

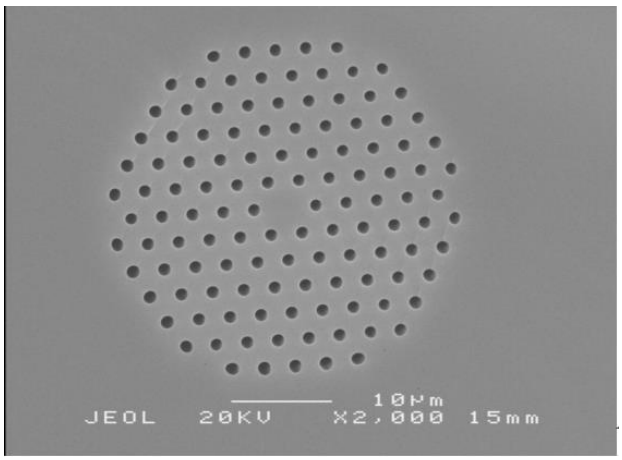

Figure 2.1 scanning electron micrograph of conventional endlessly single mode photonic crystal fibre [80]

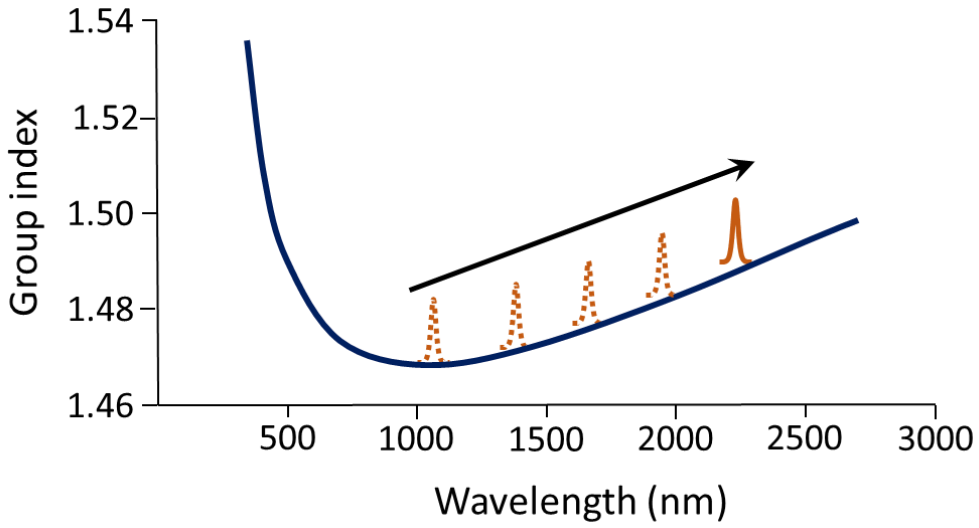

Figure 2.2 Illustration of soliton self-frequency shift in an endlessly single mode PCF

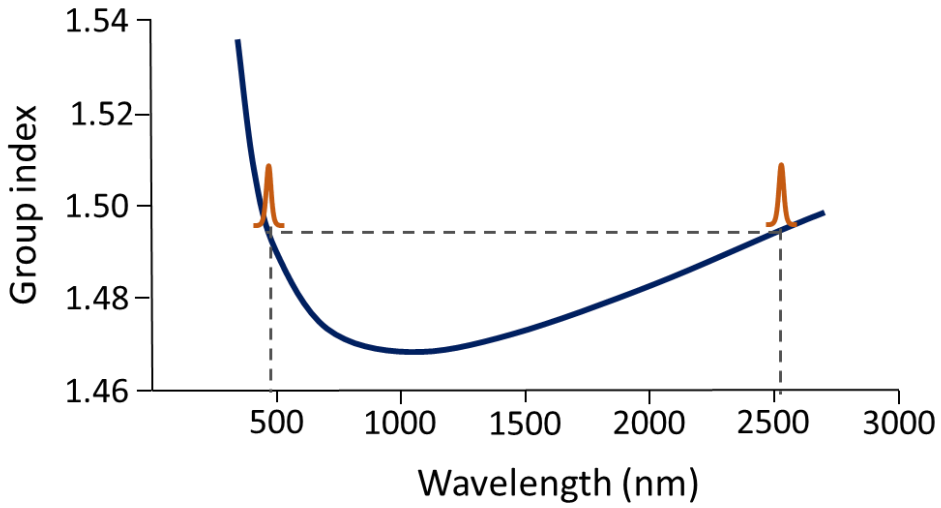

Figure 2.3 Illustration of group velocity matching in an endlessly single mode PCF

2.1.1 Experimental setup

Initial measurements were made to study the spectral and temporal characteristics of the supercontinuum light source with TCSPC detection, with the laser coupled to a fluorescence lifetime spectrometer as shown in Figure 2.4.

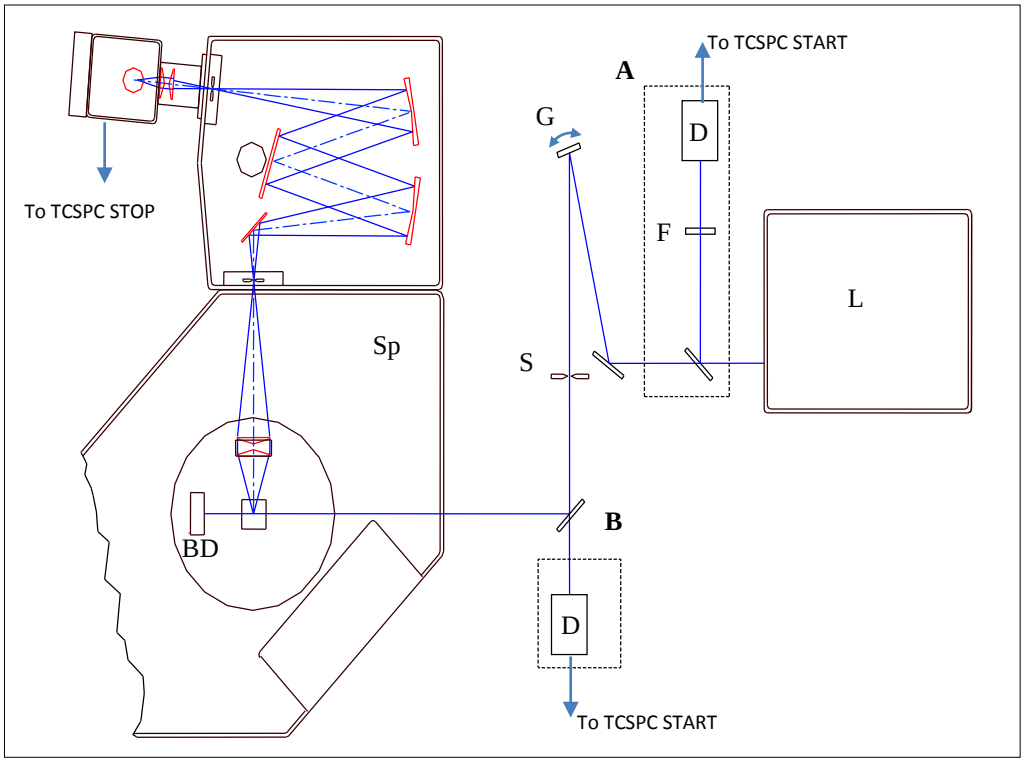

Figure 2.4 Experimental setup: Sp, FLS920 spectrometer with emission monochromator and cooled MCP-PMT detector; L, supercontinuum laser; F, 700-nm bandpass interference filter; D, fast trigger diode; G, grating on rotational mount; BD, Beam dump; S, slit; A, setup for triggering at 700 nm, B, setup for triggering on the excitation wavelength.

The supercontinuum light source (Fianium SC450-PP-2) had a specified spectral range from 450-2000 nm, a repetition rate of 20 MHz and an output power of 2 W over the full spectral range (although other repetition rates and output powers were available). The supercontinuum light source consisted of an ytterbium (Yb) based fibre laser master pump source and a specially designed photonic crystal fibre. The pump laser was specified with a fundamental pulse width of <8 ps and with a timing jitter of <1 ps. The source also had a built in pulse picker to allow the frequency to be adjusted down to as low as 100 kHz.

The TCSPC - based fluorescence lifetime spectrometer (FLS920, Edinburgh Instruments) was used as standard, but with the following modifications: the side port of the sample chamber, opposite the standard excitation arm, was used to direct the laser radiation to

the sample. A beam dump behind the sample was used to absorb the remainder of the beam not absorbed by the sample. The beam dump removes reflections that can severely affect the quality of TCSPC measurements, typically shown on a semi-logarithmic scale – reflections of >0.01% of the light show up as spurious peaks delayed by the additional path length the reflection travels. In addition, the standard PMT was replaced by the optional cooled MCP-PMT for measurements with superior time resolution. The instrumental response function for a 17 ps diode laser was measured to be 45 ps.

To spectrally resolve the supercontinuum light source, an 1800 grooves/mm grating was used, which was illuminated by the collimated laser beam. A slit was used for wavelength selection. Two amplified silicon pin diodes (OT900, Edinburgh Instruments) were used to pick up radiation at different parts of the setup in order to provide trigger pulses to the TCSPC data acquisition electronics of the FLS920 spectrometer. It should be noted that the optical system was set up to minimise any temporal effects that would originate from group delay dispersion in the instrument (this involved minimising the angle between the light incident on the grating and the exit slit). By comparing measurements that were made at zero order and at first order (with additional wavelength selection filter), we could confirm that temporal pulse displacements were less than 20 ps and pulse broadening less than 5 ps across 500 nm at a centre wavelength of 600 nm.

Monochromators themselves can introduce temporal dispersion and shift effects. In order to separate temporal dispersion effects caused by the emission monochromator from those of the laser source under investigation, all measurements reported here were made with the emission monochromator in zero order.

2.1.2 Optical power measurements

The optical power of the supercontinuum source was measured at the sample position (see Figure 2.4) for wavelengths between 450 nm and 800 nm (Figure 2.5). Note that the efficiency of the optical elements, in particular the efficiency of the grating has not been corrected for. The grating efficiency is responsible for the drop of optical power beyond 700 nm. The more than two-fold increase in optical power in the region of 480 nm and the dramatic cut-off at around 460 nm is a feature of the laser (and is in agreement with the manufacturer's specifications). Although the laser was specified to have optical output only down to 450 nm, it was possible to perform lifetime measurements down to excitation wavelength of 440 nm, due to the high sensitivity of the TCSPC based instrument.

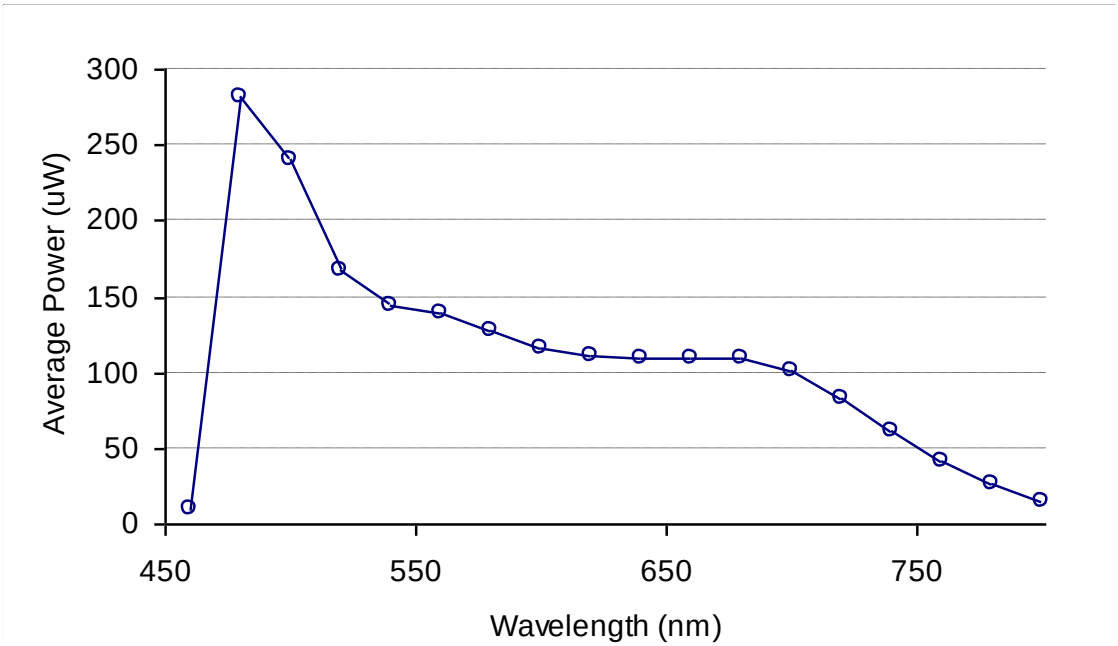

Figure 2.5 Optical power measured at the sample position, using a power meter (LM2, Coherent).

2.1.3 Pulse width and temporal position

The width and the shape of the instrument response function (IRF) are crucial indicators for the temporal resolution that can be achieved with the fluorescence lifetime spectrometer. In the absence of a suitable trigger output at the laser (the TTL output that is available does not provide sufficient timing accuracy), a beam splitter with a trigger diode (attachment **A** in Figure 2.4) was used to provide synchronization pulses for the TCSPC electronics. The smallest widths of the IRFs were only obtained with an interference filter placed in the reference beam. Various interference filters were tested. A 700 nm bandpass interference was found to work well and was used for the experiments described here.

Figure 2.6 shows two example measurements of IRFs at different wavelength. IRFs measured at shorter wavelengths than the reference wavelength are temporally delayed and have a longer duration, i.e. a larger full width at half maximum (FWHM) than those measured at the reference wavelength of 700 nm.

IRF measurements, like those shown in Figure 2.6 were measured in 5 nm steps from 450-850 nm. These IRFs were then used to calculate the wavelength dependence of pulse delay and pulse duration which are shown in Figure 2.7. The shape of the graph "pulse position versus wavelength" has the familiar look of a fibre dispersion curve. For the laser that is evaluated here the measured shift was 300 ps, when the wavelength was

changed from 500 nm to 700 nm. The temporal shift is not really surprising; the shift is simply a consequence of the fact that blue light travels through the fibre with reduced speed in comparison to red or infrared light. For practical single TCSPC measurements this shift is not an issue, as long as the IRF is measured at the wavelength of excitation. The temporal shift becomes more problematic when time resolved emission spectra (TRES) are to be generated from measurement series with a fixed emission wavelength and an incremental increase of the excitation wavelength (Excitation TRES). In this case, triggering on the excitation wavelength would be desirable as this would eliminate the temporal shift of the excitation pulses.

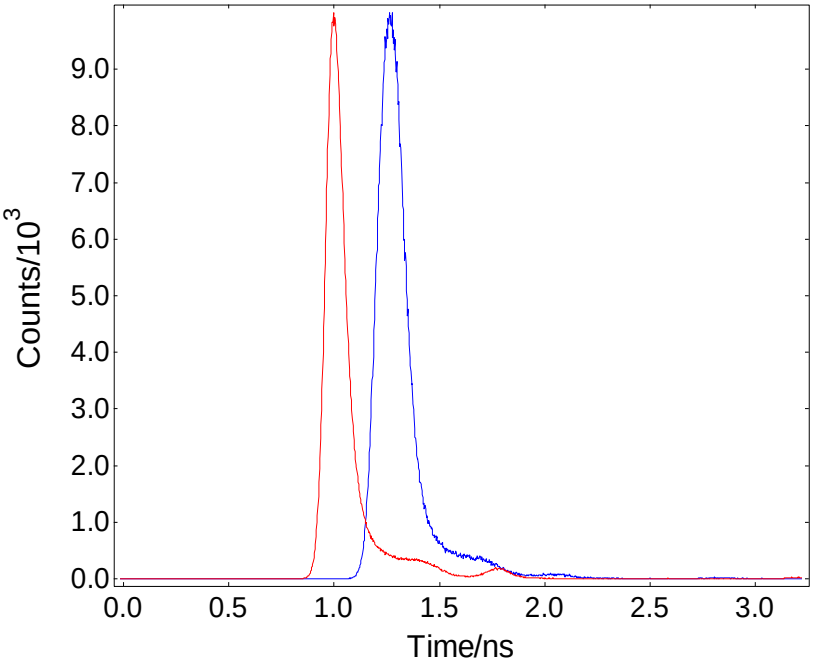

Figure 2.6 IRF measurements at 500 nm (right) and at 700 nm (left), using setup A. FWHM (500nm)=150 ps, FWHM (700nm) = 100 ps

Figure 2.7 also shows the variation in pulse width with respect to wavelength; with the maximum IRF pulse width of 170 ps at around 520 nm. The pulse width increase is a bigger problem, as it means reduced temporal resolution in this wavelength region. For the experimental setup of Figure 2.4, with the trigger pickup attachment A, a pulse width increase for shorter wavelengths could result from either: temporal jitter of the short wavelength pulses in respect to the pulses of the reference wavelength 700 nm; or broader laser pulses in the shorter wavelength region, compared to the reference wavelength.

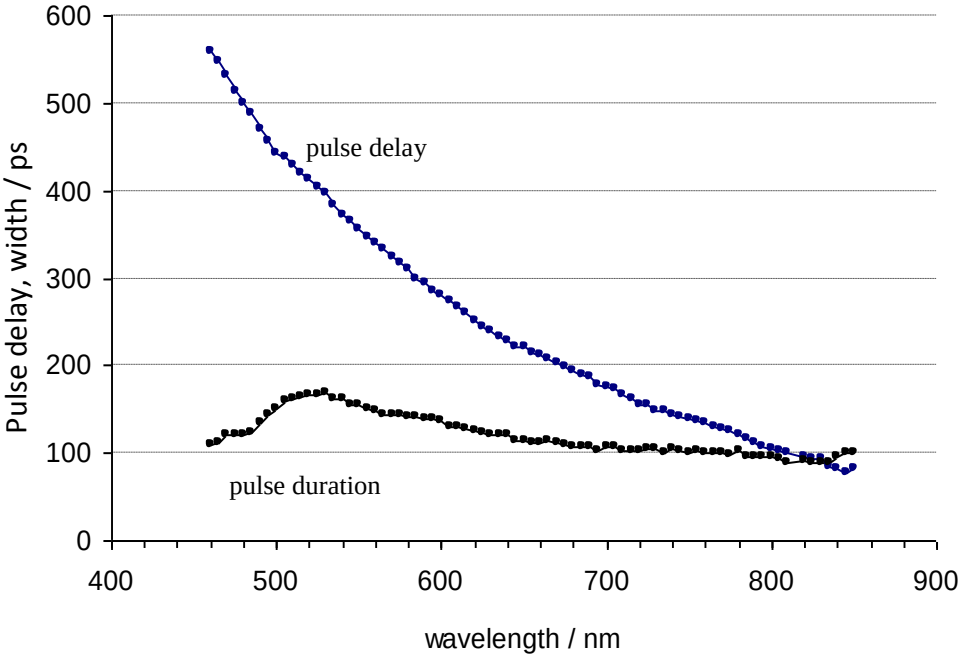

Figure 2.7 Pulse delay and pulse width with respect to the reference wavelength of 700 nm for experimental setup A

In the experimental setup of Figure 2.4 with the trigger pickup attachment B, i.e. triggering on the same wavelength pulses that pass into the spectrometer, was also possible. In trigger pick up B, the TCSPC electronics are triggered post filtering (after wavelength selection of the source). This should not only eliminate the pulse shift caused by the dispersion of the photonic crystal fibre, but should also provide an answer to whether jitter or broadening is the cause for the pulse width dependence on wavelength. The results are shown in Figure 2.8.

With the pulse triggering on the filtered excitation pulses, the dramatic shift in the peak position was eliminated, as illustrated in Figure 2.8. A much smaller, yet significant, sinusoidal shaped pulse shift with respect to wavelength remains; most likely caused by the optical system used for these experiments. However, the shape and general tendency of the change of the pulse width with respect to wavelength remain the same. This experiment leads to the conclusion that laser pulse broadening, and not pulse jitter, is the more likely reason for the pulse width increase at 520 nm.

It should be noted that the pulse width reduces again at wavelengths below 520 nm. The wavelength with the broadest pulse width is therefore different than the wavelength with maximum average power (480 nm).

Figure 2.8 Pulse shift and pulse width in dependence of the wavelength for experimental setup B

2.1.4 Pulse jitter measurements

By attaching both trigger pulses (from the setup attachments **A** and **B**) to the TCSPC data acquisition electronics, independent pulse jitter measurements can be made. The peaks measured this way are not affected by the intrinsic pulse height distribution of the MCP-PMT detector, but are solely caused by jitter of the timing electronics and the pulse jitter of the light source. The results of the measurement are summarized in Figure 2.9. For this particular experiment, the jitter of the timing electronics was 40 ps, verified by measuring the signal from one trigger diode and using a signal splitter to connect it to both TCSPC timing channels. Using the approximation that the square of the electronics jitter plus the square of the jitter of the optical pulses results in the square of the width of the jitter in the measured pulse [17], the jitter of the optical pulses can be calculated (see equation 2.1). The results are shown on the bottom of Figure 2.9.

$$\Delta\tau_{true}^2 = \Delta\tau_{measured}^2 - \Delta\tau_{instrumental}^2 \qquad (2.1)$$

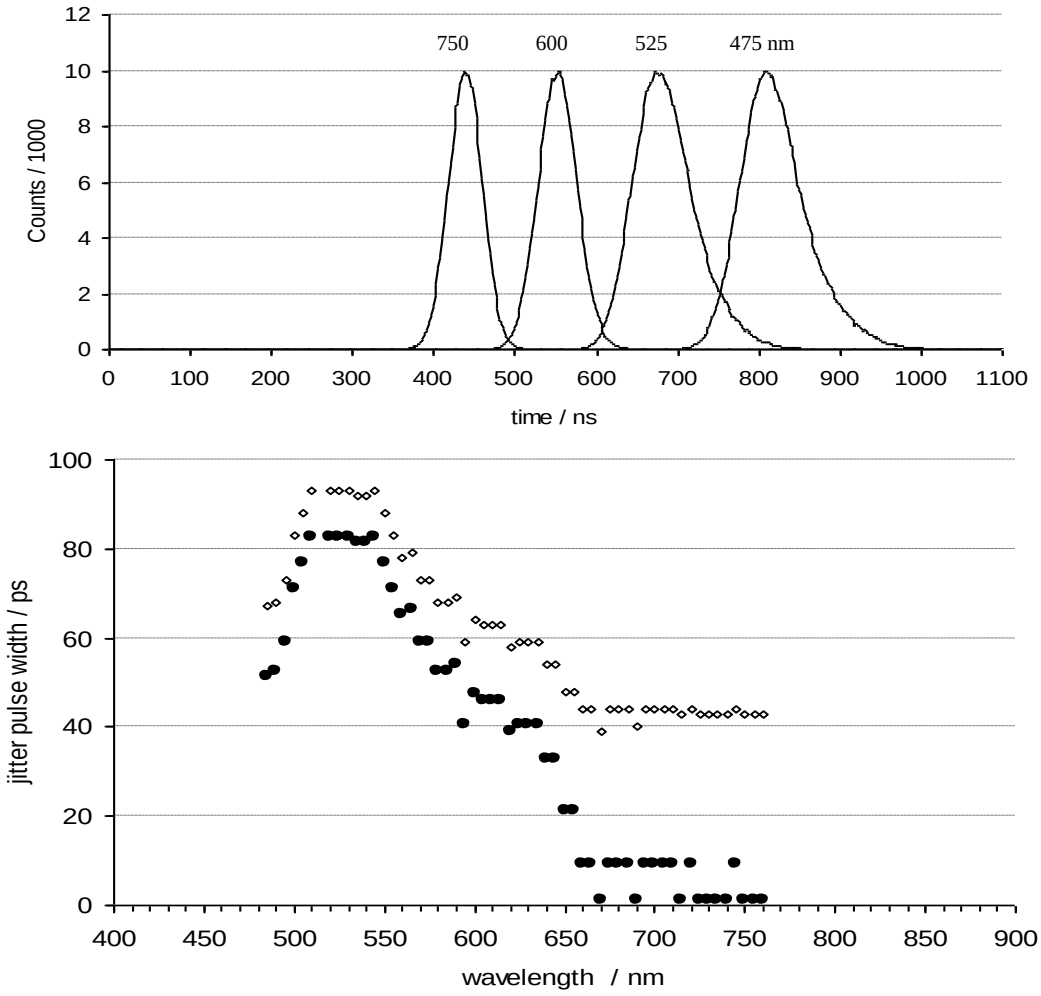

Figure 2.9 Top- examples of jitter measurements at four different wavelength. Bottom - measured (◇) and corrected (●) width of the pulse jitter for different wavelength

2.1.5 Pulse height distribution measurements

It is apparent that the pulse width and pulse jitter measurements appear to give different results. One important characteristic, the pulse height distribution of the laser pulses, has so far not been considered, i.e. the pulse to pulse variation in intensity. Although the source output looks stable, the supercontinuum in this regime has been generated from modulation instability which is an inherently noise driven process, see Section 1.3.2.

The pulse height distribution was measured using the trigger diode of the setup attachment **B**. (silicon photodiodes have negligible intrinsic pulse height distribution compared to PMT and MCP-PMT detectors with high amplification noise [81]). The lower threshold of the detection electronics was systematically increased in steps of 5 mV and the count rate of signal pulses was recorded. Subsequent differentiation of those curves resulted in

the shape of the pulse height distribution of the laser pulses with respect to the laser wavelength (Figure 2.10). The technique is similar to that used to measure a differential pulse height spectrum of pulse height distribution for PMTs [82]. The height of the curves of Figure 2.10 (vertical axis) was independently determined by monitoring the threshold at which the count rate starts to drop below the laser repetition rate of 20 MHz. This is reasonably accurate for narrow distributions (800 nm), but has increased uncertainty for the broader distributions.

By moving from longer (800 nm) to shorter (475 nm) wavelengths, the intensity distribution of the laser pulses became systematically broader, and the average pulse height decreased. While TCSPC, as a digital technique, is known to be insensitive towards pulse height fluctuations, light source fluctuations this significant are likely to cause additional problems. The constant fraction discriminator (see Section 1.1.3), which usually overcomes trigger problems from pulse height fluctuations of photomultiplier detectors [16], could cause additional broadening to the resultant IRF when pulses with extremely different heights and shape have to be processed.

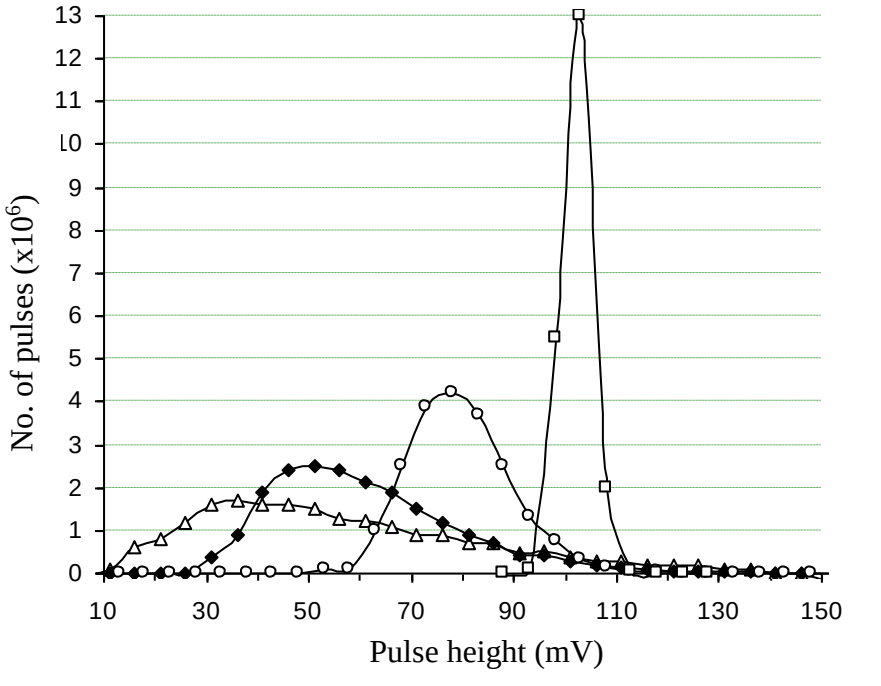

Figure 2.10 Pulse height distribution at different wavelengths: △ at 475 nm, ◆ at 525 nm, ○ at 600 nm, □ at 800 nm

2.1.6 Discussion

For a supercontinuum laser source of the type that was evaluated – an endlessly single mode PCF all fibre based source (Fianium SC450), best performance is achieved when the synchronisation (trigger) pulses are derived at the wavelength that is used for the

excitation wavelength for TCSPC experiments. This eliminates the temporal shift for pulses at different wavelengths caused by the dispersion of the photonic crystal fibre.

Even with the light source synchronised in this way to the TCSPC electronics, an increase in the width of the instrumental response function in the wavelength region of 520 nm cannot be avoided. Optical pulses from the fibre in this wavelength region were found to have a significantly broadened distribution of pulse intensities (pulse height distribution). Compared to the pulse height distribution of high gain photomultipliers, where the pulse shape remains largely unaffected, the pulse height distribution of the pulses from the fibre appear to be accompanied by changes in the temporal width of the pulses.

The supercontinuum laser has a maximum of optical power in the region of 480 nm. In this spectral range a noticeable reduction of the pulse width was observed. This could be due to different mechanisms such as soliton trapping that can occur at the blue edge of a supercontinuum (Section 2.2.6 and 2.3.3)

Further optimisation of the optical setup shown in Figure 2.4 is required for a robust, universal light source that is spectrally tunable and for use in a spectrometer based on TCSPC. The biggest limitation of this particular source for TCSPC measurements is the lower wavelength cut-off of 450 nm.

2.2 Characterisation and integration of a commercial supercontinuum source with UV output

A supercontinuum source with output below 450 nm requires a modification to the PCF used. In order to steepen the change in group index with wavelength at the red side of the zero dispersion wavelength a PCF with a similar hole pitch (Λ) as the endlessly single mode fibre used in Section 2.1 but larger hole diameters (a high-Δ PCF). A scanning electron micrograph of a similar fibre is shown in Figure 2.11. The alteration in hole diameters had the effect of having a steeper change in group index with wavelength at the red side of the zero dispersion wavelength [43], [80] and a corresponding shift in the blue extreme because of the group index matching, (Figure 2.12).

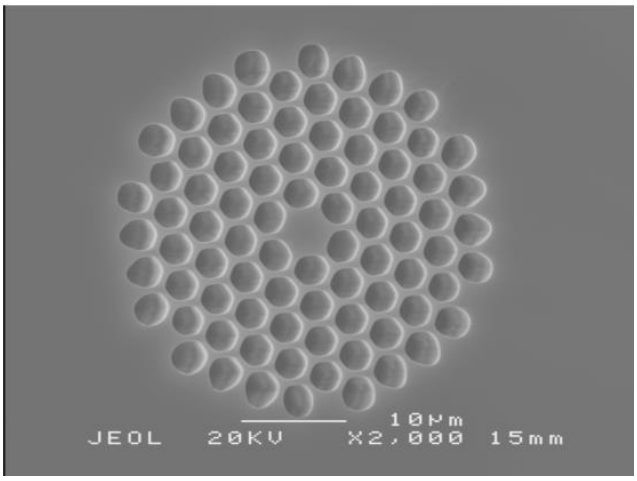

Figure 2.11 scanning electron micrograph of a large core high-delta photonic crystal fibre [80]

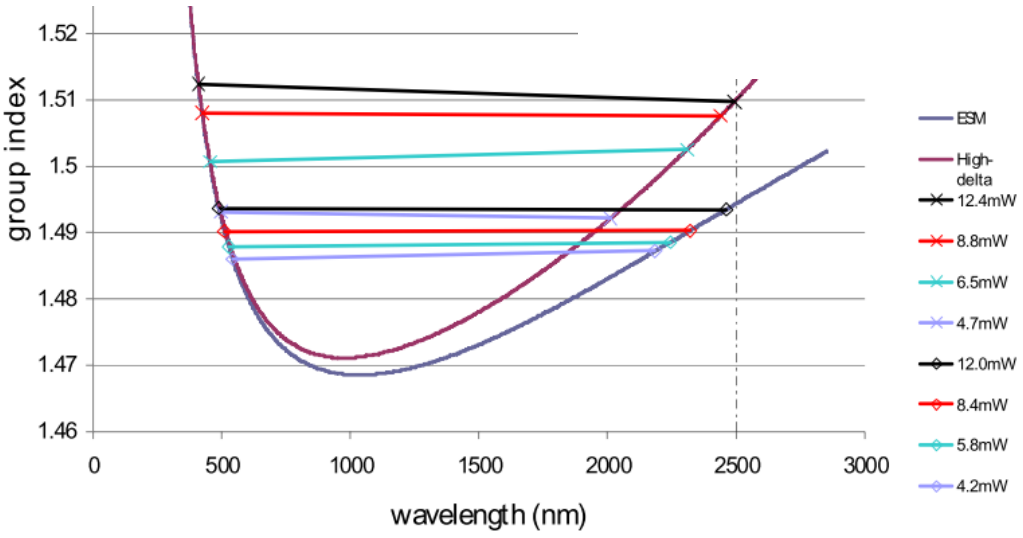

Figure 2.12 modelled group index curves for ESM fibre (blue) and high-Δ fibre (purple) [80]. *Illustration of the effect of using a High-Δ PCF on the group index and resultant blue shift of the lowest wavelength of supercontinuum generated.*

2.2.1 Experimental setup

To study the spectral and temporal characteristics of a commercial high-Δ PCF based supercontinuum light source, an SC-400 (Fianium) was coupled to a fluorescence lifetime spectrometer as shown in Figure 2.13. The SC-400 had 2 W total output power and was fitted with an integrated pulse picker to allow selection of repetition frequencies between 100 kHz and 20 MHz.

The TCSPC based fluorescence lifetime spectrometer with double monochromators (FLS920, Edinburgh Instruments) was used as standard, but with the following

modifications: the side port of the sample chamber, opposite the standard excitation arm, was used to direct the laser radiation to the sample. As before, a beam dump behind the sample was used to absorb the remainder of the beam not absorbed by the sample. In addition to the standard PMT (R928P, Hamamatsu), an NIR-PMT (R5509-72, Hamamatsu), and an InAs detector (P10090, Hamamatsu) were used for spectral measurements. Spectral correction was made by comparing the sensitivity of the emission arm (with each of the detectors connected) to tungsten and deuterium correction lamps that are traceable to a National Physical Laboratory (NPL) standard source. A cooled MCP-PMT (R3809-U50, Hamamatsu) was used for measurements with the best possible time resolution. When using the MCP-PMT, the instrumental response for a 17 ps diode laser pulse measured on the spectrometer was 45 ps. The spectrometer also contained a reference detector. The emission arm (detector and monochromator optical paths) were spectrally calibrated using NPL traceable tungsten and deuterium sources.

For spectral resolution of the supercontinuum light source a 1800 grooves/mm grating blazed at 500 nm was used in the range 300-800 nm, a 600 grooves/mm grating, blazed at 1000 nm was used in the range 800-1700 nm and a 300 grooves/mm grating, blazed at 2000 nm was used in the range 1700-3000 nm. An amplified silicon pin diode (OT900, Edinburgh Instruments) was used to pick up radiation at different parts of the setup in order to provide trigger pulses to the TCSPC data acquisition electronics of the FLS920 spectrometer. Care was taken in the experimental setup to minimise temporal effects caused from the variation in beam propagation distances at different wavelengths. By comparing measurements that were made at zero order and at first order (with additional wavelength selection filter), it was confirmed that temporal pulse displacements were less than 20 ps and pulse broadening less than 5 ps per 500 nm with a centre wavelength of 600 nm.

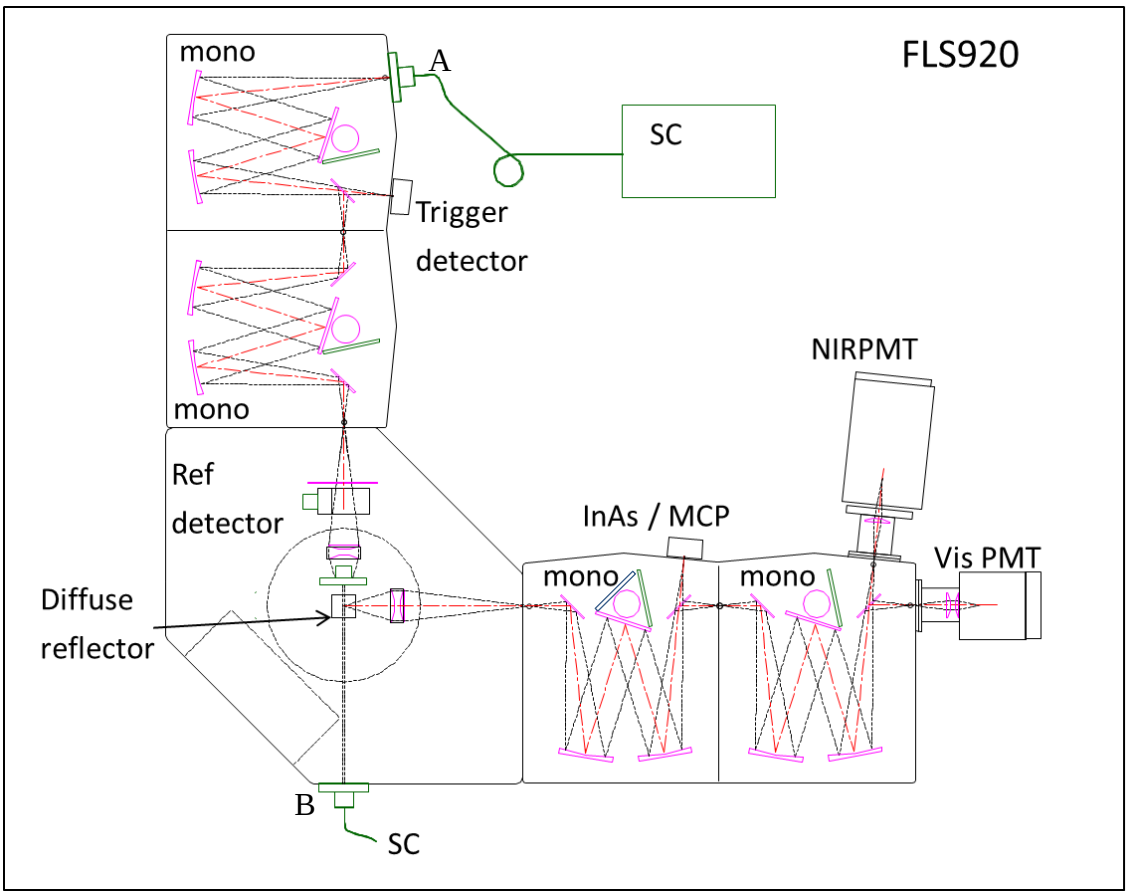

Figure 2.13 - Experimental setup for supercontinuum source characterisation – Fluorescence Spectrometer (FLS920) with double monochromators, three emission detectors, removable beam dump and two positions for the supercontinuum source (SC): A and B.

2.2.2 Spectral output

By inputting the supercontinuum source at the side port of the sample chamber of the FLS920 spectrometer (position B), corrected quasi steady state spectra of the emitted radiation were acquired using the three spectral detectors covering the range from UV to NIR. The results were then combined to give the true spectral output (in photon units) of the supercontinuum source (Figure 2.14). The spectrum shows the supercontinuum output beginning below 400 nm, two narrow peaks at 425 nm and 464 nm, a trough at 610 nm (which is the result of photo-darkening in this particular fibre), a peak at 1064 nm (from the pump laser), a trough at 1384 nm (due to OH^- absorption in the fibre) and continuing to beyond 2400 nm (where the upper limit is again given by OH^- absorption in the fibre.

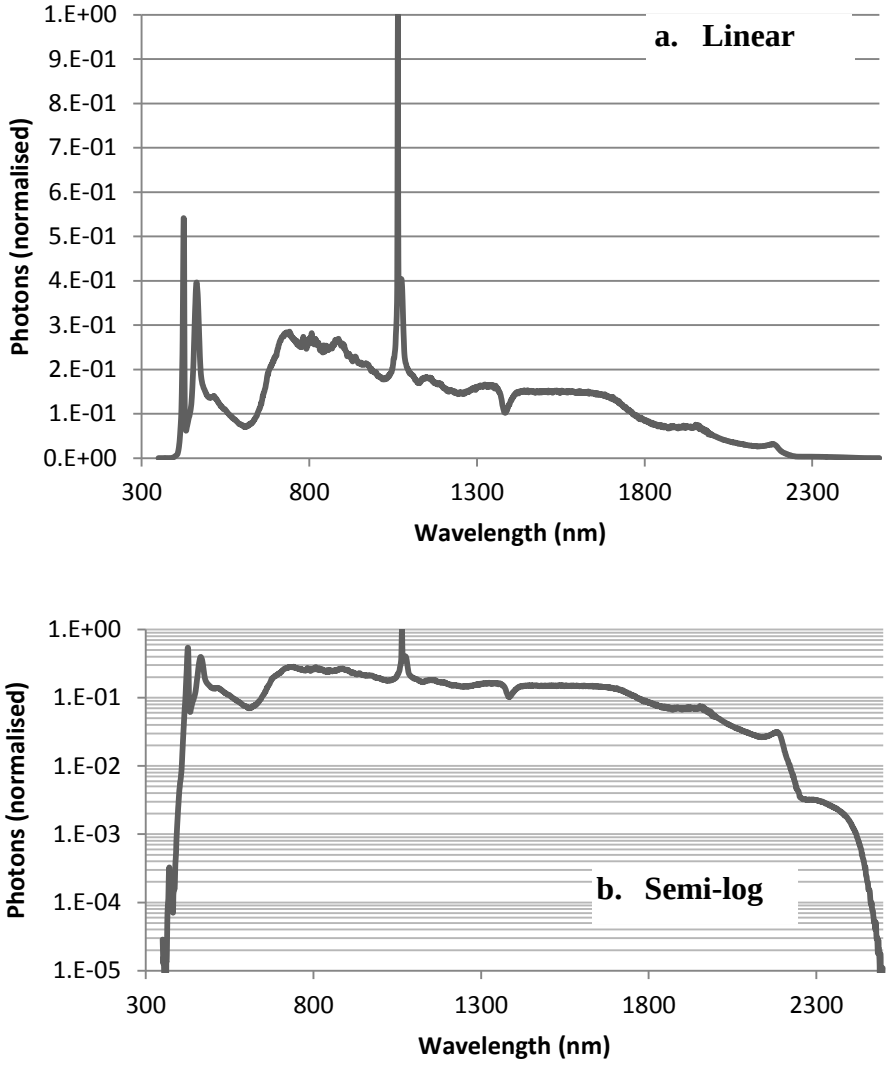

Figure 2.14 Full output spectrum (in photon units) of the supercontinuum light source in semi-log (a.) and linear (b) energy terms. The vertical axis is normalised photon units

As the supercontinuum source used was an early prototype, over time the spectral shape changed as a result of photodarkening. The PCF fibre was then changed, resulting in a change in output spectrum. Figure 2.15 shows a comparison of visible spectral output of the SC-400 with old and new PCF. The new PCF does not suffer from the photodarkening at around 630 nm and also appears to have marginally more output below 400 nm. In this case the photodarkening is caused by a partially bound oxygen atom with one free electron known as a non-bridging oxygen hole centre which has a strong absorption at 258 nm and a weaker band at 630 nm [83]–[85] (clearly visible as a visible in Figure 2.15). Although photodarkening in bulk silica is initiated by UV light [86], it has recently been shown that the predominant cause of photodarkening in PCF based supercontinuum sources is multi-photon absorption of the 1064 nm pump light [87].

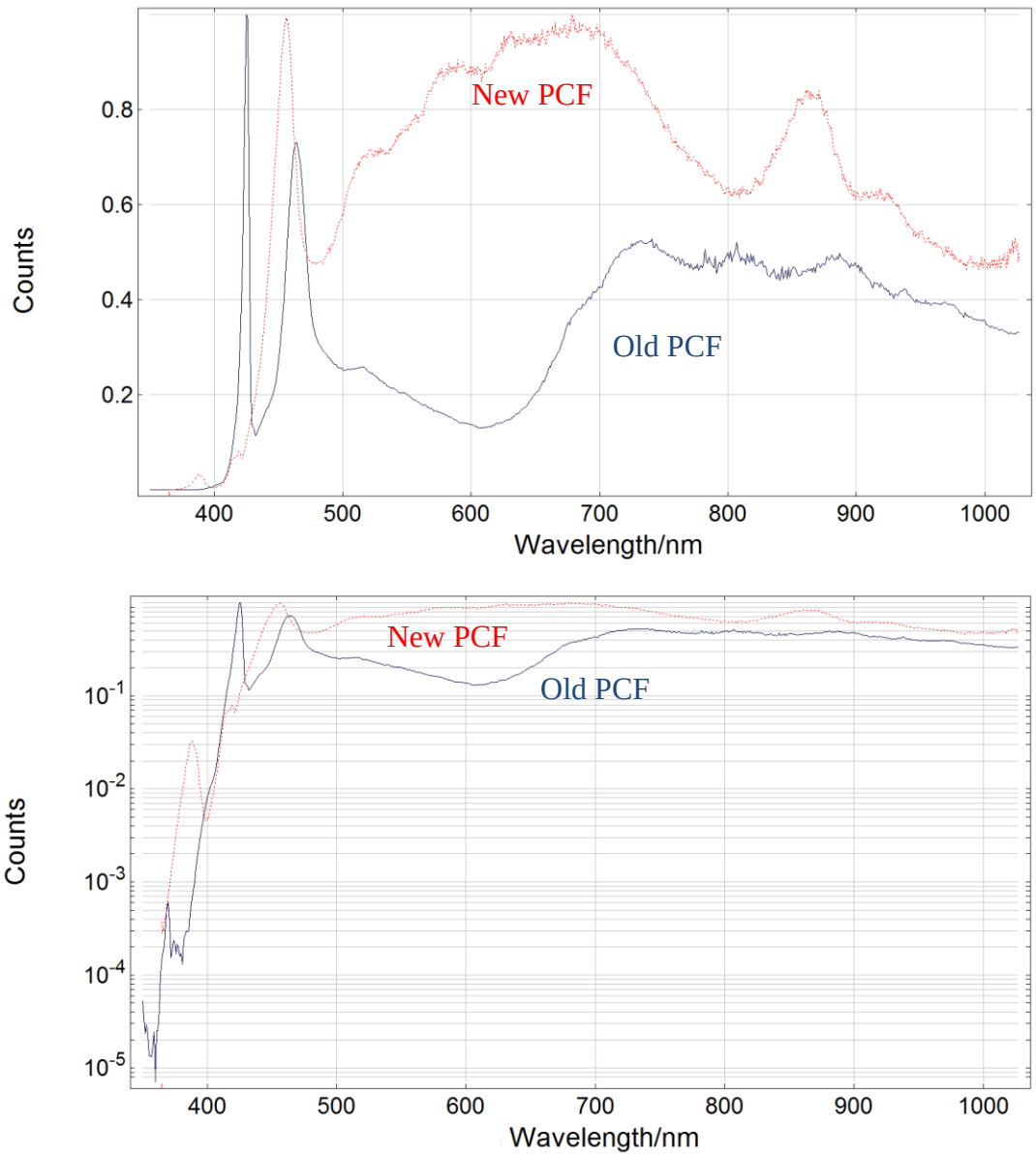

Figure 2.15 Comparison spectra of the supercontinuum with old and new PCF.

Various techniques have been used to significantly reduce the effect of photodarkening on supercontinuum sources, including thermal annealing, in order to relax the glass structure [88], and hydrogen or deuterium loading so that the hydrogen or deuterium can attach to the partially bound oxygen [89], [90].

The standard steady-state excitation source for a high end fluorescence spectrometer is a 450-W xenon arc lamp. In order to see how the light available at the sample position for the excitation of photoluminescencant samples compared between the supercontinuum source and a 450-W xenon arc lamp (Edinburgh Instruments, Xe900), both sources were connected in turn to the excitation monochromator and the signal measured on the reference detector. The reference detector is normally used to correct for the wavelength dependence of the excitation arm (including source), therefore this comparison yields

useful information as to the capabilities of a supercontinuum source in such an arrangement to excite a luminescent sample. Measurements were made with 1-nm and 5-nm slit bandwidths. The resulting curves are shown in Figure 2.16 and Figure 2.17.

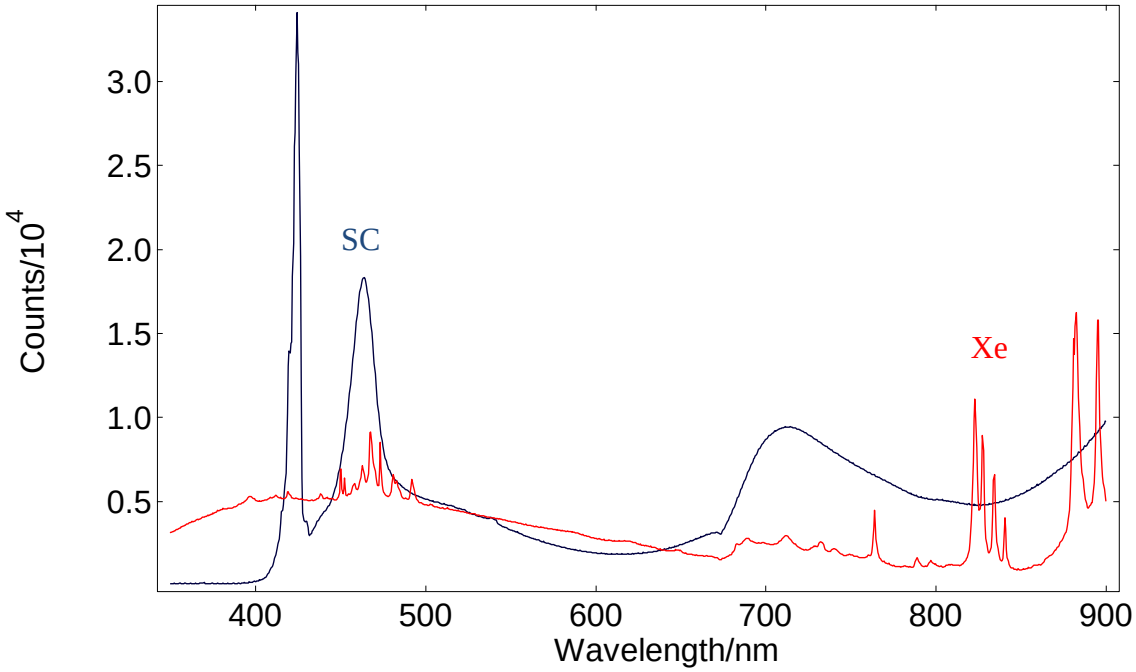

Figure 2.16 Intensity signal at the calibrated Si reference detector of the spectrometer. Monochromator bandwidth 1 nm.

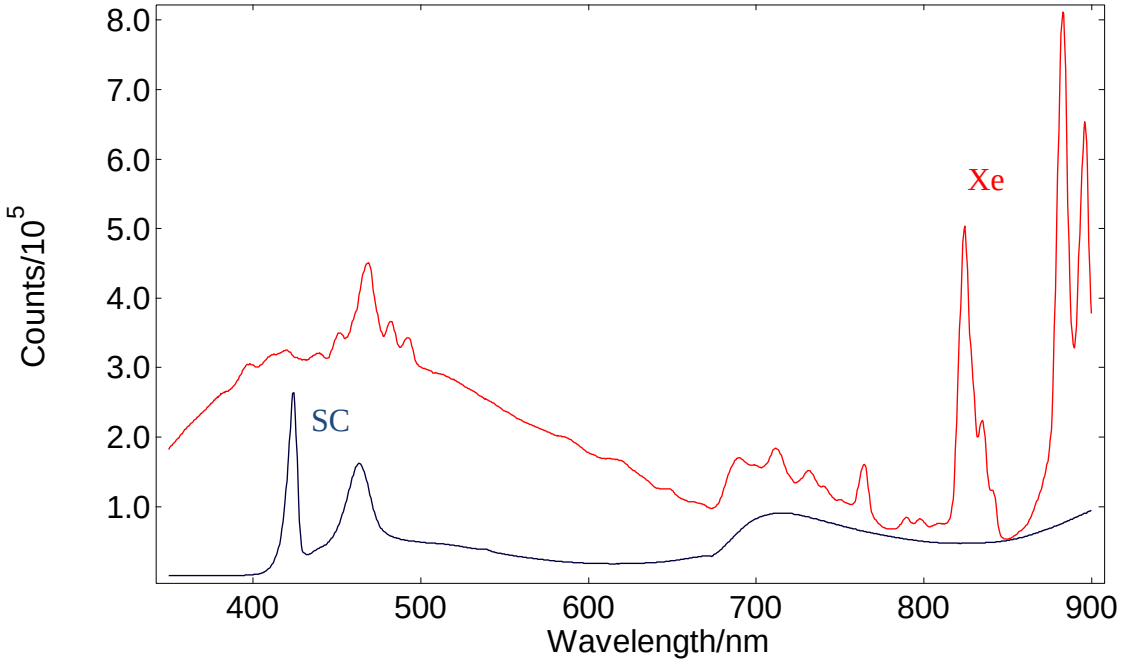

Figure 2.17 Intensity signal at the calibrated Si reference detector of the spectrometer. Monochromator bandwidth 5 nm.

The reason for the difference in relative intensity between the two sources for different bandwidths is because a xenon lamp is an extended source (the emission comes from a plasma that extends for ~3 mm) whereas the supercontinuum has a closer approximation to a point source (the PCF has a core of a few micron). The spot size of the focused SC light on the monochromators entrance slit is ~100 μm at FWTM (the full width at tenth of maximum). This was measured by closing the excitation slit to a minimum value (50 μm) and opening it until the light from the SC entered without clipping either slit. The mount for the supercontinuum source was designed with horizontal position adjustment for the focusing lens. When the beam clipped either slit a fringe pattern was clearly visible on the transmitted light; 100 μm was the size that it was possible to adjust the slits to where there was no fringe pattern visible. The spot size of the arc lamp on the first slit was ~4 mm. The excitation monochromator was a 300 mm focal length double additive monochromator using a 1200 grooves/mm grating with a dispersion of 2.7 nm/mm. Because it was a double additive monochromators the dispersion was doubled to 1.35 nm/mm. A 100-μm slit therefore equates to a 0.14-nm bandwidth (FWHM) for the resulting output. A 4-mm slit on the other hand would equate to a bandwidth of 6.75 nm (FWHM). This means that for even very small bandwidths (above 0.14 nm), all of the supercontinuum output enters the excitation monochromators and so the intensity throughput by the monochromators is purely controlled by the size of the monochromator's emission slit. Whereas for bandwidths below 6.75 nm both entrance and exit slits alter the throughput of the intensity of the xenon lamp (Figure 2.18).

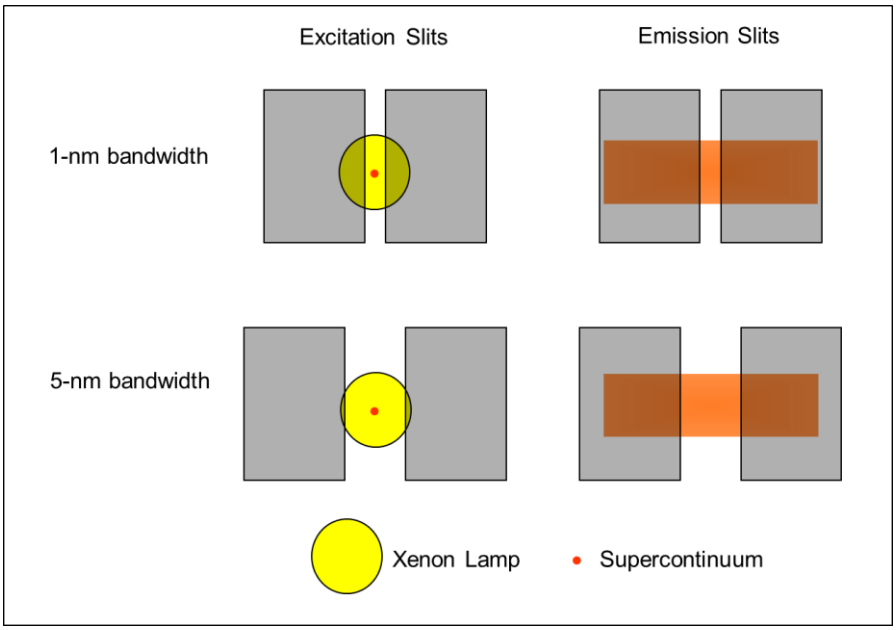

Figure 2.18 An illustration of why spot size alters the intensity throughput as a function of bandwidth.

The results show that below 400 nm the xenon arc lamp dominates (as there is little supercontinuum output), however above 400 nm it is bandwidth dependent. For large excitation bandwidths (>4 nm) the xenon arc lamp dominates, however for small bandwidths (<1 nm) the supercontinuum source dominates. This effect would be less noticeable with lower power xenon arc lamps as they have smaller plasmas, however the lower power would mean lower intensity with large slits.

The standard measure of the sensitivity of a fluorescence spectrometer is the 'water Raman signal-to-noise ratio (SNR)' [5]. The standard way to measure this is to use an ultra-pure sample of water in a quartz cuvette at the sample position. The bandwidths of the excitation and emission monochromators are set to 5 nm and the sample is irradiated with radiation at 350 nm. Water produces inelastic Raman scattering, resulting in a peak at 397 nm. The peak signal is then compared with the RMS noise at 450 nm. A spectrometer employing single photon counting has Poissonian noise statistics. The RMS noise of a signal with Poissonian noise is equal to the square root of the signal [91]. Therefore a typical value given by spectrometer manufacturers employing single photon counting detectors is the signal at 397 nm divided by the square root of the noise at 450 nm. Because the supercontinuum source did not produce radiation at 350 nm, it was not possible to compare the standard water Raman SNR for the spectrometer with a 450-W xenon arc lamp and a supercontinuum source for excitation. However, because the Raman effect is linear with wavenumber it was possible to use an increased wavelength of excitation (425 nm was chosen as it was the strongest emission wavelength of the supercontinuum). The Raman peak at 497 nm was then compared with the noise at 550 nm. The results showed that the system with the xenon arc lamp had a water Raman SNR (at 425 nm) of ~2300:1; whereas the system with the supercontinuum source had a water Raman SNR (at 425 nm) of ~1800:1 (Figure 2.19). The reason for the lower value of sensitivity of the supercontinuum is the convention of measuring this value with broad slits and the issue shown in Figure 2.18.

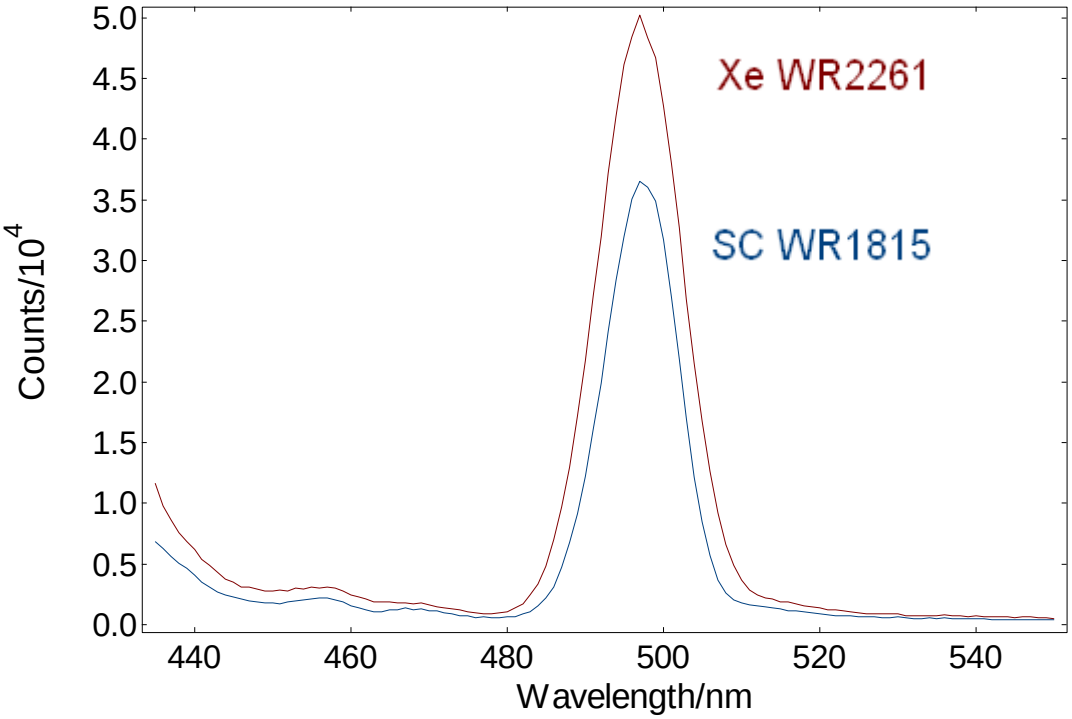

Figure 2.19 Raman signal from water measured with a supercontinuum source (SC) and xenon arc lamp (Xe) as excitation source.

2.2.3 Pulse position

In order to measure the wavelength dependent delay of the pulses from the supercontinuum, the setup in Figure 2.13 was used, with the supercontinuum connected directly to the sample chamber and the MCP-PMT used for detection. The trigger output of the source (provided from a photodiode measuring the output from the master oscillator) as a start signal for the TCSPC electronics. The instrument response function of the system (including the source) was then acquired in steps from 400 – 700 nm. A temporal shift with wavelength of the instrument response function (IRF) was observed (Figure 2.20). The temporal walk can be explained by the combination of group velocity dispersion (GVD) and soliton propagation [92]. The change in position with wavelength above 450 nm can be explained by the wavelength dependence of the refractive index of the fibre (therefore different wavelengths propagate down the fibre at different speeds). The resultant arc therefore resembles the wavelength dispersion curve of a fibre. By triggering the TCSPC electronics on the same wavelength as the measured wavelength, the temporal beam walk is significantly reduced (Figure 2.21). The temporal walk of the measured instrument response pulse was directly compared (Figure 2.22), triggering on the same wavelength was found to reduce temporal walk fourfold (from 180 ps/100 nm to 44 ps/100 nm) within the normal GVD region. Note that a sudden shift (occurring over

a wavelength change of less than 1 nm) remains between the normal GVD region and the non-dispersive region even when triggering occurs at the same wavelength as the measured wavelength. This is a function of the competing nonlinear effects that generate the supercontinuum and is discussed further in Section 2.2.6.

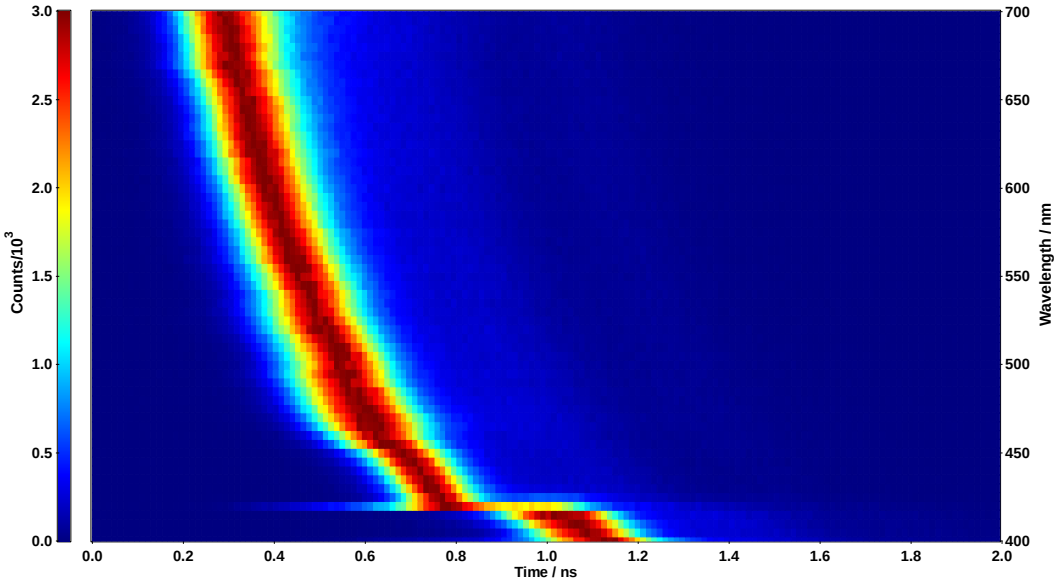

Figure 2.20 Wavelength dependence of the measured pulse position when triggering using the master oscillator source trigger (internal triggering).

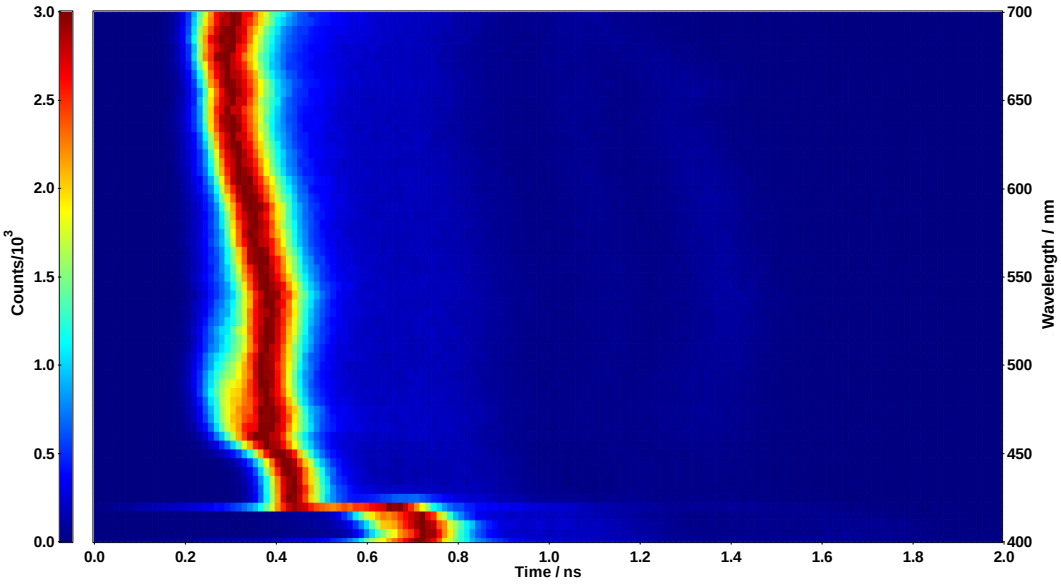

Figure 2.21 Wavelength dependence of the measured pulse position when triggering using the same wavelength as the wavelength measured of the MCP PMT detector (external triggering)..

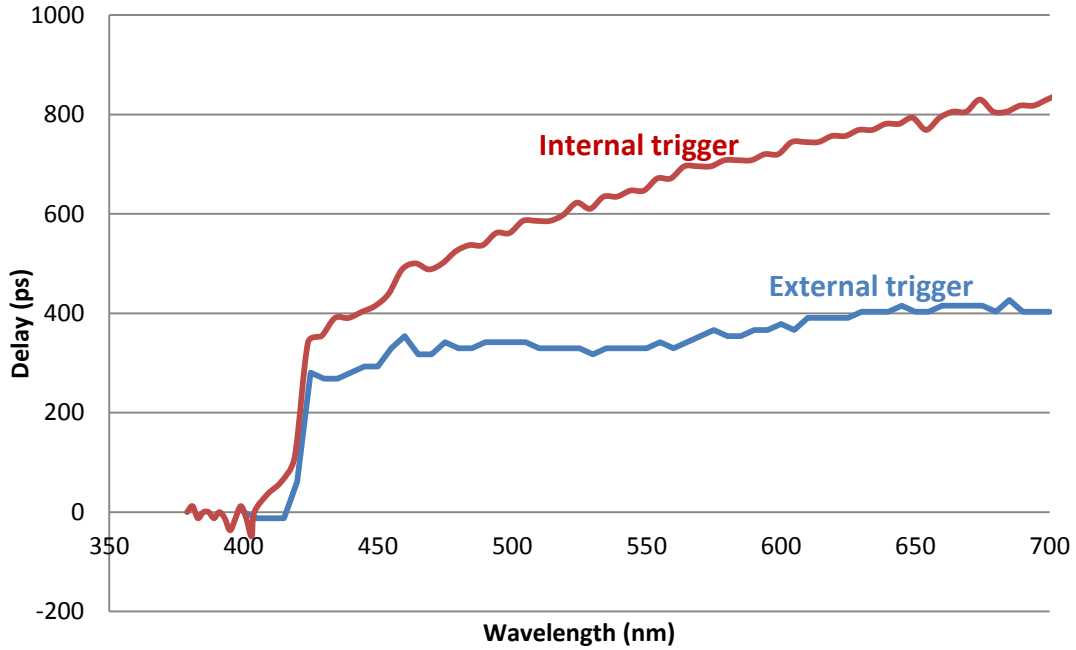

Figure 2.22 Comparison of the wavelength dependence of the temporal walk of the supercontinuum with internal and external triggering.

The results in Figure 2.22 show that if a supercontinuum source such as this one was to be integrated into a commercial lifetime fluorescence spectrometer and the internal trigger of the seed user was used to trigger the electronics, the position of the measured IRF would shift greatly depending on wavelength used. Finding a means of triggering at or near the wavelength of excitation (i.e. the wavelength transmitted by the excitation monochromator) would mitigate most of the delay above 420 nm.

2.2.4 Pulse height distribution

The pulse height distribution of the supercontinuum output was measured using the PIN trigger diode. As previously discussed (Section 2.1.4), silicon photodiodes have negligible intrinsic pulse height distribution compared to PMT. Therefore, the major cause of any variation in output pulse heights is likely to be variation in light intensity. The supercontinuum was used in position A of the experimental setup shown in Figure 2.13, with a PIN diode positioned where the diffuse reflector is shown (after wavelength separation). The PIN diode went through an inverting amplifier circuit and gave out a train of pulses consistent with the frequency of the source (1 MHz). The output of the PIN diode was viewed on an oscilloscope (Tektronics TDS3012C) for various wavelengths for a qualitative check of the pulse to pulse intensity distribution. Figure 2.23 shows a snapshot of the oscilloscope at three wavelengths. The traces show that extreme variation in height from pulse-to-pulse at 446 nm, however at 410 nm and 560 nm, the variation is much less.

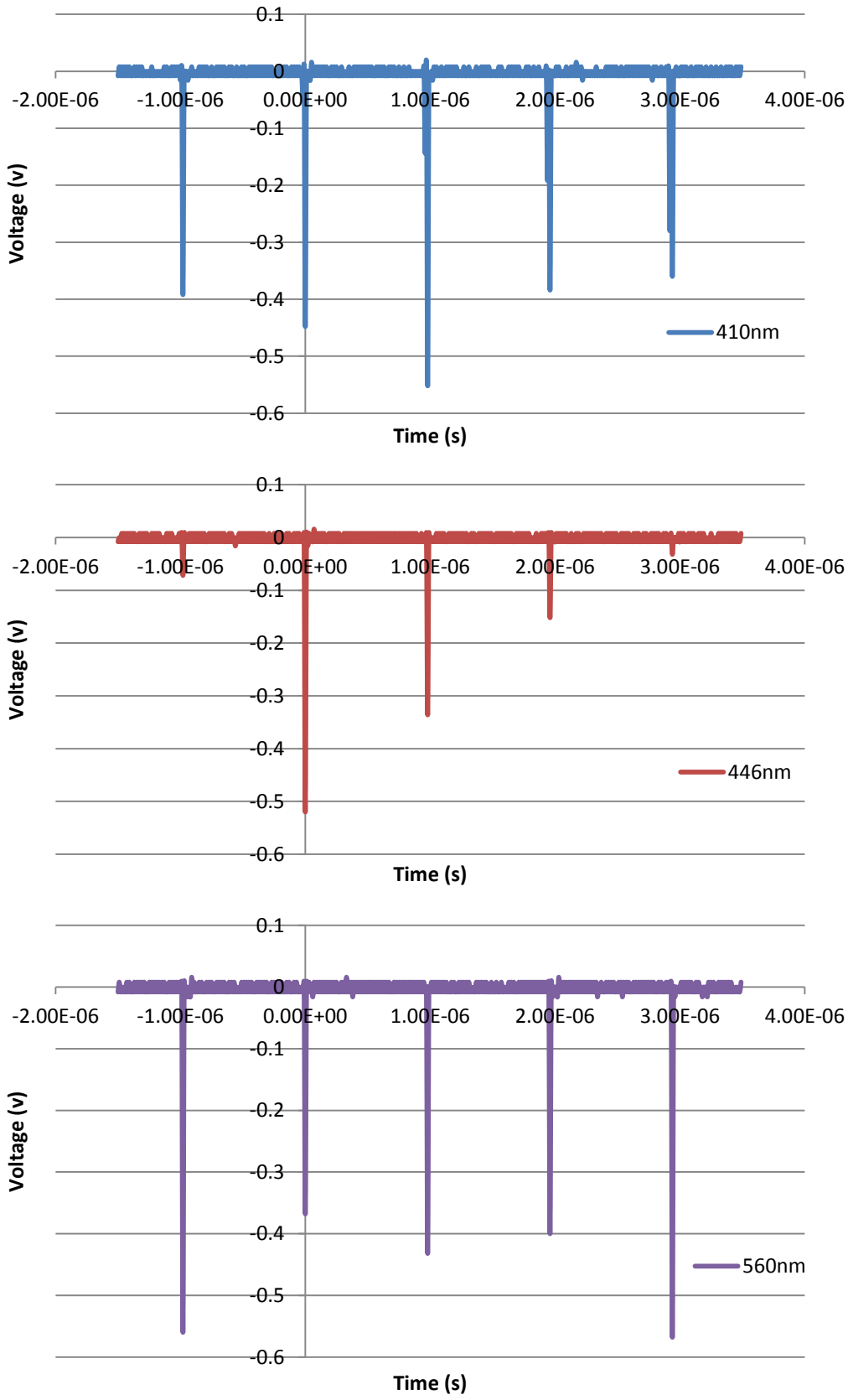

Figure 2.23 Signal output of the PIN photodiode (after inverting amplifier) when illuminated with radiation from the supercontinuum source set to 1 MHz through the excitation monochromator of the spectrometer at three different wavelengths (410, 446 and 560 nm).

The measurements on the oscilloscope show a clear wavelength dependence on pulse to pulse stability of intensity. In order to quantify this, the threshold of the detection electronics was systematically decreased in 1 mV intervals from 0 to -600 mV and the count rate of the signal pulses recorded. As the threshold for the detector increased, initially the pulses with the smallest amplitude are missed. With increasing threshold pulses of increasing amplitude are missed. Figure 2.24 shows the effect of increasing the threshold on the measured signal (with the frequency of the supercontinuum set to 1 MHz).

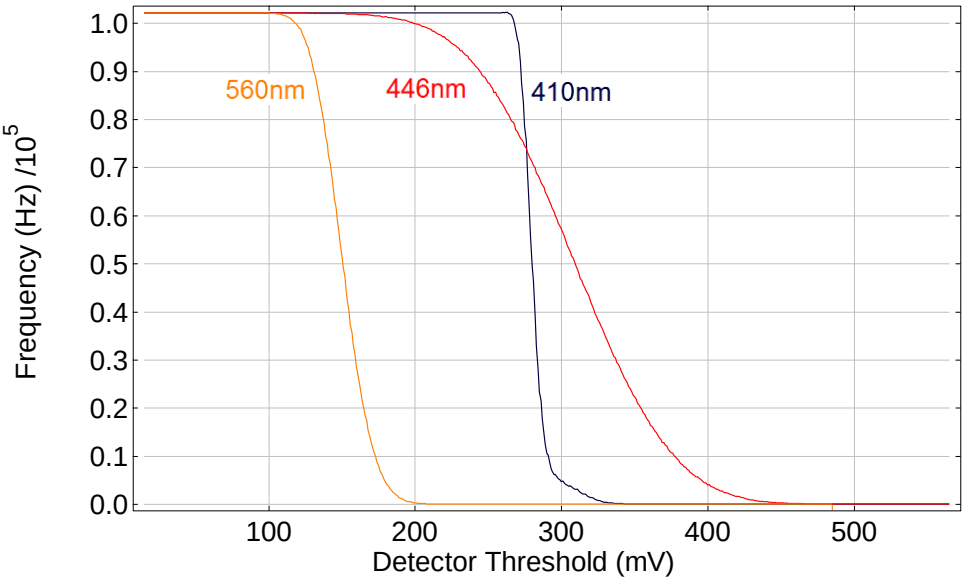

Figure 2.24 The effect of increasing the detector threshold on the measured frequency of the source

Differentiating these curves gave the pulse height differential spectrum for the three measured wavelengths. In other words, a histogram of the number of pulses being measured with intensity. The shape of the intensity pulse height distribution for the three measured wavelengths is shown in Figure 2.25. It can be noted that the distributions in intensity match well with what was observed directly from the oscilloscope (Figure 2.23) i.e. at 446 nm there was an extreme variation in pulse heights measured on the oscilloscope and a correspondingly broad pulse height distribution, whereas at 410 nm the pulse heights varied less and so the distribution was narrower.

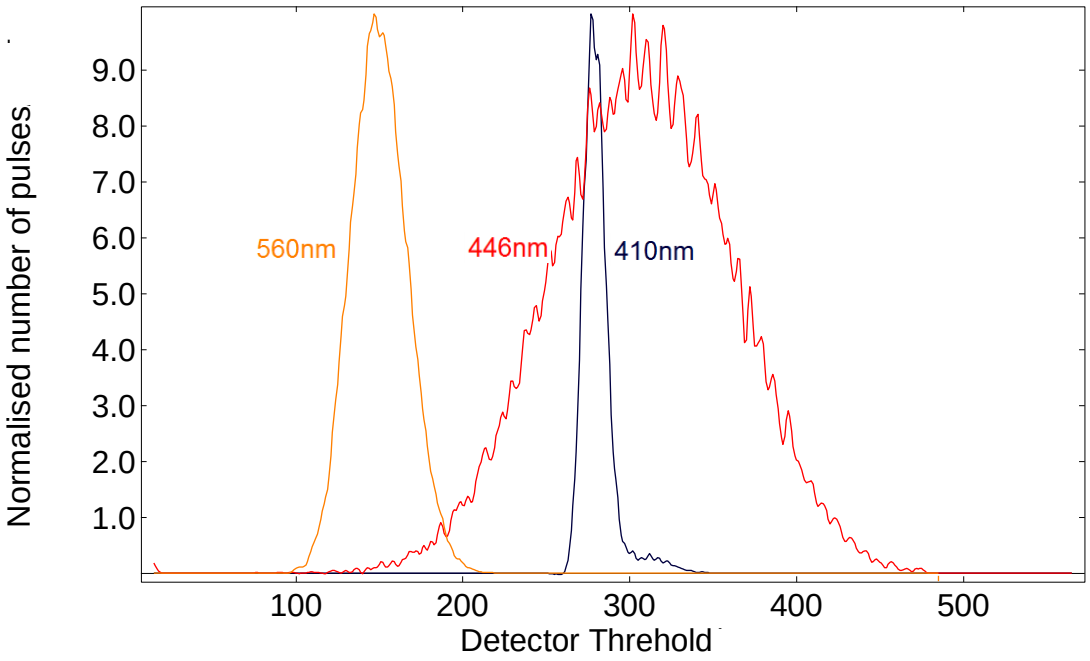

Figure 2.25 Pulse height differential spectrum - normalised pulse height distributions of the supercontinuum at three different wavelengths (410 nm, 446 nm, 560 nm).

In order to properly characterise this effect across a wider range of the source these measurements of pulse height distributions were repeated in 1-nm increments between 400 nm and 680 nm (Figure 2.26), the FWHM width of the distributions was then plotted together with the pulse position information (Figure 2.27). Note that the sharp change in temporal position between the normal GVD region and the non-dispersive region is accompanied by an equally sharp change in pulse distribution width. The corrected intensity from the supercontinuum source was compared with the pulse height distribution (Figure 2.28) which gives an indication of the complex processes involved in the supercontinuum generation. For example, while the intensity and pulse width measured at 440 nm and 570 nm are roughly equal, the light at 440 nm has a broad distribution (i.e. pulses are emitted with a broad range of pulse energies) whereas the light at 570 nm has a narrow distribution (i.e. pulses are emitted with similar energies).

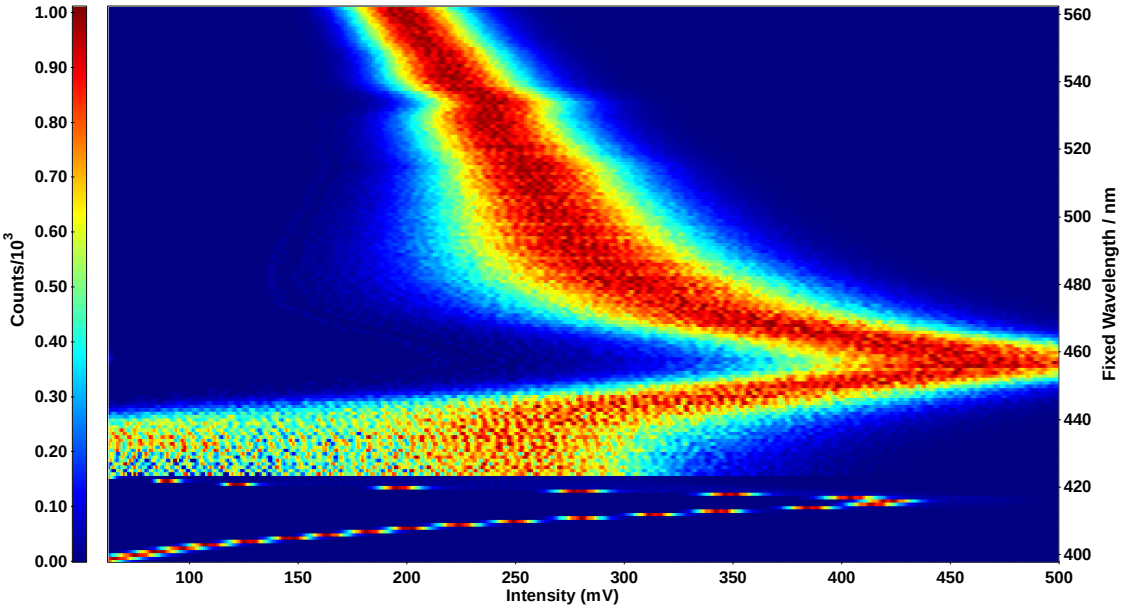

Figure 2.26 Map of the wavelength dependence of pulse height distribution.

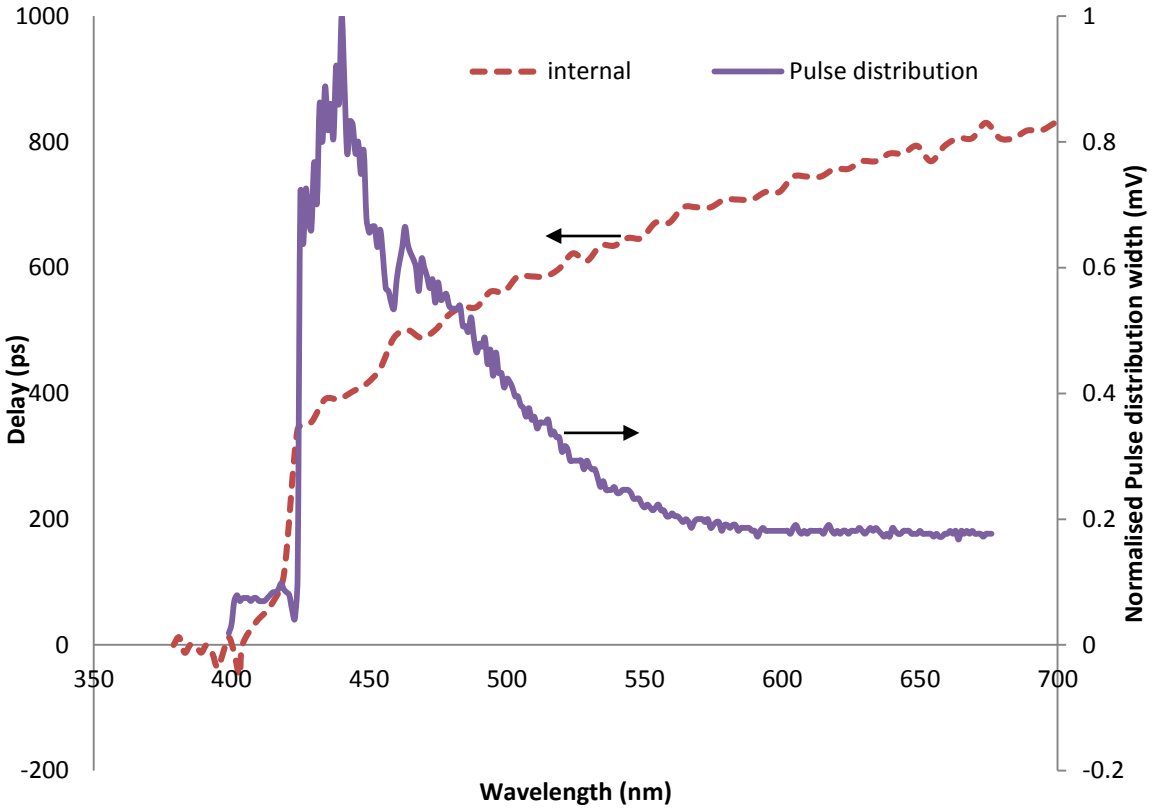

Figure 2.27 Wavelength dependence of the pulse height distribution of the supercontinuum source and change in temporal position of the pulse (with respect to source internal trigger).

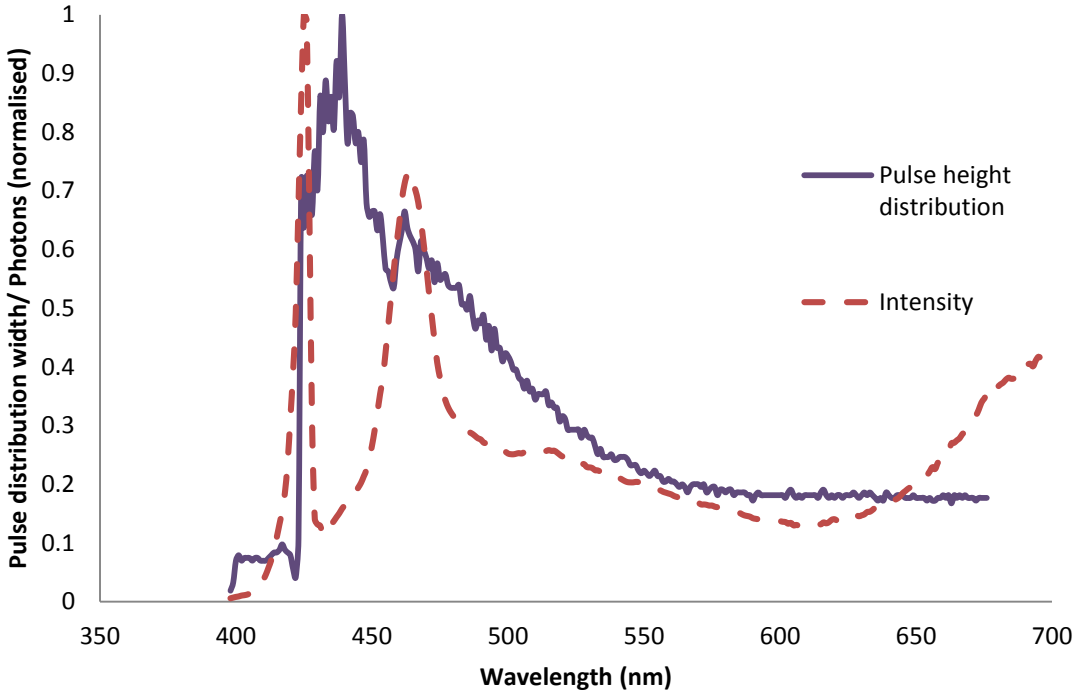

Figure 2.28 Pulse height distribution of the supercontinuum source with wavelength in comparison with the normalised intensity of the supercontinuum source output.

The complex relationship between intensity, pulse position and pulse height distribution illustrate the importance of using a constant fraction discriminator (CFD) on the start input of the TCSPC setup. The start detector and electronics must be sensitive enough to collect a wide variety of pulse energies; otherwise the measured frequency will be unstable at wavelengths with a broad pulse height distribution. The broad distribution could also cause a broadening in the measured IRF without a high quality CFD.

2.2.5 Pulse width

Although the master oscillator within the supercontinuum laser had a short pulse width of around 6 ps, the dispersion effects, together with the broad pulse distribution, act to broaden the measured instrumental response function (IRF). The critical value for the temporal resolution of a fluorescence lifetime measurements is the IRF width measured by the electronics, not the fundamental pulse width of the light (there can be various factors that cause these to diverge).

A start signal is required to measure the pulse width using TCSPC. Measurements of the IRF were compared using both the internal trigger from the laser's master oscillator trigger output and an external photodiode.

The experiment was set up as in Figure 2.13 with the supercontinuum connected to the spectrometer's excitation monochromator. A PIN diode was connected to the side of the excitation monochromator in a mount designed to allow some positional alignment and for the intensity of the radiation hitting the PIN diode to be varied using a variable neutral density filter (Figure 2.29). The PIN diode was triggered by radiation with a wavelength around 50-nm longer than that transmitted through the monochromator. This method was used as it is a practical way to trigger the TCSPC electronics in a commercial spectrometer without disturbing the radiation exciting the sample.

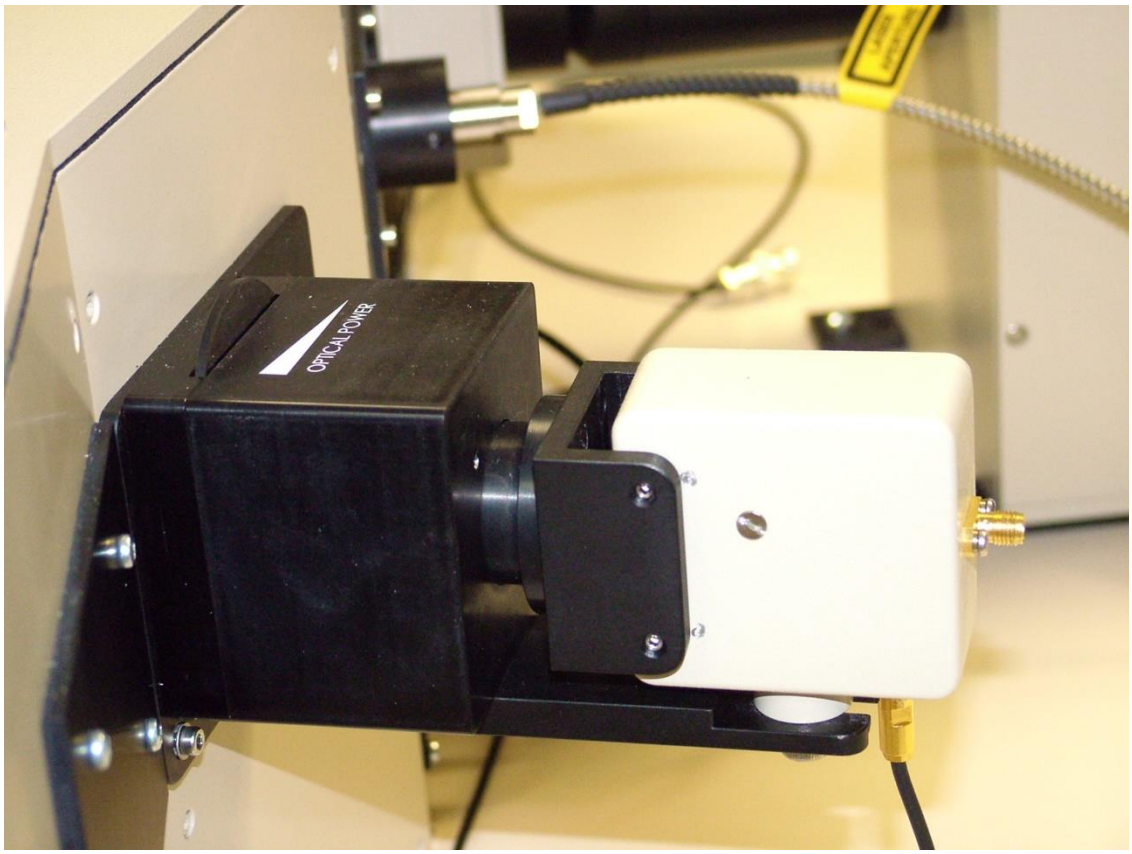

Figure 2.29 PIN diode connected to the side of the excitation monochromator.

The shape and width of the instrument response had some variation with wavelength. Examples of the IRFs measured at three wavelengths are shown in Figure 2.30 (using the leading edge internal trigger) and Figure 2.31 (using the external trigger diode). The IRF width (FWHM) was found to be 160-200 ps over the majority of the visible range using internal triggering and <150 ps measured using external triggering (Figure 2.32). The broad pulses (~350 ps) are the result of a double pulse, this can be seen at 420 nm on Figure 2.30 and Figure 2.31. The two pulses are an indication of separate nonlinear processes overlapping.

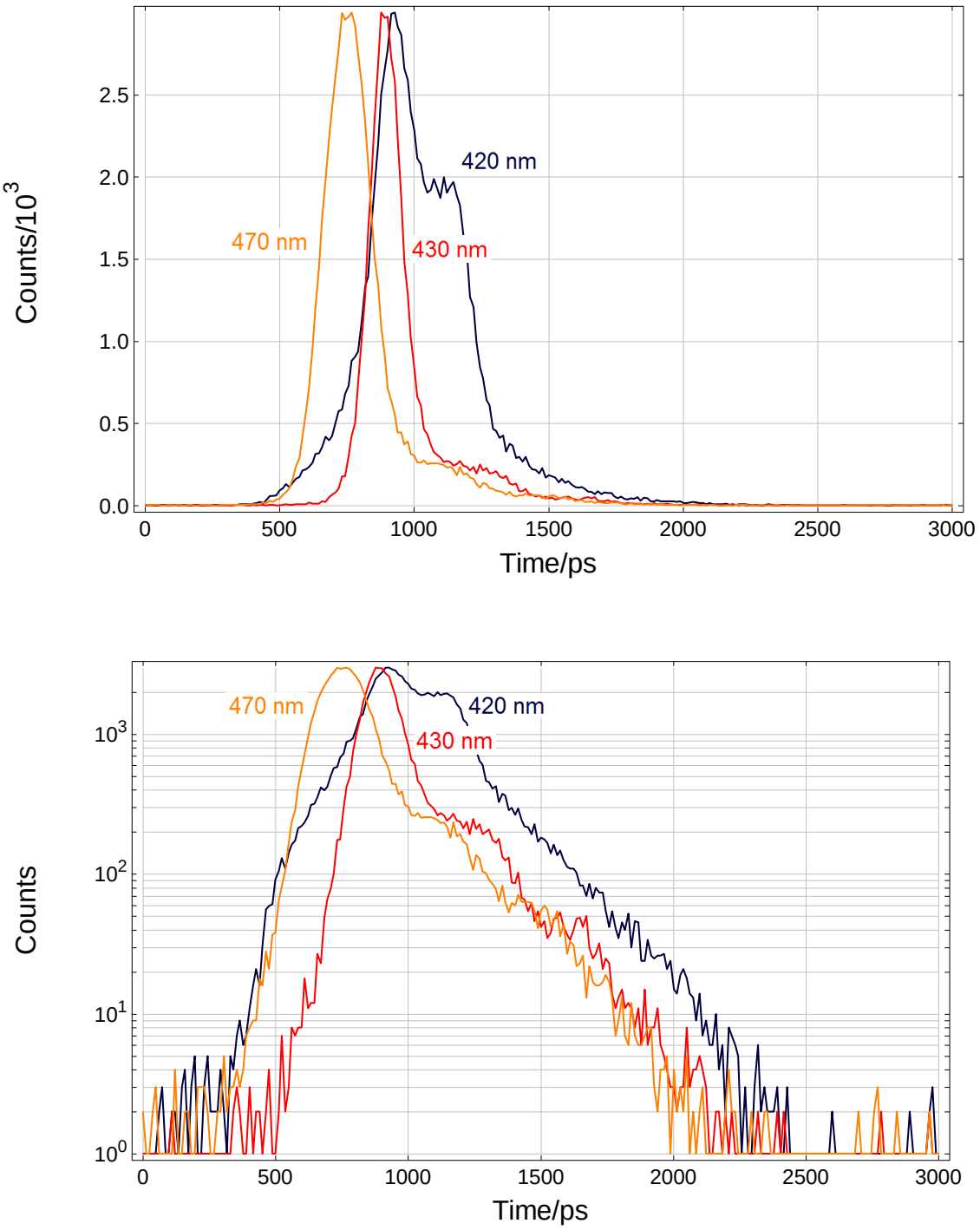

Figure 2.30 IRFs of three wavelengths from the supercontinuum (420, 430 and 470 nm) using internal triggering in linear and semi-log scale.

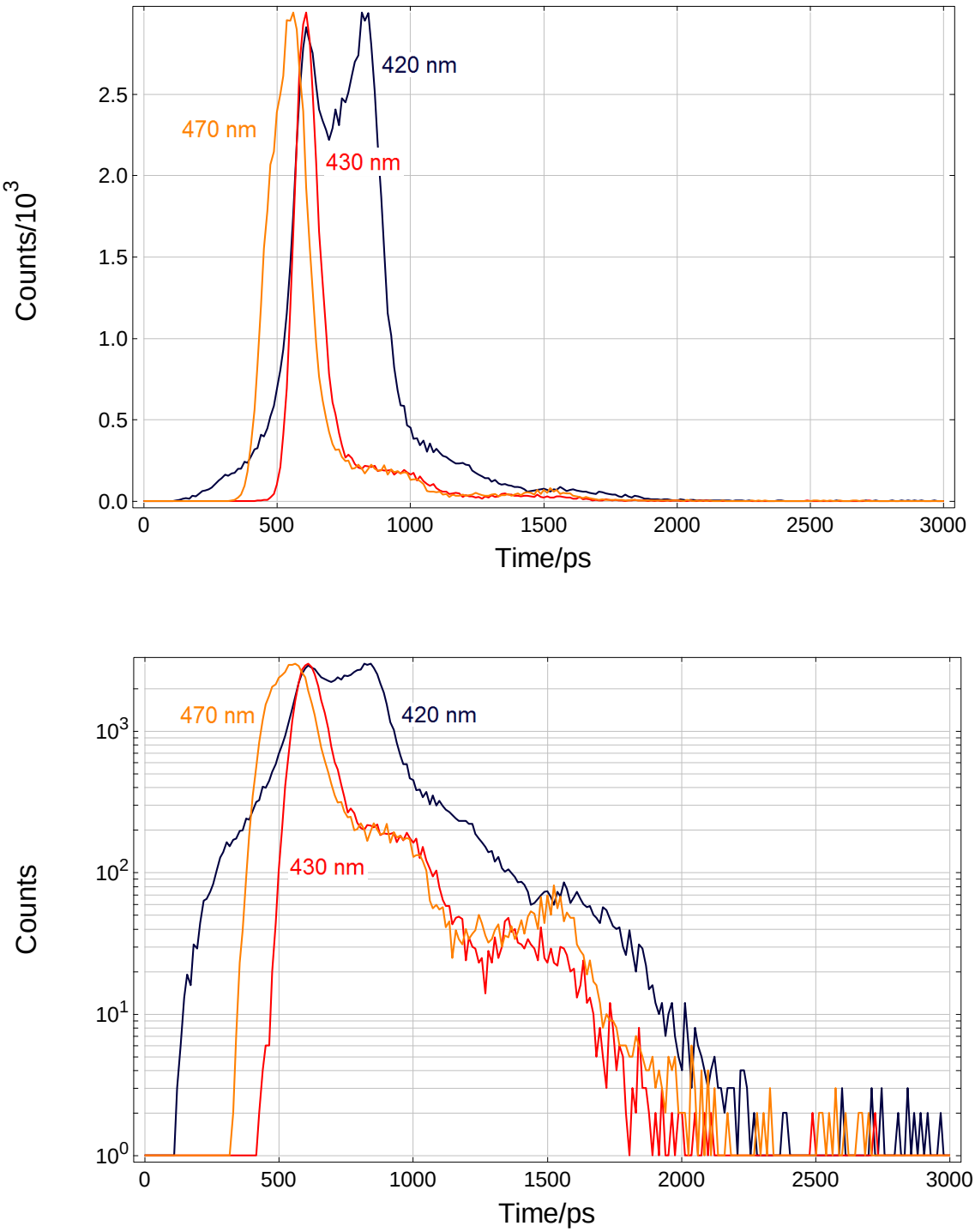

Figure 2.31 IRFs of three wavelengths from the supercontinuum (420, 430 and 470 nm) using external triggering in linear and semi-log scale.

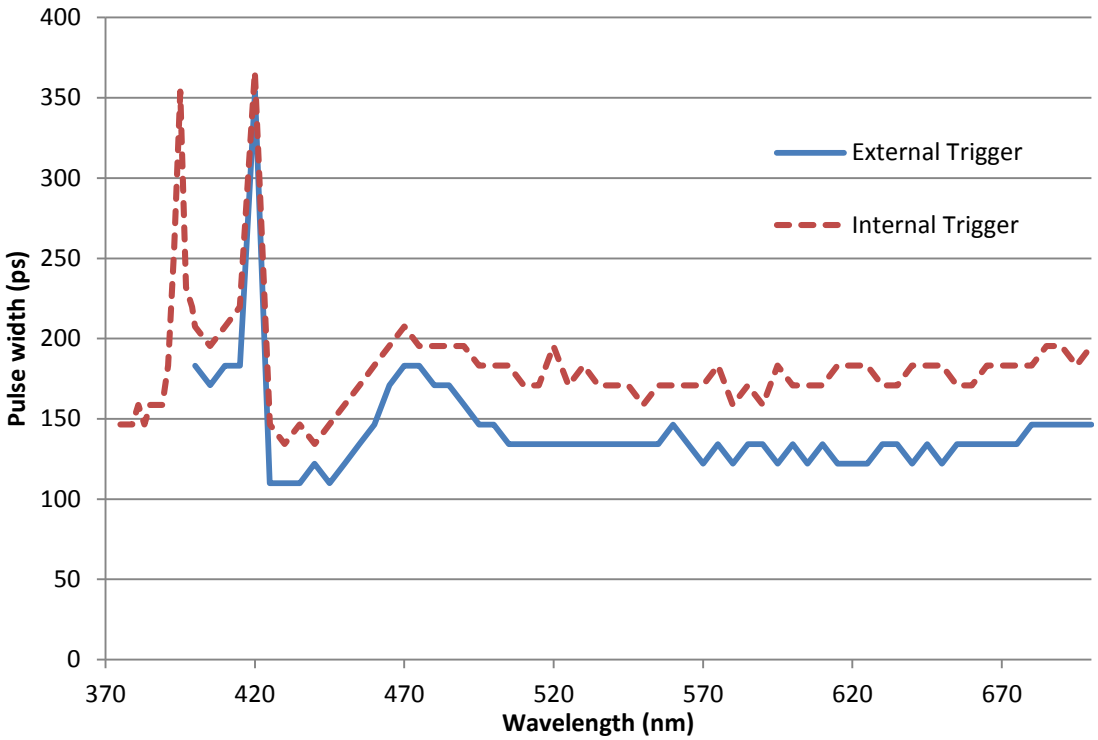

Figure 2.32 IRF pulse width (FWHM) measured with internal and external triggering.

Figure 2.33 compares the pulse height distribution with the measured pulse widths, if the width of the measured IRF was significantly broadened by the jitter of the start signal, an increase in the width of the pulse height distribution should have the effect of broadening the measured pulse width. Figure 2.33 shows no obvious correlation between pulse width and pulse height distribution, except for the sharp transition at ~420 nm.

Figure 2.34 shows a comparison of pulse width compared to intensity and Figure 2.35 shows the pulse width compared to the temporal shift of the pulse. There is some correlation, as the spike in intensity is at the same point in the spectrum as a sharp change in pulse width.

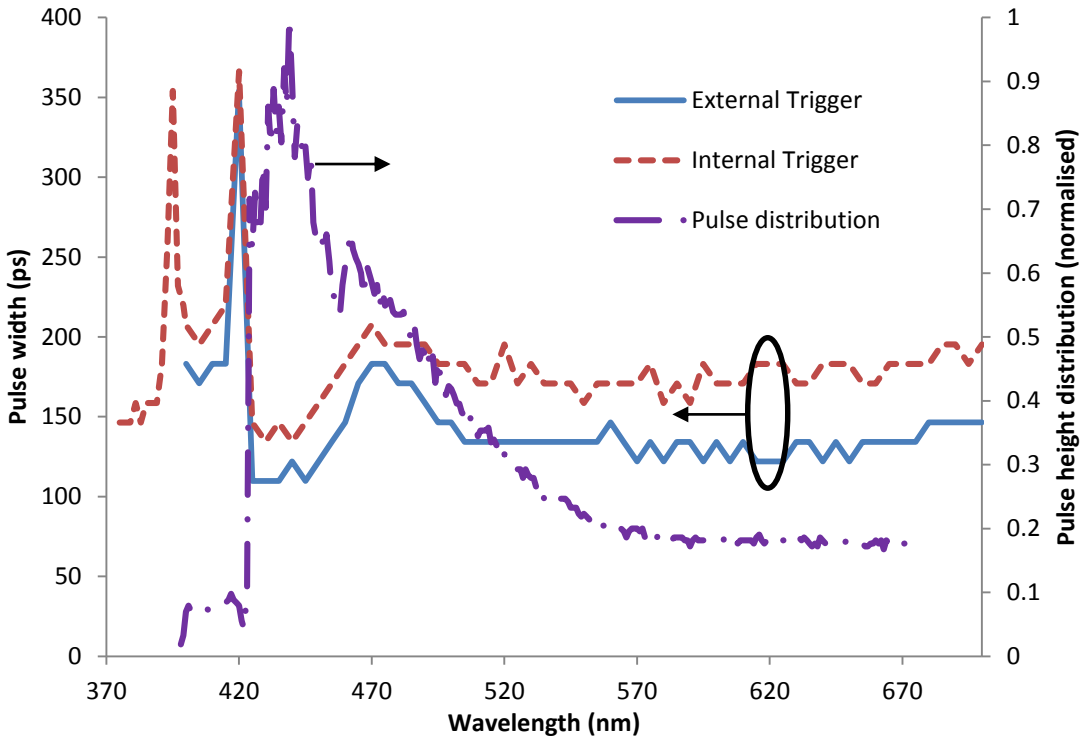

Figure 2.33 IRF pulse widths (FWHM) measured with internal and external triggering and the pulse height distribution of the supercontinuum source with wavelength

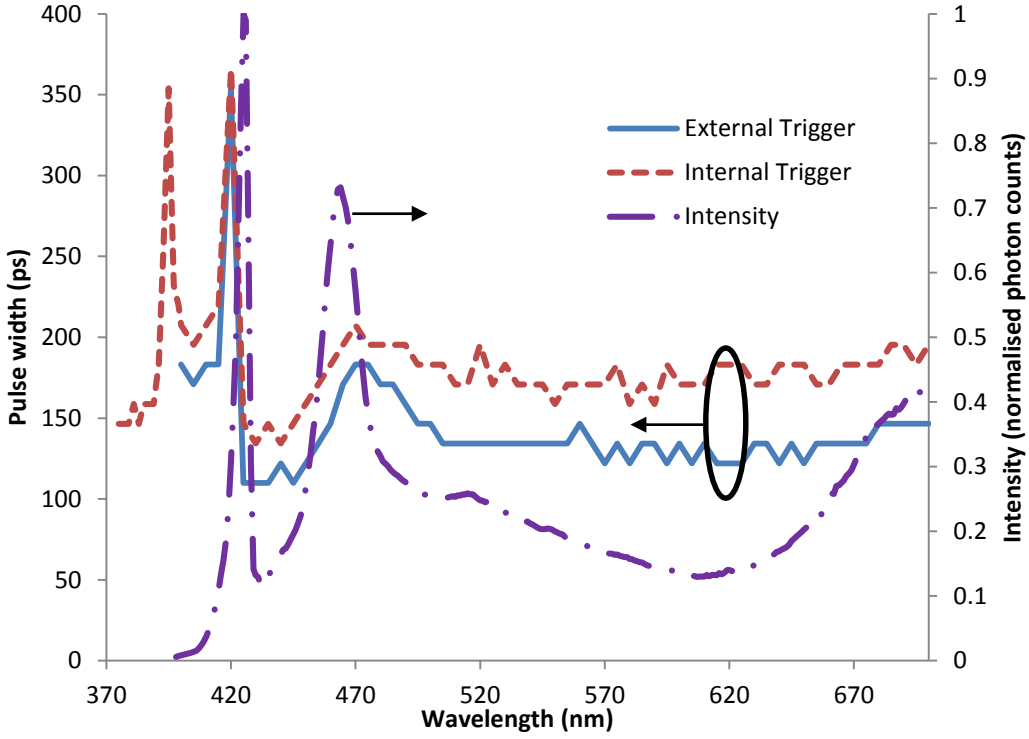

Figure 2.34 IRF pulse widths (FWHM) measured with internal and external triggering and the normalised intensity of the supercontinuum source with wavelength

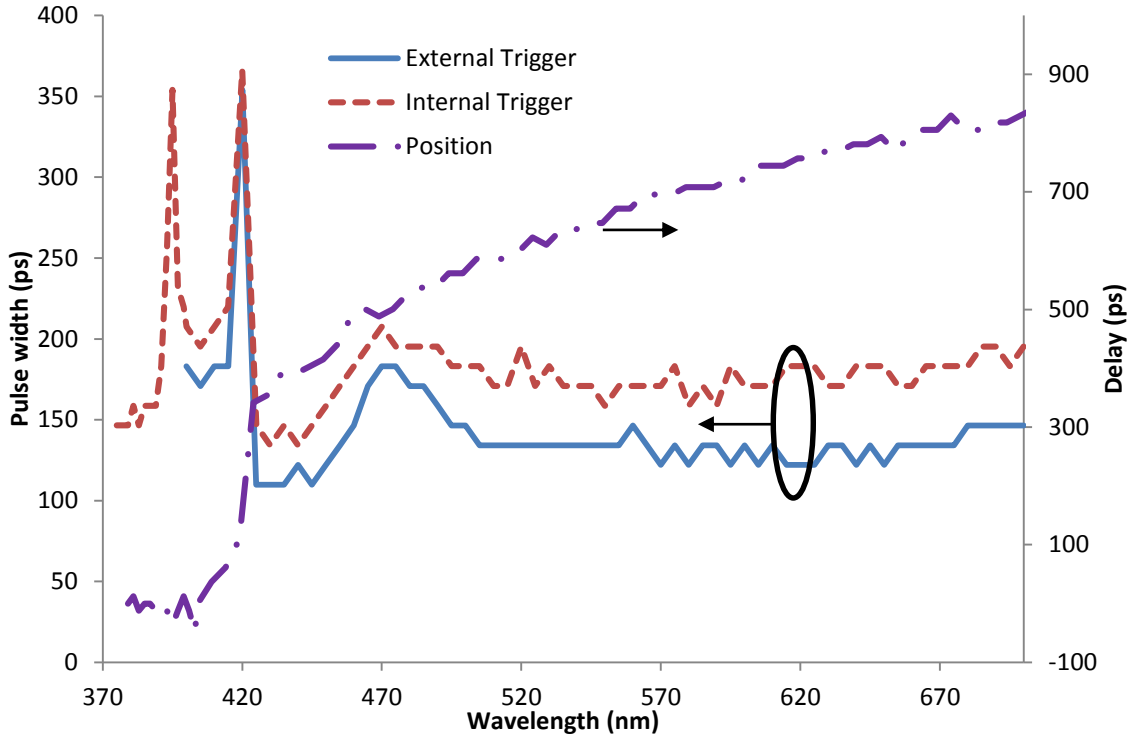

Figure 2.35 IRF pulse widths (FWHM) measured with internal and external triggering and the pulse temporal position

2.2.6 Discussion of supercontinuum generated in high-Δ PCF

A comparison of the various parameters of the supercontinuum radiation including pulse width, temporal shift, pulse height distribution and intensity is shown in Figure 2.36, illustrating the complexity of the underling process. Below 420 nm the pulses all appear to all arrive at around the same time. Because this is a region of normal GVD, it could be expected that the arrival time of the pulses should be delayed according to the dispersion of the fibre (as is observed above 420 nm). However, the pulses undergo no dispersion because of the fibre, indicating that radiation in this region contains non-dispersive wave packets. The cause of this is that the blue radiation is trapped in some manner by a co-propagating soliton on the other side of the zero GVD point [92]–[94]. The mechanism involved is that the blue radiation (i.e. below the pump wavelength) is initially generated by four wave mixing (FWM). This blue radiation is delayed with respect to the soliton initially, however, as it has a fixed frequency it moves with a constant group velocity, whereas the solitons undergo deceleration (as their frequency is shifted to wavelengths with smaller group velocity by intrapulse Raman scattering). This means that the blue radiation catches up with the soliton and overlap. As soon as they overlap a new signal is generated by FWM. The new signal also is delayed with respect to the soliton but catches up. With each scattering the delay reduces until the FWM process becomes quasi-continuous and intrapulse i.e. the FWM occurs within a quasi-

nondispersive wave propagating under the umbrella of a soliton. This continuous matching of soliton and blue pulses continues through the matching of group velocities. Because the mechanisms of blue wing formation are linked to the solitons, signal formation in the blue edge is governed by NIR dispersion as well as local dispersion (at the blue wavelength). In effect the Raman shifted soliton on the red end of the spectrum continuously scatters the blue pulse with identical group velocity almost onto itself. This process then manifests in the quasi-trapping of blue radiation and a further blue frequency shift [92]. There is a high level of pulse-to-pulse intensity stability in this region, however the temporal width of the pulses is broader (closer inspection of the pulse at 420 nm shows that the reason for broadening is that the IRF is made from a superposition of at least 2 pulses (one non-dispersive pulse and others generated by FWM and possibly Cherenkov radiation). Above 420 nm the temporal position of the pulse shifts with the dispersion characteristics of the fibre. The peak-to-peak intensity fluctuation of the pulse increases with reducing wavelength i.e. with increasing distance in energy from the pump source. This is be expected as the modulation instability that creates the supercontinuum is noise driven [95], [96]. The IRF width is reasonably constant in the region measured above 420 nm.

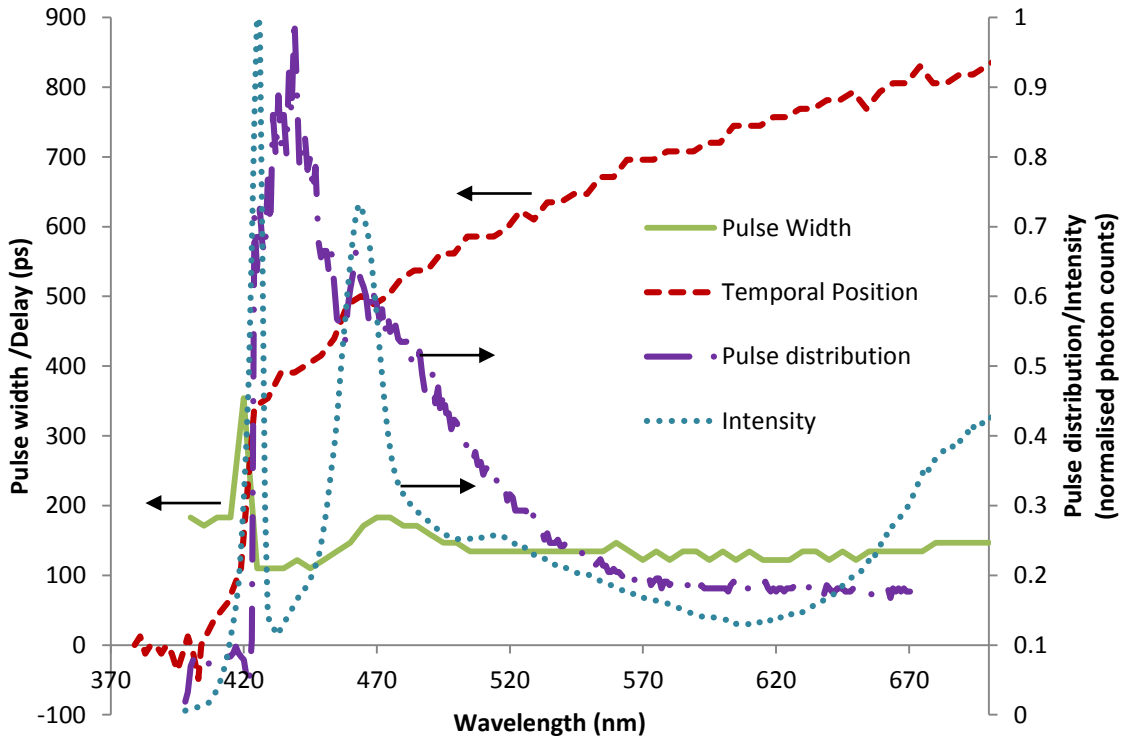

Figure 2.36 IRF pulse width, temporal peak shift, pulse distribution and intensity measured with respect to wavelength.

While TCSPC, as a digital technique, is known to be insensitive towards pulse height fluctuations, light source fluctuations to this extent are likely to cause additional problems. The constant fraction discriminator, which usually overcomes trigger problems from pulse height fluctuations of photomultiplier detectors (section 2.1.5), could cause additional broadening when pulses with extremely different heights and shape have to be processed. The pulse distribution does not have a noticeable effect on the pulse width (Figure 2.36), indicating that the CFD built into the TCSPC electronics card is dealing with the pulse height fluctuation without adding jitter. Triggering the TCSPC electronics on the measured wavelength narrows the pulse width and reduces the temporal beam walk. There are other ways that this problem could be addressed. For example, using a suitable electrical reference from the source to trigger the TCSPC electronics should narrow the pulse. In addition, the temporal position could be corrected by a software algorithm with a lookup table to account for the change in pulse position with wavelength.

2.2.7 Fluorescence lifetime measurements

In order to verify that the supercontinuum source could be used as a light source in a commercial fluorescence spectrometer I applied the system to measure the lifetimes of some common fluorophores (that are used as common benchmarks)

UV excitation

Anthracene is a solid polycyclic aromatic hydrocarbon which only absorbs light below 400 nm [5]. This means the extreme blue end of the supercontinuum spectrum has to be used for excitation. The excitation and emission spectra reveal excitation and emission peaks caused by the distinct vibrational energy levels in the molecule Figure 2.37. The supercontinuum was used in the setup shown in Figure 2.13, with excitation set to one of the excitation peaks (375 nm) and emission measured at 399 nm. The fluorescence decay and IRF were measured. To measure the IRF the sample was replaced with a solution of colloidal silica and the emission monochromator was set to the same wavelength as the excitation monochromator (375 nm). The decay was analysed using the software built into the spectrometer and found to be 4.1 ns with a goodness of fit parameter (chi-squared) of close to unity and evenly distributed residuals (Figure 2.38). Both fitting parameters indicate a good match of data and lifetime value. Reasons for poor fitting can be sample dependent (impurities) but also instrumental (radio frequency interference from the source, poor instrument setup). The decay value is as expected; degassed anthrascene in

cyclohexane has a decay of 5.2 ns [5], however, dynamic quenching reduces this value in the presence of oxygen.

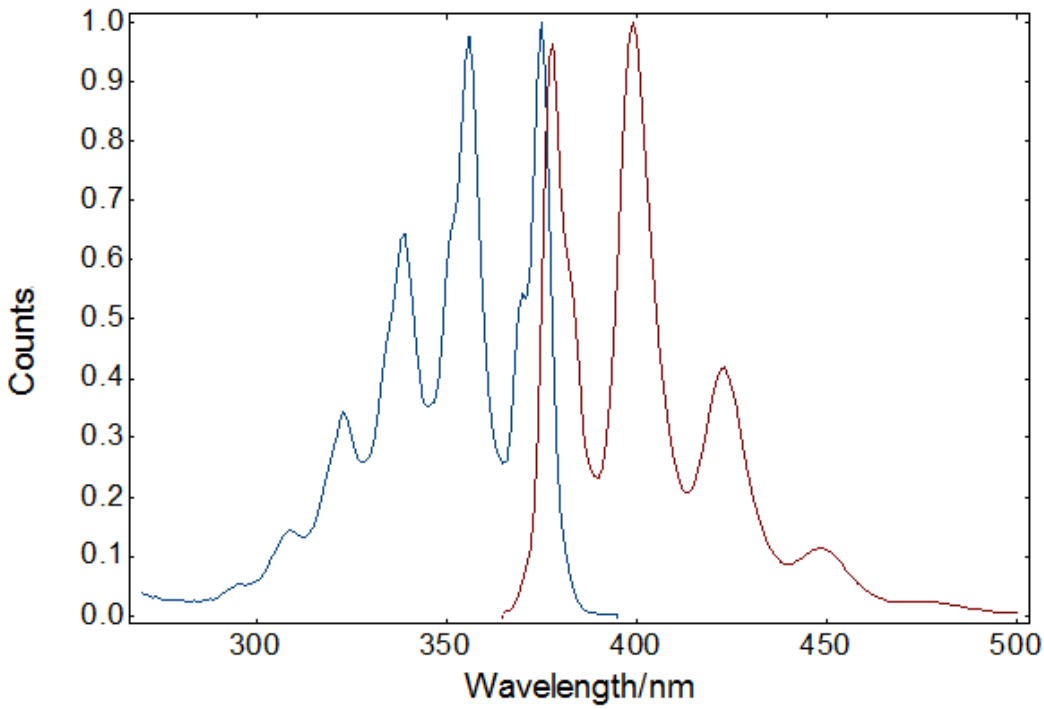

Figure 2.37 Anthracene in cyclohexane excitation and emission spectra. Measured using the setup in Figure 2.13 with a xenon lamp in place of the supercontinuum.

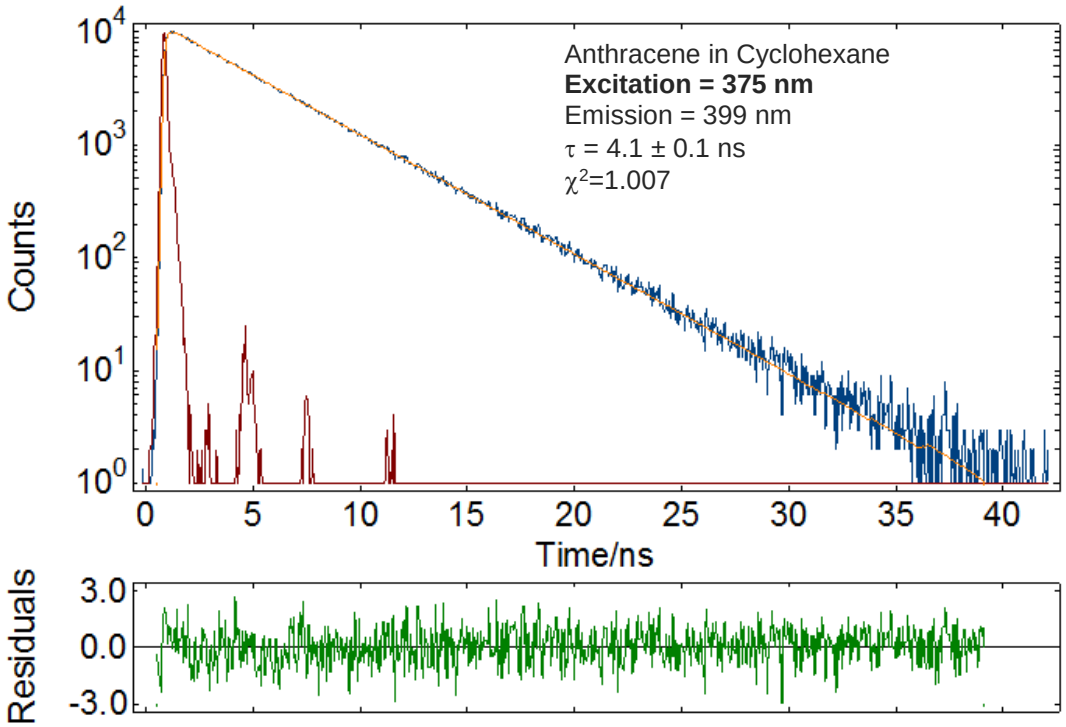

Figure 2.38 Anthracene in cyclohexane fluorescence decay

Time resolved excitation spectrum

One distinct advantage the supercontinuum source has over typical excitation sources for fluorescence lifetime is the tunability of the excitation wavelength throughout the visible range. As well as the ability to match the excitation wavelength exactly to the absorption maximum of the sample, this also allows the measurement of time resolved excitation spectra. The TCSPC electronics were triggered by with an external photodiode monitoring wavelengths a fixed offset from the excitation wavelength for simplicity of optical design (as described in section 2.2.5). A sample of the synthetic organic compound fluorescein was excited between 430 – 515 nm in 5 nm steps with the decay acquired at each wavelength for 20 seconds. The decays were then sliced with the average intensity measured every 5 ns. The resultant curves were then divided by the spectrum of the supercontinuum, measured by the reference detector so that the excitation spectra was independent of the instrument (Figure 2.39). The data were also globally analysed with advanced analysis software (FAST, Edinburgh Instruments) along with the IRF for each wavelength (Figure 2.40).

Time resolved excitation data are able to be displayed in this way by triggering on a fixed wavelength offset from the excitation wavelength. Triggering on the pump wavelength would mean the position of each decay would depend on the dispersion characteristics of the fibre. This would mean gated spectra would be skewed by instrumental error.

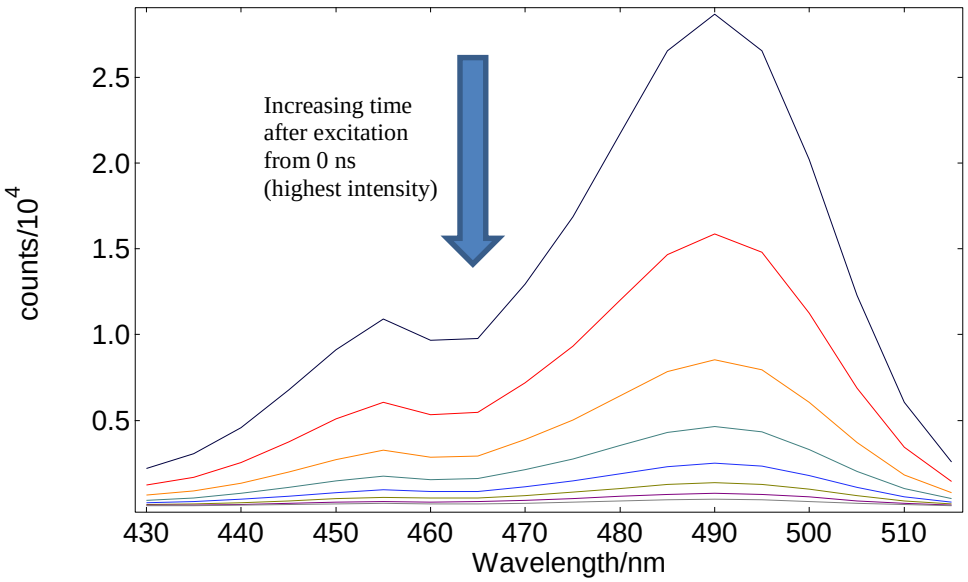

Figure 2.39 Fluorescein fluorescence excitation spectra in 2.5 ns steps after excitation (gate width=2.5 ns)

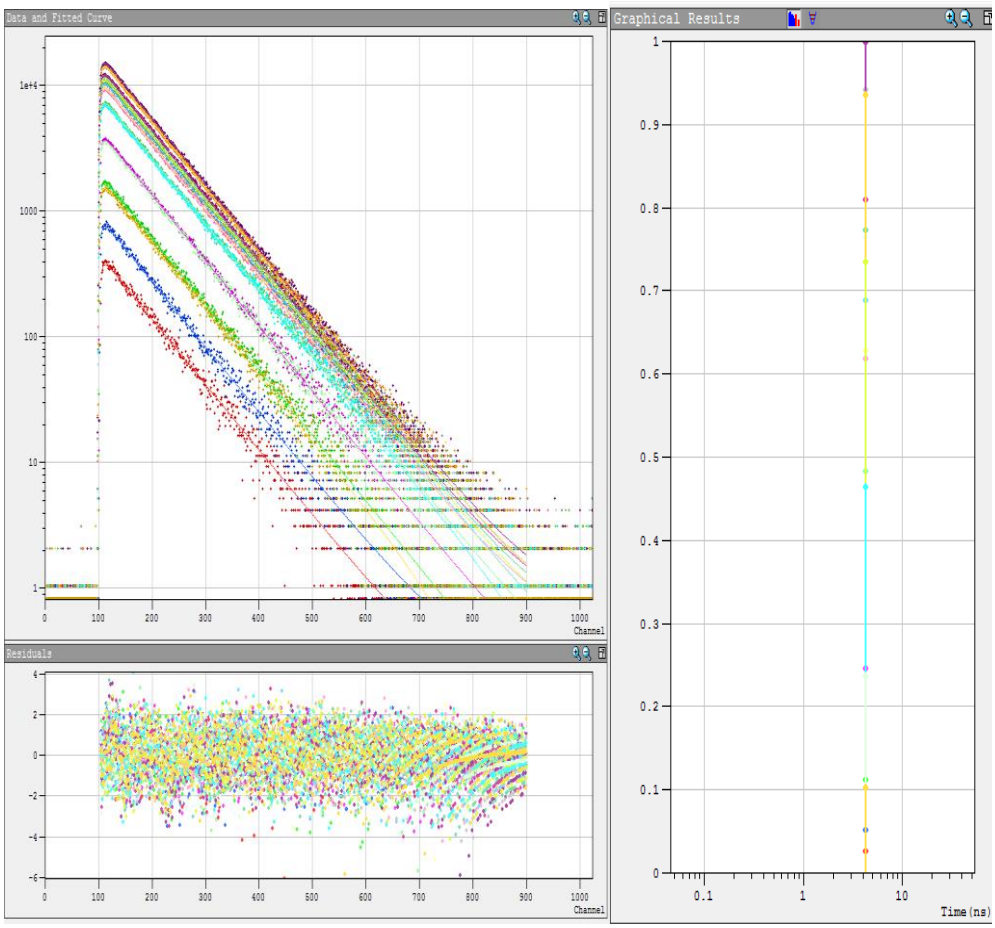

Figure 2.40 Globally analysed set of fluorescein fluorescence decays with varying excitation wavelength (430-515 nm), emission=520 nm. Top left: the fitted decays, bottom left: the residuals showing how well the fit corresponds to the data, right: lifetime and the intensity for each wavelength τ=4.071 ns, Global χ^2=1.072

2.3 Evaluation of a deep UV supercontinuum prototype

The source evaluated in Section 2.2 would serve as an effective source for a commercial fluorescence lifetime spectrometer, radiation further into the UV would be desirable as it would increase the flexibility of the instrument i.e. by allowing the direct excitation of proteins. As part of the Technology Strategy Board funded project, Whitelase, high UV-content supercontinuum sources with spectral content below 350 nm were designed and tested. The first step was testing various types of tapered fibre for their UV output. Following this, a prototype UV supercontinuum prototype was characterised containing a tapered fibre.

2.3.1 Tapered PCF

Reducing the core diameter of a high-Δ PCF (such as that characterised in Section 2.2) can have the effect of further steepening the change in group index with wavelength at

the red side of the zero dispersion wavelength. Unfortunately, small core diameters make it more difficult to couple the pump radiation into the fibre and increases the chance of damaging the input of the PCF (due to the tighter focus required). In addition, reducing the core diameter too far can shift the zero dispersion wavelength of the fibre away from the pump wavelength to such an extent that the soliton trapping will not take place and thus wavelengths below the pump laser will not be generated [97], [98] as illustrated in Figure 2.41, which shows the difference in the group index when the core of a high-Δ fibre is reduced from 6 μm to 2 μm.

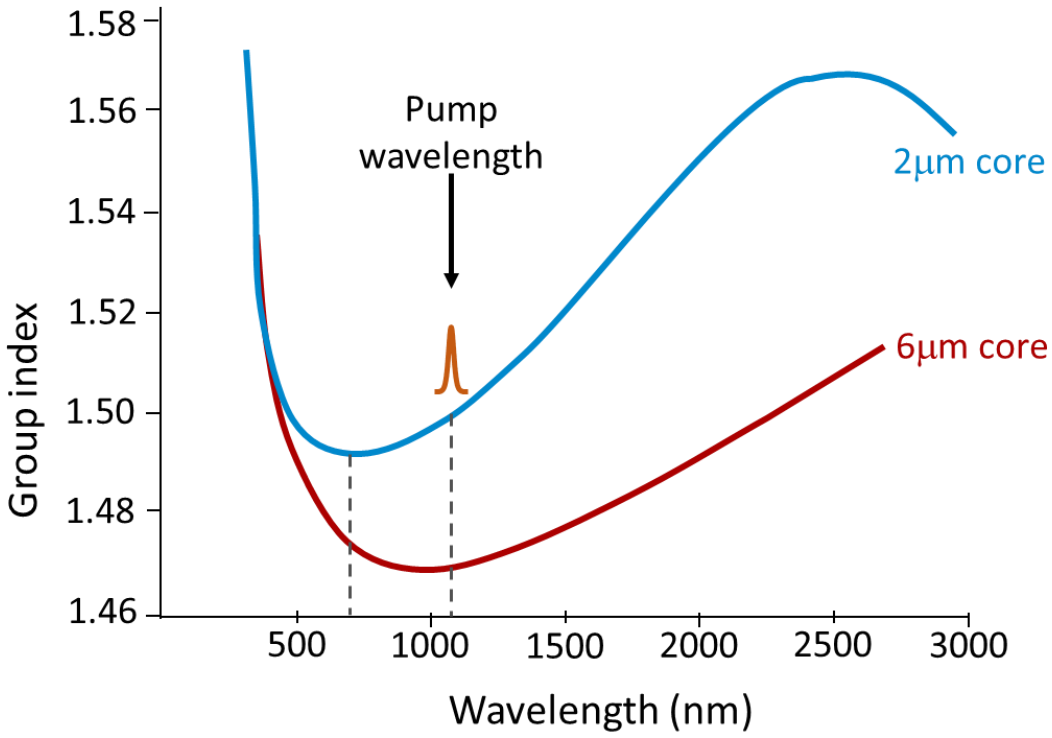

Figure 2.41 Effect of core diameter on the group index

In order to take advantage of the steeper group index slope and corresponding blue shift of the index matching wavelength of the narrower fibre core diameter, a tapered PCF fibre can be used. To taper the fibre the speed at which the fibre is drawn from the preform through the furnace is varied resulting in a gentle taper from ~6 μm to 2 μm over a length of a few meters. Thus, with a tapered fibre, the pump light enters the PCF with a larger core whereby the modulation instability, self-frequency shifting and group velocity matching takes place as with the fibre used in Section 2.2. As the fibre tapers to smaller diameters, the group index of the photons at the red extreme of the supercontinuum increases. The wavelength of the blue edge photons with the same group index thus becomes correspondingly lower. Figure 2.42 shows illustratively how the group index should change as the fibre is tapered.

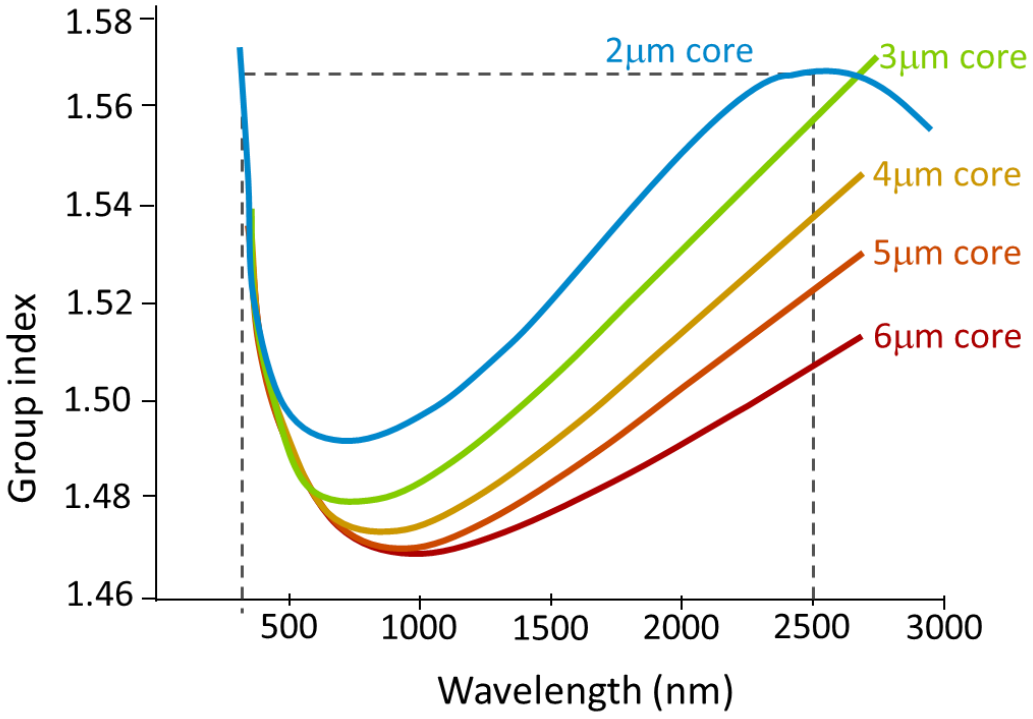

Figure 2.42 Change in group index down a length of fibre with a tapered core from 6 µm to 2 µm

2.3.2 UV-visible spectral characteristics of tapered PCF supercontinuum

In order to test the extent of UV performance possible, a test run of tapered PCF fibres was made at the University of Bath, tapering between 6 µm and 2 µm with a progression of group index similar to the illustration in Figure 2.42. Light from a picosecond fibre pump laser (6 ps pulse width, 1064 nm wavelength, 1 MHz frequency) was coupled into the PCF in order to generate the supercontinuum.

The tapered fibre was coupled into the sample chamber of the experimental setup shown in Figure 2.13. The UV-visible spectrum was then measured (Figure 2.43). On a linear scale the spectrum appears to have sharp peaks that have an appearance of random noise, however, they were stable with time (Figure 2.43). The supercontinuum was found to extend as low as 317 nm.

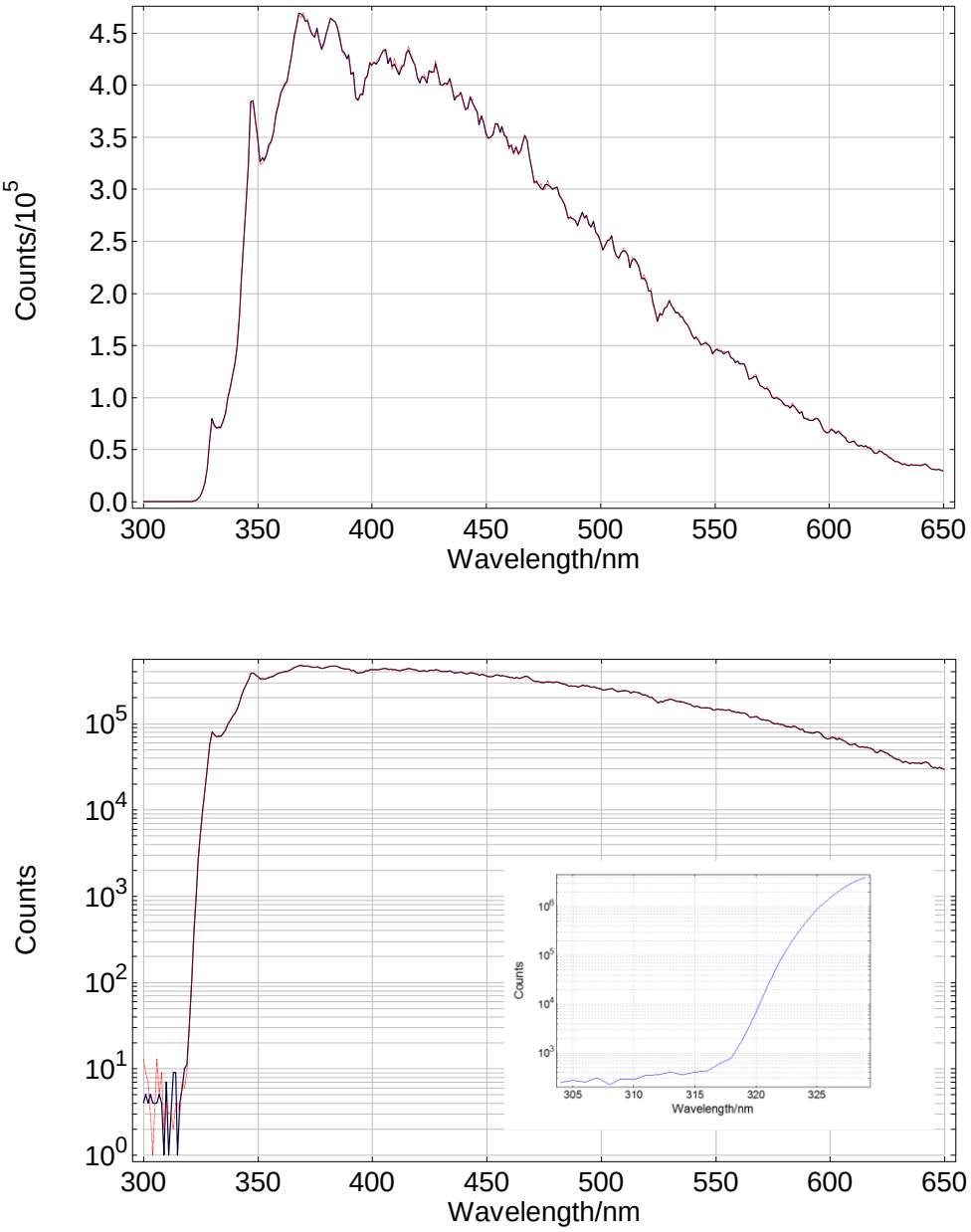

Figure 2.43. UV-vis emission spectrum of supercontinuum with tapered fibre PCF. Two scans measured one hour apart on a linear and semi-logarithmic scale with an insert showing the extreme UV edge in more detail.

2.3.3 Pulse position and IRF of tapered PCF supercontinuum

The setup in Figure 2.13 was used to measure the wavelength dependent temporal position of the pulses from the supercontinuum. The PCF was connected directly to the sample chamber (with a lens to image it onto the diffuse reflector) and the MCP-PMT used for detection. The trigger output of the pump source was used as a start signal for the TCSPC electronics. The instrument response function of the system (including the source) was then acquired in steps from 320 – 700 nm. An intensity map of the measured instrument responses is shown in Figure 2.44. The region from 320-420 nm is shown in more detail in Figure 2.45. Figure 2.44 and Figure 2.45 show that the temporal position

of the pulse alters with wavelength through the visible and UV with a trend similar to a fibre dispersion curve. The pulses following this trend are generated by four wave mixing. In the region from 320 – 370 nm there is also a non-dispersive pulse (similar to that discussed in Section 2.2.6) which extends for over 40 nm and overlaps significantly (~20 nm) with the dispersive curve. This is in contrast to the results from the high-Δ PCF where the non-dispersion region extends for ~20 nm and overlaps for <5 nm (Figure 2.46).

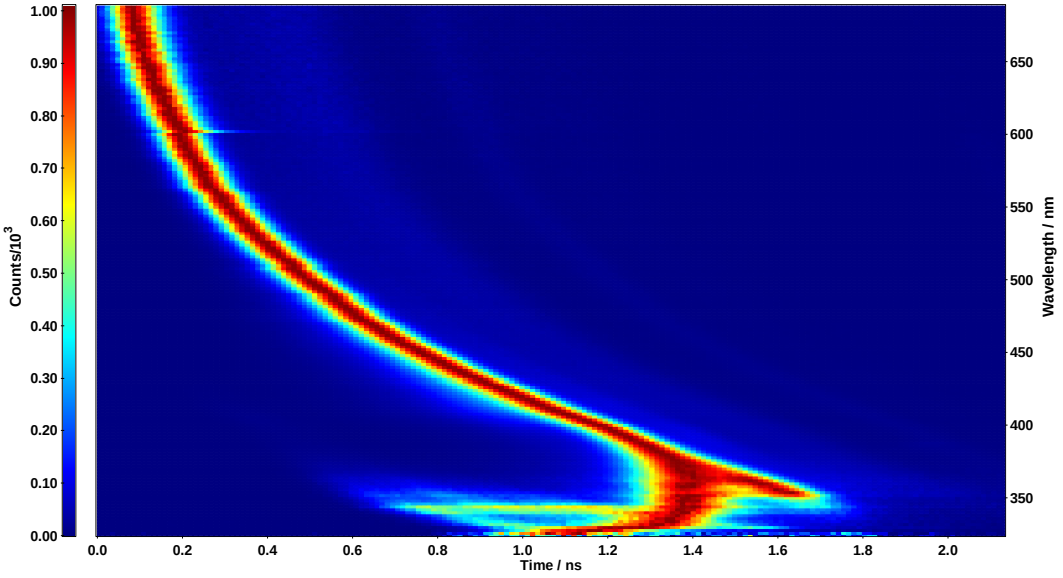

Figure 2.44 Intensity map of normalised instrument response measurements of tapered PCF supercontinuum. Parameters: 320 – 690 nm; 2 nm step; 10 s acquisition time/step

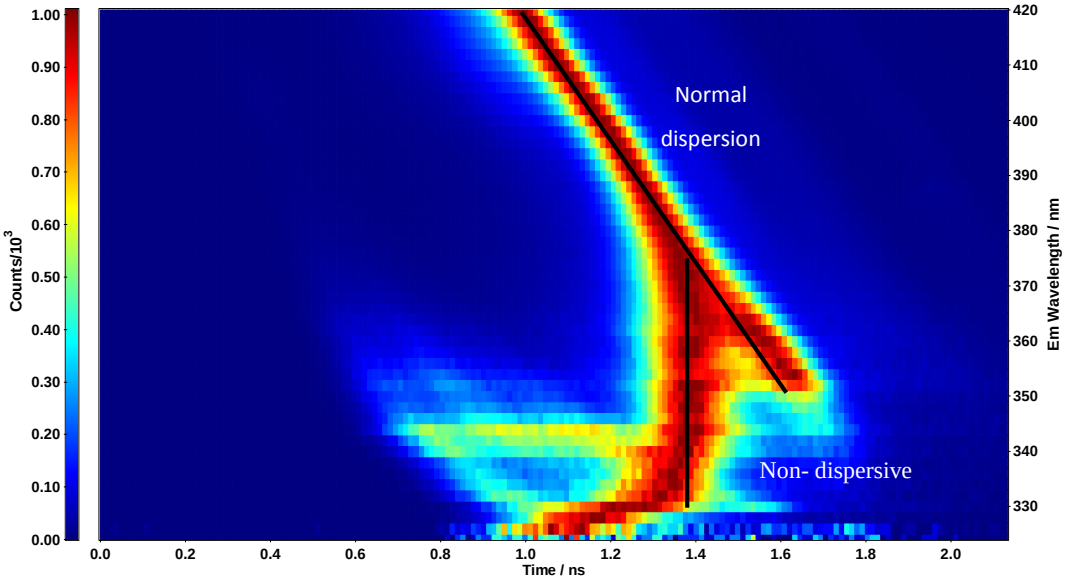

Figure 2.45 Intensity map of normalised instrument response measurements of tapered PCF supercontinuum. 320 – 420 nm 2 nm step 10 s acquisition time/step

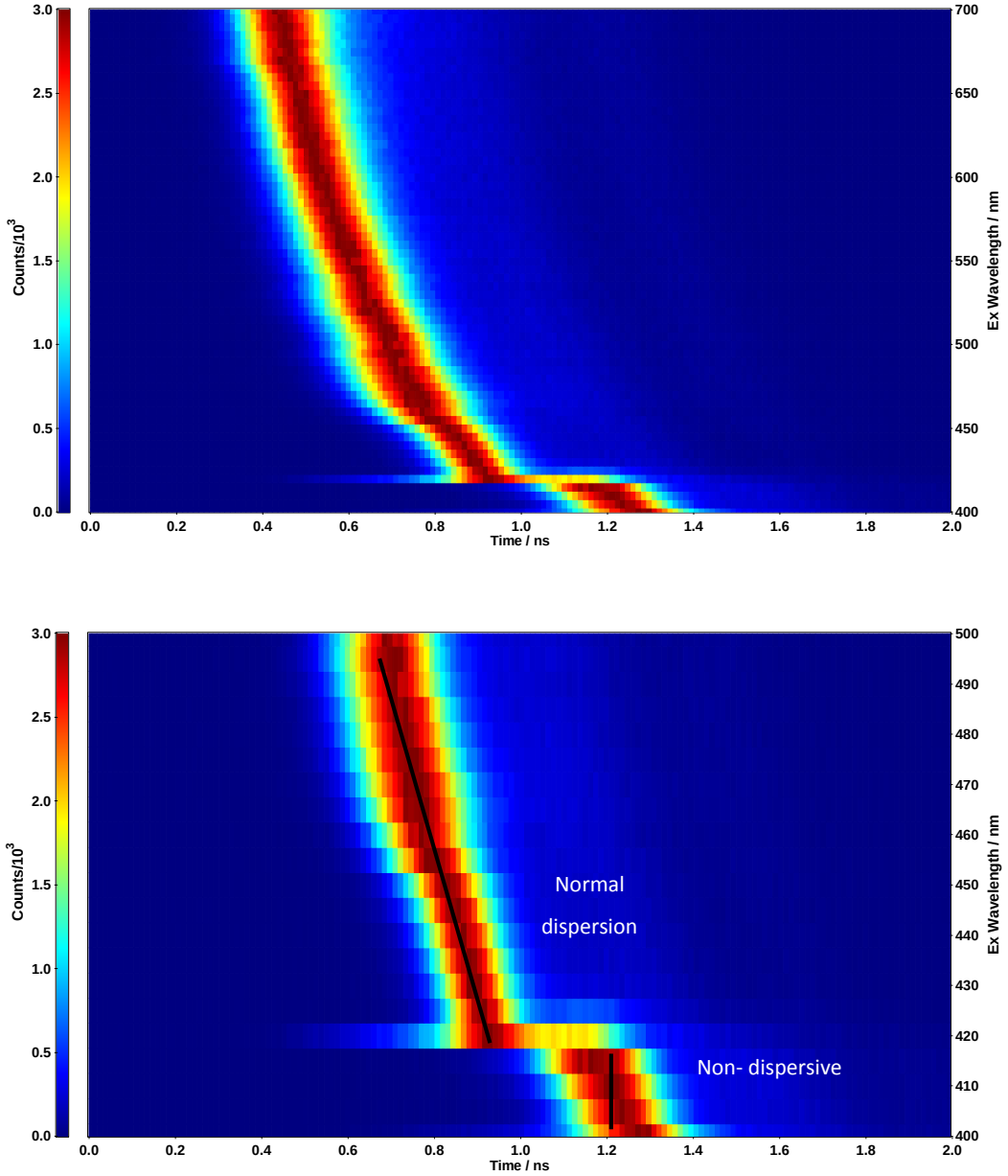

Figure 2.46 Intensity map of normalised instrument response measurements of high-Δ PCF supercontinuum. 400 – 700 nm (right) and 400-500 nm (left) 2 nm step 10 s acquisition time/step

The non-dispersive region is indicative of soliton trapping described in Section 2.2.6. Solitons need to have sufficient spectral bandwidth for Raman self-scattering to occur [48], therefore the soliton trapping process is limited to very short solitons in non-tapered optical fibres. In tapered fibres the fibre parameters at the beginning can be designed to maximise the Raman self-scattering e.g. by having the zero dispersion wavelength close to the pump wavelength. As the fibre tapers and the group index shifts to the blue the group index at the extreme blue region of the spectra begins to correspond with a region in the red with a small variation in group index (and therefore minimal dispersion), as

illustrated in Figure 2.42 with a 2 μm core. The group index variation at the end of the taper mean a much wider range of pulses can create the trapped solitons [99]. The results shown in Figure 2.44, Figure 2.45 and Figure 2.46 are in agreement with the theory [99] as the non-dispersive region is much larger (and therefore the soliton trapping effect) is greater in the tapered PCF compared with the non-tapered, high-Δ PCF.

2.3.4 Instrument response width

The pulse width of the instrumental response recorded with the tapered fibre supercontinuum was measured (Figure 2.47). It can be seen that the pulse width is reasonably stable (at around 100 ps) above 392 nm. However, at lower wavelengths the superposition of the dispersive and non-dispersive light pulses cause a sharp increase in pulse width. This effect will limit the shortest measurable lifetime in this region.

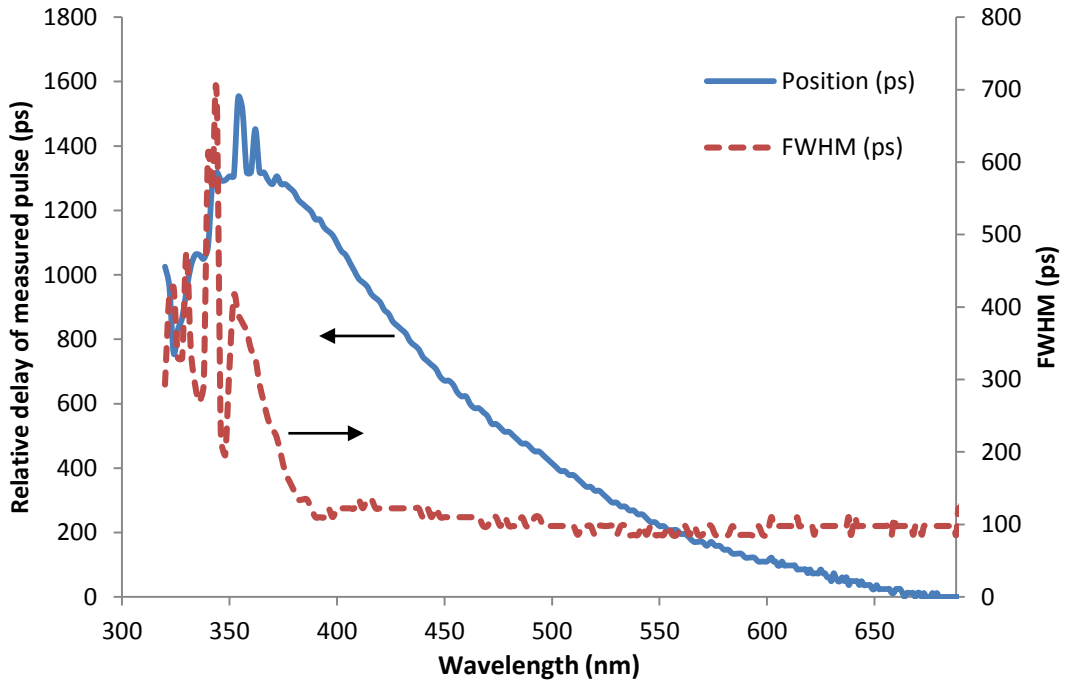

Figure 2.47 Pulse width and temporal position of tapered fibre supercontinuum.

2.3.5 Average Power

As discussed in Section 1.2, current commercial sources for TCSPC lifetime measurements in the UV are mainly limited to nanosecond flashlamps, sub-nanosecond pulsed LEDs and gain switched diode lasers. In order to compare the available optical power for commercial UV LEDs and diode lasers with the tapered fibre PCF supercontinuum a power meter head (Thorlabs) was placed at the sample position of the

spectrometer shown in Figure 2.13. To measure the lasers and LEDs, they were attached to the side of the sample chamber and focused directly onto the head (in the same manner as they would be focused onto a sample for fluorescence excitation). The supercontinuum was attached to the single monochromator input of the excitation monochromator (focal length 300 mm, F/4.2) with a bandpass set to 14 nm (similar to the bandwidth of the LEDs, although the diode lasers have a bandwidth of ~1.5 nm). All sources were run at 10 MHz repetition rate. The results are shown in Figure 2.48.

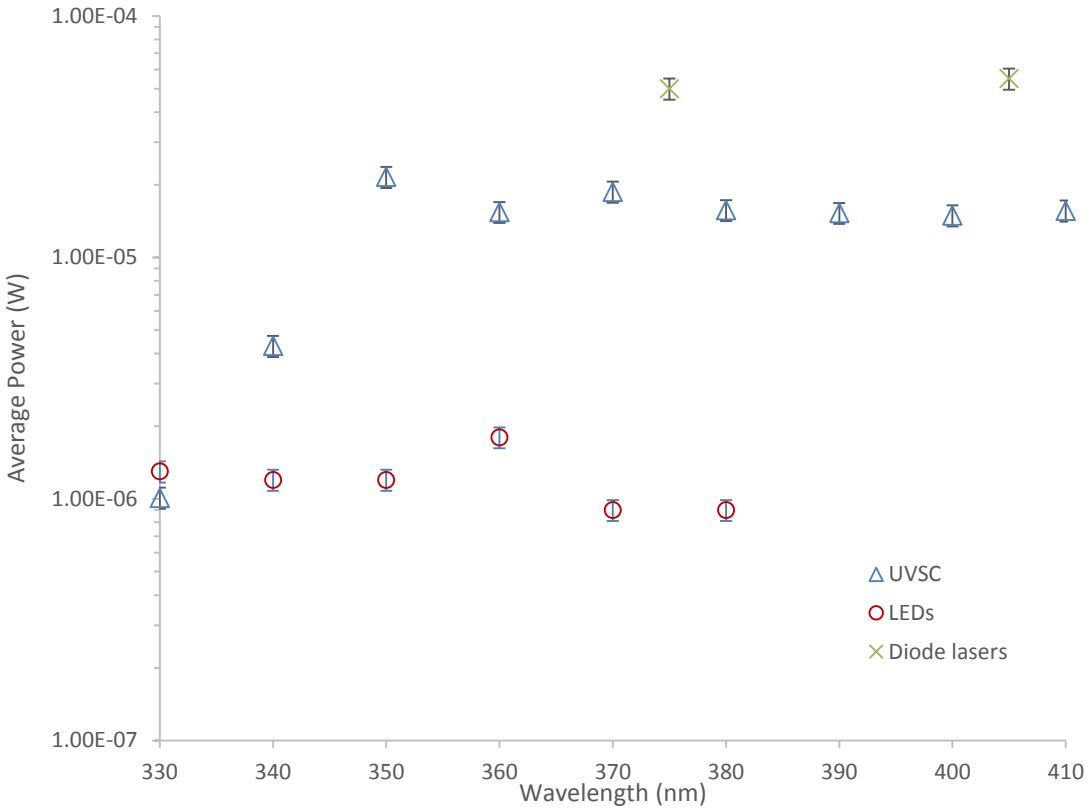

Figure 2.48 Average power of tapered fibre supercontinuum through a single monochromator with 14 nm bandwidth at 10 MHz repetition rate and commercial sub nanosecond pulsed LEDs. 10 MHz repetition rate, 14 nm bandwidth slits.

The results show that the optical power available for sample excitation from the supercontinuum source through a monochromator is significantly more than for the LEDs above 330 nm, but less than the diode lasers (although gain switched diode lasers are not available below 375 nm). As discussed in Section 1.2.6, the LED sources measured in Figure 2.48 are currently used in fluorescence lifetime spectrometers employing TCSPC. The light output from the LEDs is perfectly sufficient for the majority of TCSPC experiments. As the tapered fibre has a higher output, the use of a source like this could reduce measurement times of the weaker samples.

2.3.6 Suitability of a tapered PCF based supercontinuum source for fluorescence lifetime measurements.

The spectral coverage, power, and temporal characteristics show that, although a supercontinuum output based on a tapered fibre source does not give sufficient optical power for use as a quasi-steady state excitation source, it would be a worthwhile source for fluorescence lifetime measurements. The power available for sample excitation is greater than current sources and the pulse width is narrower. One small concern would be measurements below 390 nm, where the instrument response function varies considerably because of the overlapping nonlinear processes. This will limit the minimum lifetime measurable at any particular wavelength (the minimum measurable lifetime being in the region of $^{1}/_{10}^{th}$ of the IRF), particular care will also have to be taken when measuring the IRF of fast samples in this region in order to achieve good fitting and an accurate lifetime (mismatch between a measured IRF and the IRF convolved on the sample emission is a common cause of poor data fitting and errors when extracting lifetime data through reconvolution analysis).

2.4 Measurement of other commercial supercontinuum sources

For further comparison other commercial supercontinuum sources were also coupled into a fluorescence spectrometer and evaluated as potential light sources in fluorescence spectroscopy.

2.4.1 NKT source

A source from NKT (SuperK EXW-12) was coupled directly into the sample chamber of an experimental setup similar to that shown in Figure 2.13. An internal pulse picker was used to fix the frequency at 1 MHz (an appropriate frequency for fluorescence spectroscopy). The visible spectrum of the source was measured (Figure 2.49), the emission was found to extend down to 450 nm with a sharp peak at 475 nm The source is marketed as their “white” version (as opposed to some of their “blue” version which has emission down close to 400 nm).

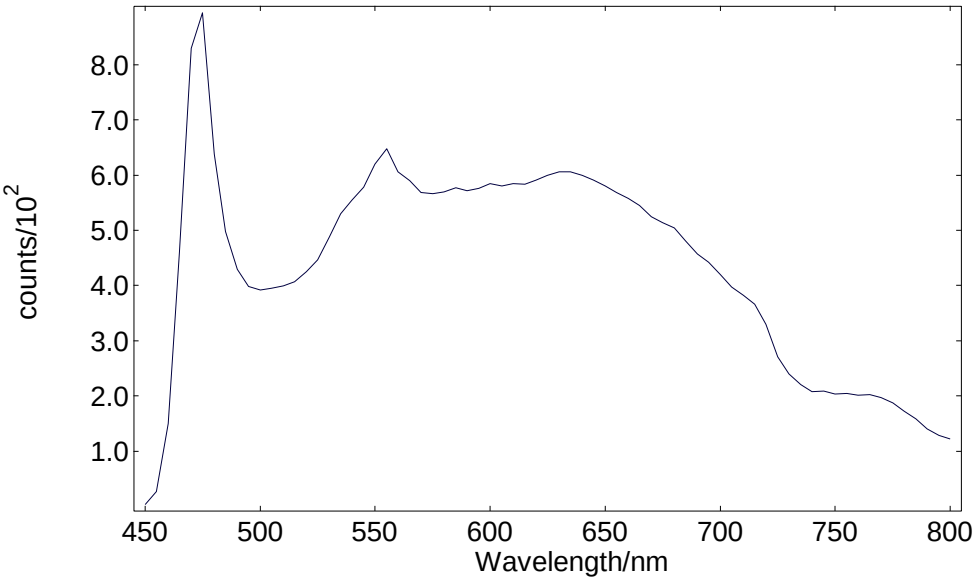

Figure 2.49 Corrected UV visible spectrum of SuperK ExW-12

The experimental setup was arranged as in Section 2.2.3 and 2.2.5, using the internal trigger (although in this case the source had a negative going NIM style trigger output compatible with the TCSPC electronics in use. The intensity map of normalised instrument response functions with wavelength is shown in Figure 2.50, showing the characteristic fibre dispersion curve. The temporal shift and pulse width were also calculated and displayed in Figure 2.51

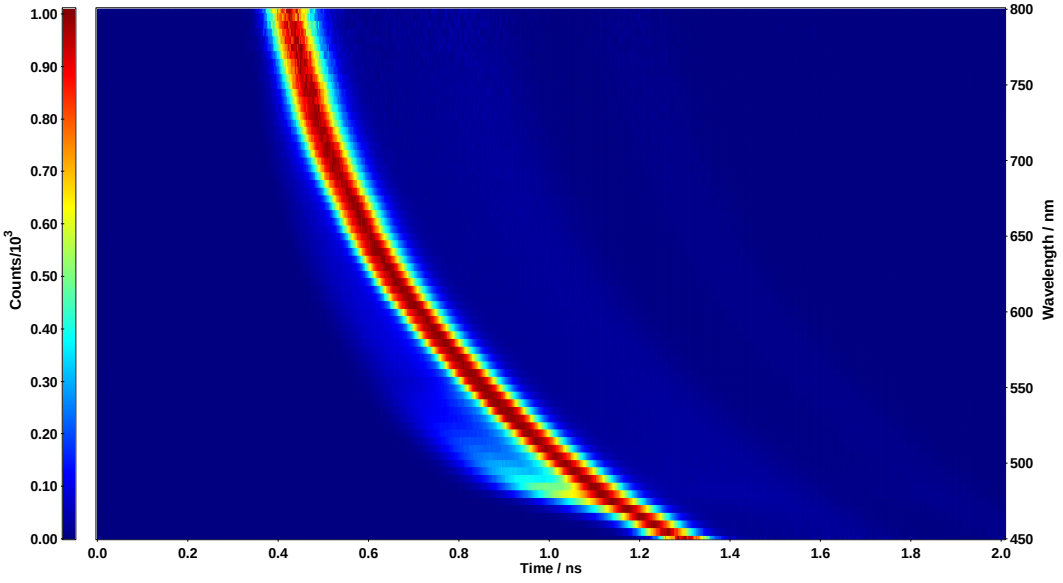

Figure 2.50 Intensity map of normalised instrument response measurements of SC-1-HE supercontinuum. 350 – 800 nm 5 nm step 60 s acquisition time/step

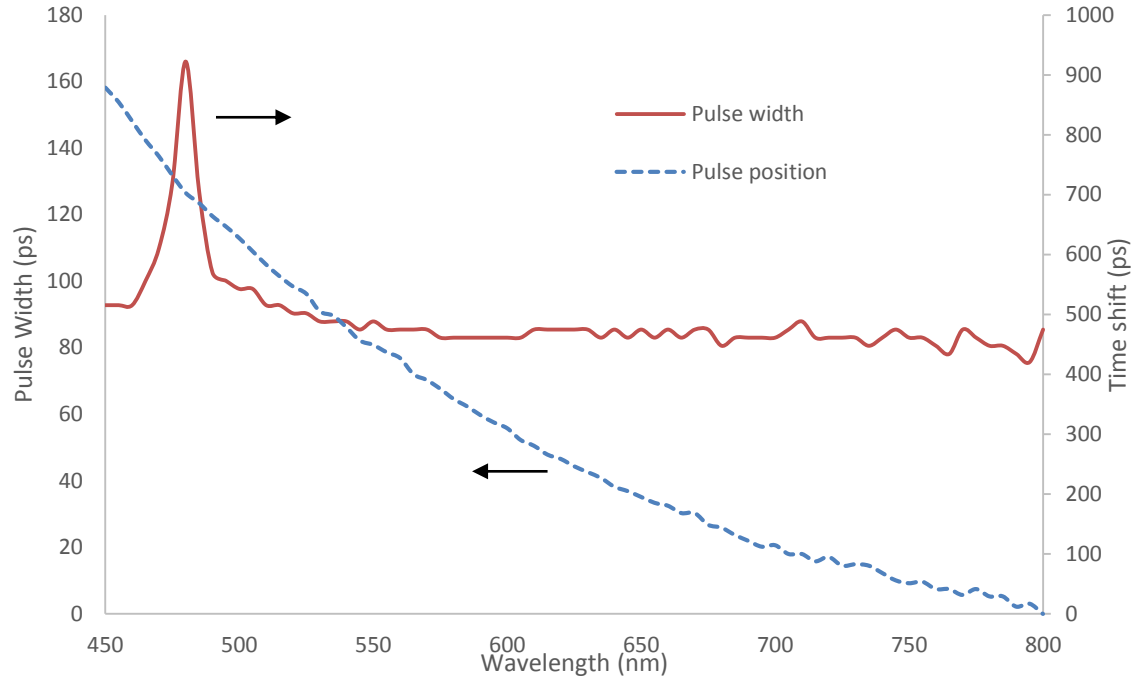

Figure 2.51 IRF pulse widths (FWHM) and pulse temporal shift of SuperK ExW-12.

The measurements show a steady shift in pulse position of 850 ps and a reasonably stable pulse width of <100 ps in the spectral range 450-800 nm. One exception is the range 465-495 nm where the pulse width rises with a peak width of 170 ps at 480 nm. Closer inspection of the data (Figure 2.52 and Figure 2.53) reveals a secondary pulse (before the main pulse) that changes amplitude and with a marginally different temporal shift from the main pulse. At 480 nm this secondary peak is at its largest whilst still being distinct from the main pulse. At the peak of intensity at 475 nm the two peaks are no longer resolvable as separate in time.

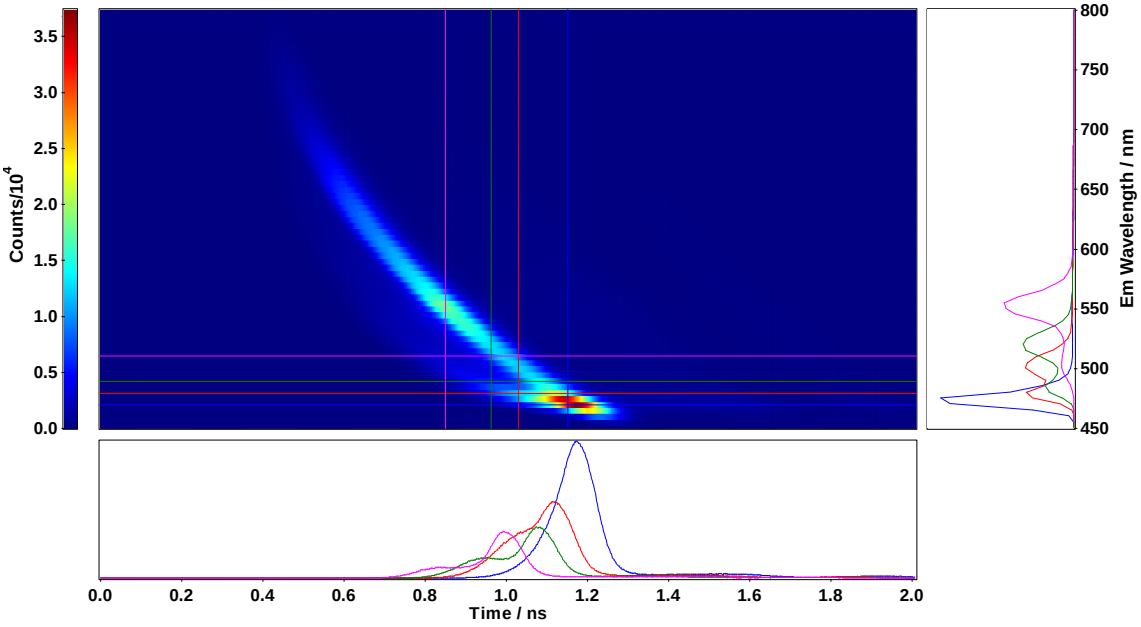

Figure 2.52 Temporal and spectral profiles of SuperK ExW-12 at various wavelengths and temporal positions

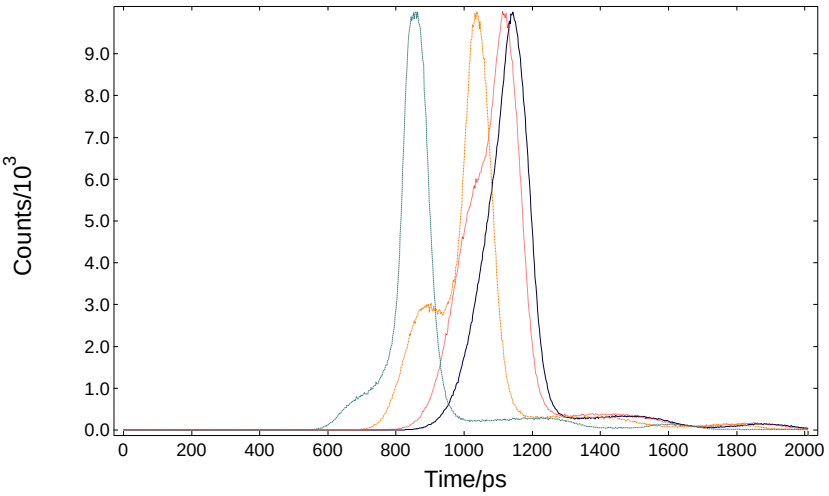

Figure 2.53 Selected IRFs of SuperK ExW-12, normalised and linear scale at 550 nm, 500 nm, 480 nm and 475 nm (left to right)

The SuperK ExW-12 has characteristics very similar to the source tested in Section 2.1, meaning it is likely to contain an endlessly single mode PCF. The IRF pulse widths were marginally smaller, however, this could be related to the triggering method (the negative trigger pulses of the SuperK ExW-12 allow the CFD to be employed of the start signal). The change in pulse position was greater for the SuperK ExW-12 over the range 455 nm – 800 nm (854 ps compared to 550 nm) indicating either slightly different group velocity dispersion characteristics of the fibre or that the SuperK ExW-12 has a longer fibre that the SC-400 under test in Section 2.1 (55 % longer).

2.4.2 YSL Source

A source from YSL Photonics (SC-1-HE) was coupled directly into the sample chamber of an experimental setup similar to that shown in Figure 2.13. The UV-visible emission spectrum was measured (Figure 2.54). The source shows considerable UV output down to 350 nm.

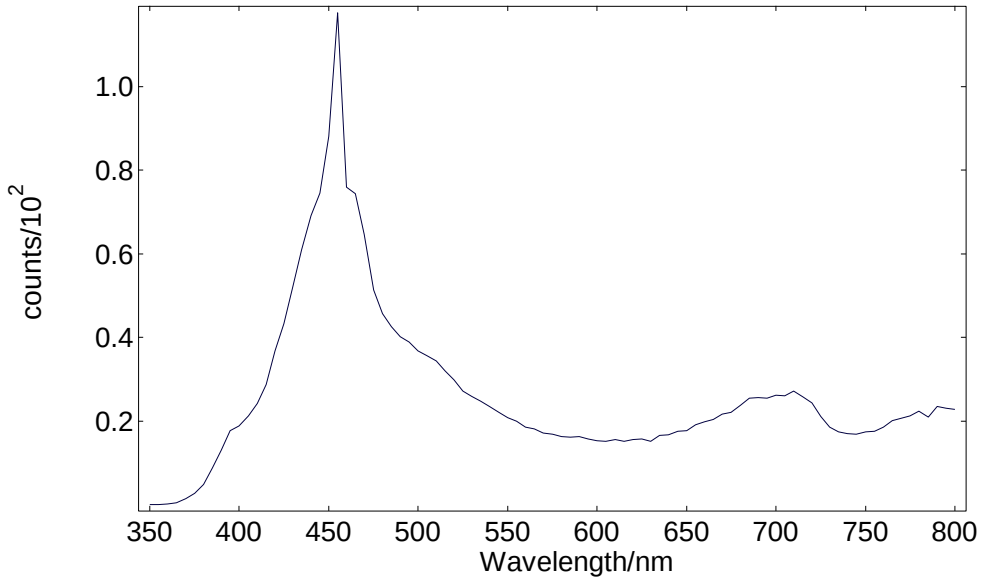

Figure 2.54 Corrected UV visible spectrum of YSL SC-1-HE

The experimental setup was then arranged as in Sections 2.2.3 and 2.2.5, using the internal trigger. The intensity map of normalised instrument response functions with wavelength is shown in Figure 2.55, showing a disjointed fibre dispersion curve. The temporal shift and pulse width were also calculated and displayed in Figure 2.56.

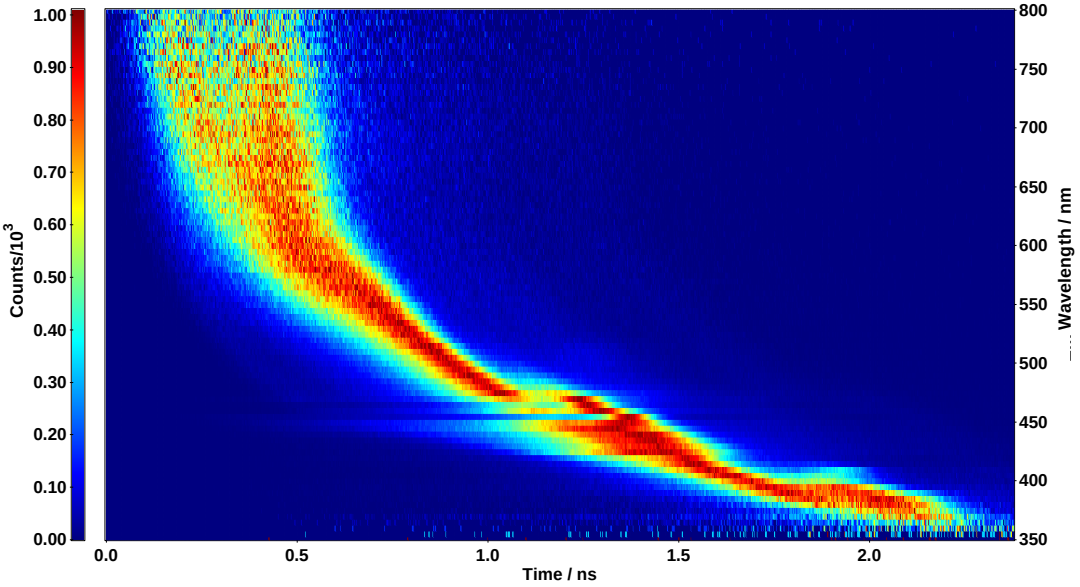

Figure 2.55 Intensity map of normalised instrument response measurements of SC-1-HE supercontinuum. 350 – 800 nm 5 nm step 30 s acquisition time/step

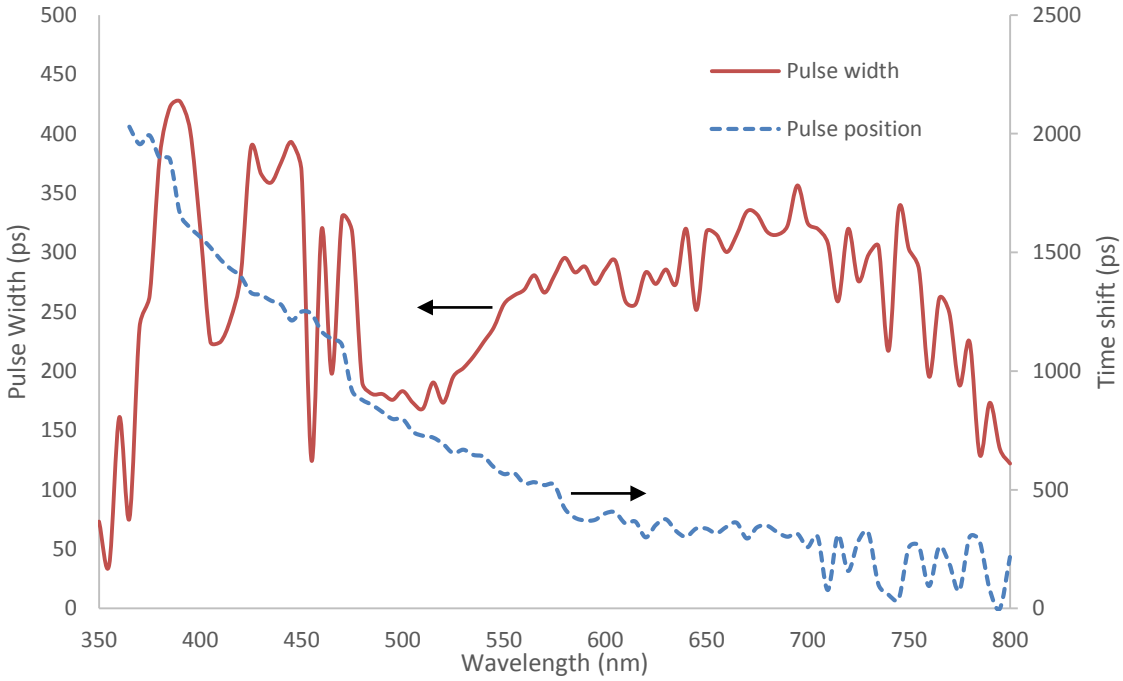

Figure 2.56 IRF pulse widths (FWHM) and pulse temporal shift of SC-1-HE.

The SC-1-HE has characteristics different from the sources previously tested. Although it has a spectral shape similar to the source containing a tapered fibre characterised in 2.3, the temporal characteristics are very different. The tapered PCF source had a reasonably flat pulse width in the range 392 – 700 nm, with a wider pulse width at lower wavelengths caused by different overlapping pulses. Using the SC-1-HE as a source yields a minimum measured IRF of 175 ps at around 500 nm, with broader IRFs at both sides as high as 400 ps (selected IRFs are illustrated in Figure 2.57). Figure 2.55 shows how the pulse appears to completely break into two at wavelengths above 650 nm. The broader IRFs would restrict the fastest fluorescence phenomena able to be measured. In addition the temporal shift measured is greater than any other source tested (2000 ps between 365 and 800 nm) indicating either much longer fibres, or very different dispersion characteristics of the PCF employed. This source has very different temporal characteristics (measured IRF as a function of wavelength) than the others tested, for example all other sources tended to have stable or narrowing pulse widths with increasingly red wavelengths. One speculation is that a different type of pump source is used in this case (perhaps with a broader pulse width).

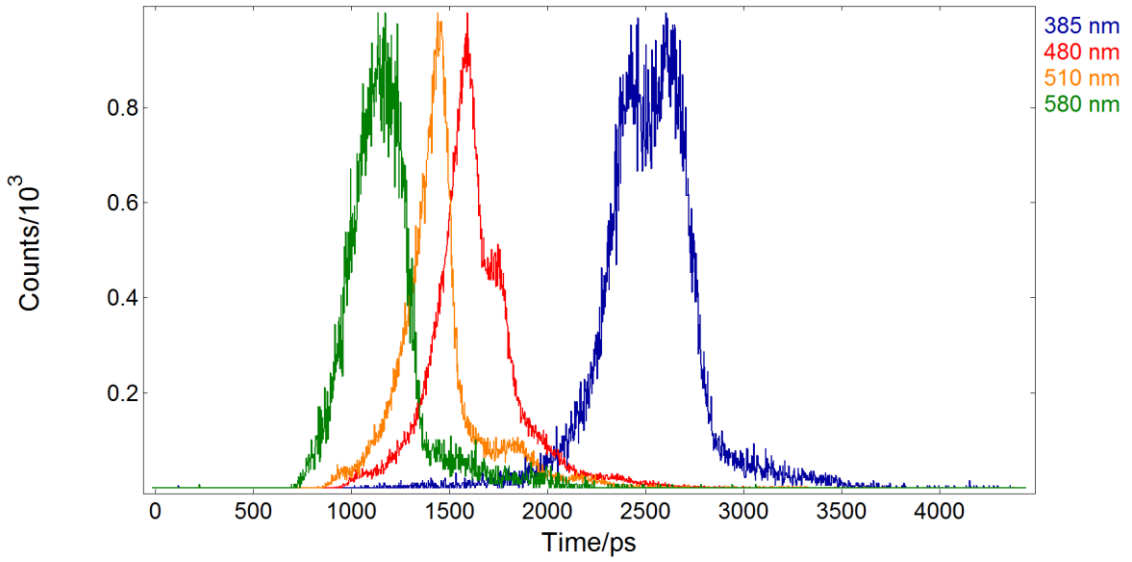

Figure 2.57 Selected IRFs of SC-1-HE, normalised and linear scale at 580 nm, 510 nm, 480 nm and 385 nm (left to right)

2.5 Conclusions

Various supercontinuum sources were evaluated with different designs of photonic crystal fibre. An endlessly single mode PCF was evaluated initially, this was found to emit a supercontinuum that extended down to 440 nm. Next, a supercontinuum source based on a high-Δ PCF was evaluated. It was found that the change in fibre design (which led to a shift in the group index) extended the blue edge of the spectrum to below 400 nm. Following this, an experiment was conducted coupling light from a 1064 nm 1 MHz picosecond source into a fibre that had a core tapering from 6 μm to 2 μm (which resulted in a corresponding shift in group index curve along the length of the fibre). This tapering extended the blue extent of the supercontinuum spectrum to <320 nm. For comparison two commercial supercontinuum sources from other manufacturers were also evaluated.

Supercontinuum sources emit highly temporally structured light that can be complex to deal with compared to alternative discrete picosecond sources. The pulse width, pulse height distribution, temporal position and intensity are all highly wavelength dependant, because of the complex nature in which the supercontinuum is generated along the length the PCF. However, provided they are carefully integrated with the spectrometer and timing electronics, supercontinuum sources provide a useful, flexible source for lifetime and in some cases quasi-steady state fluorescence spectroscopy. The best performance is achieved with careful triggering of the TCSPC electronics. In addition, triggering on the wavelength of interest (or at a fixed wavelength from the excitation) avoids the fibre dispersion curve being overlaid on time resolved excitation spectra.

Whatever synchronisation method is used to trigger the TCSPC electronics, the width of the instrumental response function is significantly broader than the width expected with a 6 ps pump source. This pulse broadening cannot only be due to jitter caused by a broad pulse height distribution, as the pulse height distribution varies significantly and the pulse width does not vary proportionally with it. The major reason for the wavelength dependence of the measured IRF width is secondary pulses with different spectral and temporal positional characteristics overlapping.

Fluorescence lifetimes down to $^{1}/_{10}^{th}$ of the IRF can be accurately measured using the TCSPC technique [16]. As even the broadest pulse widths measured with any of the sources was far less than 1 ns, fluorescence lifetimes above >100 ps could be able to be accurately measured (Section 3.4.10). 100 ps is sufficient for vast majority of fluorescent lifetime applications and all sources (apart from the YSL source) have pulse widths of <200 ps, meaning that lifetimes down to <20 ps may be analysed.

CHAPTER 3 - A NOVEL METHOD OF SUPERCONTINUUM SPECTRAL SELECTION

One of the drawbacks of a PCF based supercontinuum source when it comes to its use in fluorescence spectroscopy is that, like other conventional sources such as lamps, but unlike other laser based sources such as OPOs, all the wavelengths are generated at once. In fluorescence spectroscopy it is important to select the wavelength to be used for excitation while suppressing all others. Fluorescence effects are orders of magnitude in intensity lower than the excitation, due to both the fluorescence quantum yield and the fact that the emission is spectrally broad (compared with the excitation), therefore the light used to excite the sample must be spectrally pure. Current methods of spectral selection have some disadvantages discussed in Section 3.1. This chapter will introduce a novel type of monochromator based on wedge interference filter technology (Section 1.4.8), with distinct advantages over other methods of spectral selection of a supercontinuum source for fluorescence spectroscopy.

The chapter will begin describing work using a wedge bandpass filter and then progress onto investigations using variable edge filters. Variable edge filters allow the possibility of tuning the bandpass of the transmitted light by moving the filters with respect to each other.

3.1 Current methods of spectral selection

3.1.1 Diffraction grating based monochromator

The most popular form of spectral selection in a research grade fluorescence spectrometer is a monochromator containing a dispersive element. In Chapter 2 a monochromator based on a Czerny-Turner design was used for wavelength selection of the supercontinuum radiation. A Czerny-Turner monochromator consists of an entrance slit, concave mirror (to collimate the light), a plane reflective diffraction grating, a second concave mirror (to focus the light diffracted from the grating) and an exit slit (see Figure 3.1). The bandwidth is determined by the focal length of the concave mirrors, the groove density of the diffraction grating and the width of the entrance and exit slits. Wavelength selection is controlled by rotating the grating on its axis. The rotation of the grating used to be carried out by way of a sine bar (which allowed the wavelength position of the grating to vary linearly with the motor rotation); however, with modern monochromator

turrets are often controlled with a direct drive. This has become possible thanks to microstepping stepper-motors, which allowing a greater precision than was previously available. A turret based design allows multiple gratings to be attached simultaneously, meaning a monochromator can have wide wavelength coverage without sacrificing resolution at low wavelengths. When using a grating based monochromator, optics should be used to illuminate as much of the diffraction grating as possible in order to maximise the efficiency and resolution of the grating [69], [100] (Equation (3.1)).

$$mN = \frac{\lambda}{\Delta\lambda} \qquad (3.1)$$

where m is the diffraction order and N is the total number of groves illuminated on the grating surface.

The diffractive optics have an adverse effect on beam profile, meaning the beam is no longer diffraction limited.

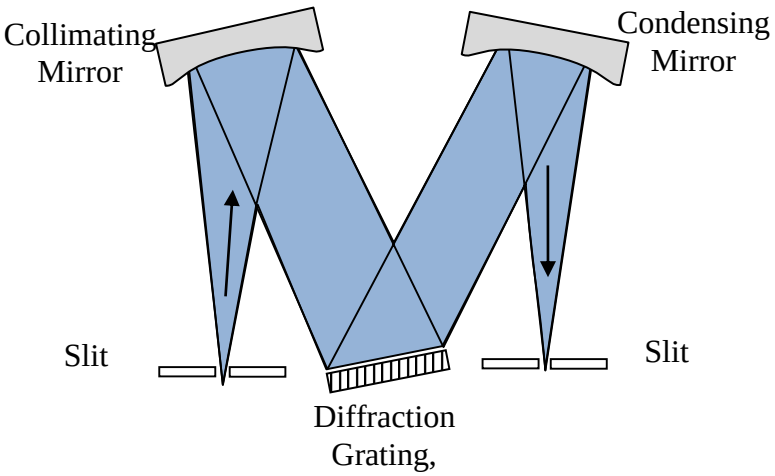

Figure 3.1 Czerny-Turner Monochromator

3.1.2 Acousto-optic tunable filter

An alternative method of spectral selection involves the use of an acousto-optic tunable filter (AOTF). An AOTF is an optical scanning filter based on an isotropic crystal with a large stress-optic coefficient and a piezoelectric modulator (acting as a Bragg cell) [101]. The piezoelectric device is driven by an RF field, which in turn generates a periodic change in refractive index of the crystal [102].

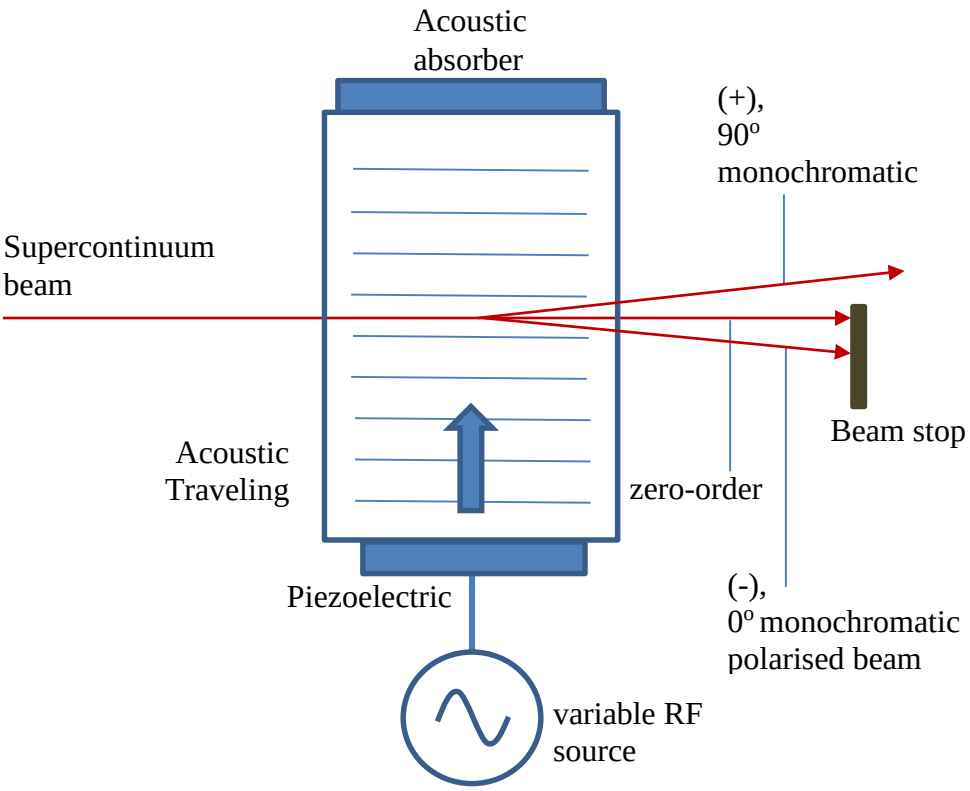

Figure 3.2 Schematic with AOTF

The AOTF can have a high throughput (40-70 %) and narrow bandwidth (<4 nm) [103]. Additionally, they have some novel features such as simultaneous wavelength transmission (which can be useful for applications like stimulated emission depletion microscopy) and the supercontinuum output remains diffraction limited. However, AOTFs have limited wavelength coverage (for example 400-650 nm by one filter), meaning that multiple units are required to cover the spectral output of the supercontinuum. In addition, the background suppression of the AOTF is often not sufficient for fluorescence experiments, light from other wavelengths of the supercontinuum can bleed through to such an extent that they effect the fluorescence emission spectrum by altering the shape or causing a spike on the front of the fluorescence decay. A further limitation is spectral scanning. Changing between wavelengths can be extremely fast (<5 μs), but the parameters for each transmission channel (wavelength of transmission) have to be setup first to ensure an optimum transmission profile. Although they can have narrow transmission bandwidths, increasing the bandwidth involves overlapping acoustic orders. This takes time and is much more complex than simply opening the slits in a diffraction grating based monochromator.

3.2 Interference filter based monochromator

A rig was built in order to make proof-of-principle tests of the feasibility and effectiveness of using a wedge interference filter based monochromator in fluorescence spectroscopy. In the initial tests an off-the-shelf bandpass wedge interference filter was used (Veril S 60, Schott). The filter was specified to work between 400 – 700 nm with an out of band blocking of <0.01 % and peak transmission of >35 % at 450 nm, >45 % at 550 nm and >40 % at 650 nm.

A prototype was designed and constructed (see Figure 3.3). Radiation from a mercury lamp was coupled into an optical fibre (500 μm diameter), the uncollimated output of this fibre was mounted on a stage with x, y and an angle adjustment. A variable pinhole was mounted on rail equipment (Linos Photonics) 15 cm from the fibre. The radiation from the mercury lamp that passed through the pinhole was assumed to be collimated. The collimated light from the pinhole passed through the wedge bandpass interference filter (Veril S 60 Schott) and was incident on a liquid fibre light guide (Newport, 3 mm diameter). The other end of the light guide was coupled to the sample position of a fluorescence spectrometer (FLS920, Edinburgh Instruments) with a double 300-mm focal length emission monochromator (to optimise stray light suppression). The detector used to collect spectra was a red sensitive photomultiplier tube, PMT (Hamamatsu Photonics, R928P) in a Peltier cooled housing. The spectral range of the emission arm of the spectrometer was 200-870 nm; the double monochromator had a wavelength accuracy of 0.2 nm, a repeatability of 0.05 nm and stray light suppression of 10^{10}, it was therefore suitable for testing the performance of the wedge filter device (which was specified to have a spectral range of transmission of 400-700 nm and a fixed spectral bandpass of 15 nm).

The wedge filter was mounted on a 3-inch linear stage which was in turn connected to a stepper motor. The stepper motor was powered and controlled by an Edinburgh Instruments FLS920 spectrometer controller (CD920). Edinburgh Instruments standard spectrometer software (F900) was altered so that the filter was able to be moved in equidistant steps

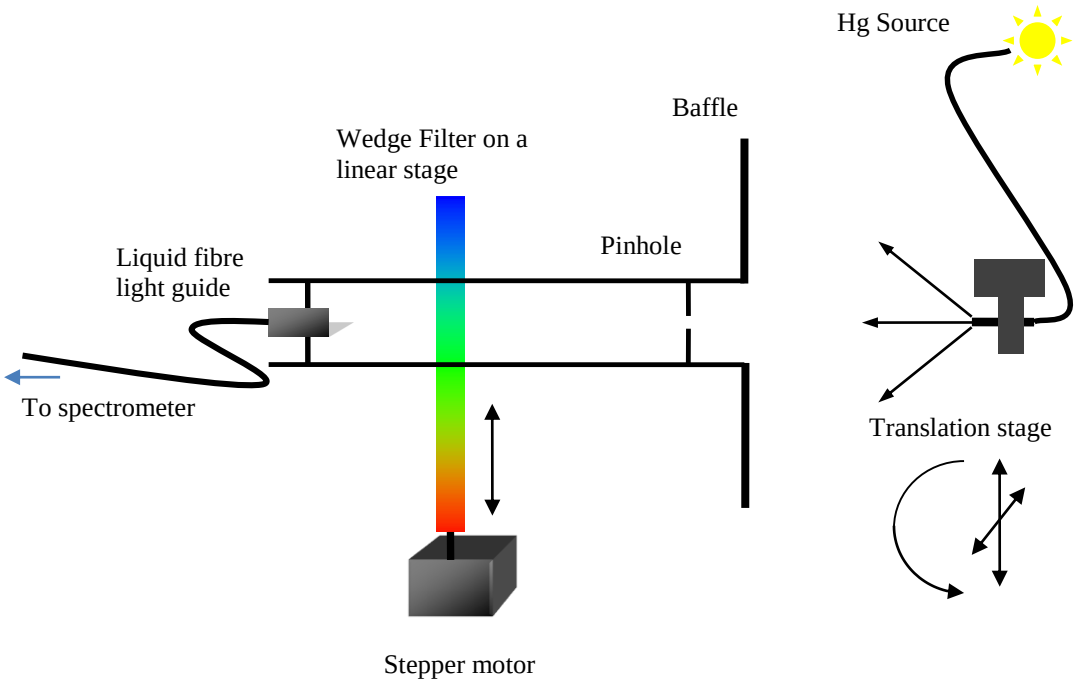

Figure 3.3 Prototype wedge filter monochromator, calibration setup

In order to test the sensitivity and effectiveness of the system, the fluorescence emission spectra from common fluorophores was measured. To do this the experimental rig was modified as shown in Figure 3.4. A lens was added in front of the pinhole to collimate the fluorescence emission (to increase the amount of fluorescence signal collected) and a 405-nm picosecond pulsed diode lasers (EPL405, Edinburgh Instruments) was used to excite the sample The laser was run at 20 MHz repetition rate in order to act as a quasi-CW excitation source. The emission monochromator of the spectrometer was set to zero order, so that the so that spectral scanning was carried out purely by moving the filter.

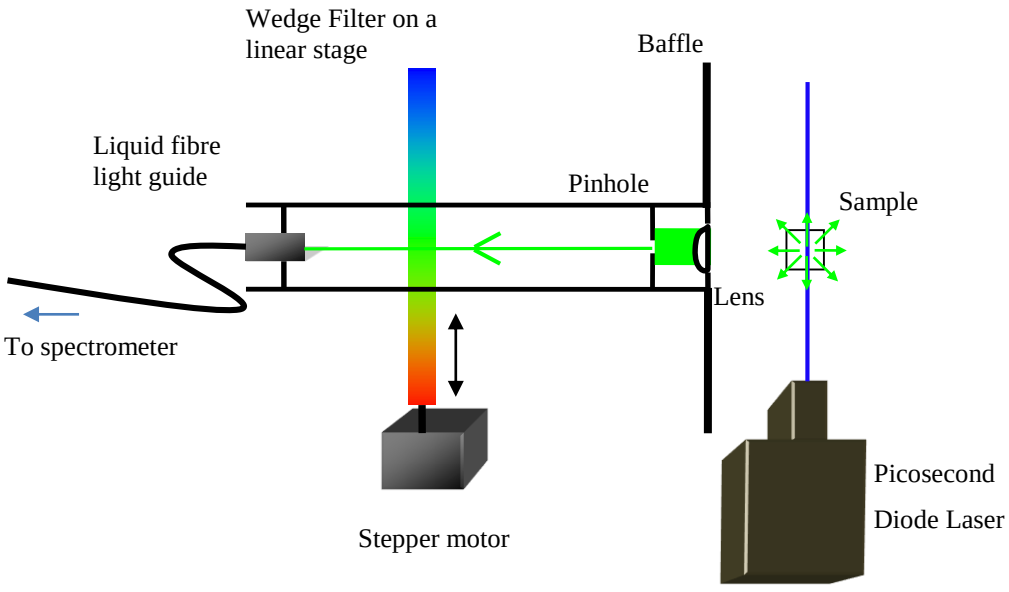

Figure 3.4 Prototype wedge filter monochromator, measurement setup

3.2.1 Calibration and stray light suppression

The spectrometer's control software (F900) was setup so that it would turn the stepper motor (and therefore move the filter) in equal steps. In order to check the linearity of the transmission band of the filter with position, a scan of the mercury source and the second harmonic from a Nd:YAG laser at 532 nm was made. The peak positions measured were then related to known mercury lines (and the laser line). The result, Figure 3.5, shows the linearity of the filter device by plotting the mercury positions with a linear trend line. There are only 6 data points measured, however, the result indicates that the position of the filters transmission band is linear to wavelength over the range 400-600 nm. From the data it was possible to calculate a step size (in nm/mm) and offset, to allow the wavelength calibration of scans with the filter device.

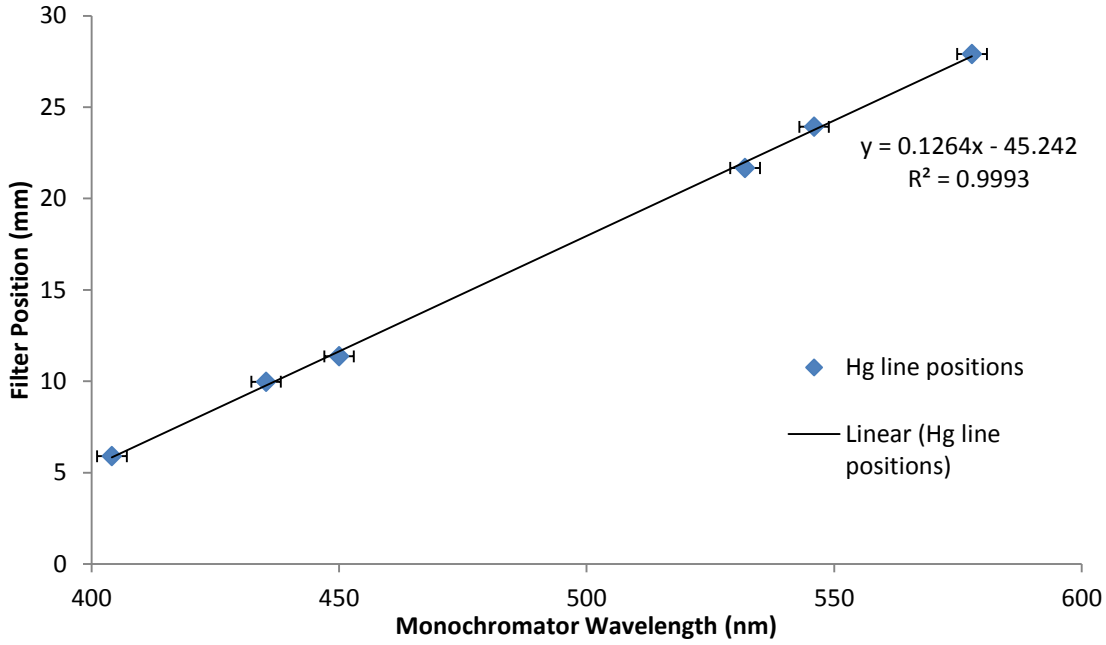

Figure 3.5 Linearity of filter compared to mercury line positions (from a monochromator)

In order to check the effect of the aperture on the spectral bandwidth of the instrument, the aperture width was varied between 0.5 mm and 5 mm, Figure 3.6, this shows that there was little variation in the spectral band pass with wavelength; however the diameter of the collection fibre after the filter is 3 mm, therefore the measurement is only valid for iris diameters up to 3 mm (assuming correct optical alignment). Between 0.5 and 3 mm the spectral bandpass of the filter was found to change by only 1 nm (15 nm at 0.5 mm and 16 nm at 3 mm).

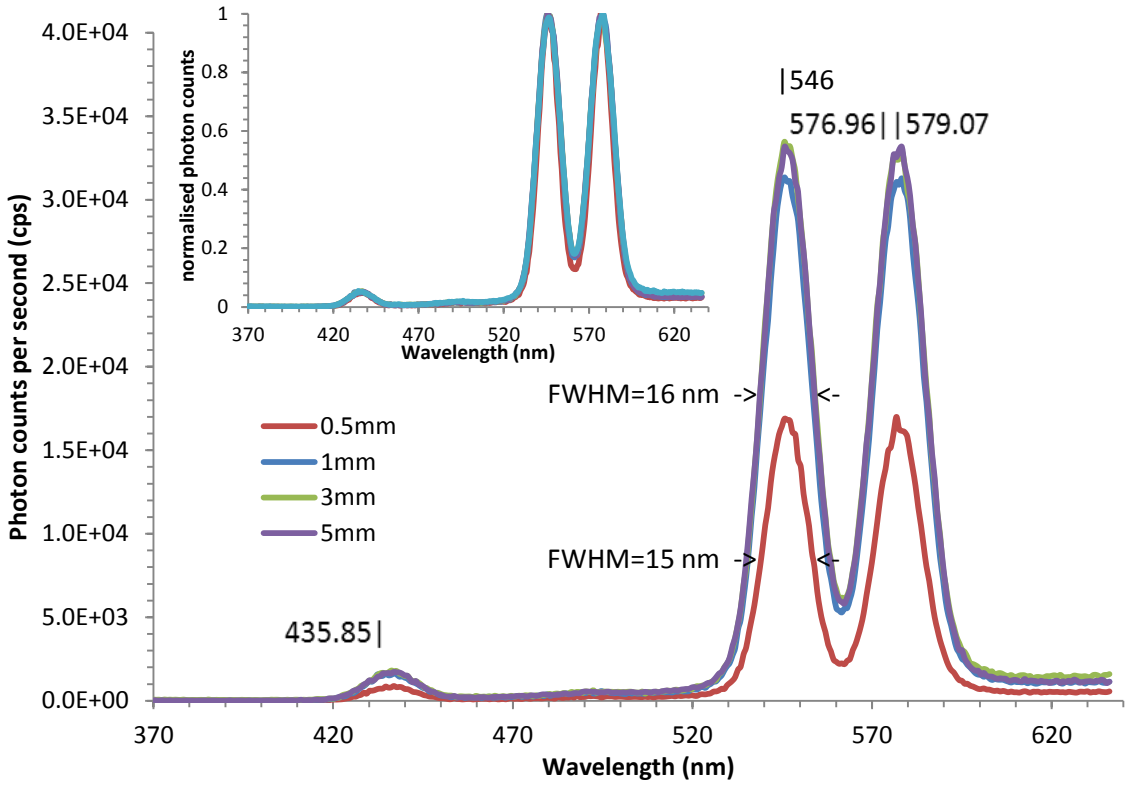

Figure 3.6 Effect of variation of front pinhole diameter on spectral bandpass and original measured intensity and normalised (insert)

To measure stray light suppression, the filter was set to transmit three mercury lines in turn (435.9 nm, 546.1 nm and the doublet at 577.0 and 579.1 nm). The fluorescence spectrometer was then used to scan the spectrum of the lamp beam transmitted by the interference filter system. The results, Figure 3.7, show how the filter transmits one mercury line and supresses others (outside of the bandpass of the filter at that position). Figure 3.7 also shows the theoretical bandpass of the filter placed in the three mercury line positions. The transmission function was assumed to be Gaussian with a 15 nm FWHM and a background equal 0.01 % of peak transmission (specified out-of-band blocking) plus the measured detector dark counts (30 cps).

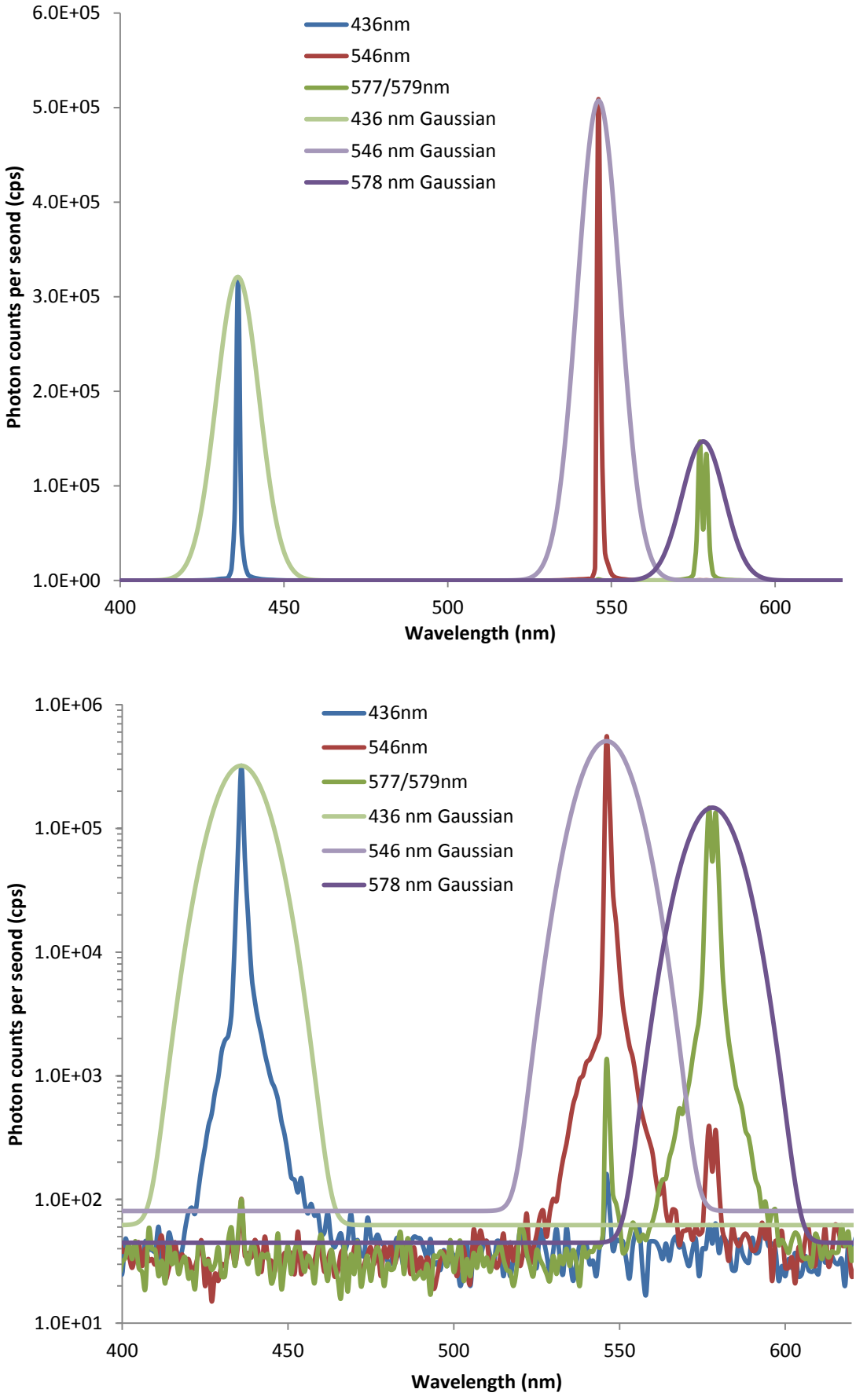

Figure 3.7 Mercury lines through the filter spectrometer measured using a fluorescence spectrometer (top – linear, bottom – semi-log)

For comparison, the filter was removed from the system and the resultant mercury spectrum was also measured and compared with the results with the filter in Figure 3.8.

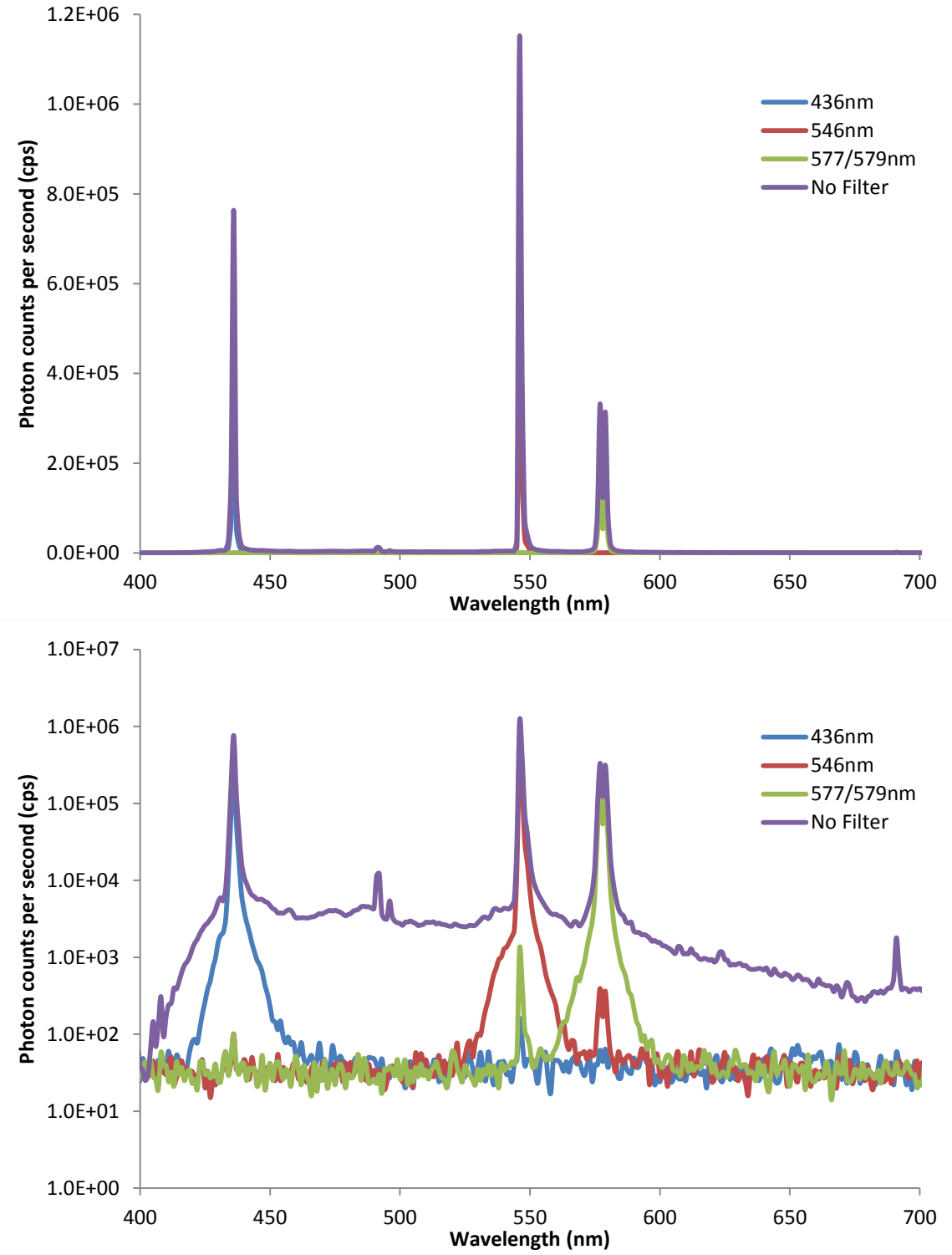

Figure 3.8 Mercury lines through the filter spectrometer measured using a fluorescence spectrometer. Top – Linear scale, bottom – semi-log scale.

Figure 3.7 and Figure 3.8 show that the filter suppresses unwanted radiation by more than three orders of magnitude when the peak is a large distance (>100 nm) from the actual central wavelength of the filter. Closer to the pass band of the filter, this figure is reduced. In Figure 3.7, the 546 nm (red) scan shows a 3.5 order reduction of the 577/579 nm doublet; however, the 577/579 nm (green) scan shows only 2 orders of magnitude reduction of the 546 nm line. The reason for this is an asymmetry in the filter out of band suppression (as the filter appears to supress higher wavelengths more effectively than lower ones. The results also show a reasonably good correlation with the theoretical transmission.

3.2.2 Fluorescence measurements

The system was then used in the configuration shown in Figure 3.4. A sample of fluorescein was placed in the sample position and the filter was scanned over the emission band to acquire the emission spectrum, this was compared to the true spectrum, obtained by measuring the same sample in the fluorescence spectrometer (Figure 3.9).

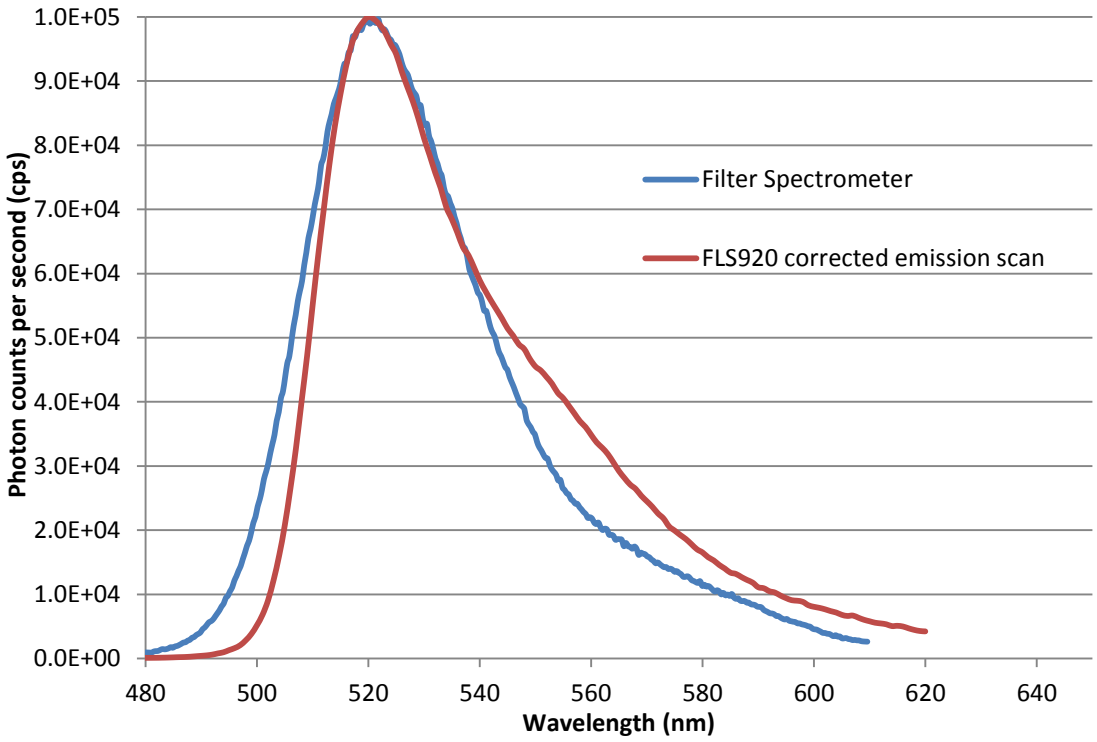

Figure 3.9 Emission scan of Fluorescein made on the filter device (blue) and the true spectrum measured on a commercial fluorescence spectrometer (red)

This measurement was repeated with the dye 9-ammino-acridine (Figure 3.10).

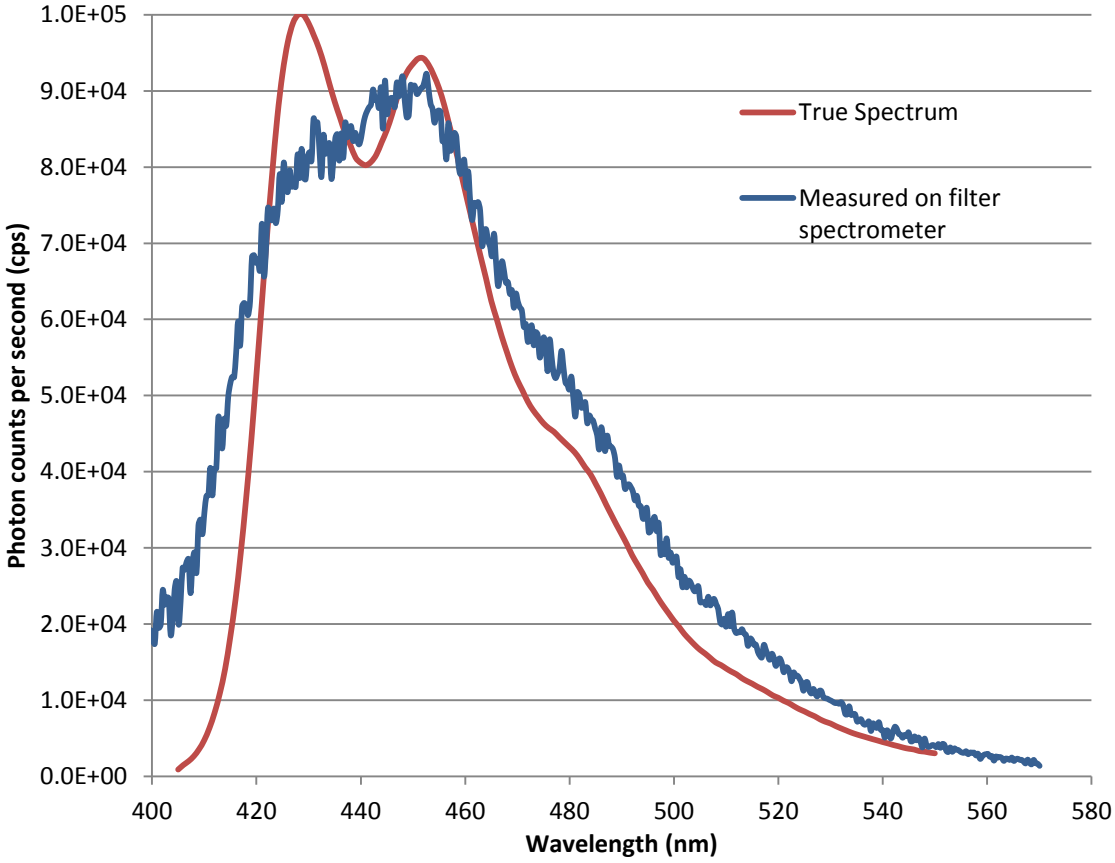

Figure 3.10 Emission scan of 9-ammino-acridine made on the filter device (blue) and a fluorescence spectrometer (red)

The measurements of fluorescein, Figure 3.9 show good correlation, however the emission spectra of the 9-ammino-acridine dye shows a significantly different shape. The peaks are not well defined in the filter spectrometer as the bandwidth of the device is 15 nm and the spectral separation of the two peaks is 10 nm. In both measurements the width of the samples emission band measured on the filter spectrometer is broader than the sample because of the effect device's broad bandwidth.

The results show that measurements of the fluorescence emission spectra of samples using a spectrometer based on a wedge bandpass filter are indeed possible. The differences between the spectra measured on the fluorescence spectrometer and the filter device are likely due to the wavelength dependence of transmission of the filter.

3.3 Spectral separation of a supercontinuum source using a wedge bandpass interference filter

A commercial supercontinuum light source (SC-400, Fianium) was used together with the experimental setup shown in Figure 3.11.

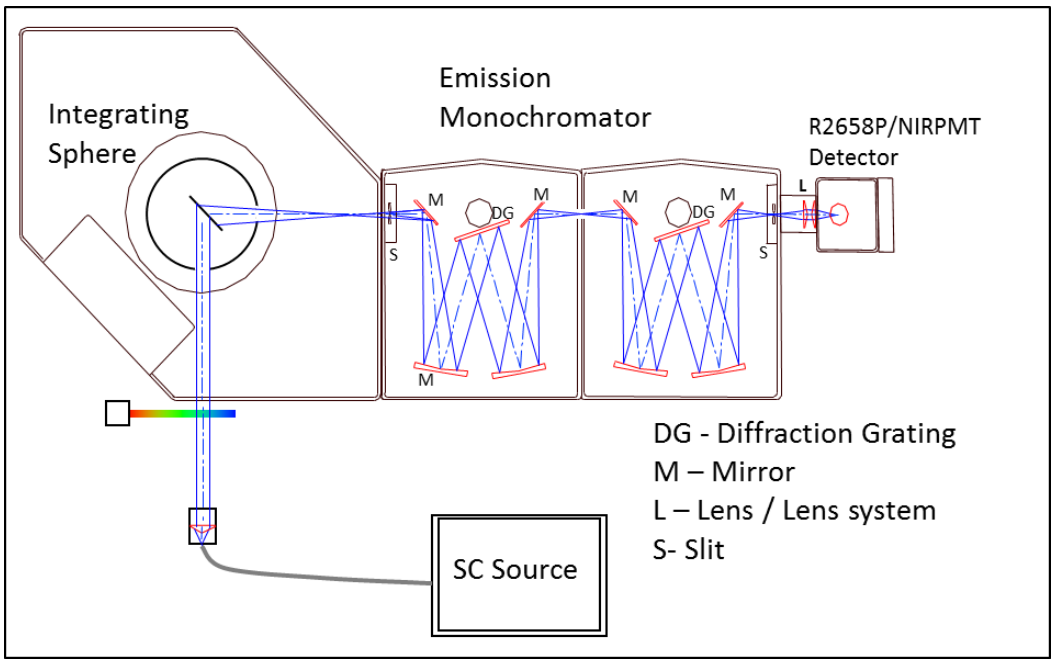

Figure 3.11 Experimental setup for the measurement of the supercontinuum spectra through a wedge bandpass interference filter

The filter was moved in 99 equal steps (0.59 mm/step), at each step the spectrum of the light transmitted by the filter was measured. Figure 3.12 shows the spectrum measured at each step overlaid together on one graph.

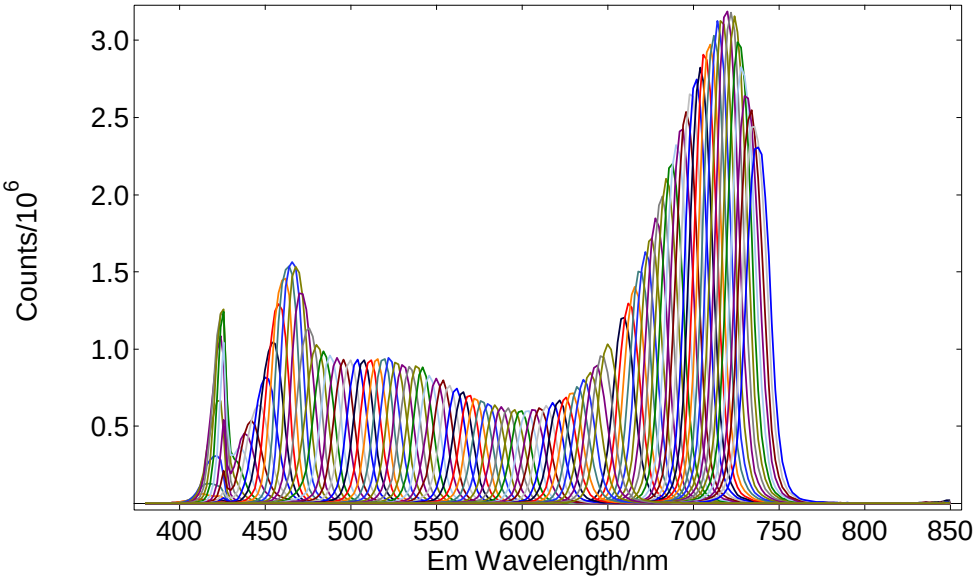

Figure 3.12 Spectra of the supercontinuum through the bandpass filter at 99 linear steps

The spectrum of the supercontinuum (Figure 3.13) is clearly visible with the superimposed spectra through the filter (Figure 3.12). The peak intensity of each pass band was plotted against filter position (Figure 3.14). The relatively broad bandwidth of the filter compared to some of the features in the supercontinuum spectrum mean that the spectrum measured through the filter is broadened. The band pass of the light transmitted

by the filter was plotted against the central wavelength of each band (Figure 3.15). To get an impression of the change in transmission of the filter for different wavelengths of the supercontinuum the peak intensity (Figure 3.14) was divided by the corrected spectrum of the supercontinuum (Figure 3.13). To account for the wide bandwidth of the filter transmission Gaussian smoothing was performed on the corrected spectrum before the division. Although this did not properly correct for the spectrum, it removed the majority of the features allowing the trend to be seen more clearly.

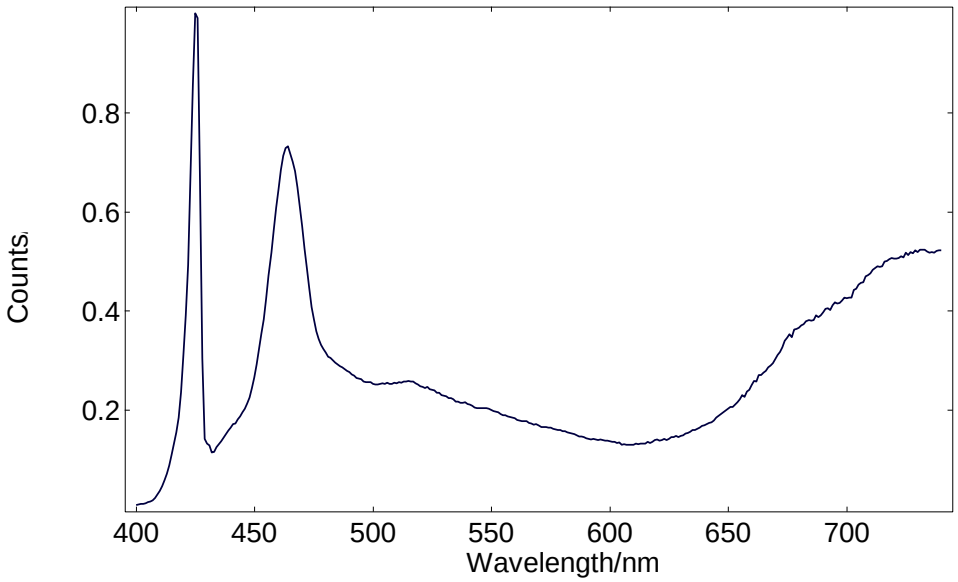

Figure 3.13 True spectrum of supercontinuum source that was used with the bandpass filter

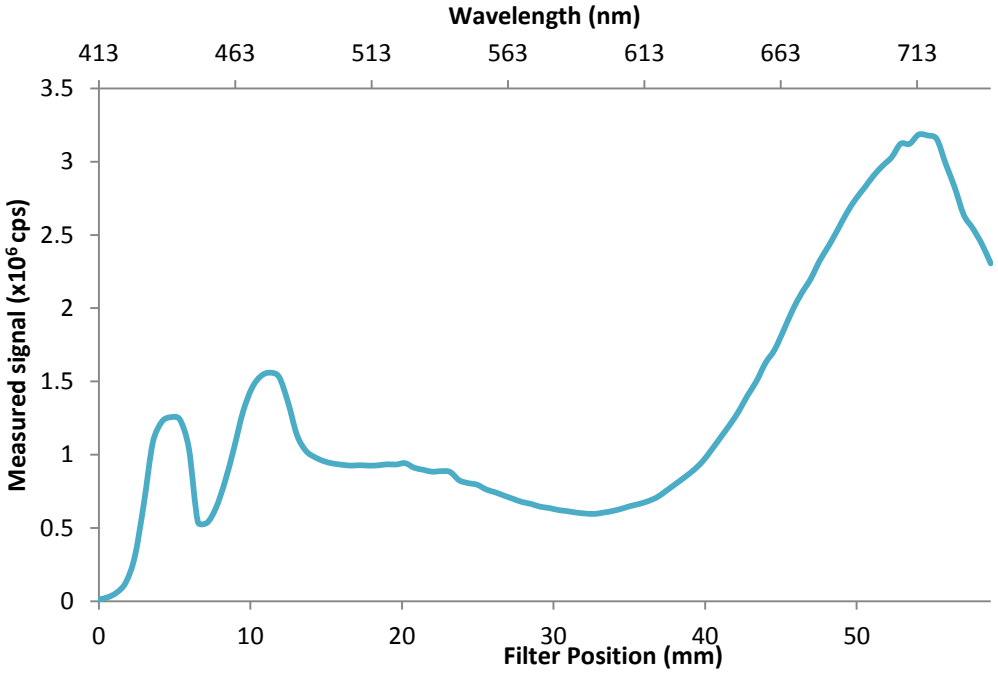

Figure 3.14 Peak intensity transmitted through the filter against filter position

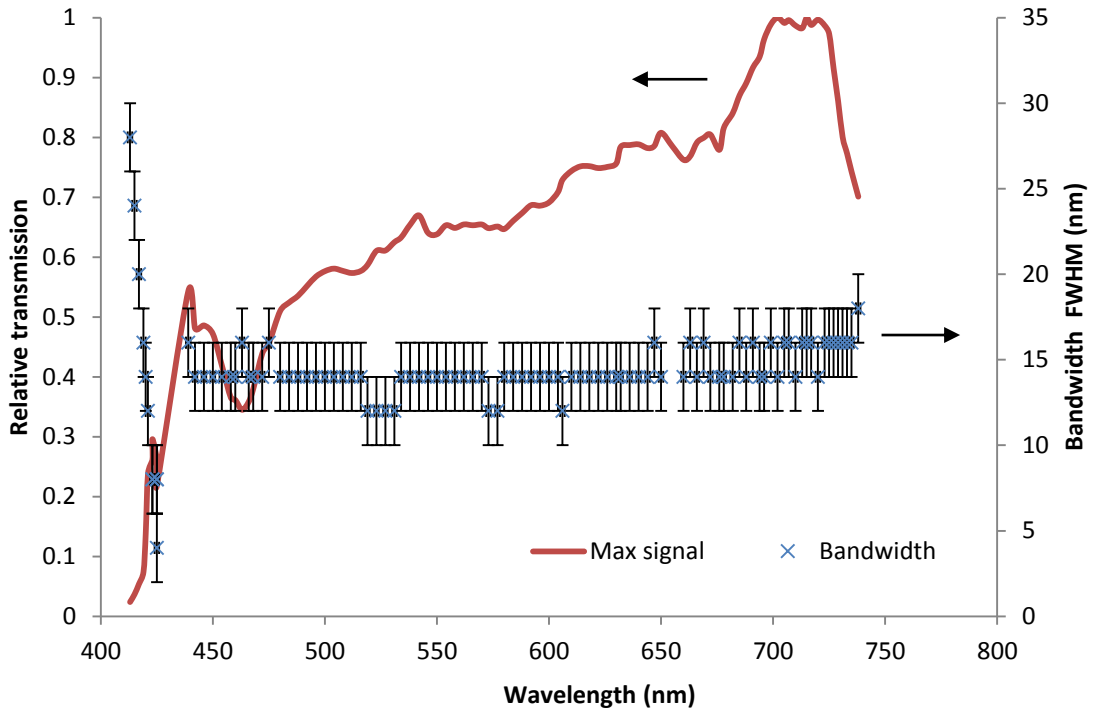

Figure 3.15 Bandwidth (FWHM) as a function of central wavelength superimposed with filter transmission trend

In order to investigate the wavelength linearity of the filter, the central wavelength of each pass band was then plotted against wavelength (Figure 3.16). This was more accurate than with the measurement shown in Figure 3.5 as there were many more data points measured. The data match reasonably well to a linear trend, however, the data are

closely approximated by a linear fit only in the central region between 442 – 650 nm (Figure 3.17).

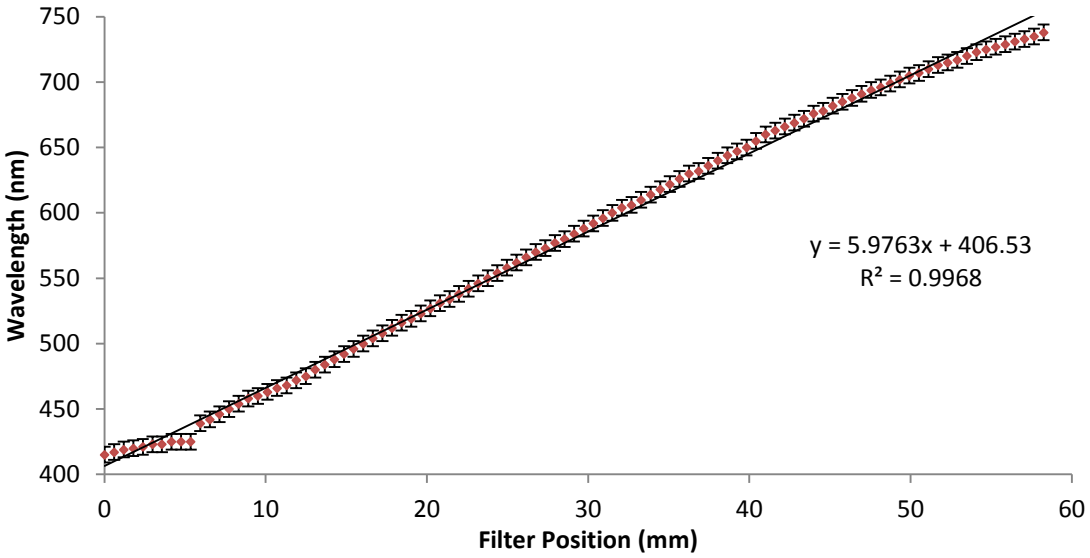

Figure 3.16 Filter position against wavelength with a linear trend line over the full range

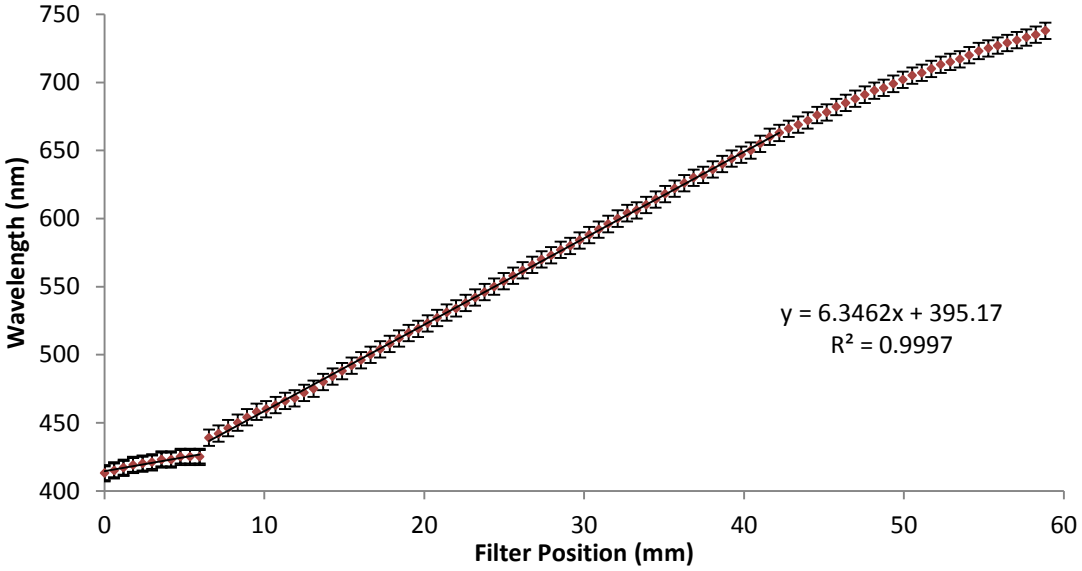

Figure 3.17 Filter position against wavelength with a linear trend lines in the region 442 – 650 nm

3.3.1 Conclusions

The wavelength dependence of the bandwidth of the filter changes sharply between 413 nm and 439 nm, however this is due (in a large part) to the sharp features in the supercontinuum spectrum (Figure 3.13). Above 439 nm the bandwidth is reasonably stable. The transmission of the filter shows a gentle slope of increasing transmission toward the red side of the filter (with transmission falling off quickly at the extremes of

the filters range), therefore the shape of the spectrum transmitted by the filter is mostly dictated by the spectral shape of the supercontinuum.

The wavelength transmission with filter position appears to be mostly linear in the central region of the filter (with transmission 442 – 650 nm), Figure 3.17. At wavelengths below this there is a sharp transition and change in wavelength with position appears more gradual, however, this is because of the sharp feature from the supercontinuum dominating (as the pass band is a superposition of supercontinuum spectral output and filter transmission). In the red edge of the filter operation, the shape begins to look increasingly nonlinear. These results indicate that different parts of the filter have different multilayer structures with different characteristics.

These measurements show that a device for spectral selection of supercontinuum radiation would need to take account of the nonlinearity of the filter and the bandwidth changes in the output.

With a wedge filter design there will be an increase in bandwidth with increasing illumination area (as areas of the filter with different transmission characteristics are illuminated). When using the supercontinuum source, however, the bandpass is also affected by the peaks on the blue edge of the spectrum.

3.4 Design of a system for spectral selection and bandwidth control

Bandwidth control would be a useful feature of a wavelength separation device for a supercontinuum source designed for use in fluorescence spectroscopy. Control of the bandwidth adds flexibility to enhance the usefulness of the source. When measuring the fluorescence lifetime of a sample, a narrow excitation bandpass is often not important, therefore a broad pass band may be utilised to increase excitation intensity when measuring weakly emitting samples. Conversely, samples with a small Stokes shift can require an excitation wavelength close to the emission wavelength, in which case a narrow excitation bandwidth is desirable. The structured nature of the supercontinuum radiation means that even when a fixed bandpass, wedge interference filter is used, as in Section 3.3, the resultant transmitted radiation does not have a fixed bandwidth.

In order to have a spectral selection device with wedge interference filters capable of altering bandwidth the multiple filters have to be moved with respect to each other as well

as translated across the source beam. The design of the wedge interference filters is critical to the operation and performance of the device. The filters used in the wavelength selection device were commissioned by Edinburgh Instruments to have transmission in excess of 90 % over the range 350-750 nm. In addition, a high number of layers were used in order to ensure a sharp transmission transition edge. The sharp transmission edge is required to allow control of bandwidth by moving the low to high transmitting edge of one filter with respect to the high to low edge of another filter.

3.4.1 Theoretical bandwidth control considerations

To calculate the effect on the transmitted band of using two wedge interference filters with different offsets, two Gaussian transmission bands were generated theoretically (Figure 3.18). The two transmission bands were then recalculated with different offsets (0, 10 nm, 20 nm, 30 nm and 40 nm). As Figure 3.19 shows the change in offset has no effect on transmitted bandwidth, only the transmission is reduced.

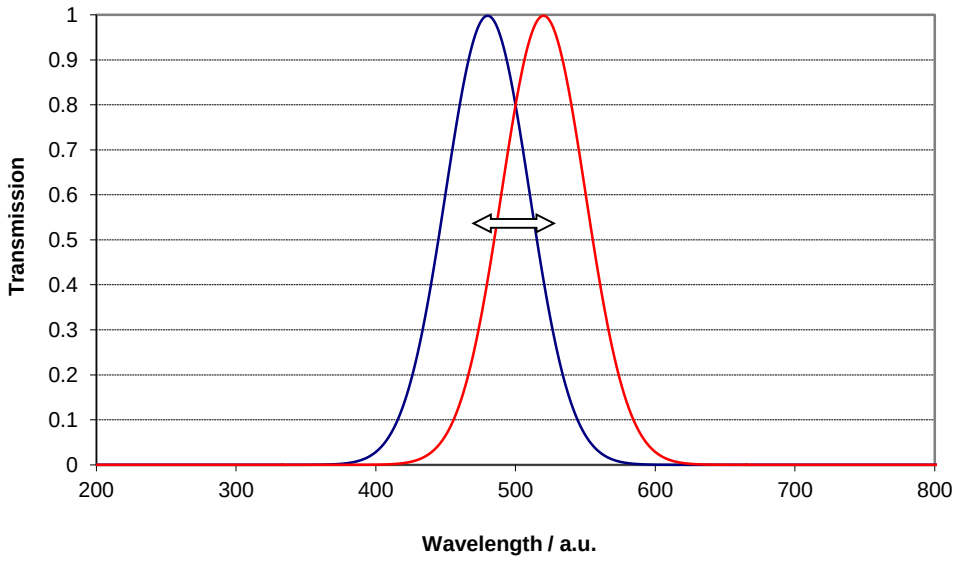

Figure 3.18 Two Gaussian bands offset from each other

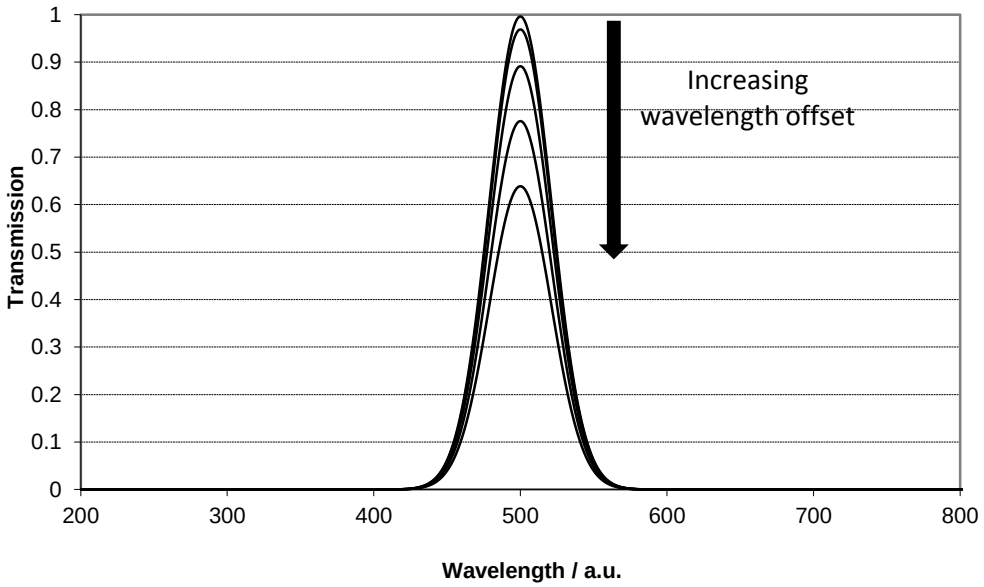

Figure 3.19 Theoretical transmission of two Gaussian pass bands with centre wavelengths offset by 0 nm, 10 nm, 20 nm, 30 nm, 40 nm

These calculations were repeated using two top hat (double Gauss) shaped transmission bands (Figure 3.20). The two transmission bands were recalculated with different offsets (0, 10 nm, 20 nm, 30 nm and 40 nm). As Figure 3.21 shows the change in offset reduces the spectral bandwidth up to a limit, after which the transmission will decrease. From these calculations it is clear that the minimum achievable bandwidth of two movable wedge filters will depend only on the sharpness of the band edge (the high wavelength edge of the filter with the low wavelength offset and the low wavelength edge of the filter with the high wavelength offset).

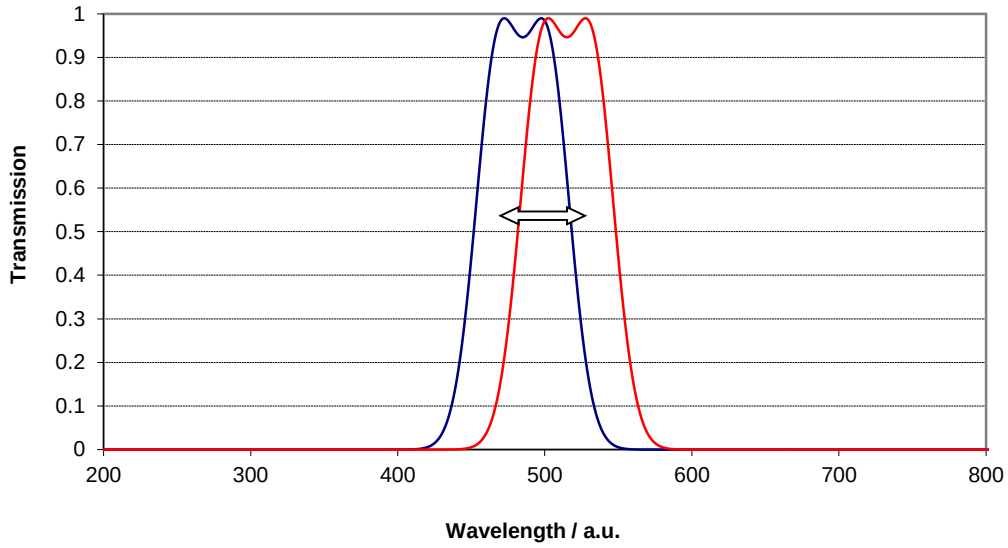

Figure 3.20 Two top hat (double Gauss) bands offset from each other

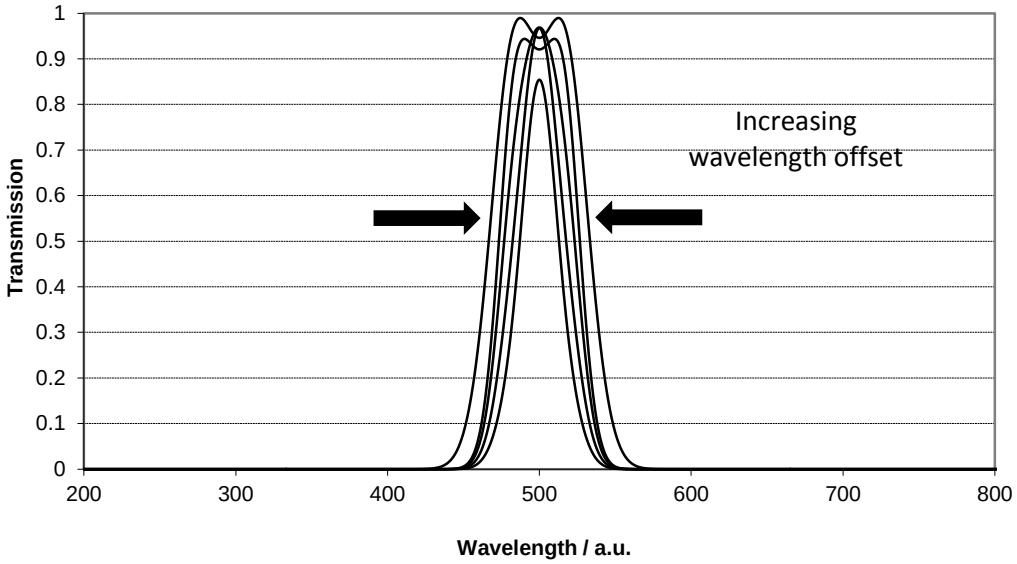

Figure 3.21 Theoretical transmission of two top hat (double Gauss) pass bands with centre wavelengths offset by 0 nm, 10 nm, 20 nm, 30 nm, 40 nm

The theoretical results show that the steeper the band edges of the filter the narrower the achievable transmission band. There are a number of ways to increase the edge steepness. The simplest way is to increase the number of layers in the filter design [68], this will cause an increase in the ripple in the pass band as the first minimum will be brought closer to the edge. Alternatively, higher order stacks can be used. Higher order stacks are quarter wave stacks that are designed with thicknesses corresponding to multiples of the wavelength of transmission (m=2, 3, 4, Equation (3.2)) [104].

$$m = \frac{\delta}{2\pi} = \frac{2n_s d_s}{\lambda} \qquad m=0,1,2\ldots \qquad (3.2)$$

where n_s is the refractive index and ds the thickness of the layers.

The steepness of the edge will increase in proportion with the order for a given number of layers. Unfortunately, the rejection width is inversely proportional to order number (Equation (3.3)).

$$\Delta\lambda = \frac{\lambda}{m} \qquad (3.3)$$

This can, however, be extended with the use of further first order stacks within the coating design. In addition the permissible errors in layer thickness reduce as order number increases. This means that wedge interference filters with steep band edges need to have rather complex layers with various first order and higher order stacks with high precision

in layer thickness. This has now become possible thanks to advances in modelling software and thin-film equipment.

3.4.2 Experimental Setup

In order to evaluate the method of spectral selection based on the wedge interference filters, the supercontinuum source was coupled directly to a specially designed module containing two filter drives. The filter drives consisted of a stepper motor and a lead screw controlling a translation stage with the filter mounted. The filter module was in turn connected to a fluorescence spectrometer (Lifespec-II, Edinburgh Instruments), Figure 3.22. The filters in the module were mounted on stepper motor driven translation stages, the stepper motors were connected to a PC via a USB interface and custom software was used to control their position in the laser beam.

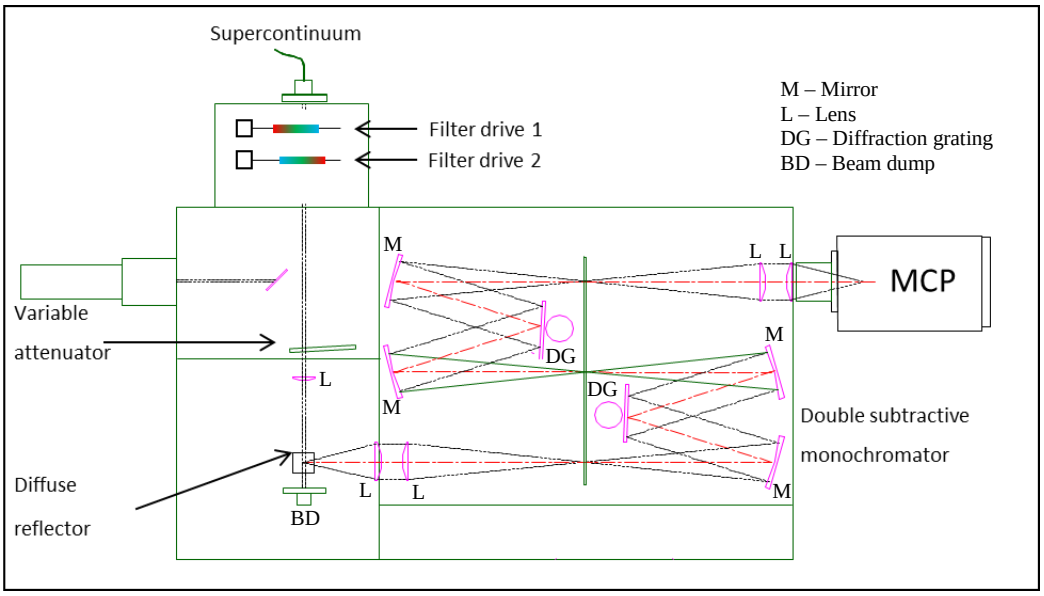

Figure 3.22 Experimental setup for the characterisation of a module for wavelength selection of a supercontinuum source with bandwidth control

The output from the filter module was coupled directly into the sample chamber of a steady state fluorescence spectrometer (Edinburgh Instruments, FLS920) to compare the light available for sample excitation (Figure 3.23).

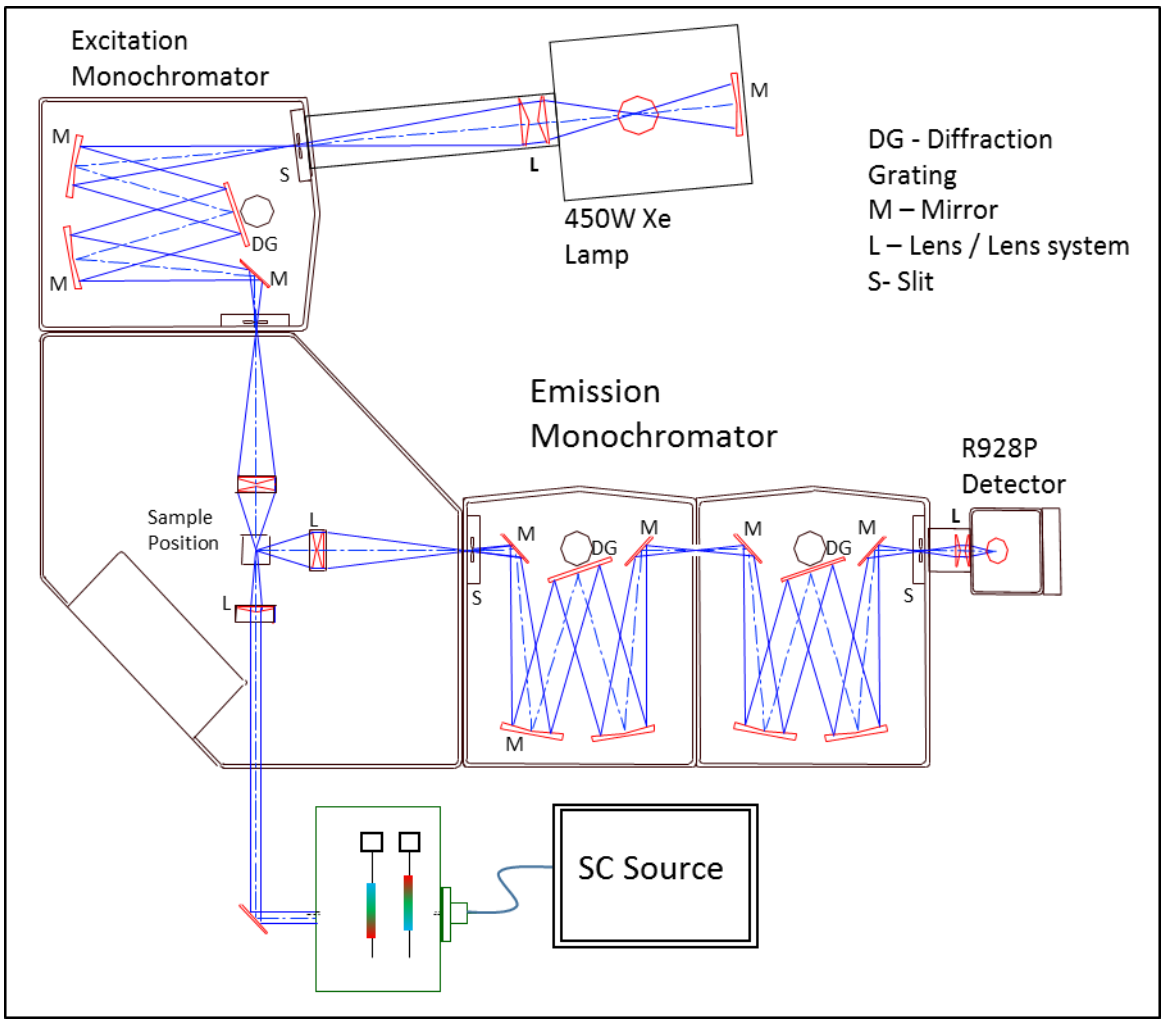

Figure 3.23 Experimental setup for power comparison measurements

3.4.3 Measurements of wavelength selection using two wedge filters

Using the setup shown in Figure 3.22, with a short wave pass (SWP) wedge filter (LVSWP, Delta) in one drive and a wedge long wave pass (LWP) filter (LVLWP, Delta) in the other drive, the spectral emission of the supercontinuum laser was acquired over a limited wavelength range without the filters in the beam path (Figure 3.24). The filters were then moved to various wavelengths and the resultant spectrum measured. The results show that the two filters transmit over 88% of a given wavelength at each wavelength chosen (at 480 nm 93%, 550 nm 88%, 646 nm 91% and 736 nm 89%).

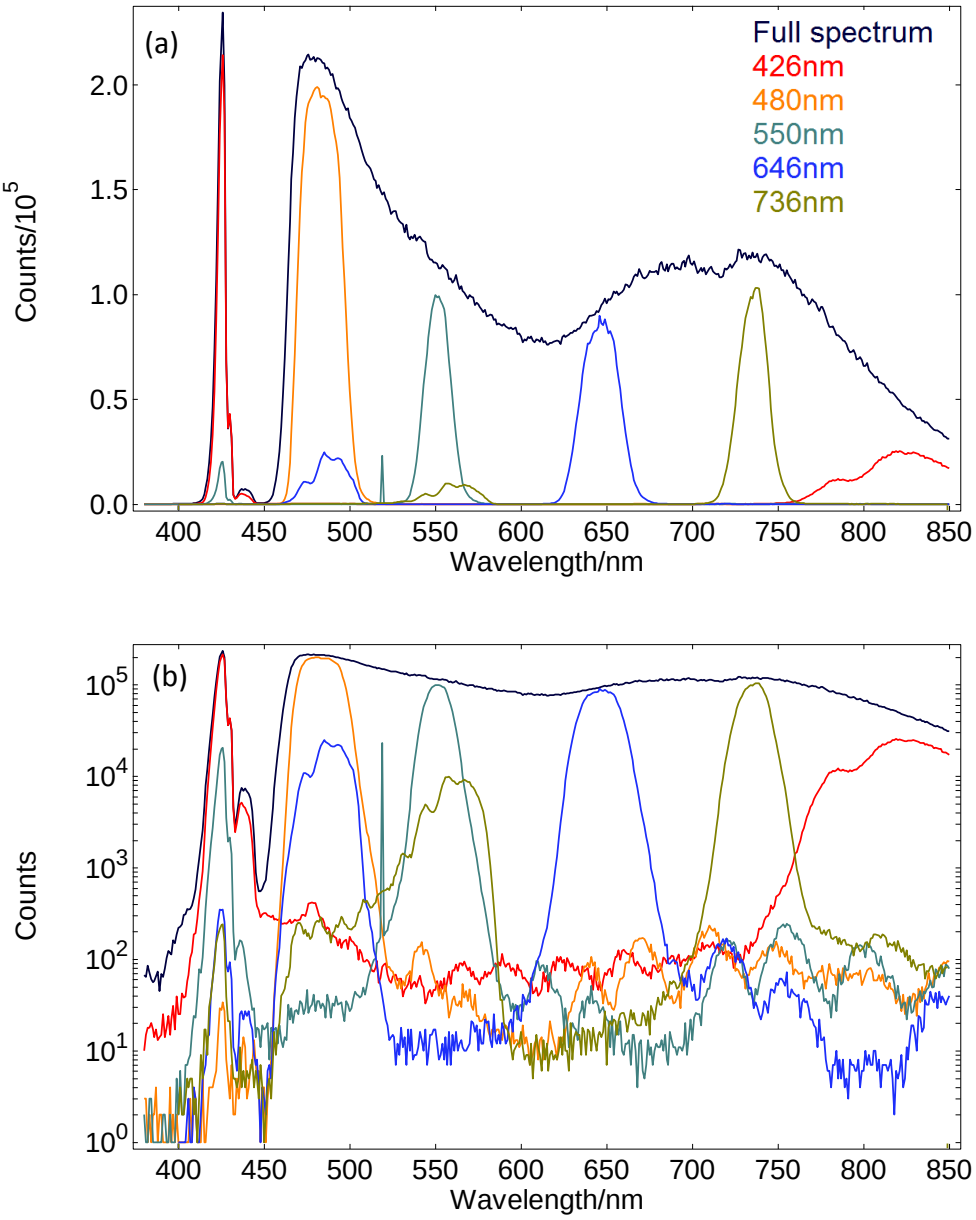

Figure 3.24 Scan of supercontinuum source through experimental setup with no filters (full spectrum) and at central transmission wavelengths of 426 nm, 480 nm, 550 nm, 646 nm and 736 nm (a – linear; b – semi-log)

The manufacturer's stated transmission data for the filters are shown in Figure 3.25 and Figure 3.26. It can be seen that, although the theoretical curves do show some out of band transmission, the measured data appear to be worse than the theory.

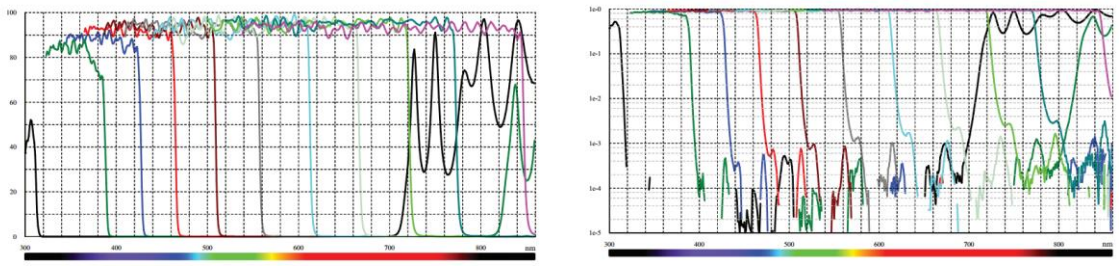

Figure 3.25 Theoretical transmission curves for similar SWP filter at various positions. Source: www.delta.dk

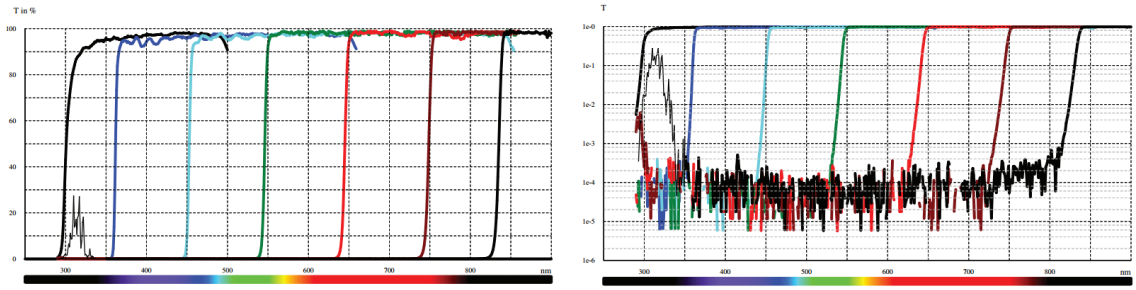

Figure 3.26 Theoretical transmission curves for similar LWP filter at various positions. Source: www.delta.dk

Measurements were then made using the wedge interference filters to check the effect on bandwidth of altering the offset between the filters. The emission from the supercontinuum source was acquired (with both filters removed) between 590-700 nm using the setup shown in Figure 3.22. The filters were then both set to transmit at 645 nm. By controlling the positions of the filters with respect to each other, it was possible to alter the bandwidth of the radiation transmitted. Figure 3.27 shows that at 650 nm the bandwidth may be altered from 45 nm to 14 nm with a reduction in overall transmission from 95 % to 65 %. The higher value tallies with the manufacturers specifications of >92 % for each filter in the region 500 – 850 nm. The reduction is transmission is due to the overlap in band edges.

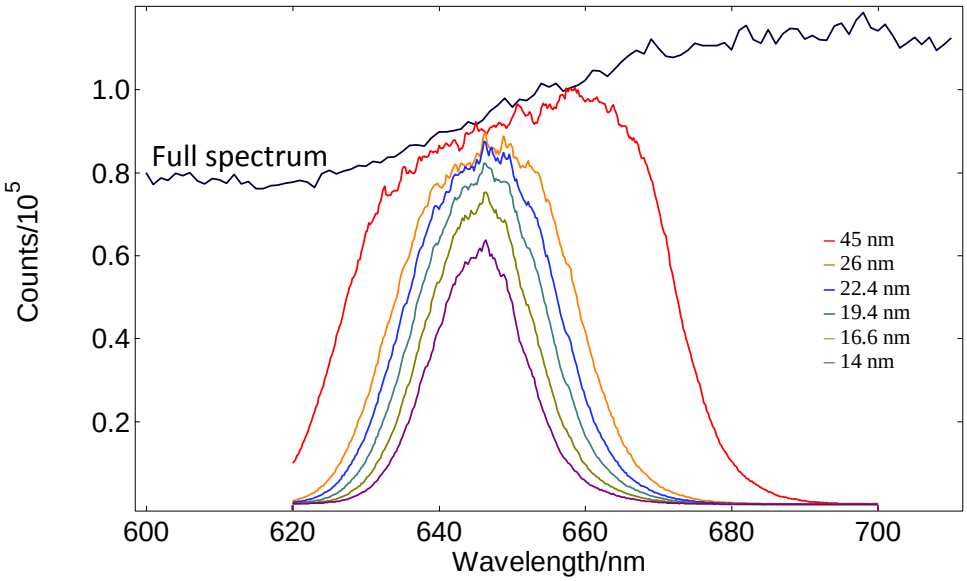

Figure 3.27 Bandwidth control using two wedge interference filters at: $\Delta\lambda$ = 45 nm, transmission = 95 %; $\Delta\lambda$ = 26 nm, transmission = 90 %; $\Delta\lambda$ = 22.4 nm, transmission = 89 %; $\Delta\lambda$ = 19.4 nm, transmission = 84 %; $\Delta\lambda$ = 16.6 nm, transmission = 76 %; $\Delta\lambda$ = 14 nm, transmission = 65 %.

The results show that by using a simple software program it is possible to control the filters in such a way as to alter the central wavelength and bandwidth transmitted. In addition, the transmitted beam remains collimated, diffraction limited and >88 % of a selected wavelength is transmitted.

The stray light suppression of unwanted wavelengths approaches 1 part in 10^3 over a large part of the range (Figure 3.24). There are two areas of concern when considering this device as an excitation source for fluorescence spectroscopy. At wavelengths ~100-150 nm below the central transmission band there is significant transmission. In addition, the physical part of the filter that transmits <450 nm also transmits significant radiation >750 nm. This would cause scattered light problems when exciting a sample below 450 nm and trying to measure the emission above 750 nm. In addition, measurements of fluorescence emission are almost always made at wavelengths above the excitation, often around 50-400 nm above. The residual throughput of the filters is likely to show up when measuring the fluorescence signal.

3.4.4 Measurements of wavelength selection using three wedge filters

Two Delta wedge filters (a SWP and a LWP) were placed close together at the first linear stage of the wavelength selection module. The two filters were arranged to throughput a reasonably broad spectral band (54 nm at 500 nm). An example spectrum is shown in Figure 3.28

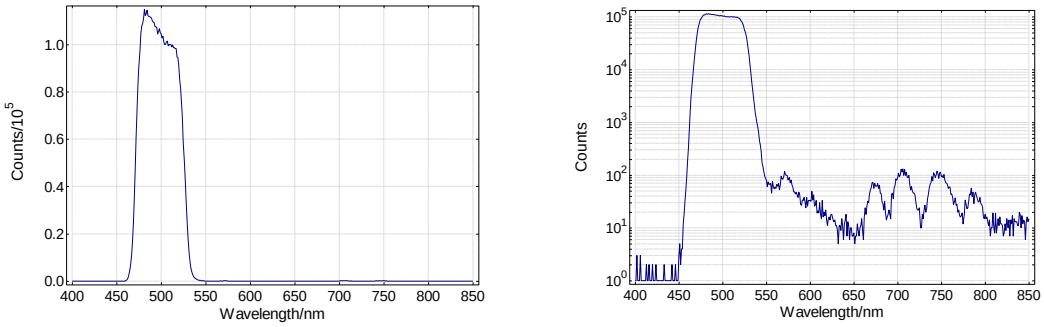

Figure 3.28 Throughput of one SWP and one LWP wedge interference filter attached to filter drive 1 and arranged to have a bandwidth of 54nm at 500nm

With the pass band set to 500 nm, the out of band suppression is greater than 10^3 over the entire measured range (similar to the measurement with a central wavelength of 480 nm shown in Figure 3.24.

A second SWP filter, was connected to the second stage and controlled by the software. An additional SWP filter was chosen as, in fluorescence spectroscopy, it is important to have spectrally purity in the region where the fluorescence emission is to be measured. By moving this across the pass band created by the first two filters, the transmitted pass band was reduced from 54 nm to 7 nm

The extra filter also increases the out of band suppression to greater than 10^4 (outside the pass band of the first two filters).

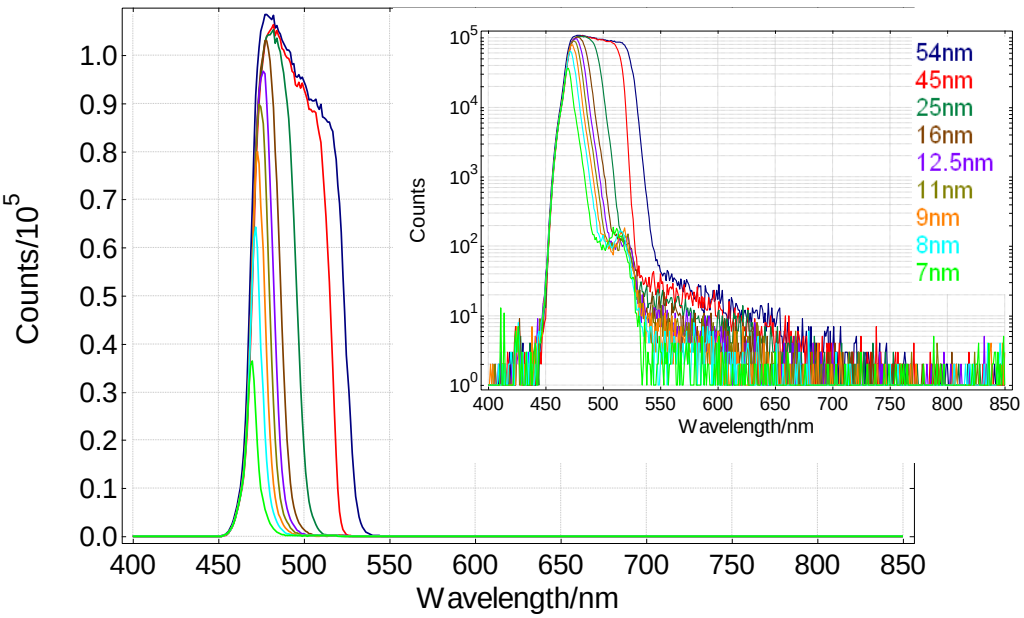

Figure 3.29 Bandwidth control of supercontinuum throughput by moving the SWP wedge filter connected to filter drive 2 – centre wavelength 500 nm

With the first filter module set for a central wavelength of 690 nm, the bandpass (without the effect of the second filter module) is 31 nm. The reason for the difference is that the band edge of the wedge filters does not shift linearly with wavelength along the length of the filter. Using the second filter drive module allows the bandpass to be reduced to 11 nm with an alteration in transmission from 91-40 %, the out of band suppression is greater than 10^4 over the majority of the range (see Figure 3.30).

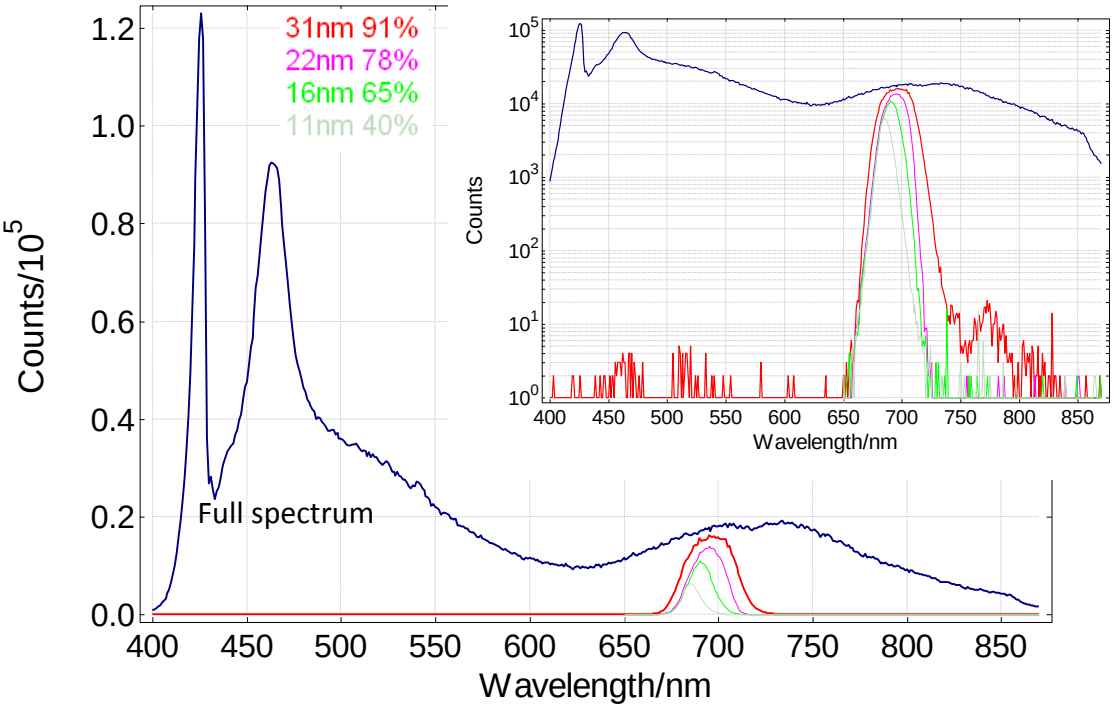

Figure 3.30 Bandwidth control of supercontinuum throughput by moving the SWP wedge filter connected to filter drive 2 – centre wavelength 690nm

In order to test the performance of the filter device at the blue extreme of the supercontinuum radiation, the filters were used to select a wavelength at the blue edge of the supercontinuum output (403 nm). The filters in the first filter drive were left unchanged with respect to each and the second filter drive was used to reduce the pass band to 10 nm. Figure 3.31 shows that the out of band suppression was between 10^3 and 10^4 over the range up to 719 nm. However, because the amount of light available from the supercontinuum is low at 403 nm, there is unwanted wavelengths transmitted by the filter at up to 5 % of the transmitted light. In addition, above 719 nm the supercontinuum throughput is high enough to exceed the desired wavelength.

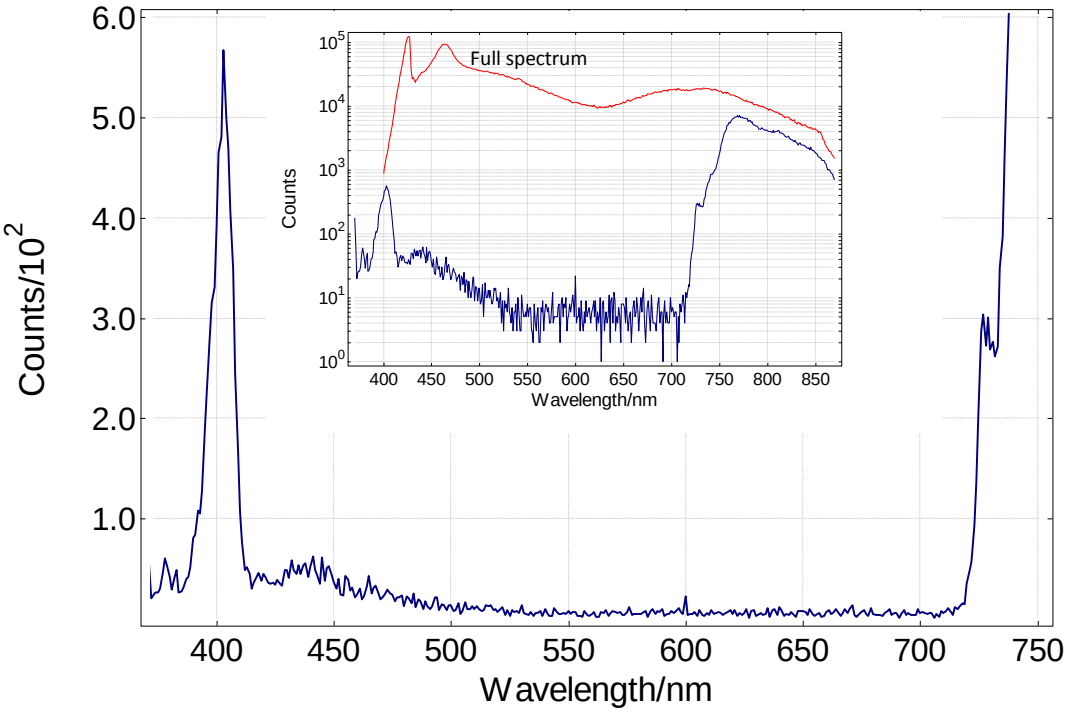

Figure 3.31 Wavelength suppression at 403 nm throughput

3.4.5 Improved method of wavelength selection using three wedge filters

In order to improve the results obtained from the previous prototype. A new prototype wavelength selector was designed with various new features (Figure 3.32 and Figure 3.33). The supercontinuum has significant NIR output well beyond the blocking range of the SWP wedge filter (as shown in Chapter 2). In order to block this radiation the incoming supercontinuum beam was reflected off two cold mirrors (Edmond Optics). A further consideration was that the filters were tilted to avoid retro-reflections back into the fibre and between the filters Tilting the filters has the effect of altering the path length and therefore shifting the edge (however, as the filter position is calibrated it does not alter the result). To speed up the movement time between wavelengths the filter drive mechanism was changed from a lead screw to a belt drive. In addition, lenses were fitted to improve the minimum transmitted bandwidth.

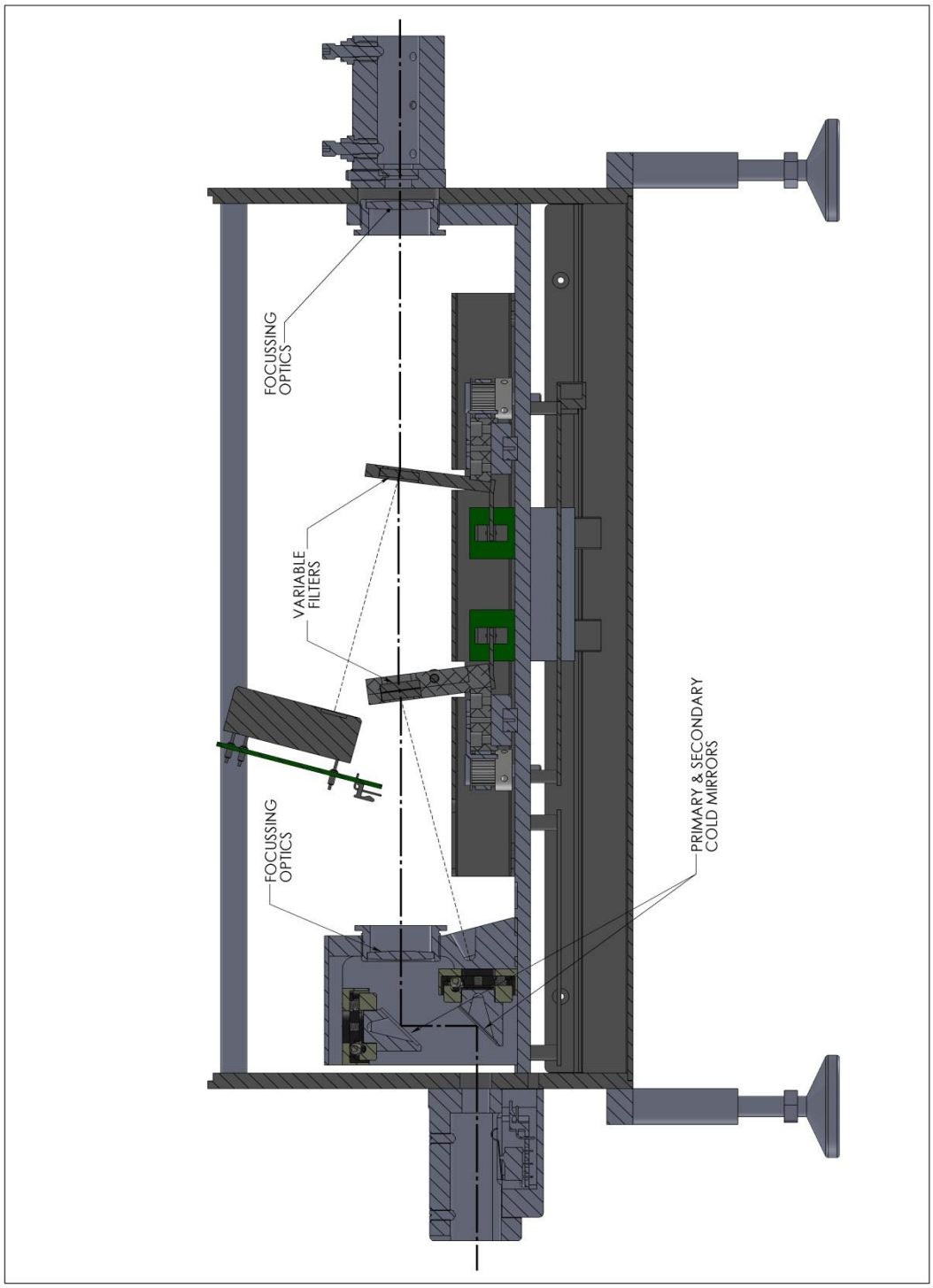

Figure 3.32 Second prototype wavelength selector design schematic

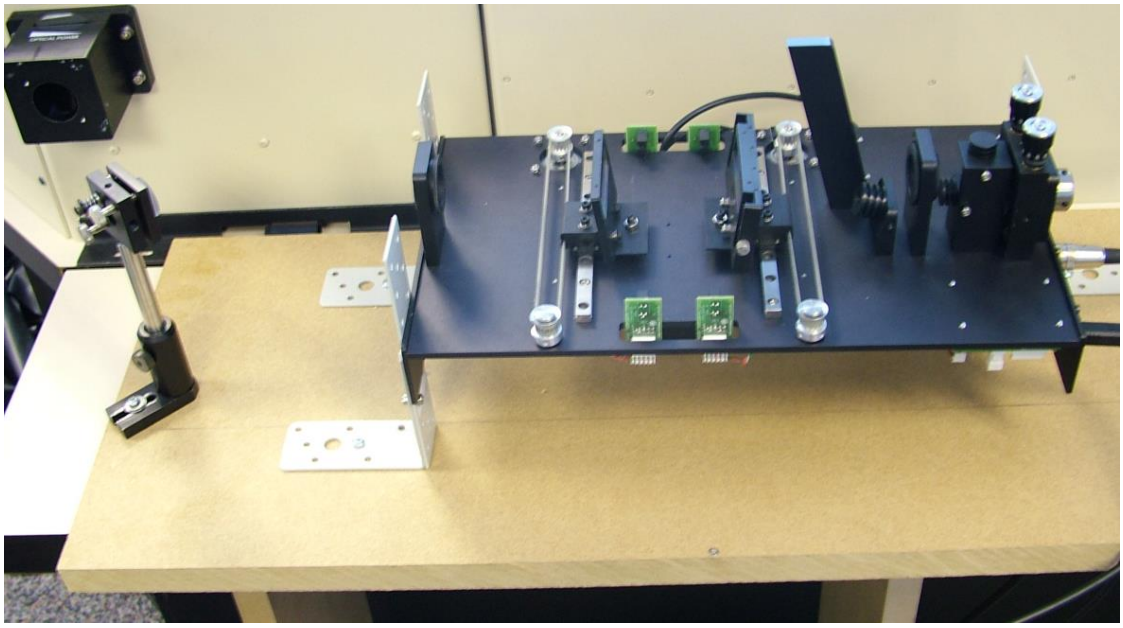

Figure 3.33 Second prototype wavelength selector rig

Lenses

In order to achieve the sharpest transmission band edge from an interference filter parallel light should be used as discussed in Section 1.4.6 and [68]. However, the layer thickness of standard interference filters does not vary with position. In wedge shaped interference filters, reducing the size of the radiation spot on the filter (in the long axis) should have the effect of reducing the width differential of the layers and therefore narrowing the bandpass.

To test this the supercontinuum source was focused through a lens with a focal length of 150 mm. A LWP wedge filter was then placed at various distances from the lens. Figure 3.34 shows how the band edge is sharper when the lens is used and how the band gets sharper as the filter is moved closer to the focus. At distances beyond 90 mm there is little extra benefit. This corresponds to a beam size with a diameter of 420 μm. Figure 3.35 shows the relationship between beam diameter incident on the filter and the 10 % - 90 % transition width of the filter, showing the initial steep decrease when the width is reduced from 1200 μm to 600 μm, then a much shallower decrease to 110 μm. The prototype was thus designed with the first filter module 90 mm from the lens and the second filter module after the focus 210 mm from the lens (where the beam size should be roughly the same). A second lens was then placed 300 mm after the first lens to re-collimate the beam (Figure 3.32).

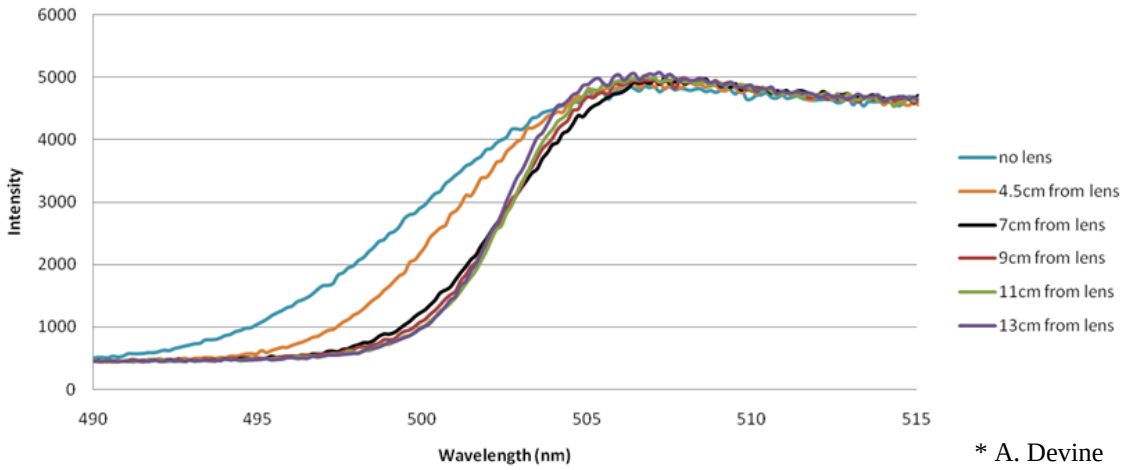

* A. Devine

Figure 3.34 The sharpness of the transmission band edge of the LWP wedge filter placed in converging supercontinuum radiation at various distances from the focusing lens.

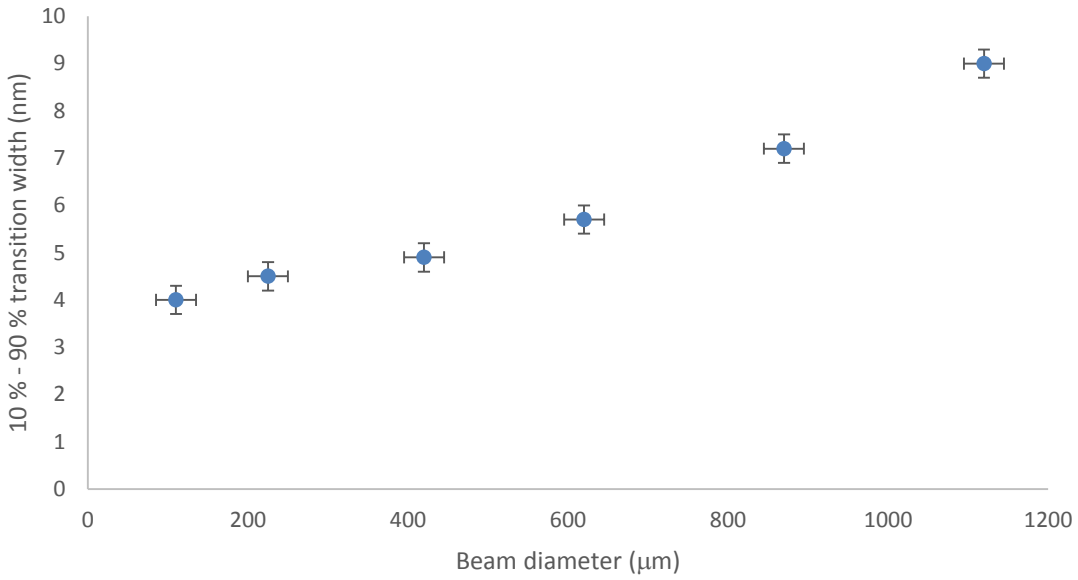

Figure 3.35 Effect of spot size on 10 % - 90 % transition width at 532 nm

To test the effect of the lenses on the minimum achievable bandpass and the transmission of the device, the new device was used in conjunction with the spectrometer used in the previous experiments (Figure 3.22). The first filter module was set with a centre wavelength of 650 nm then, with no lenses in place, the second filter module was moved in order to reduce the bandwidth transmitted. By moving both filters out of the beam for comparison, the transmission of the device could be measured (not including the effect of the cold mirrors). The lenses were then fitted to the device and the experiment was repeated. For comparison, the measurements were also made at 650 nm. Figure 3.36 shows the effect of the using the lenses in the system. Using lenses results in a significantly narrower bandwidth for a similar level of transmission and a narrower minimum bandwidths. For example, at 460 nm with a transmission of 75 %, a bandwidth

of 14.5 nm can be achieved without lenses, however, using lenses, a similar 72 % transmission a bandwidth of 6.5 nm is possible.

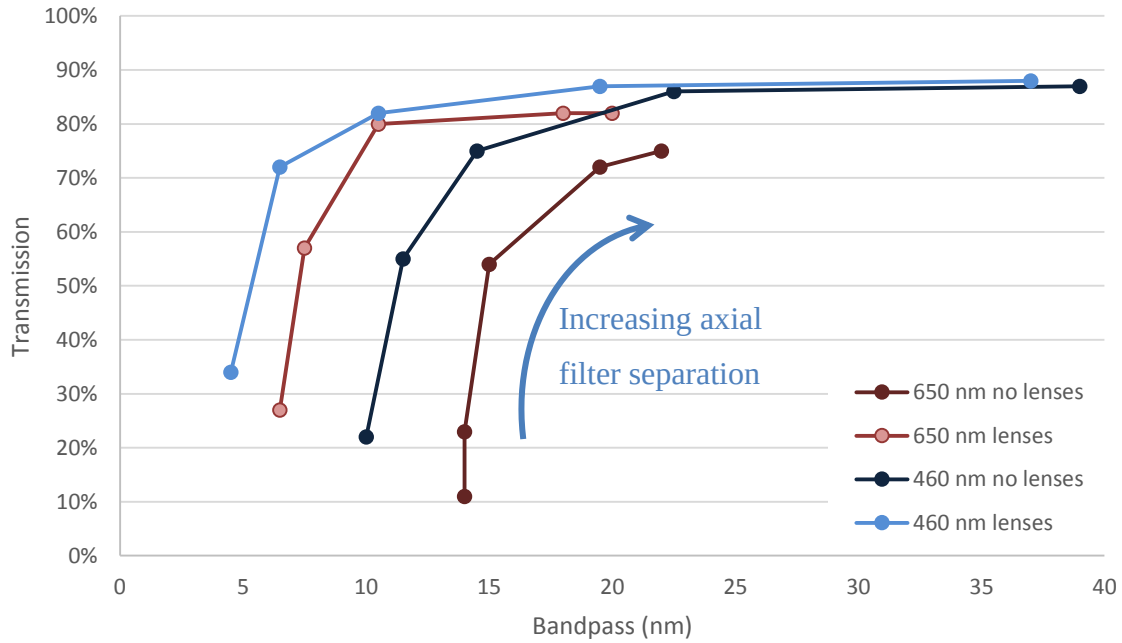

Figure 3.36 The effect of using lenses in the prototype on bandpass and transmission. The filters were moved across the beam in order to shift the band edges

3.4.6 Software

Figure 3.29 shows how by only moving the second filter module to control the bandwidth, the central wavelength also changes. For use as an excitation source in a fluorescence spectrometer, a user would wish to select a central wavelength and bandpass i.e. to change the bandpass both filters should move in a similar manner to slits in a grating monochromator. The band edge does not move linearly with position and the sharpness also has a wavelength dependence to add further complexity.

An algorithm was developed to take account of the filter characteristics. The method that was found to work best was to characterise the edge of each filter independently at two different wavelengths. The emission monochromator of the fluorescence spectrometer that the device was connected to was set to a discrete wavelength in the blue. The SWP filter was removed from the beam and the LWP filter was scanned across the supercontinuum. The 10 %, 50 % and 90 % transmission positions were then entered into the software. This was repeated in the red part of the spectrum and then the whole process was repeated for the SWP filter. The second SWP filter was not calibrated, therefore the

bandpass control only worked up to the maximum passband of the first SWP and LWP filter set – normally set around 50 nm. The calibration graphical wizard is shown in Figure 3.37.

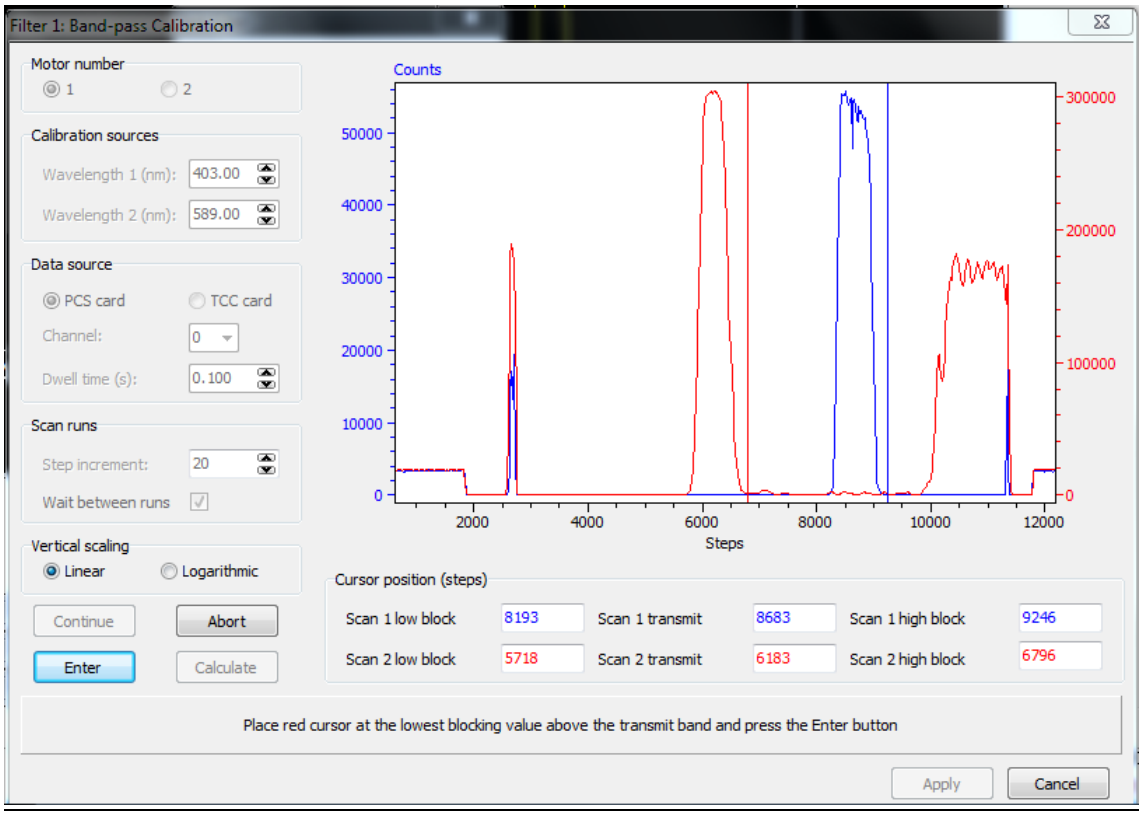

Figure 3.37 Filter module calibration screen

Linear trend lines were then used to plot the movements of the low mid and high transmission of the filters. This allowed the central wavelength and bandpass to be estimated for any two filter positions. A Graphical User Interface (GUI) was then written to allow selection of centre wavelength and bandwidth (Figure 3.38).

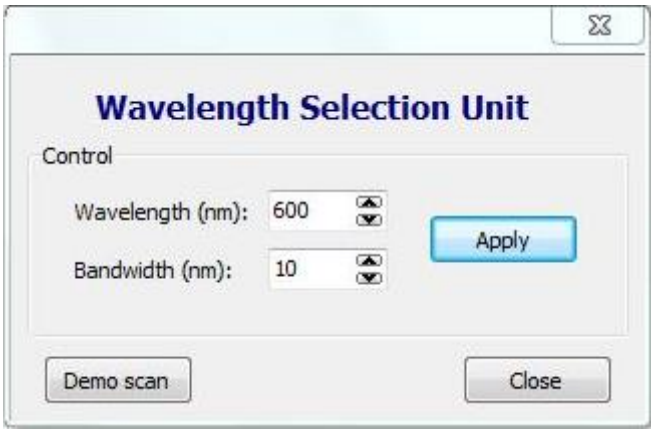

Figure 3.38 Software GUI for wavelength and bandwidth control of the supercontinuum radiation by the filter modules

3.4.7 Calibrated bandwidth measurements

The spectrum of the SC was measured with both filter modules out of the supercontinuum beam (the cold mirrors remained in the beam so that only the visible spectrum was transmitted). The filters were then placed with centre wavelengths of 456 nm, 550 nm and 650 nm and the bandwidth tuned, the results are shown in Figure 3.39. Dividing the bandwidth scans by the measured supercontinuum spectrum gives the transmission of the filter at the different bandwidths (Figure 3.40).

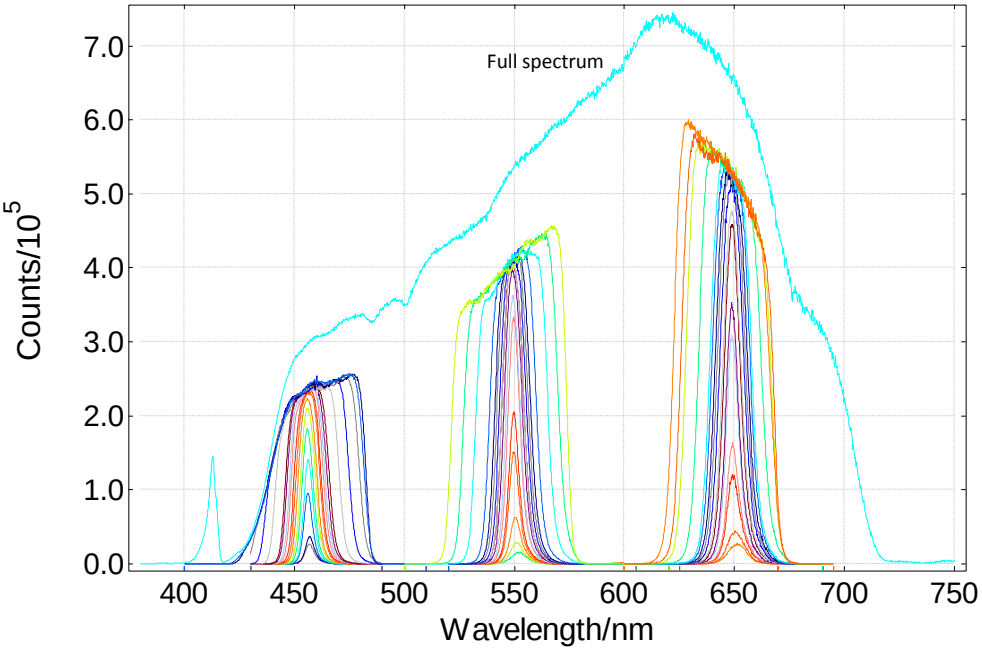

Figure 3.39 Supercontinuum spectrum through the prototype device without the filter modules and with and with the throughput set to 456 nm, 550 nm and 650 nm at various bandwidths

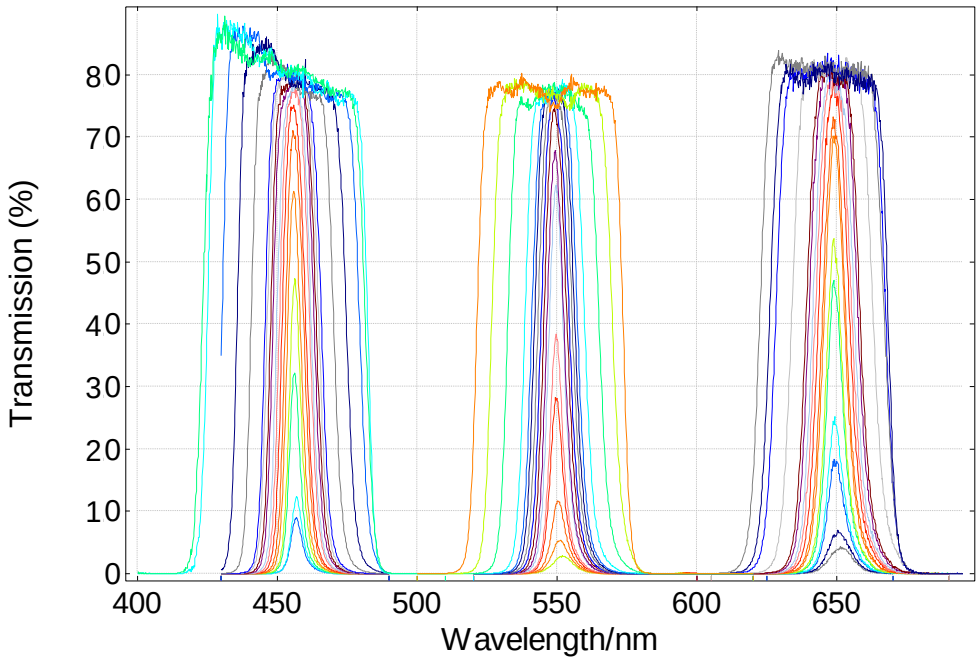

Figure 3.40 Prototype transmission scans at various bandwidths at 456 nm, 550 nm and 650 nm

The bandwidths are plotted against transmission in Figure 3.41. This shows that the transmission is fairly independent of bandwidth above 10 nm, where transmission is always greater than 75 %. Below 10 nm the bandwidth decreases rapidly and the minimum achievable bandwidth is narrower in the blue (because of the wavelength dependence of the band edges of the wedge filters). The lowest achievable bandwidths were 6.4 nm at 640 nm, 5.2 nm at 545 nm and 4.2 nm at 456 nm.

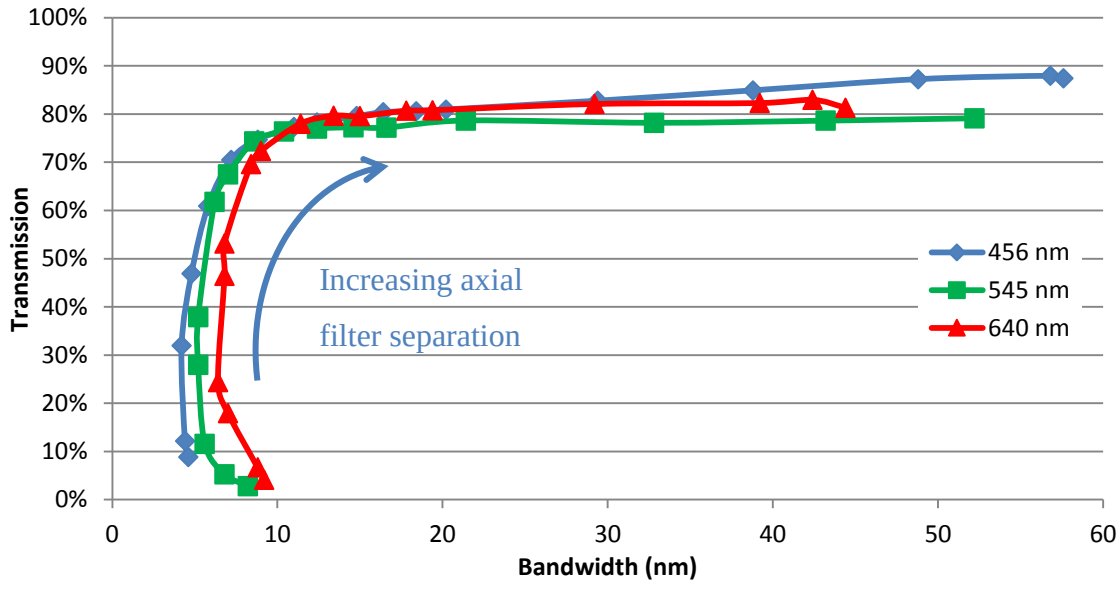

Figure 3.41 Bandwidth dependence on transmission at 456 nm, 550 nm and 650 nm

Broad bandwidth scan

For weakly fluorescing samples it can be useful to use a broad bandwidth for excitation. This is also a feature that is difficult to achieve with alternative methods of spectrally selecting a supercontinuum such as an AOTF. The maximum bandpass of the first filter module was increased (by moving the LWP and SWP filter apart from each other). This resulted in a maximum bandpass of 40 nm at 670 nm (the maximum bandpass is thus broader at lower wavelengths). The throughput was then measured with a broad bandwidth between 410 nm and 680 nm (Figure 3.42). The resultant transmissions are shown in Figure 3.43. The results show fairly constant transmission at wavelengths between 430 nm and 700 nm.

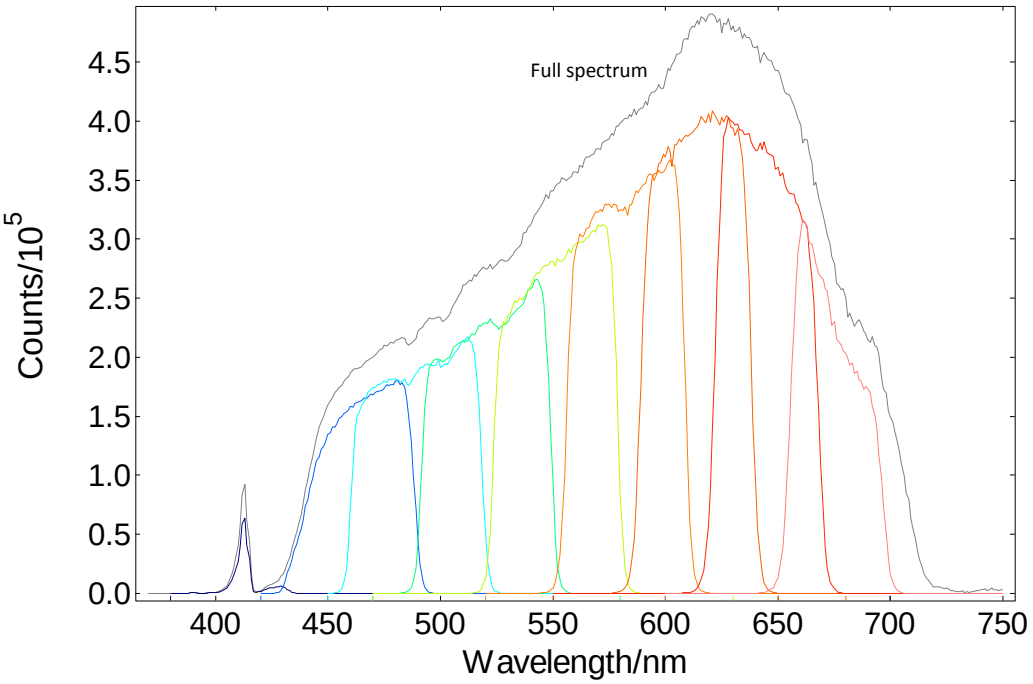

Figure 3.42 Supercontinuum spectrum through the prototype device without the filter modules and with broad bandwidths at 9 intervals along the spectrum

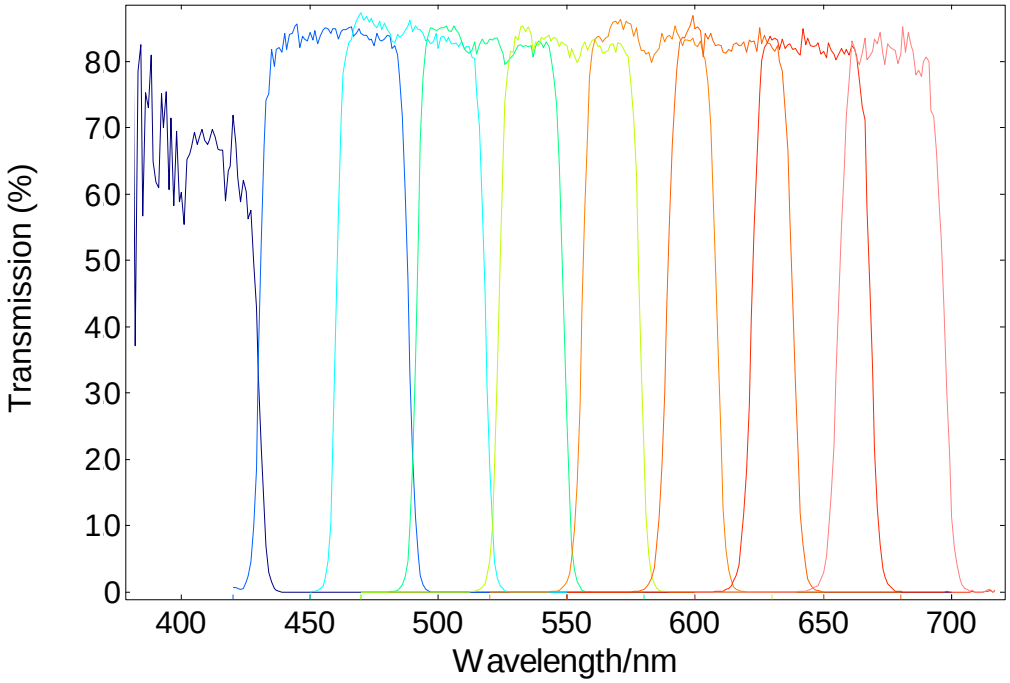

Figure 3.43 Prototype transmission scans with bandwidths >40 nm between 410 nm and 680 nm.

3.4.8 Average Power for Fluorescent Sample Excitation

In order to compare the optical power available for excitation of fluorescent samples, the experimental setup from Figure 3.23 was used. The prototype wedge wavelength selection device was set up with a bandwidth of 7.5 nm, the shape of the throughput at various wavelengths (measured with the emission arm of the spectrometer) is shown in Figure 3.44, with a diffuse scatterer placed at the sample position.

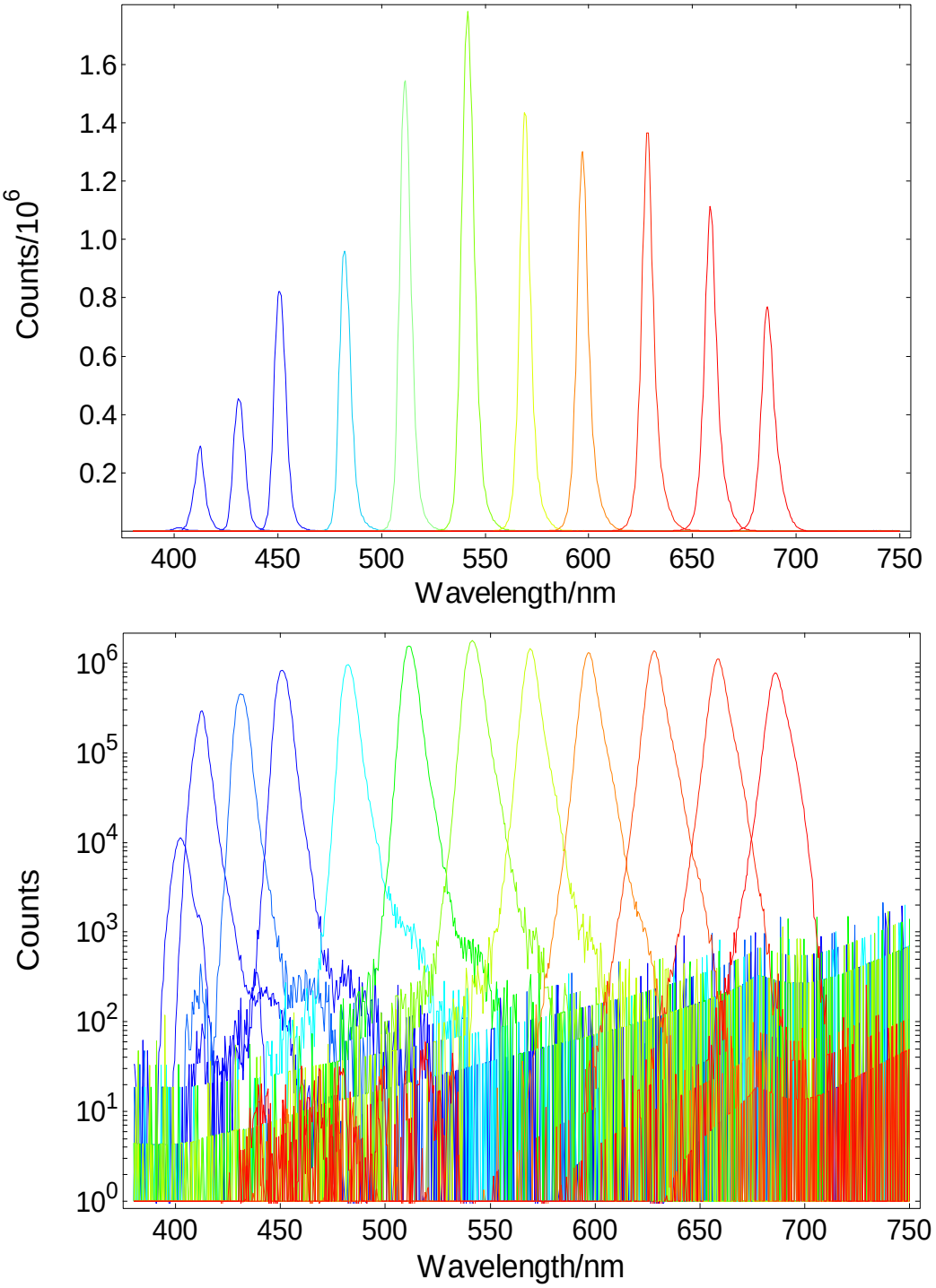

Figure 3.44 Spectral throughput of the prototype filter device with 7.5 nm bandwidth in steps from 402 – 686 nm (top linear, bottom semi-logarithmic scale)

A calibrated power meter was placed at the sample position and used to measure the average power of the light hitting the sample position from the spectrometers standard light source (450 W Xe900, Edinburgh Instruments) through a monochromator with the bandwidth set to 7.5 nm. This was compared to the average power from the prototype wavelength selector using a commercial supercontinuum source (Fianium SC-400) and the prototype UV supercontinuum device described in Section 2.3 (Figure 3.45).

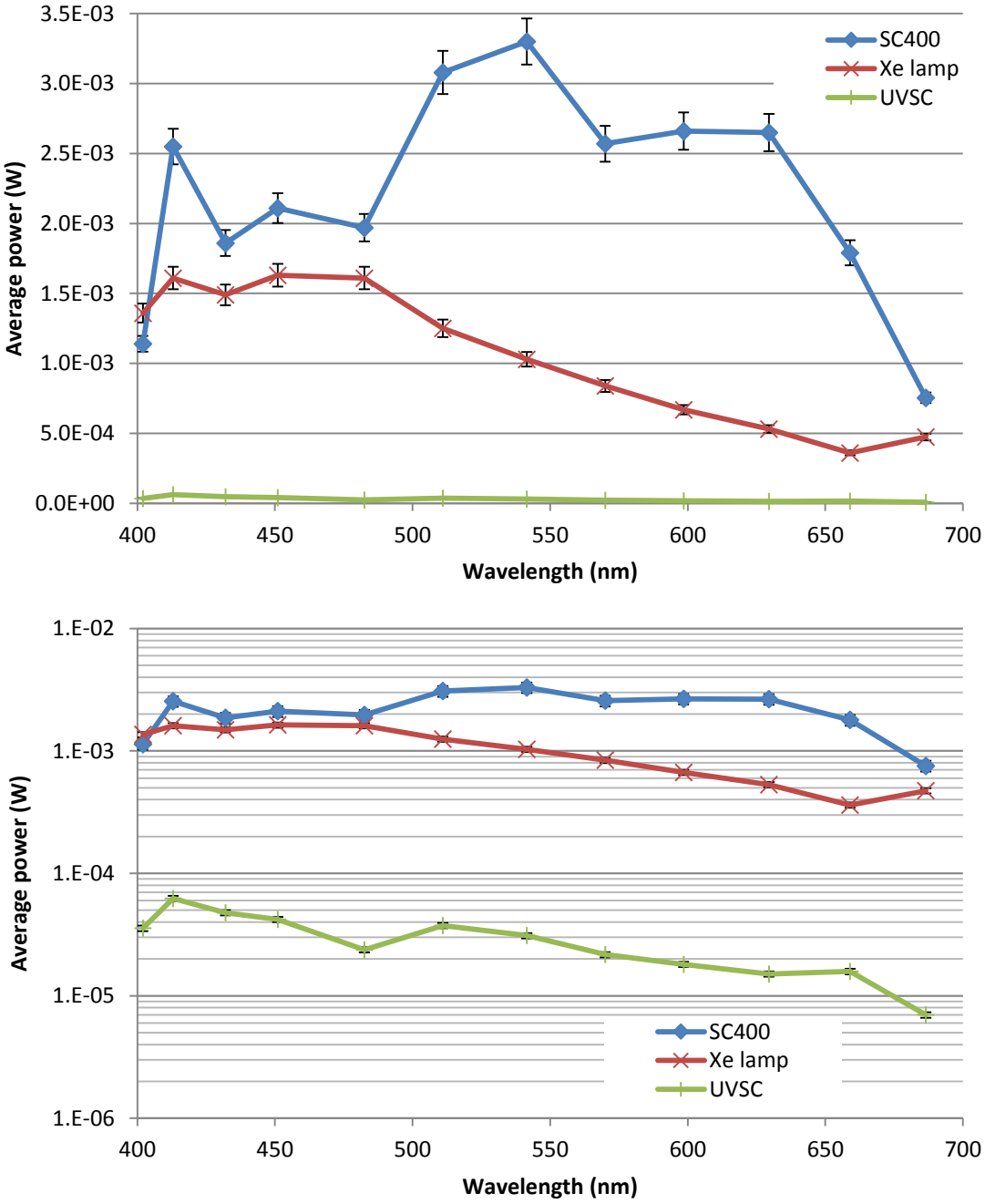

Figure 3.45 Average power available for sample excitation from 450-W xenon lamp and two supercontinuum sources through the prototype wavelength selection device and the standard excitation arm of a commercial spectrometer (bandwidth 7.5 nm)

The results show that the prototype wavelength selection device together with the SC-400 provides more excitation power across the full visible spectrum than the spectrometers standard excitation source when using a bandwidth of 7.5 nm. This can be contrasted with the results in section two when the monochromator was used for wavelength selection of the supercontinuum. In this case the supercontinuum provided more light when narrow bandwidths (1 nm) were used, but the xenon lamp provided more light when broader bandwidths were used (5 nm), as shown in Figure 3.46. This is due to the different spatial qualities of the sources (as discussed in Section 2.2.2)

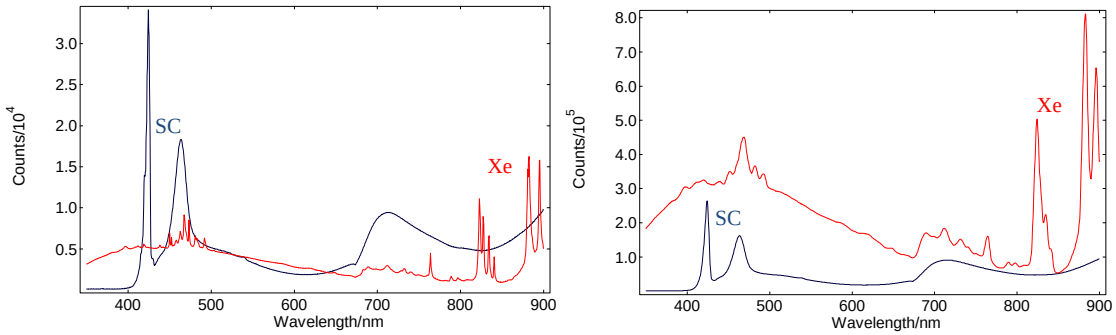

Figure 3.46 Intensity signal at the calibrated Si reference detector of fluorescence spectrometer. Monochromator bandwidth 1 nm (left) and 5 nm (right).

3.4.9 Triggering for fluorescence lifetime measurements

As discussed in Chapter 2, it is desirable when making fluorescence lifetime measurements using TCSPC, to trigger the electronics by the same wavelength as is used to excite the sample to avoid a wavelength dependence on instrument response temporal position. To achieve this with the wavelength selection prototype a high speed PMT (Hamamatsu, H7440) was positioned in the unit so that the light reflected off the filter in the second filter module was incident on the detector. Although the light used to trigger was not of exactly the same wavelength as the transmitted light, because the first filter module selects a pass band of light (that the second filter module modifies), the light used for triggering will normally be broader of a slightly higher wavelength than the light exciting the sample.

To measure the wavelength dependence of the width of the Instrument Response Function (IRF) of supercontinuum radiation through the prototype wavelength selection device the experimental setup from Figure 3.22 was used, with the spectrometers monochromator set to zero order (transmitting all wavelengths). The instrument response function of the system (including the source) was then acquired in steps from 400 – 740 nm. An intensity map of the measured instrument responses is shown in Figure 3.47.

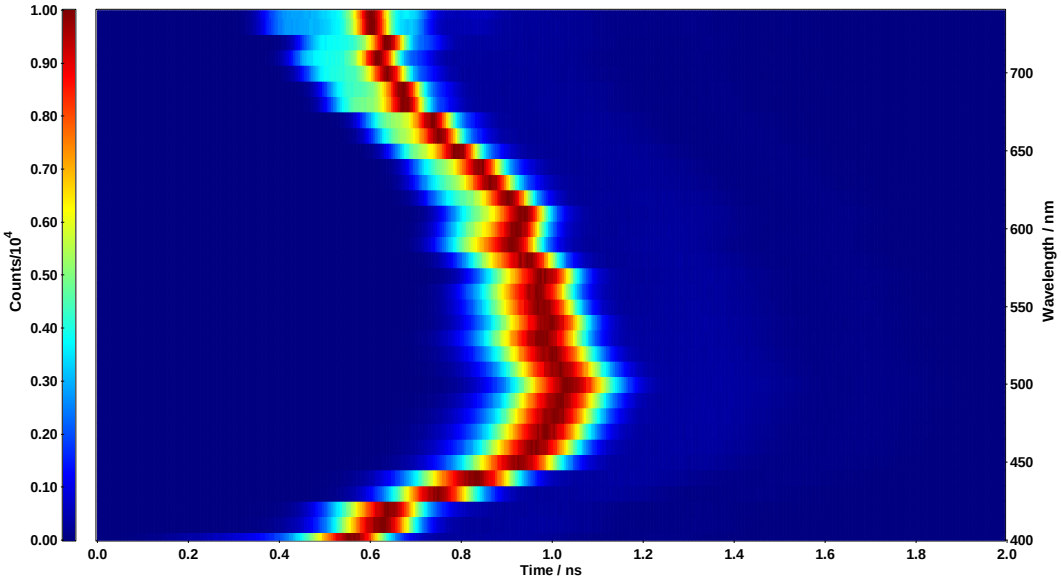

Figure 3.47 Intensity map of instrument response measurements of supercontinuum measured through wavelength selector. Parameters: 400 – 740 nm; 10 nm step; variable measurement time / step to 10'000 data points in the peak

The wavelength dependence of instrument response width and temporal shift have been calculated and are shown in Figure 3.48 and Figure 3.49 respectively. The error bars shown correspond to the smallest step size of the IRF data (4.88 ps)

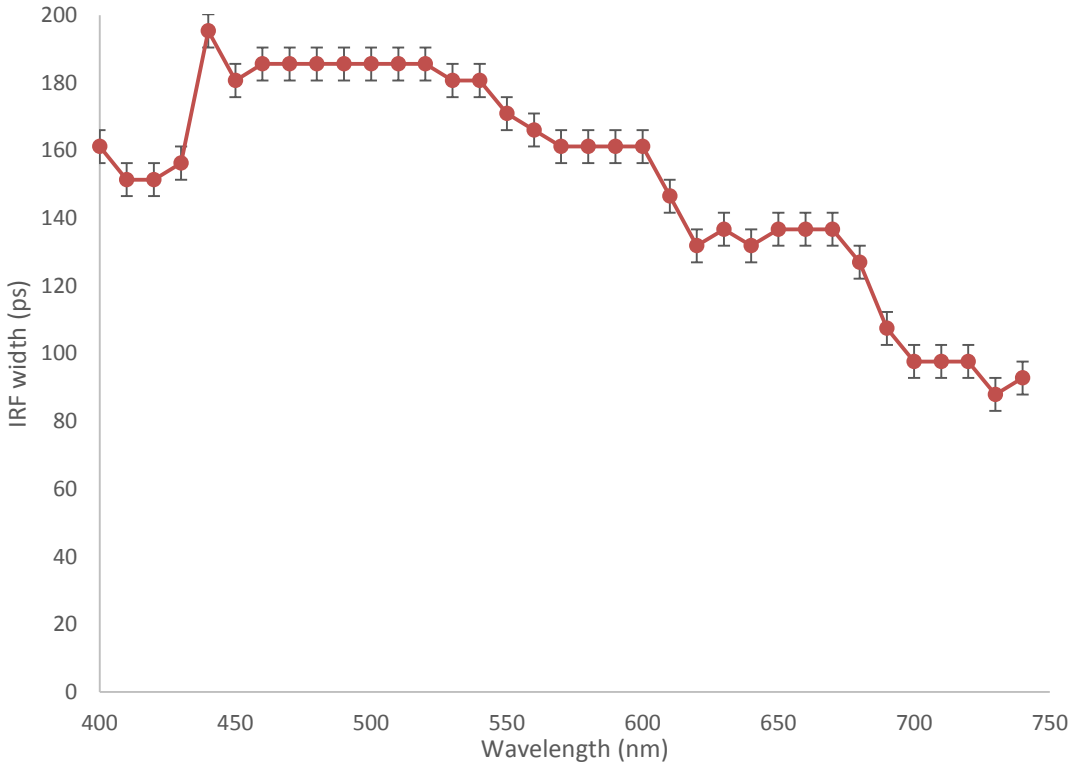

Figure 3.48 IRF pulse widths (FWHM) of supercontinuum source measured through the prototype wavelength selection device as a function of wavelength

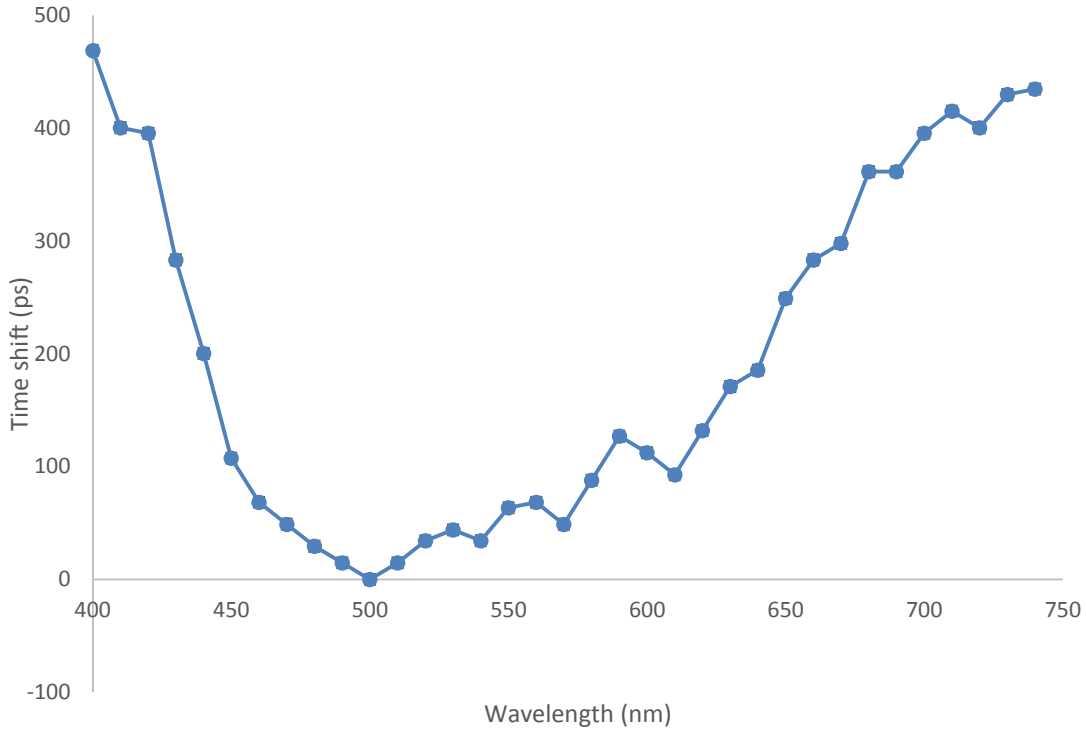

Figure 3.49 Pulse temporal shift of supercontinuum source measured through the prototype wavelength selection device as a function of wavelength

The measurements show the pulse position is relatively stable between 450 nm and 620 nm, however beyond either side of this wavelength the position has a strong wavelength dependence. The pulse width generally decreases with increasing wavelength from just under 195 ps at 440 nm to less than 92 ps at 740 nm. The large change in pulse position corresponds with the band edges of the filters. At the edge of multilayer filters there is strong group delay dispersion [35] (especially filters with hundreds of layers).The trigger is positioned before the last filter, therefore the change in pulse position in the blue and red edge of the spectrum (shown in Figure 3.49) could be partly down to the dispersion effects of the fibre.

3.4.10 Results and the use of the device for fluorescence lifetime measurements

In order to verify that the supercontinuum source with wedge interference filter based wavelength selection could be used as a light source in a commercial fluorescence lifetime spectrometer, the experimental setup used in Figure 3.22 was used to measure the temporal properties of some common fluorophores (that are used as benchmarks).

Erythrosin B is an organoiodine compound with an absorption maximum of 530 nm and a fluorescence lifetime that is solvent dependent. In water it is known to have a

fluorescence lifetime of 89 ±3 ps [105]. These parameters make the lifetime challenging to measure with a standard fluorescence spectrometer. The lifetime is faster than the instrument response from the majority of instruments and the absorption maximum is in a region that is not well served with high repetition rate pulsed light sources. The supercontinuum source with its narrow temporal response and strong output in the visible makes it ideal for measuring samples of this type.

A decay of Erythrosin B was acquired and analysed using the a dedicated fluorescence analysis program (FAST, Edinburgh Instruments) and found to be 88 ±1 ps with a goodness of fit parameter (chi-squared) of close to unity and evenly distributed residuals (Figure 3.50). The lifetime was found by using Reconvolution analysis to take account of the effect of the IRF on the decay (the effect of the IRF can clearly be seen on the red decay data on Figure 3.50). Both fitting parameters indicate a good match of data and lifetime value. The result shows that the excitation light was successfully suppressed (as a single exponential lifetime was acquired), it also shows that high quality decay data can be acquired for samples that decay faster than the IRF of the system.

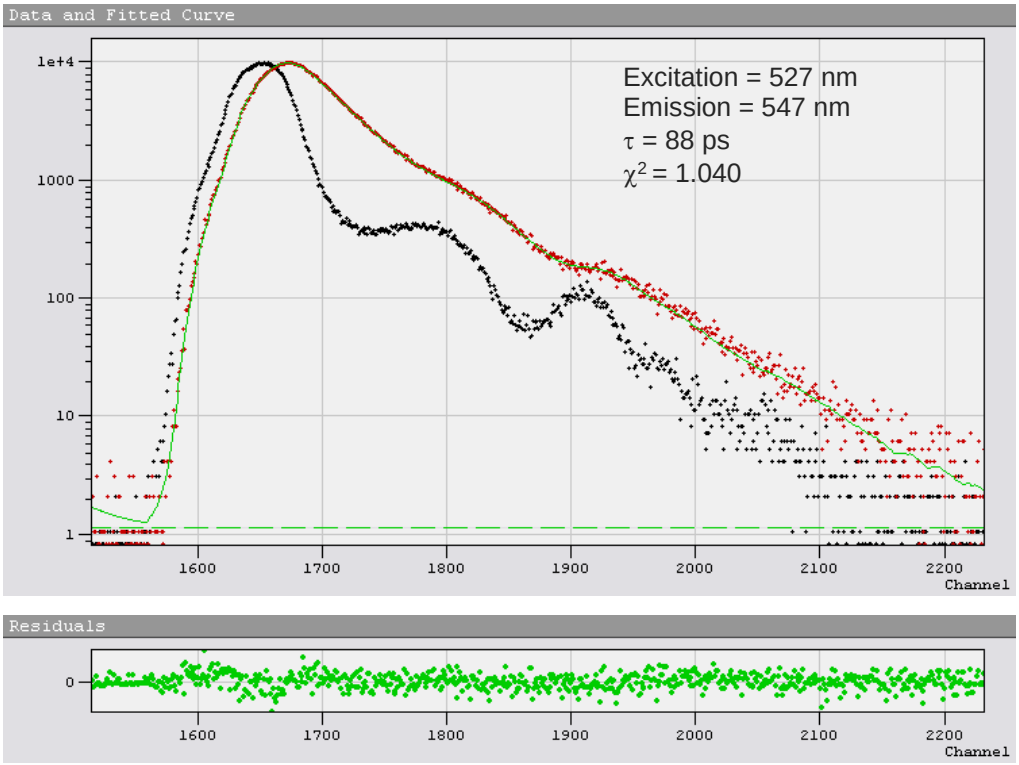

Figure 3.50 Erythrosin B in water fluorescence decay

Measurements of fluorescence anisotropy are a powerful tool for biomedical research [5]. The measurements involve measuring the extent of the polarisation of the fluorescence emission from the sample. Measuring the time dependence of this (the anisotropy decay)

gives information about a molecules shape and environment by way of the rotational diffusion time.

To measure the fluorescence anisotropy the sample has to be excited with vertically polarised light and the difference between vertical and horizontally polarised emission compared as a ratio to the total sample emission (Equation (3.4). A correction factor (the G factor) also has to be measured to correct for any polarisation dependence of the emission monochromator. The corrected anisotropy then becomes Equation (3.5) (where G is the ratio of vertical to horizontal emission with horizontal excitation - $\frac{I_{HV}}{I_{HH}}$).

$$r = \frac{I_{VV} - I_{VH}}{I_{VV} + 2I_{VH}} \qquad (3.4)$$

$$r = \frac{I_{VV} - GI_{VH}}{I_{VV} + 2GI_{VH}} \qquad (3.5)$$

Rhodamine B is a common fluorophore with an absorption maximum at 543 nm (a region not well served with high repetition rate excitation sources). Because the radiation from the supercontinuum source is unpolarised a Glan-Thomson polariser in a motorised mount was fitted to the excitation arm of the spectrometer (before the sample). To analyse the polarisation of the emitted light a second Glan-Thomson polariser was fitted in the emission arm. The unpolarised nature of the supercontinuum radiation meant that the spectrometer was able to be used to automatically measure the horizontally and vertically polarised emission from the sample under with vertical excitation (Figure 3.51) and the G-factor correction with horizontally polarised excitation. This allowed the anisotropy decay to be calculated (Figure 3.52).

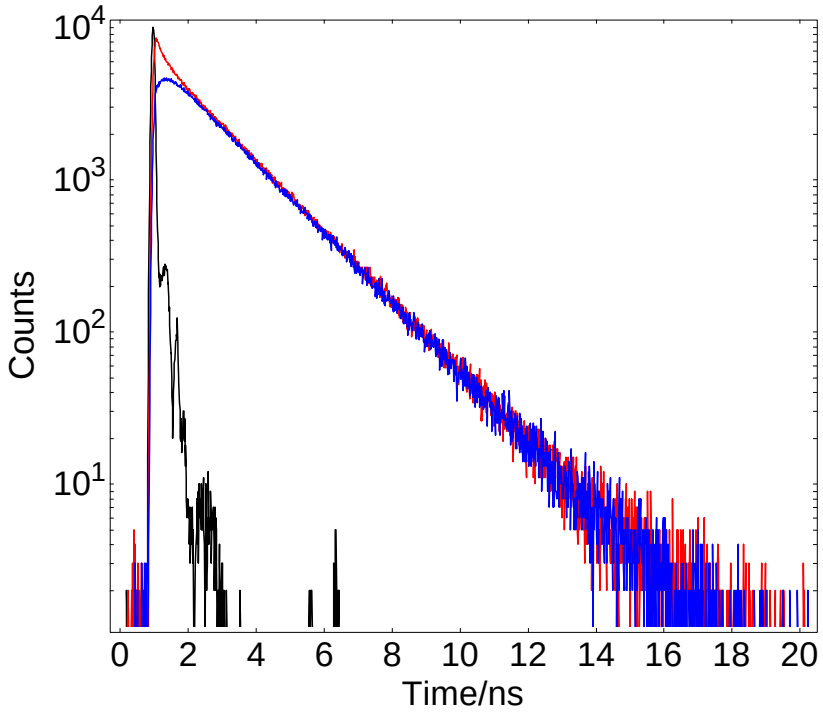

Figure 3.51 Rhodamine B polarised decays. Excitation 540 nm, emission 565 nm. Red – vertically polarised excitation, vertically polarised emission. Blue – vertically polarised excitation, horizontally polarised emission

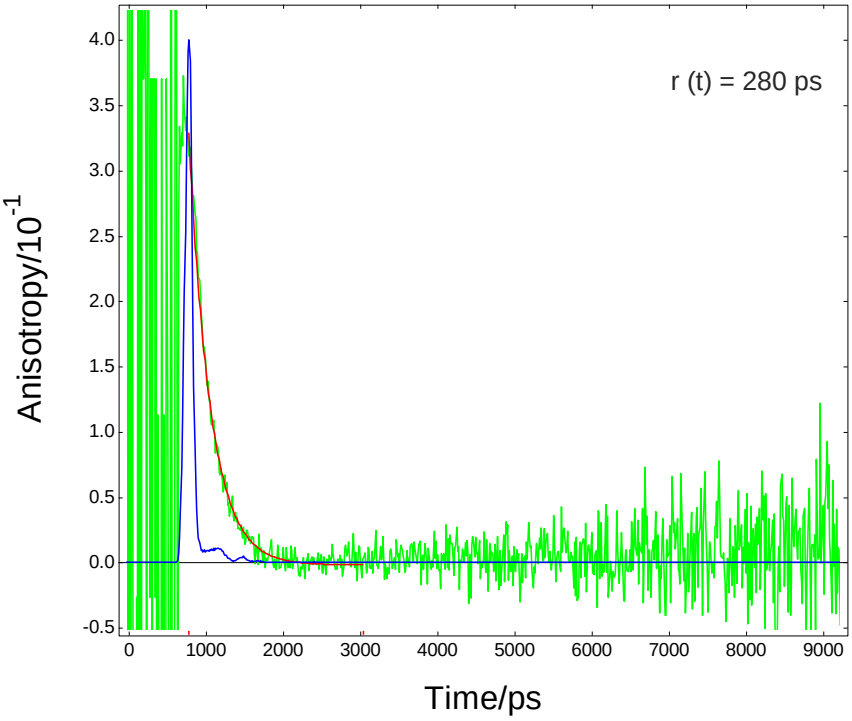

Figure 3.52 Rhodamine B anisotropy decay (green), fit (red) and IRF (blue)

3.4.11 Conclusions

A prototype device for wavelength selection of supercontinuum radiation was designed, built and tested. Three approaches with wedge interference filters were tried: one fixed bandpass filter, two filters (one SWP and one LWP) and three filters (two SWP and one LWP).

Proof of principle experiments were carried out by building a simple fluorescence spectrometer with a laser excitation source and a moving fixed bandpass wedge filter for emission wavelength tuning. Results were obtained similar to those obtained with a commercial fluorescence spectrometer for some standard fluorophores. The device was used for wavelength separation of a supercontinuum. This also worked well, however, the sharp peaks in the supercontinuum spectra (caused by the various nonlinear effects – see Section 1.3), meant that the bandwidth fluctuated with wavelength.

Using two edge filters one SWP and one LWP, with sharp transitions and having their lateral position controlled separately allowed the transmission wavelength and bandpass to be controlled by moving the filters with respect to each other. This also worked well however, the stray light suppression was limited, therefore it would be of limited use for fluorescence spectroscopy, where a highly pure monochromatic excitation source is required. Stray light suppression was found to be approaching 1 part in 10^3, however there was significant leakage above 750 nm.

A three filter device was then constructed and tested. This involved a SWP and LWP filter together with a wide bandpass, then a second SWP filter to adjust control the central transmitted wavelength and bandpass. The additional filter cleaned up the out of band transmission so that the resultant light was pure enough for fluorescence excitation. The stray light suppression was increased to 1 part in 10^4 outside of the pass band of the two filter and spurious light above 750 nm was removed. In addition lenses were used to reduce the size of the beam passing through the filter, although the non-parallel light would broaden the band of a filter, using a smaller spot had the overall effect of sharpening the band edges. This allowed a decrease in the minimum bandpass (from ~11 nm to ~4 nm).

As validation, the three filter device was used to measure some standard samples in fluorescence lifetime spectroscopy. The fluorescence anisotropy of Rhodamine B was measured, along with the fluorescence lifetime of Erythrosine B in water.

A wavelength separation device based on wedge interference filters was found to have distinct advantages over the alternatives (AOTFs and grating based monochromators). These were mainly the combination of good stray light suppression, wide tunability across the visible region, continuous bandwidth control and a small form factor. In addition, the beam quality is maintained, meaning that the transmitted light can be focused back into a single mode fibre where necessary.

Further improvements have since been made to the prototype device and it has been productionised, and marketed as separate modules with two and three filter designs, depending on the application. These modules are sold for a variety of applications including fluorescence spectroscopy.

CHAPTER 4 - IMPROVED STRAY LIGHT REJECTION IN AN EMISSION MONOCHROMATOR

The most common problem encountered by spectroscopists when measuring fluorescent samples, especially if those samples are highly scattering or have a low quantum yield, is stray light. With modern high power light sources such as high power xenon arc lamps and supercontinuum sources and available for excitation, the limit on detection is generally not related just to the number of photons trying to be measured, but rather how well the signal can be discriminated from spurious signal. All monochromators allow other wavelengths to be transmitted alongside the desired wavelength [106]. Stray light can arise from any optical surface, light leaks, scattering baffles, etc., however, the primary contribution is the scattered light from the grating itself. There are two components [107] - a Lorentzian-type component and a constant background consistent with Rayleigh Scattering (which depends upon $(1/\lambda)^4$). Replica gratings are worse than originals and amplify the scattered light thus exacerbating the problem for lower cost instruments.

The ability of a monochromator to suppress the unwanted stray light is known as its stray light suppression. A common way to measure the stray light of a monochromator is to use a monochromatic light source such as a line from a mercury source or a laser and compare the transmitted wavelength at the peak with wavelengths away from the nominal bandpass set for the monochromator. The resultant ratio is the figure for stray light suppression. This figure is only of limited use however, as the measurement to which it pertains is not a real-life use of a monochromator in a fluorescence spectrometer. In a fluorescence spectrometer the excitation monochromator selects a single wavelength from a polychromatic source and the emission monochromator is used to measure spectra in the presence of many other wavelengths of light (the excitation wavelength, other emission bands). In addition the stray light suppression of a monochromator changes with wavelength and slit bandwidth and it is generally worse in the UV as there is more Rayleigh scattering.

The most typical measurement of the sensitivity of a fluorescence spectrometer is the signal to noise ratio measured using the Raman band of water (see Section 2.2.1). Pure water is excited at 350 nm and the Raman signal is monitored at 397 nm. The ratio of this signal to the RMS noise of the background (measured at 450 nm) gives the water Raman signal to noise ratio. In spectrometers employing single photon counting (SPC)

electronics the only noise is photon noise (which is characterised by a Poisson distribution) [16]. A Poisson distribution has a standard deviation equal to the square root of the number of events [108] therefore the RMS noise can be approximated to be the square root of the measured photon counts. The water Raman 'signal to noise ratio' is a figure of merit used by fluorescence spectrometer manufacturers as an indication of system sensitivity. The value is only of limited benefit as the measured figure often is more sensitive to the purity of the water used than the sensitivity of the instrument; however, the Raman scattering peak from water is weak, sample independent and gives a reasonable indication of a fluorescence spectrometers ability to supress unwanted Rayleigh scattered excitation light. Other measurements of sensitivity, such as lowest measurable concentration of a fluorophore tend to be even more sample dependent – in preparing ultralow sample concentrations, sample preparation errors would introduce a large source of error.

Currently the best way to improve the stray light performance of a monochromator is to use a double monochromator. However, double monochromators add considerable expense and size to an instrument (Figure 4.1). Furthermore, at either extreme of the spectral range of a blazed grating, a monochromator's throughput drops off. This decrease in throughput is squared in a double monochromator.

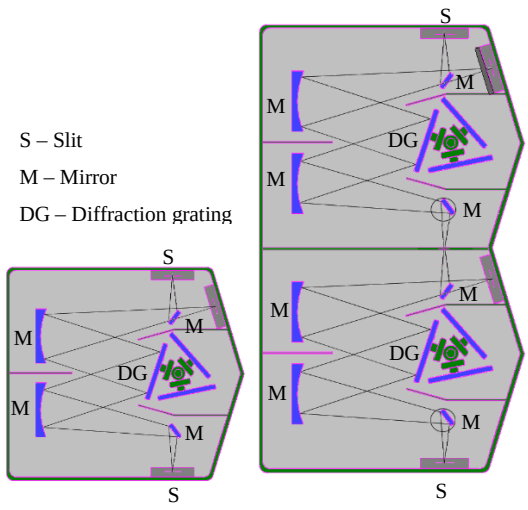

Figure 4.1 Complexity comparison between single monochromator (left) and double monochromator (right)

A device with a stray light suppression performance close to that of a double monochromator without the increased size and complexity could be useful for future generations of fluorescence spectrometers.

This chapter describes a prototype design for a fluorescence spectrometer employing a wedge interference filter alongside the standard emission monochromator. By employing two wavelength separation devices together (a grating monochromator with high spectral resolution and a wedge interference filter with high throughput) the advantages of both are exploited. The experiments were carried out as a proof-of-principle test of the feasibility of such a device.

4.1 Experimental Setup

A mount was designed and constructed in order to allow a variable interference filter to be mounted within the emission monochromator of a standard fluorescence spectrometer (Edinburgh Instruments, FLS920), Figure 4.2. The mount was connected to a 3-inch linear stage which was, in turn, connected to a stepper motor. The stepper motor was powered and controlled by the spectrometer controller (CD920). Edinburgh Instruments' standard spectrometer software (F900) was altered so that the filter was able to be moved as a proxy for a monochromator. The bandpass variable interference filter (Veril S 60, Schott) was placed in the mount. This was the same filter as was used to measure fluorescence spectra in Section 3.2 and to select sections of supercontinuum radiation in Section 3.3. The filter has a specified spectral range of 400- 700 nm, a usable length of 38 mm, a dispersion of 6.0 – 7.9 nm/mm and an out-of-band blocking of <0.01 %

The FLS920 spectrometer consisted of a 450-W xenon lamp as an excitation source and single excitation and emission monochromators (300-mm focal length) fitted with 1800 g/mm diffraction gratings. The monochromators had a wavelength accuracy of 0.2 nm with 0.05 nm repeatability and stray light suppression of 10^5. The detector was a red sensitive photomultiplier tube, PMT (Hamamatsu Photonics R928P) cooled to have a dark count rate of less than 50 counts per second. The spectral range of the emission arm of the spectrometer was 200-870 nm

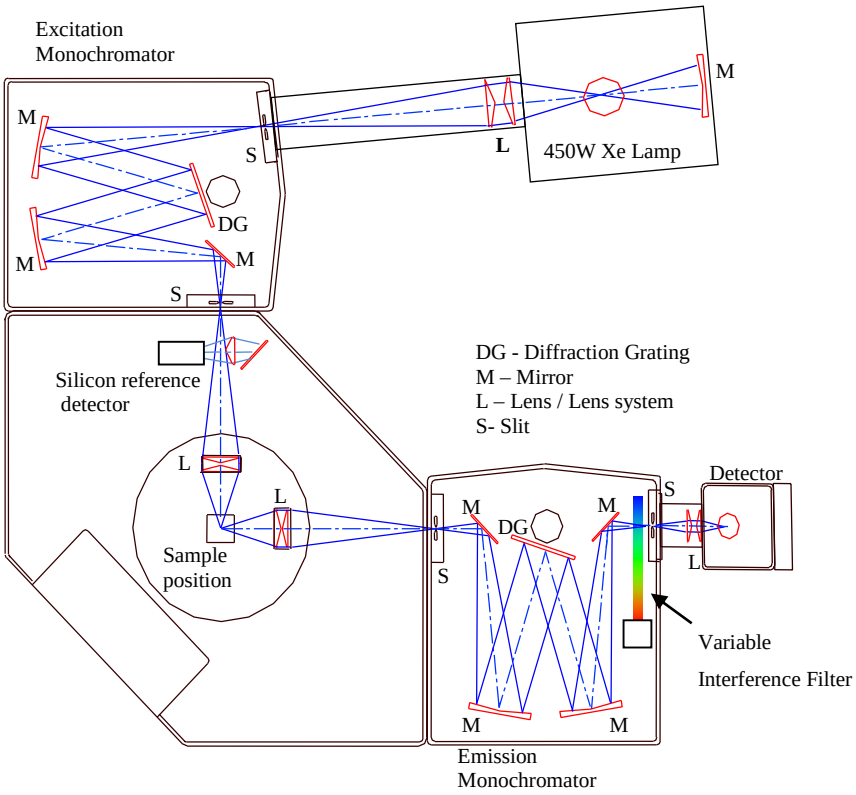

Figure 4.2 Standard fluorescence spectrometer with a variable interference filter

The interference filter was set up in the spectrometers control software (F900) to be a second emission monochromator, however, the spectrometer software was geared toward diffraction grating based monochromators, therefore it was not possible to calibrate the filter from within the software. Wavelength calibration of the filter drive was required to facilitate simultaneous scans of the grating and filter.

As shown in Section 3.2.1, the wedge bandpass filter was linear over the range 400-600 nm. A mercury lamp was used in order to calibrate the filter within the system. The mercury source was coupled into an optical fibre; the other end of the optical fibre was positioned in the sample position where sample emission would emanate, it was thus possible to scan the emission monochromator and measure the spectrum of mercury. Two scans were performed: firstly, with the variable filter moved out of the beam, the grating was scanned and secondly, with the grating set to zero order (so that the grating acted like a mirror reflecting all wavelengths), the filter was scanned. By overlaying the two scans, Figure 4.3, it was possible to match the mercury positions and thus calculate wavelength offset and step values to calibrate the filter and thus allow synchronous tuning of grating and filter.

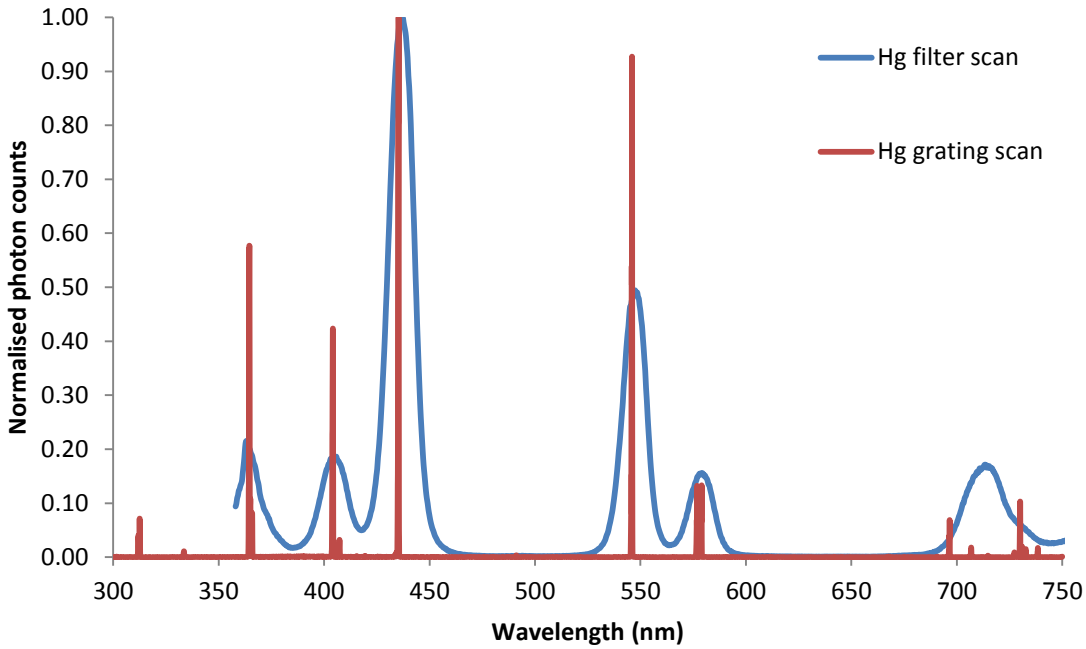

Figure 4.3 Linearity of filter compared to actual mercury line positions

The FWHM widths of the mercury lines measured by scanning the filter (Figure 4.3) are ~15 nm, meaning that the non-parallel nature of the light incident on the filter is not having an appreciable effect on the bandpass.

4.2 Filter transmission

The next stage was to measure the variation in filter transmission with wavelength in situ. In order to accomplish this a calibrated tungsten lamp (NPL traceable) was used. With the filter out of the emission monochromator, a scan of the lamp was made using high pass filters to remove second order effects where necessary (the effect of the filters were taken into account). The resultant scan was divided by the known spectrum of the lamp to give a correction file for the emission channel of the instrument. The resultant 'correction file' shows the sensitivity of the instrument with wavelength and includes detector response, monochromator and optical effects such as chromatic aberrations from the lenses. The scan of the tungsten lamp was then repeated tuning the grating and filter synchronously to generate a correction file of the emission arm of the spectrometer with the filter and grating monochromator. Figure 4.4 shows the correction files of the emission arm with and without the synchronously tuning wedge interference filter. The

sharp feature at 450 nm is a Woods anomaly from the grating, caused by a surface plasmon effect [109].

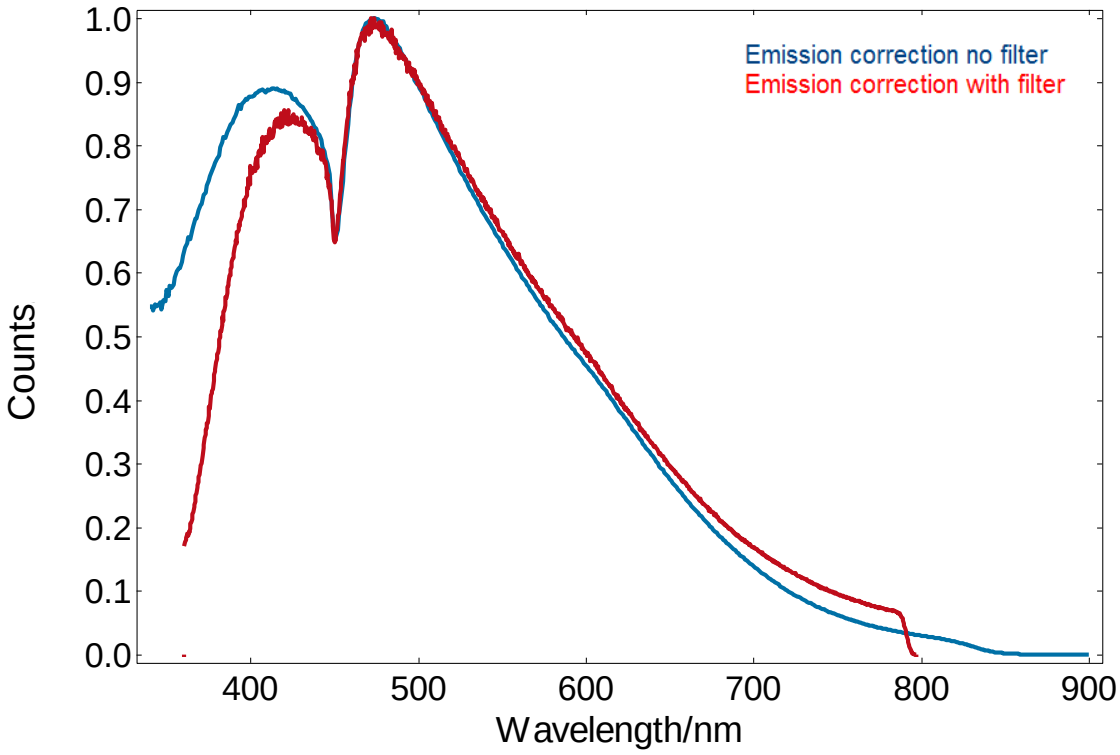

Figure 4.4 Emission correction of spectrometer system with and without wedge interference filter scanning simultaneously with the grating

The measurements of the lamp with and without filter were done without changing any of the optics; therefore the ratio of the two measurements of the tungsten gives the wavelength dependence of the filter transmission in the spectrometer (Figure 4.5). The small bump at 450 nm is not likely to be a real effect of the filter, but rather due to a mismatch in dividing the two scans due to the sharp features in the monochromator transmission at that wavelength. Also the increase in transmission after 700 nm is because it is beyond the band edge of the filter, so although the transmission efficiency of the desired wavelength increases it no longer blocks other wavelengths.

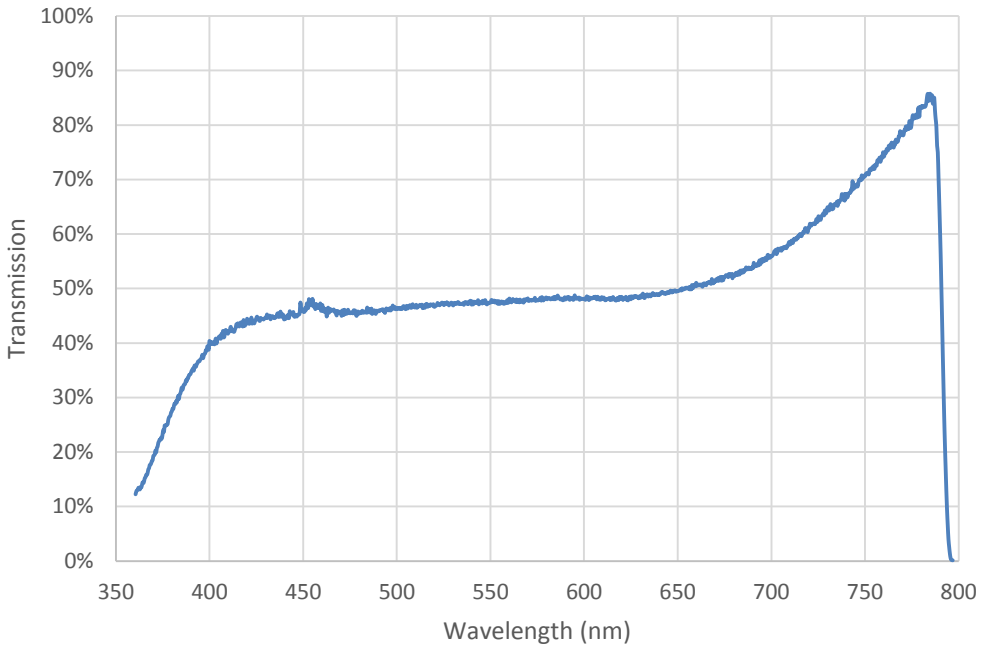

Figure 4.5 Transmission of wedge interference filter in a monochromator with 1-nm bandwidth slits

For comparison, the variable filter was placed in an absorption spectrophotometer (Cary 50, Varian) and the transmission was measured at various positions along the filter, the results are shown in Figure 4.6. The results in Figure 4.6 show a higher transmission than the transmission measured with the filter in the monochromator (Figure 4.5).

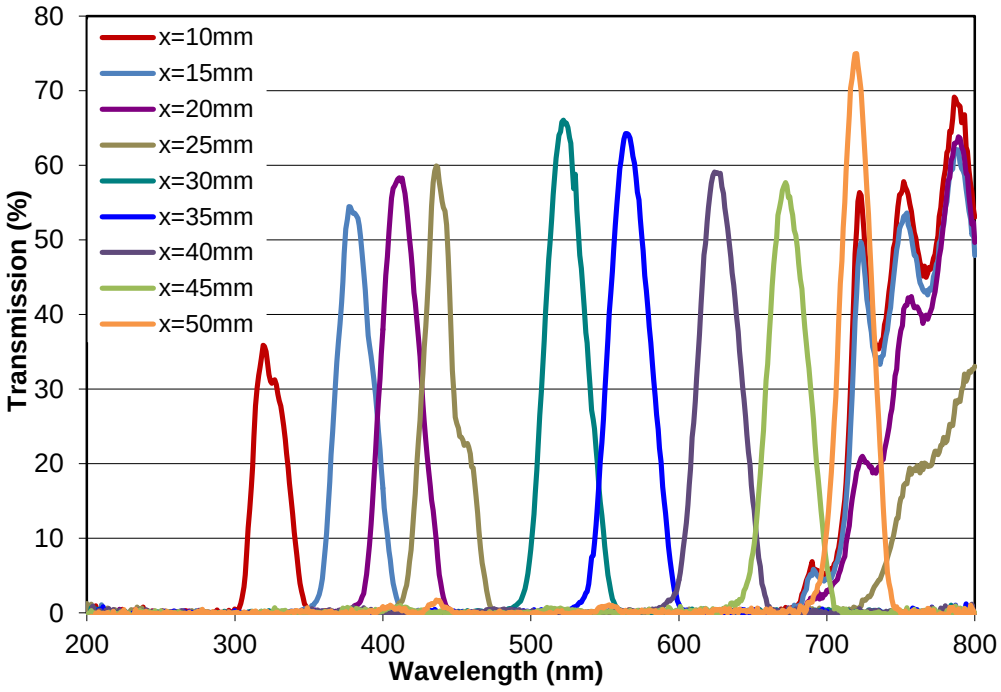

Figure 4.6 Transmission of wedge interference filter with position in an absorption spectrometer.

The next stage was to investigate the reason for the disparity in transmissions measured in Figure 4.5 and Figure 4.6. The beam path in the monochromator was checked and clipping of the beam on the sides of the filter was discounted, the entire beam passed through the filter when it was placed in the monochromator. The transmission of the filter bandwidth was investigated, this was done by measuring light scattered from the xenon lamp at 397 nm. This wavelength was chosen as it is where the Raman signal of water is measured for sensitivity measurements. The signal measured on the detector after the monochromator and filter was divided by the signal from the reference detector (to take account of variations in lamp output), this in turn was divided by the same measurement with the filter out of the beam to give the transmission of the filter in the experimental setup. This was repeated for different slit bandwidths and the results are shown in Figure 4.7.

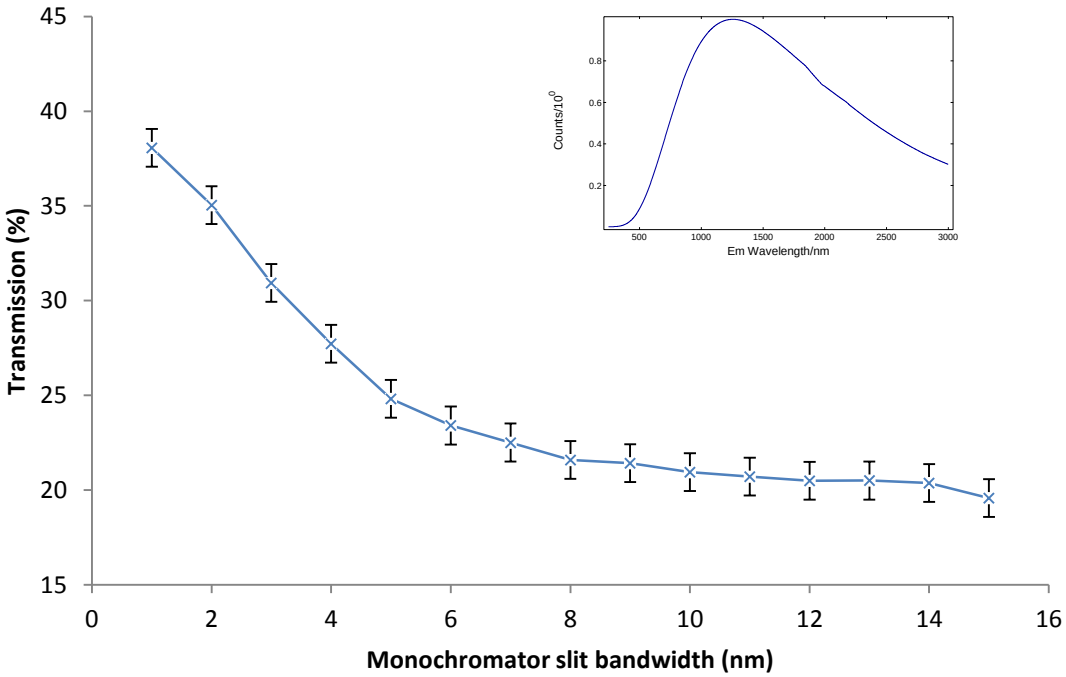

Figure 4.7 Transmission of wedge interference filter as a function of monochromator slit width (inset – broadband source spectrum)

The reason for this disparity between the transmission of the filter measured by the absorption spectrometer and measured with the filter placed within the emission monochromator is most likely because the cone of incident light that travels through the filter in the monochromator extends over areas of the filter where the filter does not transmit the wavelength of interest. As the slits are opened (x-axis of a Figure 4.7) a larger area of filter is used outside of the transmission region of interest.

In order to test the effect of the filter on the bandwidth of the monochromator the apparatus was set up as shown in Figure 4.8. The output of a Nd:YAG laser with a second harmonic output at 532 nm was used as the light source. The radiation was incident on a diffuse scatterer and from this on to the entrance slit of the monochromator. The setup was used in order to fully illuminate the slit with the laser radiation and thus reduce optical effects i.e. if the slit was not over illuminated the entrance slit would not have an effect on the measurement (see Section 2.2.2, Figure 2.18). A 4-order neutral density filter was used to reduce the laser power to protect the detector. The laser line was scanned using the single grating monochromator with and without the wedge filter (aligned to allow maximum transmission at 532 nm) for various bandwidths. Figure 4.9 shows the measured FWHM bandwidth with and without the filter against the theoretical bandwidth.

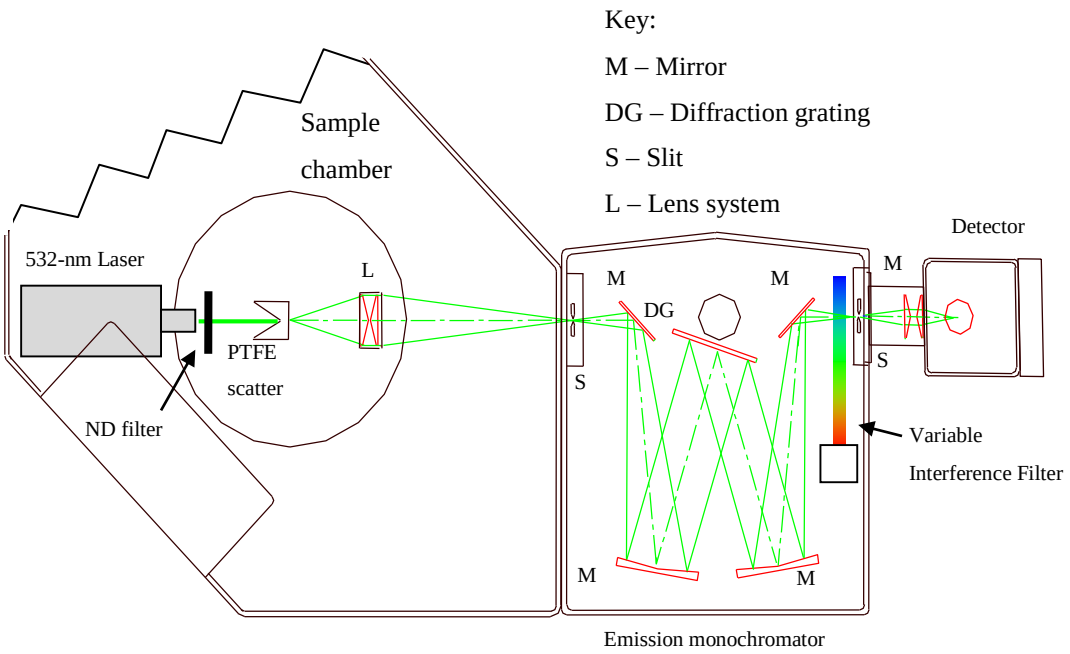

Figure 4.8 Setup for measuring laser line using a monochromator employing a variable interference filter

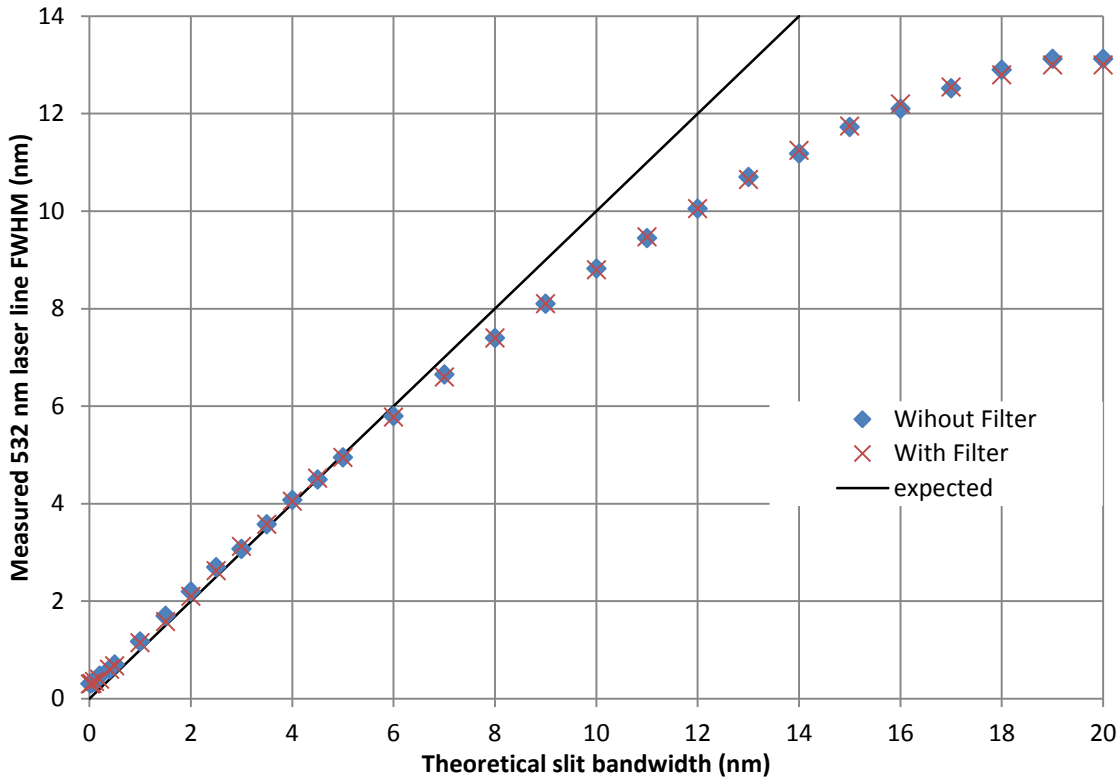

Figure 4.9 Measurement of measured laser bandwidth with slit width

Figure 4.9 shows that the addition of the filter has little effect on the measured FWHM. It also shows a disparity between the theoretical bandwidth and the measured bandwidth, this is likely to be due to a non-homogeneous illumination of the slit, especially far from the centre. Although the measured FWHM remains approximately the same with the addition of the filter, the spectral shape of the transmitted light does change. This gets more pronounced with increasing slit bandwidth (examples are shown in Figure 4.10).

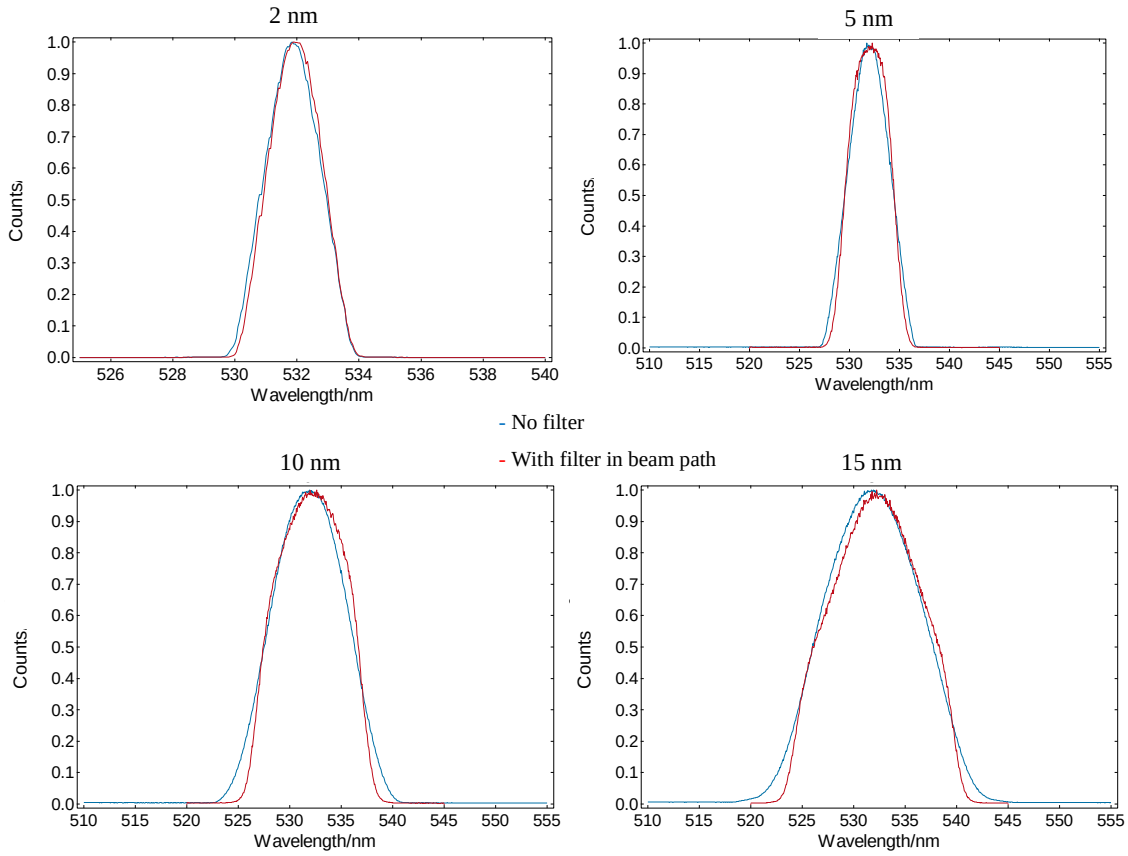

Figure 4.10 Examples of scans of laser line for various bandwidths with and without a variable interference filter (normalised).

By finding the ratio of the integrals of the curves, it was found that the alteration of the spectral shape was partially responsible for the change of the transmission of the filter with increasing bandpass. There was a 1-2 % reduction for bandwidths of 2 nm and 5 nm, 3 % for a 10 nm bandwidth, 5 % for a 15 nm bandwidth and 6 % for a 20 nm bandwidth.

4.3 Stray light rejection

The next step was to compare the stray light rejection of a monochromator employing a grating and wedge filter with the performance of a single monochromator and, additionally, how the stray light suppression compared with that of a double monochromator. To study the stray light suppression, the setup in Figure 4.8 was used, a scan of the laser peak was made without the filter and then with the filter in line with the monochromator wavelength. The measurements on the 532 nm peak were measured with a 4 OD neutral density filter so as not to saturate the detector. The laser is monochromatic (bandwidth <1 nm), therefore any signal measured elsewhere can be

attributed to scattered light. The spectrum of the laser was then scanned, with the diffraction grating and wedge filter and compared with the spectrum without the wedge filter (Figure 4.11 and Figure 4.12).

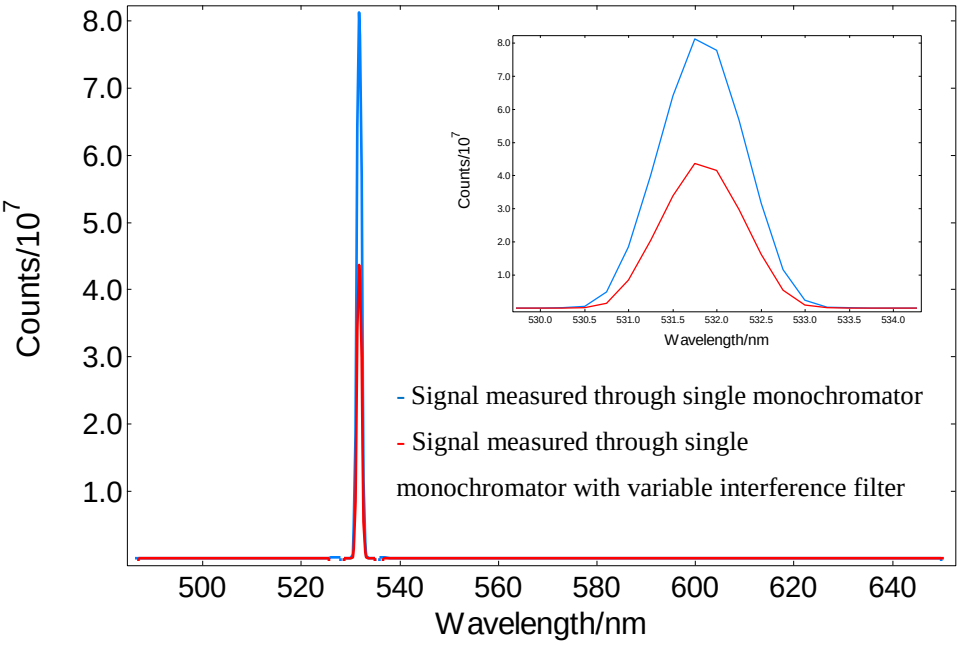

Figure 4.11 Comparison of signal and stray light measurement of a single monochromator and a monochromator employing one grating and a variable interference filter (linear scale)

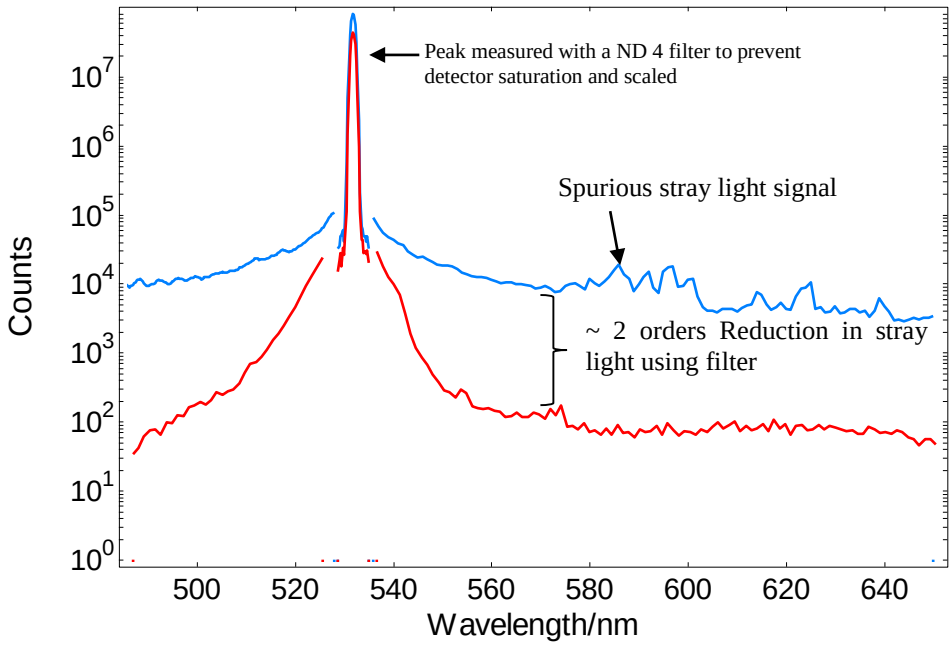

Figure 4.12 Comparison of signal and stray light measurement of a single monochromator and a monochromator employing one grating and a variable interference filter (semi-log scale)

For comparative purposes the measurement was repeated on a double monochromator and compared with the first monochromator of the double monochromator (Figure 4.13 and Figure 4.14). The stray light rejection of the first half of a double monochromator appears different to that of a single monochromator. The stray light rejection of a monochromator is affected by the diffusive properties of the grating. These properties are different for each individual grating depending on the blaze wavelength, groove density and which master was used. Gratings from the same master made in different batches also vary in their efficiency and scattering properties. The double monochromator employed in these measurements uses gratings with a lower grove density, 1200 g/mm, compared with the standard single monochromator, 1800 g/mm. This is to compensate for the drop in grating efficiency at the extremes of their transmission when they are employed in a double monochromator arrangement. When a wedge interference filter is used, it can be employed alongside a standard single monochromator, this accounts for the difference in performance between the single monochromator used with the double monochromator and that used with the filter.

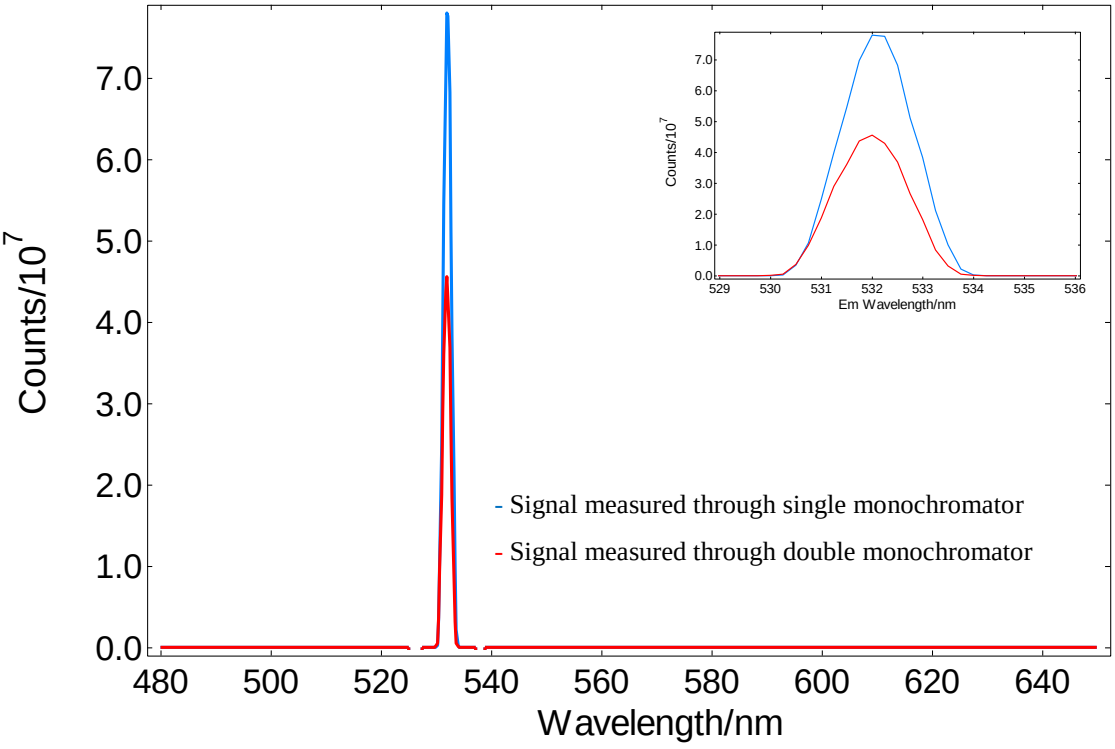

Figure 4.13 Comparison of signal and stray light measurement of the first monochromator of a double monochromator and a double monochromator (linear scale)

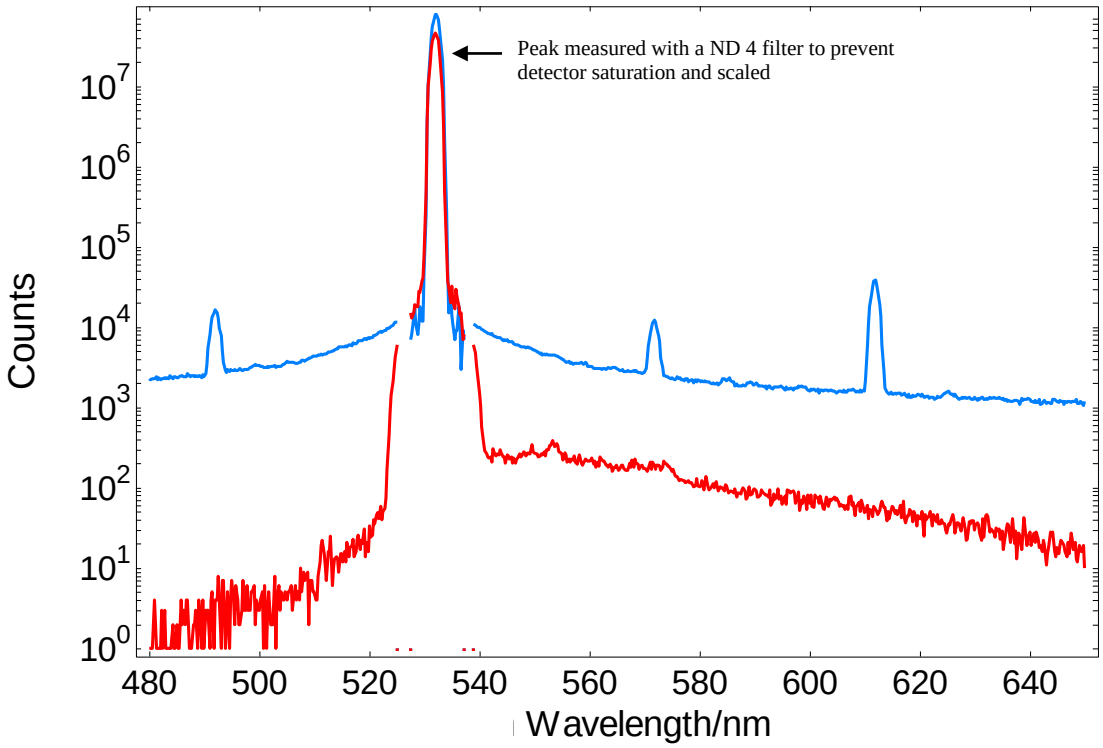

Figure 4.14 Comparison of signal and stray light measurement of the first monochromator of a double monochromator and a double monochromator (semi-log scale)

In order to get a more quantitative measure of stray light rejection the spectra measured using variable filter were normalised to the peak of the single monochromator. The percentage drop in signal between the spectra of their respective backgrounds was then found using an interpolation technique (as the step sizes were different). This was repeated for the double monochromator and the results are shown in Figure 4.15.

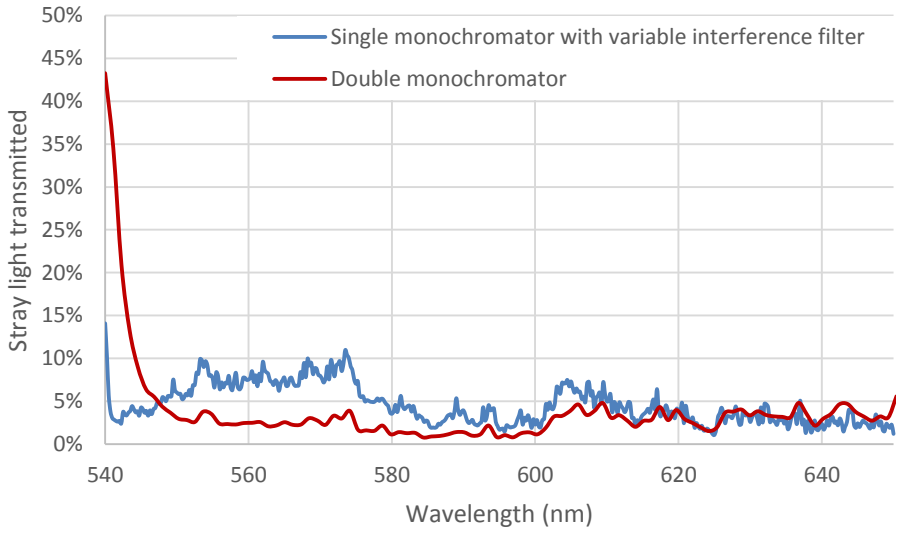

Figure 4.15 Percentage stray light rejection improvement with the addition of a second monochromator or a variable interference filter

As mentioned previously (Section 2.2.2), the most common measurement of the sensitivity of a fluorescence spectrometer is the water Raman measurement. A spectrum of the Raman band of water excited at 350 nm was measured with the variable filter set to the peak of the signal (397 nm) and at the noise level (450 nm), this was compared with a measurement made on the single monochromator without the filter (Figure 4.16).

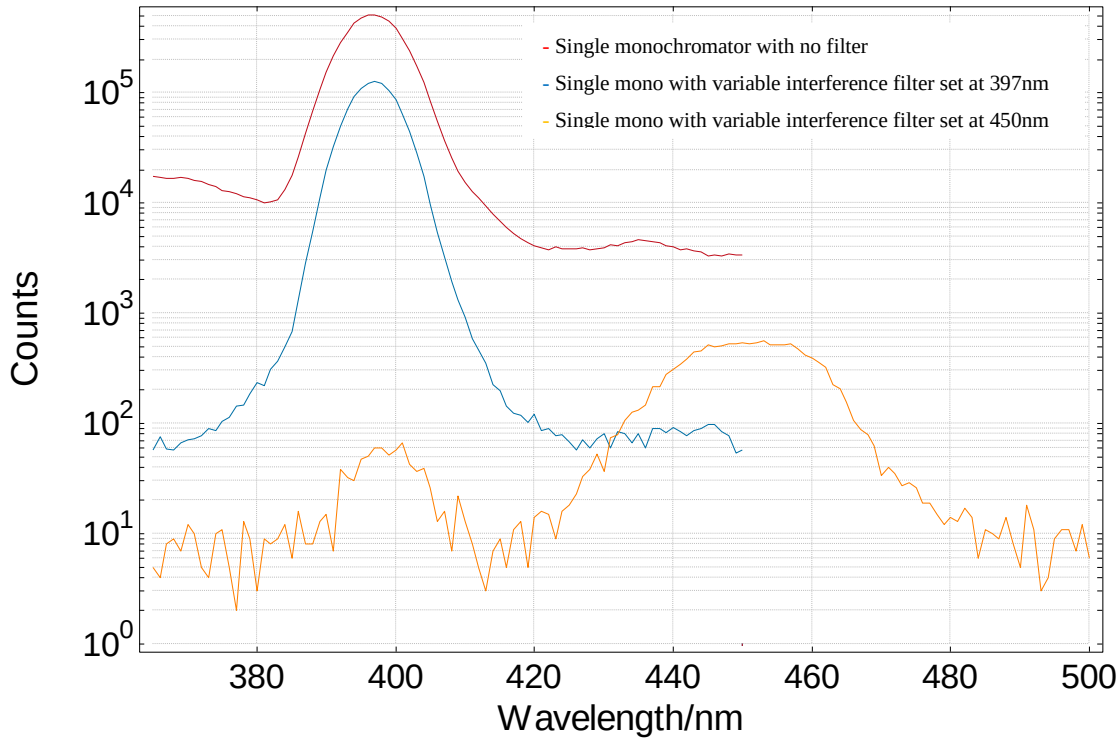

Figure 4.16 Measurement of Raman signal from water with single monochromator and the effect of the wedge filter

The water Raman signal to noise ratio calculated using the single monochromator was ~8700:1. Using the filter set at 397 nm the result was ~16,600:1, however in practical situations the filter would scan with the grating. Therefore, using the noise signal at 450 nm with the filter placed at the same wavelength the water Raman signal to noise ratio was ~5400:1. This value is lower than the value measured with the single monochromator due to the low transmission of the filter at this wavelength (because the measurement is the signal divided by the square root of the noise, the effect of a reduction in transmission is more weighted than the reduction in scattered light). If the transmission of the filter were to be 66 % at 397 nm with the same stray light rejection properties the

signal to noise ratios of single mono and signal mono with interference filter would be equal. This experiment highlights another failing in using the water Raman signal to noise ratio as a test of sensitivity of a fluorescence spectrometer – although the stray light suppression is improved, the water Raman SNR is reduced because the peak signal is lower, meaning that the system with less scattered light has a lower SNR.

4.4 Measurement examples

Bulk zinc oxide (ZnO) is a white powder used as an additive in materials such as paint. It has a low emission efficiency and is highly scattering (hence its use in white paint). As such it is a challenge to measure. Figure 4.17 shows the uncorrected emission spectrum of ZnO with and without the synchronously scanned wedge interference filter. Without the synchronously tuned wedge filter the classic Lorentzian scattering peaks completely swamp the emission spectrum, the peaks are clearly a stray light effect as altering the excitation wavelength alters their positions. However, carrying out an emission scan with the filter (Figure 4.17 and Figure 4.18) removes the majority of these peaks leaving the ZnO emission reasonably pure.

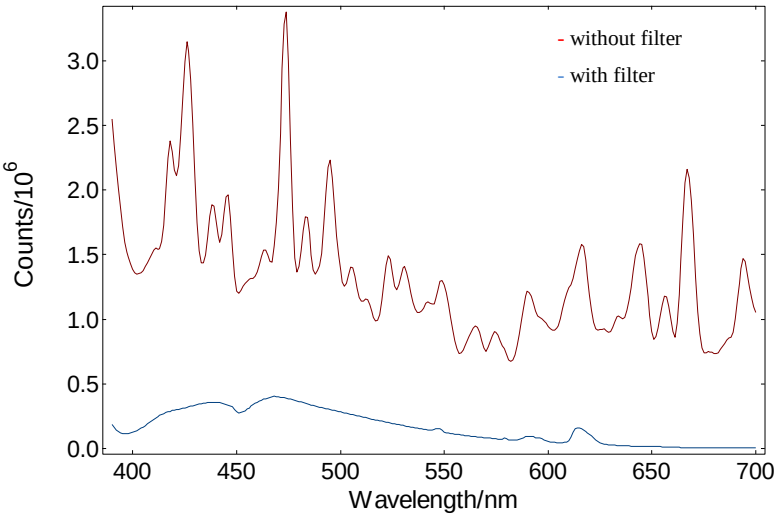

Figure 4.17 Emission Spectrum ZnO (uncorrected) λ_{EX}=380 nm $\Delta\lambda_{EX}$=3 nm, $\Delta\lambda_{EM}$=0.5 nm, 1 nm step, 0.2 s dwell, 5 repeats

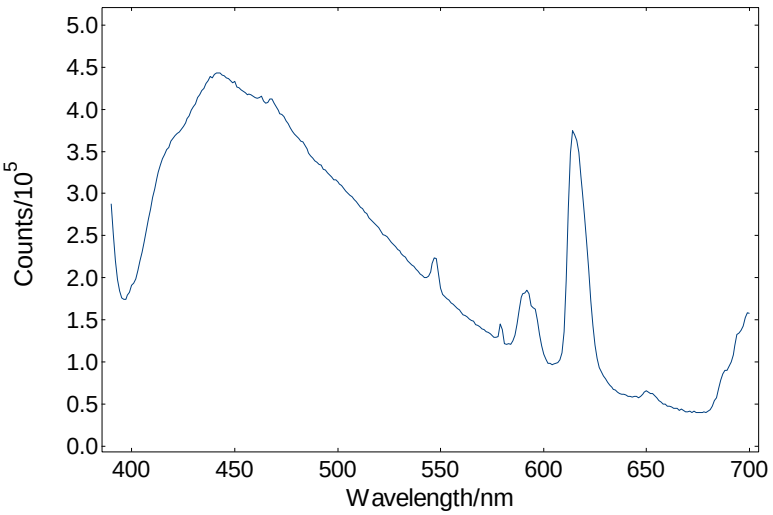

Figure 4.18 Emission Spectrum ZnO (spectrally corrected) using single monochromator with variable filter λ_{EX}=380 nm $\Delta\lambda_{EX}$=3 nm, $\Delta\lambda_{EM}$=0.5 nm, 1 nm step, 0.2 s dwell, 5 repeats

4.5 Conclusions

A continuously variable wedge interference filter was fitted to a diffraction grating based emission monochromator in a commercial fluorescence spectrometer. The filter drive was designed in such a way to mimic the sine drive in a monochromator, meaning that the spectrometer's control software could be used to drive the filter synchronously with the diffraction grating.

The filter was found to be linear in terms of wavelength and did not have a large effect on the spectral shape of the light transmitted by the monochromator. The results show that the addition of a wedge interference filter to a single monochromator did not improve the sensitivity figure quoted for a spectrometer, the water Raman signal-to-noise ratio, which dropped from ~8700:1 to ~5400:1. However, measurements of the stray light from the monochromator showed that the addition of the synchronous filter to the single monochromator reduced the stray light by two orders of magnitude (a similar level to a double monochromator). Measurements of the highly scattering sample ZnO also showed that the addition of the synchronously tuned filter improved the quality of the emission spectrum obtained. A possible solution to the disparity between the standard measurement for SNR and the ability of the system to suppress stray light could be to specify a water Raman value at a standard irradiance.

CHAPTER 5 - CONCLUSION

5.1 Technical achievements of the thesis and discussion

This thesis has evaluated new technology and its implementation into commercial fluorescence lifetime spectrometers. Various supercontinuum sources were evaluated and systems were designed to integrate a supercontinuum source into commercial fluorescence spectrometers. The work involved in the thesis was innovative and added new knowledge. Specifically it led to the first published work on the application of commercial supercontinuum sources in fluorescence spectroscopy [110], the first paper explaining the technical considerations of using a supercontinuum source (with a ESM PCF) with TCSPC [110] and a second paper expanding the work with a high-Δ PCF and a description of wavelength and bandpass control of a supercontinuum with wedge interference filters [111]. The work towards the thesis also led to the first commercial monochromator product for wavelength and bandpass control of supercontinuum sources employing wedge interference filters. The product has since been optimised further leading to dozens of units sold both as a component integrated into Edinburgh Instruments fluorescence spectrometers and as an OEM product, Fianium Superchrome^{TM} (with two- and three-filter designs). Fluorescence spectrometers with a combination of grating and wedge interference filters have also been sold into the market as beta test units. A patent application has been submitted for the work involved [112].

Chapter 2 of the thesis described a thorough investigation of the dynamics and spectral extent of various supercontinuum sources when measured with the tools used in fluorescence spectroscopy – fluorescence spectrometers, single photon counting detectors and time correlated single photon counting electronics. The work revealed important information regarding the pulse widths of commercial supercontinuum sources relevant to TCSPC. The manufacturers' normally only quote the pulse width of the pump source in their specifications (generally ~5 ps), however this work showed that the actual output can vary considerably with wavelength and between sources and is considerably wider than the input pulse. Assuming a 40 ps instrumental response without considering the source (caused by the optics, electronic jitter and detector response) and the fact that the measured instrument response is a sum of squares, the lowest measured instrument response function of ~80 ps means that 64 ps is because of the source – either jitter or pure optical broadening. At some wavelengths the measured pulse width was considerably broader (particularly at the blue edge), analysis of the temporal profile showed that this was often due to the complex nature of the supercontinuum generation.

In some cases the blue region included photons generated through soliton trapping with zero wavelength dispersion, or a different dispersion profile, these overlapped with the photons generated through FWM with a temporal profile in consonance with that expected because of fibre dispersion.

The spectral dependence on the pulse height dispersion was also found to vary considerably with wavelength, in agreement with the theory. Because the supercontinuum in the picosecond regime is generated from modulation instability, which is seeded by noise, at increasing wavelengths from the pump, the pulse height distribution increases. Without a high quality constant fraction discriminator, this would result in a broader pulse. However, at the wavelength where the dispersion profile changes the intensity distribution also changes and becomes very narrow. This is in good agreement with the theory that a process other than MI (soliton trapping) is generating the blue edge of some supercontinua. The measurements made during this thesis gave a novel way to visualise and understand the supercontinuum output by adding the dimension of pulse height distribution.

At the beginning of the project wavelength separation of supercontinuum sources was typically carried out using AOTFs. These have advantages such as a narrow bandpass and the ability to make fast changes between wavelengths, however they are often not suitable for fluorescence measurements as they do not have a high level of out of band rejection and cannot scan a through the continuum (as required for excitation scans). Diffraction grating based monochromators offer a far better option for fluorescence spectrometers, they offer a tunable wavelength and bandwidth along with excellent out of band transmission, and the work involved in Chapter 2 also informed the optimal way to couple the supercontinuum with a grating monochromator. However, there are fluorescence applications where a diffraction grating has strong disadvantages in terms of throughput and the beam quality of the transmitted light. A device for wavelength selection based on wedge interference filters, as described and evaluated in Chapter 3, can offer a broad, continuously spectrally tunable output with tunable bandwidth and out of band rejection suitable for fluorescence. This device has particular advantages in applications, such as fluorescence microscopy, where a spectrally pure, diffraction limited spot is required. Since the work carried out for this thesis was completed alternative devices based on volume Bragg grating technology have become available. They offer a broader tuning range than the wedge interference filter based device (400 – 1000 nm) and excellent out-of-band suppression, however they do not have a tunable

bandwidth. This means that for applications with high optical power requirements, wavelength selection based on a wedge interference filter still has advantages: the transmission is higher and the power throughput can be increased simply by moving the two filters apart and thus increasing the bandwidth.

Chapter 4 addressed the evaluation of an improved method for wavelength selection involving a diffraction grating and a synchronously scanning wedge interference filter. It was shown that such a device could have advantages in terms of stray light rejection over a single monochromator. In particular, a fluorescence spectrometer with such a device would be able to measure samples with higher scattering compared to emission than a standard system i.e. increased sensitivity. The results also showed comparable stray light performance to a double grating monochromator over the transmission range of the filter. A double grating monochromator (particularly one with grating turrets) has advantages in terms of flexibility and wavelength coverage: extra gratings can be added to cover the spectral range from the deep UV to NIR (200 nm – 5500 nm) with one monochromator, whereas the filter tested only worked in the visible range. Other filters could be designed to cover higher wavelength ranges, however there would be practical implications to exchanging filters in such a system. This is a particular problem in the deep UV (200-340 nm) where thin film materials have not yet lead to a wedge filter with coverage in this region. A device based on a single grating and wedge interference filter does offer important advantages over a double monochromator in terms of cost, complexity, throughput and size, meaning that there are applications where it would be preferable.

5.2 Outlook

The work carried out for this thesis integrating a supercontinuum source showed how best to integrate a supercontinuum source with a fluorescence spectrometer and that high quality data can be acquired from such a combination. As a result of this work, the supercontinuum source is now a common option for Edinburgh Instruments spectrometers, providing researchers with additional flexibility and functionality.

Since the work carried out for this thesis there have been further advances to lower the minimum wavelength from a supercontinuum. Rather than extending the UV output from the PCF fibre, devices have been developed with an angle tunable KTP crystal on the output. The KTP crystal allows second harmonic generation providing output to

<250 nm. In addition advances in gain-switched diode technology give the possibility of using them to produce a supercontinuum source frequency selectable up to megahertz at a significant cost saving (fibre laser pumps have a fixed frequency and therefore require the additional expense of an integrated pulse picker to achieve lower frequencies).

The results of the study and applications of wedge interference filters showed the possibilities of using new devices based on advances in thin film technology to create new devices with improved performance over current devices on the market. The constraints on the wedge filter performance are the steepness of filter's edge (which limits the narrowest bandpass) and the wavelength coverage (which is limited by the materials used in the thin film and the range of wavelengths in which they do not absorb light). Since the experiments contained in this thesis the filters have improved, with steeper edges. These improved filters are already employed in wavelength selection devices for supercontinuum sources manufactured by Edinburgh Instruments.

In the future, advances in thin film materials should result in a broader usable wavelength range for the wedge interference filter (particularly in the UV). Even without the UV coverage of the filter, it should be possible to tune down to 250 nm in a supercontinuum system with a SHG crystal, using the filter before the crystal.

REFERENCES

[1] J. W. Rohlf, *Modern Physics from aα to Z*. Wiley, 1994.

[2] J. F. W. Herschel, " ’Αμόρφωτα No. I. On a Case of Superficial Colour Presented by a Homogeneous Liquid Internally Colourless," *Philos. Trans. R. Soc. London*, pp. 143–145, 1845.

[3] S. Udenfriend, "Development of the spectrophotofluorometer and its commercialization", *Protein Sci.*, vol. 4, no. 3, pp. 542–551, 1995.

[4] A. Jablonski, "Theory of the polarization of photoluminescence of colored solutions", *Z. Phys.*, vol. 96, pp. 236–246, 1935.

[5] J. Lakowicz, *Principles of fluorescence spectroscopy*, 3rd ed. New York: Springer, 2007.

[6] T. Forster, "Energiewanderung und fluoreszenz", *Naturwissenschaften*, vol. 33, no. 6, pp. 166–175, 1946.

[7] H. C. Gerritsen, R. Sanders, A. Draaijer, C. Ince, and Y. K. Levine, "Fluorescence lifetime imaging of oxygen in living cells", *J. Fluoresc.*, vol. 7, no. 1, pp. 11–15, 1997.

[8] J. R. Lakowicz, H. Szmacinski, K. Nowaczyk, and M. L. Johnson, "Fluorescence lifetime imaging of free and protein-bound NADH", *Proc. Natl. Acad. Sci.*, vol. 89, no. 4, pp. 1271–1275, 1992.

[9] S. Habuchi, M. Cotlet, J. Hofkens, G. Dirix, J. Michiels, J. Vanderleyden, V. Subramaniam, and F. C. De Schryver, "Resonance energy transfer in a calcium concentration-dependent cameleon protein", *Biophys. J.*, vol. 83, no. 6, pp. 3499–3506, 2002.

[10] L. Stryer, "Fluorescence energy transfer as a spectroscopic ruler", *Annu. Rev. Biochem.*, vol. 47, no. 1, pp. 819–846, 1978.

[11] D. Nather, R. Fenske, R. Hurteaux, S. Majno, and S. Smith, "Time-correlated single photon counting: an advancing technique in a plate reader for assay development and high throughput screening", *PROCEEDINGS-SPIE ...*, 2006.

[12] G. Laczko, I. Gryczynski, Z. Gryczynski, W. Wiczk, H. Malak, and J. R. Lakowicz, "A 10-GHz frequency-domain fluorometer", *Rev. Sci. Instrum.*, vol. 61, no. 9, pp. 2331–2337, 1990.

[13] J. W. Goodman, *Introduction to Fourier Optics*. Roberts & Company, 2005.

[14] W. Meiling and F. Stary, *Nanosecond pulse techniques*. Gordon and Breach, 1968.

[15] C. Lewis, W. R. Ware, L. J. Doemeny, and T. L. Nemzek, “The Measurement of Short-Lived Fluorescence Decay Using the Single Photon Counting Method”, *Rev. Sci. Instrum.*, vol. 44, no. 2, pp. 107–114, 1973.

[16] D. O’Connor, *Time-correlated Single Photon Counting*. Elsevier Science, 1984.

[17] W. Becker, *Advanced Time-Correlated Single Photon Counting Techniques*. Springer, 2005.

[18] G. Hungerford and D. J. S. Birch, “Single-photon timing detectors for fluorescence lifetime spectroscopy”, *Meas. Sci. Technol.*, vol. 7, no. 2, pp. 121–135, 1996.

[19] T. Louis, G. H. Schatz, P. Klein-Boelting, A. R. Holzwarth, G. Ripamonti, and S. Cova, “Performance comparison of a single-photon avalanche diode with a microchannel-plate photomultiplier in time-correlated single-photon counting”, *Rev. Sci. Instrum.*, vol. 59, no. 7, pp. 1148–1152, 1988.

[20] M. D. Eisaman, J. Fan, A. Migdall, and S. V. Polyakov, “Invited Review Article: Single-photon sources and detectors”, *Rev. Sci. Instrum.*, vol. 82, no. 7, p. 071101, 2011.

[21] L. Hundley, T. Coburn, E. Garwin, and L. Stryer, “Nanosecond fluorimeter”, *Rev. Sci. Instrum.*, vol. 38, no. 4, pp. 488–492, 1967.

[22] D. J. S. Birch and R. E. Imhof, “Coaxial nanosecond flashlamp”, *Rev. Sci. Instrum.*, vol. 52, no. 8, pp. 1206–1212, 1981.

[23] S. Hutchins, I. Rech, G. Buller, I. Labanca, K. J. Gordon, M. Ghioni, S. Cova, and S. Pellegrini, “Single photon detector tests for the LHC synchrotron light diagnostics”, in DIPAC, 2005.

[24] W. Koechner, *Solid-State Laser Engineering*. Springer, 2006.

[25] “Coherent Inc. Chameleon Family Lasers Enabling Multiphoton Imaging.” [Online]. Available: http://www.coherent.com/products/?1557/Chameleon-Family. [Accessed: 25-Jun-2014].

[26] “Mai Tai one box tunable ultrafast lasers.” [Online]. Available: http://www.spectra-physics.com/products/ultrafast-lasers/mai-tai. [Accessed: 25-Jun-2014].

[27] T. N. Singh-Rachford, A. Nayak, M. L. Muro-Small, S. Goeb, M. J. Therien, and F. N. Castellano, “Supermolecular-chromophore-sensitized near-infrared-to-visible photon upconversion”, *J. Am. Chem. Soc.*, vol. 132, no. 40, pp. 14203–14211, Sep. 2010.

[28] “pulseSelect | A·P·E.” [Online]. Available: http://www.ape-berlin.de/en/products/pulse-picker/pulseselect. [Accessed: 25-Jun-2014].

[29] “Picosecond light Sources - Lasers & LEDs - Edinburgh Photonics.” [Online]. Available: http://www.edinburghphotonics.com/lasers-leds/picosecond pulsed lasers and LEDs/. [Accessed: 25-Jun-2014].

[30] R. K. Sreejith, V. N. Yadav, N. K. Varshney, S. K. Berwal, C. G. Suresh, S. M. Gaikwad, and J. K. Pal, “Conformational characterization of human eukaryotic initiation factor 2alpha: a single tryptophan protein”, *Biochem. Biophys. Res. Commun.*, vol. 390, no. 2, pp. 273–9, Dec. 2009.

[31] B. Bozic-Weber, V. Chaurin, E. C. Constable, C. E. Housecroft, M. Meuwly, M. Neuburger, J. A. Rudd, E. Schonhofer, and L. Siegfried, “Exploring copper(I)-based dye-sensitized solar cells: a complementary experimental and TD-DFT investigation”, *Dalt. Trans.*, vol. 41, no. 46, pp. 14157–14169, 2012.

[32] P. Martín-Ramos, M. D. Miranda, M. R. Silva, M. E. S. Eusebio, V. Lavín, and J. Martín-Gil, “A new near-IR luminescent erbium(III) complex with potential application in OLED devices”, *Polyhedron*, vol. 65, pp. 187–192, Nov. 2013.

[33] R. R. Alfano and S. L. Shapiro, “Emission in the region 4000 to 7000 Å via four-photon coupling in glass”, *Phys. Rev. Lett.*, vol. 24, no. 11, p. 584, 1970.

[34] N. G. Bondarenko, I. V Eremina, and V. I. Talanov, “Broadening of spectrum in self focusing of light in crystals”, *Sov. J. Exp. Theor. Phys. Lett.*, vol. 12, p. 85, 1970.

[35] G. P. Agrawal, *Nonlinear Fiber Optics*. Academic Press, 2013.

[36] C. Lin and R. H. Stolen, “New nanosecond continuum for excited-state spectroscopy”, *Appl. Phys. Lett.*, vol. 28, no. 4, pp. 216–218, 1976.

[37] P. L. Baldeck and R. Alfano, “Intensity effects on the stimulated four photon spectra generated by picosecond pulses in optical fibers”, *Light. Technol. J.*, vol. 5, no. 12, pp. 1712–1715, 1987.

[38] I. Ilev, H. Kumagai, K. Toyoda, and I. Koprinkov, “Highly efficient wideband continuum generation in a single-mode optical fiber by powerful broadband laser pumping”, *Appl. Opt.*, vol. 35, no. 15, pp. 2548–2553, 1996.

[39] A. Hasegawa and F. Tappert, “Transmission of stationary nonlinear optical pulses in dispersive dielectric fibers. I. Anomalous dispersion”, *Appl. Phys. Lett.*, vol. 23, no. 3, pp. 142–144, 1973.

[40] L. F. Mollenauer, R. H. Stolen, and J. P. Gordon, “Experimental observation of picosecond pulse narrowing and solitons in optical fibers”, *Phys. Rev. Lett.*, vol. 45, no. 13, p. 1095, 1980.

[41] D. Mogilevtsev, T. A. Birks, and P. S. J. Russell, “Group-velocity dispersion in photonic crystal fibers”, *Opt. Lett.*, vol. 23, no. 21, pp. 1662–1664, 1998.

[42] N. G. R. Broderick, T. M. Monro, P. J. Bennett, and D. J. Richardson, “Nonlinearity in holey optical fibers: measurement and future opportunities”, *Opt. Lett.*, vol. 24, no. 20, pp. 1395–1397, 1999.

[43] J. Ranka, R. Windeler, and A. Stentz, “Visible continuum generation in air-silica microstructure optical fibers with anomalous dispersion at 800 nm”, *Opt. Lett.*, vol. 25, no. 1, pp. 25–27, 2000.

[44] W. J. Wadsworth, J. C. Knight, A. Ortigosa-Blanch, J. Arriaga, E. Silvestre, and P. S. J. Russell, “Soliton effects in photonic crystal fibres at 850 nm”, *Electron. Lett.*, vol. 36, no. 1, pp. 53–55, 2000.

[45] J. M. Dudley and S. Coen, “Supercontinuum generation in photonic crystal fiber”, *Rev. Mod. Phys.*, vol. 78, no. 4, pp. 1135–1184, 2006.

[46] V. P. Yanovsky and F. W. Wise, “Nonlinear propagation of high-power, sub-100-fs pulses near the zero-dispersion wavelength of an optical fiber”, *Opt. Lett.*, vol. 19, no. 19, pp. 1547–1549, 1994.

[47] J. Travers, “Blue extension of optical fibre supercontinuum generation”, *J. Opt.*, 2010.

[48] J. P. Gordon, “Theory of the soliton self-frequency shift”, *Opt. Lett.*, vol. 11, no. 10, pp. 662–664, 1986.

[49] J. Herrmann, U. Griebner, N. Zhavoronkov, A. Husakou, D. Nickel, J. C. Knight, W. J. Wadsworth, P. S. J. Russell, and G. Korn, “Experimental evidence for supercontinuum generation by fission of higher-order solitons in photonic fibers”, *Phys. Rev. Lett.*, vol. 88, no. 17, p. 173901, 2002.

[50] I. Cristiani, R. Tediosi, L. Tartara, and V. Degiorgio, “Dispersive wave generation by solitons in microstructured optical fibers”, *Opt. Express*, vol. 12, no. 1, pp. 124–135, 2004.

[51] P. K. A. Wai, C. R. Menyuk, Y. C. Lee, and H. H. Chen, “Nonlinear pulse propagation in the neighborhood of the zero-dispersion wavelength of monomode optical fibers”, *Opt. Lett.*, vol. 11, no. 7, pp. 464–466, 1986.

[52] J. N. Elgin, T. Brabec, and S. M. J. Kelly, “A perturbative theory of soliton propagation in the presence of third order dispersion”, *Opt. Commun.*, vol. 114, no. 3, pp. 321–328, 1995.

[53] W. H. Reeves, D. V Skryabin, F. Biancalana, J. C. Knight, P. S. J. Russell, F. G. Omenetto, A. Efimov, and A. J. Taylor, “Transformation and control of ultra-short pulses in dispersion-engineered photonic crystal fibres”, *Nature*, vol. 424, no. 6948, pp. 511–515, 2003.

[54] B. Kibler, J. M. Dudley, and S. Coen, “Supercontinuum generation and nonlinear pulse propagation in photonic crystal fiber: influence of the frequency-dependent effective mode area”, *Appl. Phys. B*, vol. 81, no. 2–3, pp. 337–342, 2005.

[55] L. Tartara, I. Cristiani, V. Degiorgio, F. Carbone, D. Faccio, M. Romagnoli, and W. Belardi, “Phase-matched nonlinear interactions in a holey fiber induced by infrared super-continuum generation”, *Opt. Commun.*, vol. 215, no. 1, pp. 191–197, 2003.

[56] S. Coen, A. H. L. Chau, R. Leonhardt, J. D. Harvey, J. C. Knight, W. J. Wadsworth, and P. S. J. Russell, "Supercontinuum generation by stimulated Raman scattering and parametric four-wave mixing in photonic crystal fibers", *JOSA B*, vol. 19, no. 4, pp. 753–764, 2002.

[57] G. Sansone, G. Steinmeyer, C. Vozzi, S. Stagira, M. Nisoli, S. De Silvestri, K. Starke, D. Ristau, B. Schenkel, and J. Biegert, "Mirror dispersion control of a hollow fiber supercontinuum", *Appl. Phys. B*, vol. 78, no. 5, pp. 551–555, 2004.

[58] D. V Skryabin, F. Luan, J. C. Knight, and P. S. J. Russell, "Soliton self-frequency shift cancellation in photonic crystal fibers", *Science (80-.).*, vol. 301, no. 5640, pp. 1705–1708, 2003.

[59] F. G. Omenetto, N. A. Wolchover, M. R. Wehner, M. Ross, A. Efimov, A. J. Taylor, V. V. R. K. Kumar, A. K. George, J. C. Knight, and N. Y. Joly, "Spectrally smooth supercontinuum from 350 nm to 3 μm in sub-centimeter lengths of soft-glass photonic crystal fibers", *Opt. Express*, vol. 14, no. 11, pp. 4928–4934, 2006.

[60] R. H. Stolen, J. P. Gordon, W. J. Tomlinson, and H. A. Haus, "Raman response function of silica-core fibers", *JOSA B*, vol. 6, no. 6, pp. 1159–1166, 1989.

[61] W. Wadsworth, N. Joly, J. Knight, T. Birks, F. Biancalana, and P. Russell, "Supercontinuum and four-wave mixing with Q-switched pulses in endlessly single-mode photonic crystal fibres", *Opt. Express*, vol. 12, no. 2, pp. 299–309, 2004.

[62] R. Hooke, *Micrographia: Or, Some Physiological Descriptions of Minute Bodies Made by Magnifying Glasses. With Observations and Inquiries Thereupon*. James Allestry, 1667.

[63] H. Crew, "Thomas Young's place in the history of the wave theory of light", *J. Opt. Soc. Am*, vol. 20, no. 3, p. 101, 1930.

[64] J. von Fraunhofer, "Versuche uber die Ursachen des Anlaufens und Mattwerdens des Glases und die Mittel, denselben zuvorzukommen (1817)", *Joseph von Fraunhofer's Gesammelte Schriften, Munich*, p. 35, 1888.

[65] H. D. Taylor, "Lenses", British Patent No. 29561 (1904).

[66] F. Kollmorgen, "Light transmission through telescopes", *Trans. Am. Illum. Eng. Soc*, vol. 11, pp. 220–228, 1916.

[67] C. Fabry and A. Pérot, "Theorie et applications d'une nouvelle methode de spectroscopie interferentielle", *Ann. Chim. Phys*, vol. 16, no. 7, p. 115, 1899.

[68] H. A. Macleod, *Thin-Film Optical Filters*, 3rd ed. Bristol: IOP Publishing Ltd, 2001.

[69] M. Born, E. Wolf, A. B. Bhatia, P. C. Clemmow, D. Gabor, A. R. Stokes, A. M. Taylor, P. A. Wayman, and W. L. Wilcock, *Principles of Optics:*

Electromagnetic Theory of Propagation, Interference and Diffraction of Light. Cambridge University Press, 1999.

[70] S. D. Smith and O. S. Heavens, "A tunable infra-red interference filter", *J. Sci. Instrum.*, vol. 34, no. 12, p. 492, 1957.

[71] D. A. Palmer and C. A. Whitlock, "An improved monochromator using a single graded interference filter", *J. Phys. E.*, vol. 11, no. 10, p. 996, 1978.

[72] P. Jacquinot, "The luminosity of spectrometers with prisms, gratings, or Fabry-Perot etalons", *JOSA*, vol. 44, no. 10, pp. 761–765, 1954.

[73] S. D. Smith, "Infra-red Multilayers," Ph. D. Thesis, University of Reading, 1956.

[74] H. D. Polster, "A symmetrical all-dielectric interference filter", *JOSA*, vol. 42, no. 1, pp. 21–23, 1952.

[75] S. D. Smith, "Design of multilayer filters by considering two effective interfaces", *JOSA*, vol. 48, no. 1, pp. 43–49, 1958.

[76] C. R. Pidgeon and S. D. Smith, "Resolving power of multilayer filters in nonparallel light", *JOSA*, vol. 54, no. 12, pp. 1459–1464, 1964.

[77] A. Gorbach and D. Skryabin, "Light trapping in gravity-like potentials and expansion of supercontinuum spectra in photonic-crystal fibres", *Nat. Photonics*, vol. 1, no. 11, pp. 653–657, 2007.

[78] G. Genty, S. Coen, and J. Dudley, "Fiber supercontinuum sources", *JOSA B*, vol. 24, no. 8, pp. 1771–1785, 2007.

[79] D. Skryabin and A. Gorbach, "Colloquium: Looking at a soliton through the prism of optical supercontinuum", *Rev. Mod. Phys.*, vol. 82, no. 2, p. 1287, 2010.

[80] J. Stone and J. Knight, "Visibly 'white' light generation in uniform photonic crystal fiber using a microchip laser", *Opt. Express*, vol. 16, no. 4, pp. 2670–2675, 2008.

[81] F. Robben, "Noise in the measurement of light with photomultipliers", *Appl. Opt.*, vol. 10, no. 4, pp. 776–796, 1971.

[82] H. P. K. K, *Photomultiplier Tubes*, 3a ed. Hamamatsu City: Hamamatsu Photonics K.K., 2007.

[83] L. Skuja, "Optically active oxygen-deficiency-related centers in amorphous silicon dioxide", *J. Non. Cryst. Solids*, vol. 239, no. 1, pp. 16–48, 1998.

[84] L. Skuja, K. Kajihara, M. Hirano, and H. Hosono, "Visible to vacuum-UV range optical absorption of oxygen dangling bonds in amorphous SiO_2", *Phys. Rev. B*, vol. 84, no. 20, p. 205206, 2011.

[85] H. Hosono, Y. Ikuta, T. Kinoshita, K. Kajihara, and M. Hirano, “Physical disorder and optical properties in the vacuum ultraviolet region of amorphous SiO_2”, *Phys. Rev. Lett.*, vol. 87, no. 17, p. 175501, 2001.

[86] K. Kajihara, L. Skuja, M. Hirano, and H. Hosono, “Formation and decay of nonbridging oxygen hole centers in SiO_2 glasses induced by F 2 laser irradiation: In situ observation using a pump and probe technique”, *Appl. Phys. Lett.*, vol. 79, no. 12, pp. 1757–1759, 2001.

[87] J. Stone, W. Wadsworth, and J. Knight, “1064 nm laser-induced defects in pure SiO_2 fibers”, *Opt. Lett.*, vol. 38, no. 15, pp. 2717–2719, 2013.

[88] K. Kajihara, Y. Ikuta, M. Oto, and M. Hirano, “UV–VUV laser induced phenomena in SiO_2 glass”, *Nucl. Instruments …*, vol. 218, pp. 323–331, 2004.

[89] K. Nagasawa, Y. Hoshi, Y. Ohki, and K. Yahagi, “Improvement of radiation resistance of pure silica core fibers by hydrogen treatment”, *Jpn. J. Appl. Phys. 1*, vol. 24, no. 9, pp. 1224–1228, 1985.

[90] J. Stone, “Interactions of hydrogen and deuterium with silica optical fibers: A review”, *J. Light. Technol.*, vol. 5, no. 5, pp. 712–733, 1987.

[91] W. Schottky, “Über spontane Stromschwankungen in verschiedenen Elektrizitätsleitern”, *Ann. Phys.*, vol. 362, no. 23, pp. 541–567, 1918.

[92] A. Gorbach, D. Skryabin, J. Stone, and J. Knight, “Four-wave mixing of solitons with radiation and quasi-nondispersive wave packets at the short-wavelength edge of a supercontinuum”, *Opt. Express*, vol. 14, no. 21, pp. 9854–9863, 2006.

[93] M. Frosz, P. Falk, and O. Bang, “The role of the second zero-dispersion wavelength in generation of supercontinua and bright-bright soliton-pairs across the zero-dispersion wavelength”, *Opt. Express*, vol. 13, no. 16, pp. 6181–92, Aug. 2005.

[94] N. Nishizawa and T. Goto, “Characteristics of pulse trapping by use of ultrashort soliton pulses in optical fibers across the zero-dispersion wavelength”, vol. 10, no. 21, pp. 1151–1159, 2002.

[95] M. Lighthill, “Contributions to the theory of waves in non-linear dispersive systems”, *IMA J. Appl. Math.*, vol. 1, no. 3, pp. 269–306, 1965.

[96] G. Whitham, “A general approach to linear and non-linear dispersive waves using a Lagrangian”, *J. Fluid Mech.*, vol. 22, no. 02, pp. 273–283, 1965.

[97] A. Gorbach and D. Skryabin, “Theory of radiation trapping by the accelerating solitons in optical fibers”, *Phys. Rev. A*, vol. 76, no. 5, p. 053803, 2007.

[98] P. Beaud, W. Hodel, B. Zysset, and H. Weber, “Ultrashort pulse propagation, pulse breakup, and fundamental soliton formation in a single-mode optical fiber”, *J. Quantum Electron. IEEE*, 1987.

[99] J. Travers and J. Taylor, “Soliton trapping of dispersive waves in tapered optical fibers”, *Opt. Lett.*, vol. 34, no. 2, pp. 115–117, 2009.

[100] C. A. Palmer, E. G. Loewen, R. G. Laboratory, and T. RGL., *Diffraction Grating Handbook*. Thermo RGL : Richardson Grating Laboratory, 2002.

[101] C. E. Webb and J. D. C. Jones, *Handbook of Laser Technology and Applications: Applications*. Institute of Physics, 2004.

[102] R. G. Hunsperger, *Integrated Optics: Theory and Technology*. Springer, 2009.

[103] A. Farina, I. Bargigia, P. Taroni, and A. Pifferi, “Note: comparison between a prism-based and an acousto-optic tunable filter-based spectrometer for diffusive media”, *Rev. Sci. Instrum.*, vol. 84, no. 1, p. 16109, 2013.

[104] P. Baumeister, *Optical Coating Technology*. SPIE Press, 2004.

[105] N. Boens, W. Qin, and N. Basaric, “Fluorescence lifetime standards for time and frequency domain fluorescence spectroscopy”, *Anal. Chem.*, vol. 79, no. 5, pp. 2137–2149, 2007.

[106] M. H. Sharpe and Irish D., “Stray light in diffraction grating monochromators”, *Opt. Acta Int. J. Opt.*, vol. 25, no. 9, pp. 861–893, 1978.

[107] T. N. Woods, R. T. Wrigley III, G. J. Rottman, and R. E. Haring, “Scattered-light properties of diffraction gratings”, *Appl. Opt.*, vol. 33, no. 19, pp. 4273–4285, 1994.

[108] P. Fornasini, *The Uncertainty in Physical Measurements: An Introduction to Data Analysis in the Physics Laboratory*. Springer, 2008.

[109] R. H. Ritchie, E. T. Arakawa, J. J. Cowan, and R. N. Hamm, “Surface-plasmon resonance effect in grating diffraction”, *Phys. Rev. Lett.*, vol. 21, no. 22, p. 1530, 1968.

[110] R. Fenske, D. U. Näther, M. Goossens, and S. D. Smith, “New light sources for time-correlated single-photon counting in commercially available spectrometers”, in *Optics East 2006*, 2006, p. 63720H–63720H.

[111] R. Fenske, D. U. Näther, R. B. Dennis, and S. D. Smith, “The supercontinuum laser as a flexible source for quasi-steady state and time resolved fluorescence studies”, in *SPIE LASE*, 2010, p. 75800R–75800R.

[112] R. Fenske, D. Nather, and S. Smith, “Monochromator comprising variable wavelength selector in combination with tunable interference filter”, *US Pat. App. 13/123,931*, 2009.